ON THE RELATIONSHIP BETWEEN MICROSTRUCTURE MECHANICAL PROPERTIES AND WELD METAL HYDROGEN ASSISTED COLD CRACKING

---

by

Walter L. Costin, B.Sc., M.Sc.

A thesis submitted for the degree of Doctor of Philosophy at the

School of Mechanical Engineering

The University of Adelaide

Australia

Submitted:

Accepted:

ABSTRACT

Hydrogen introduced during shielded metal arc welding with cellulosic welding consumables can severely degrade the fracture resistance of the deposited weld metal and promote Weld Metal Hydrogen Assisted Cold Cracking (WM HACC), which is a particular type of weld defect with distinctive characteristics. Failure typically occurs after the deposited weld has cooled down to temperatures below 200°C and can initiate within minutes to even days after welding. Due to its time-delayed nature the onset of WM HACC may be undetected and can result in catastrophic failure.

Many important properties of weld metal such as strength, toughness and the resistance to WM HACC are a function of its microstructure, comprised of diverse constituents with characteristic features and different mechanical properties, which co-exist and interact at the smallest microstructural dimensions. Hence, conventional test methods used to determine the bulk material's properties are not suitable to evaluate the intrinsic properties of its individual microstructural constituents. Because of these experimental limitations, there is a lack of understanding of microstructural aspects that control the mechanical properties and the resistance to HACC at the micro-scale.

Therefore, a major objective of the current work was to address these limitations by employing advanced characterisation and micro-mechanical testing techniques to evaluate the fundamental link between microstructure, mechanical properties and HACC susceptibility for individual weld metal microstructural constituents.

This first part of the work examined the microstructure and mechanical properties of acicular ferrite and upper bainite in weld metal. Two localised microstructural regions, one acicular ferrite and the other one upper bainite, were first selected and then characterised using a high-resolution Scanning Electron Microscope (SEM) and Electron Backscattered Diffraction

(EBSD). Semi-empirical models, based on microstructural aspects and physical principles, were used to determine the theoretical yield strengths of both microstructures. Different micro-mechanical tests were then conducted within each of the initially selected microstructural regions to characterise their intrinsic mechanical properties. Conventional nanoindentation and an advanced characterisation procedure were employed to obtain the yield strength, hardness, elastic modulus and strain hardening exponent. Micro-fracture tests in combination with linear and non-linear approaches of fracture mechanics were used to evaluate the deformation behaviour, fracture behaviour and fracture resistance. This study provided experimental evidence for a direct link between the microstructure and yield strength of acicular ferrite and upper bainite. It was thereby possible to identify the individual contributions of particular microstructural features. Furthermore, the relationship between strength, hardness and toughness was evaluated for both microstructures and the elastic and plastic components of their CTOD's, could be identified. The results also showed that the fracture toughness values measured in microscopic regions of acicular ferrite and upper bainite were at least by an order of magnitude lower than the typical range for the fracture toughness of steels, obtained from conventional fracture tests. This may result from the fact that micro-fracture tests imply small specimen dimensions, which could cause a confinement of plastic deformations that contribute significantly to the fracture resistance. The results may also indicate that not all fracture toughening mechanisms are activated at the micro-scale. Nevertheless, it is worth noting that the fracture toughness values measured in this work, for a relatively ductile material, are higher than those reported for brittle and semi-brittle materials, tested with similar methods at the micro-scale. In the current literature, at such small scales, no empirical data on the fracture toughness of specific microstructural constituents in weld metal is available. Hence, it was not possible to directly verify the results.

The second part of the work examined the microstructure and HACC propagation resistance of acicular ferrite and upper bainite in weld metal. A modified version of the Welding Institute of

Canada (WIC) weldability test was employed to generate WM HACC under controlled conditions. The hydrogen crack propagation through selected microstructural regions of acicular ferrite and upper bainite was then characterised using EBSD. Where The Unit Crack Path (UCP) was utilised as a parameter to evaluate the HACC propagation resistance of both microstructures. Fractographic observations were conducted with a high resolution SEM, to characterise the fracture behaviour in the selected microstructural regions. The investigations showed that HACC propagates along a path of least resistance through the surrounding microstructure, where the UCP was significantly shorter for acicular ferrite than for upper bainite, thereby implying more frequent changes in direction and thus increased dissipation of energy from the crack driving force. The results indicate that acicular ferrite, increases the localised resistance to HACC propagation more than upper bainite, despite its higher strength, hardness and lower fracture toughness, which are all properties usually considered to be detrimental for the HACC resistance of the bulk material. The outcomes of this study suggest that macroscopic observations of the correlation between mechanical properties and HACC susceptibility are not necessarily applicable at the micro-scale. Which also implies that mechanical properties per se are not a good indicator of absolute HACC susceptibility and in fact may be misleading in terms of the intrinsic susceptibility of particular microstructural constituents.

The third part of the work examined the microstructure and HACC initiation resistance of acicular ferrite in weld metal. A selected microscopic region of acicular ferrite was characterised using a high resolution SEM in combination with EBSD. Micro-fracture tests were then conducted at different loads on a hydrogen pre-charged specimen, that was fabricated into the selected region with a Focused Ion Beam (FIB). Linear Elastic Fracture Mechanics (LEFM) was applied to determine the range for the threshold stress intensity factor, K_{th}, to initiate HACC. The microstructure, deformation behaviour as well as the fracture behaviour were examined and compared with the data obtained from first part of the work, where a micro-

fracture test was conducted on an uncharged specimen, that was fabricated into the same region of acicular ferrite. This study showed that the obtained range for the threshold stress intensity factor of acicular ferrite was well below the threshold values for weld metal as well as low and medium carbon steels with similar yield strengths. This indicates that, at the micro-scale, hydrogen cracks can grow at stress intensity factors well below the threshold values measured with conventional tests at the macro-scale. It seems that also in this case critical fracture toughening mechanisms may not be activated if the specimen dimensions are very small. The crack growth rate in acicular ferrite, also appeared to be significantly lower than typically observed for the bulk material. Besides plastic deformations during fracture and the threshold stress intensity to initiate fracture, the yield strength and the Young's modulus also decreased due to the presence of hydrogen, which correlates well with previous observations and proposed hydrogen embrittlement models.

DECLARATION

I certify that this work contains no material which has been accepted for the award of any other degree or diploma in my name, in any university or other tertiary institution and, to the best of my knowledge and belief, contains no material previously published or written by another person, except where due reference has been made in the text. In addition, I certify that no part of this work will, in the future, be used in a submission in my name, for any other degree or diploma in any university or other tertiary institution without the prior approval of the University of Adelaide and where applicable, any partner institution responsible for the joint-award of this degree.

I give consent to this copy of my thesis, when deposited in the University Library, being made available for loan and photocopying, subject to the provisions of the Copyright Act 1968.

The author acknowledges that copyright of published works contained within this thesis resides with the copyright holder(s) of those works.

I also give permission for the digital version of my thesis to be made available on the web, via the University's digital research repository, the Library Search and also through web search engines, unless permission has been granted by the University to restrict access for a period of time.

I acknowledge the support I have received for my research through the provision of an Australian Government Research Training Program Scholarship.

09/01/2017

Walter L. Costin Date

LIST OF PUBLICATIONS

The following journal and conference publications were completed as part of this research.

Journal publications:

Costin, W.L., Lavigne, O., Kotousov, A. 2016, "A study on the relationship between microstructure and mechanical properties of acicular ferrite and upper bainite," Materials Science and Engineering: A 663, pp. 193-203.

Costin, W.L., Lavigne, O., Kotousov, A., Ghomashchi, R., and Linton, V., 2016, "Investigation of hydrogen assisted cracking in acicular ferrite using site-specific micro-fracture tests," Materials Science and Engineering: A, 651, pp. 859-868.

Costin, W.L & Basak, AK 2015, 'Micro-micromechanical Properties of Weld Metal', Microscopy and Microanalysis, vol. 21, no. S3, pp. 2159-2160.

Ghomashchi, R, Costin, W.L. & Kurji, RN 2015, 'Evolution of weld metal microstructure in shielded metal arc welding of X70 HSLA steel with cellulosic electrodes: A case study', Materials Characterization, vol. 107, 9//, pp. 317-326.

Lavigne, O, Gamboa, E, Costin, W. L., Law, M, Luzin, V, Linton, V 2014, 'Microstructural and mechanical factors influencing high pH stress corrosion cracking susceptibility of low carbon line pipe steel', Materials Science & Engineering A.

Lavigne, O, Gamboa, E, Luzin, V, Law, M, Giuliani, M & Costin, W.L. 2014, 'The effect of the crystallographic texture on intergranular stress corrosion crack paths', Materials Science and Engineering: A, vol. 618, pp. 305-309.

Conference publications:

Costin, WL, Lavigne, O & Kotousov, A 2016, 'Characterisation of fracture and HAC resistance of an individual microstructural constituent with micro-cantilever testing', 15th International Conference on Fracture and Damage Mechanics, Key Engineering Materials, Alicante, Spain, vol. 713, pp. 66-69.

Costin, W.L. & Kotousov, A 2014, 'Testing localized microstructural architectures with miniaturised cantilever beams A2 - Ye, Lin', Recent Advances in Structural Integrity Analysis - Proceedings of the International Congress (APCF/SIF-2014), Woodhead Publishing, Oxford, pp. 590-594.

Costin, W.L., Lavigne, O, Linton, V, Brown, I.H., Kotousov, A, Barbaro, F.J. & Ghomashchi, R 2013, 'Micromechanical examination of the relationship between weld metal microstructure and Hydrogen Assisted Cold Cracking', paper presented at 6th Pipeline Technology Conference, Ostend, Belgium, 7–9 October 2013.

Costin, W.L., Brown, I.H., Green, L & Ghomashchi, R 2012, 'Application of FIB/SEM/EBSD for evaluation of residual strains and their relationship to weld metal hydrogen assisted cold cracking', 2012 9th International Pipeline Conference, American Society of Mechanical Engineers, pp. 343-353.

Brown, I.H., Costin, W.L., Barbaro, F & Ghomashchi, R 2012, 'Application of SEM-EBSD for measurement of plastic strain fields associated with weld metal hydrogen assisted cold cracking', 2012 9th International Pipeline Conference, American Society of Mechanical Engineers, pp. 335-341.

ACKNOWLEDGEMENTS

This work was funded by the Energy Pipelines CRC, supported through the Australian Government's Cooperative Research Centres Program. The cash and in-kind support from APIA through its Research and Standards Committee is also gratefully acknowledged.

I would like to thank my supervisors Associate Professor Dr. Reza Ghomashchi, Associate Professor Dr. Andrei Kotousov and Mr Ian Brown as well as my industry advisors Professor Dr. Valerie Linton, Professor Dr. Frank Barbaro and Mr. Leigh Fletcher for their tireless support, discussions, and general guidance throughout my candidature.

Thanks to Dr. Olivier Lavigne, Dr. Nicolas Coniglio, Dr. Erwin Gamboa, Mr. Rahim Kurji and Mr. Krzysztof Borkowski for their support, inspiration and insightful discussions.

Special thanks are also due to Adelaide Microscopy, its former director Mr John Terlet its current director Dr Angus Netting, Mr Leonard Green and Dr. Animesh Basak. Without their dedication and wealth of knowledge this work would not have been possible.

TABLE OF CONTENTS

LIST OF FIGURES

LIST OF TABLES

LIST OF EQUATIONS

LIST OF ABBREVIATIONS

AIDE	Adsorption Induced Dislocation Emission
B	Bainite
B(GB)	Grain Boundary Bainite
B(I)	Intragranular Bainite
B-AF	Bainitic Acicular Ferrite
bcc	Body Centred Cubic
B-FP(I)	Intragranular Bainite Plates
B-FS(A)	Bainitic Ferrite with Aligned Carbide
B-FS(I)	Intragranular Bainite Sheaves
B-FS(LB)	Lower Bainite
B-FS(NA)	Bainitic Ferrite with Non-Aligned Carbide
B-FS(UB)	Upper Bainite
BSE	Backscattered Electrons
CR	Centre of Rotation
CSL	Coincident Site Lattice
COA	Crack Opening Angle
CTOD	Crack Tip Opening Displacement
EBSD	Electron Backscattered Diffraction
EBSP	Electron Backscatter Diffraction Pattern
ECAD	Equivalent Circular Area Diameter
EPFM	Elastic-Plastic Fracture Mechanics
fcc	Face Centred Cubic

FE	Field Emission
Fe_3C	Cementite
FIB	Focused Ion Beam
GD-OES	Glow Discharge Optical Emission Spectroscopy
H	Hydrogen
HAC	Hydrogen Assisted Cracking
HACC	Hydrogen Assisted Cold Cracking
HAGB	High Angle Grain Boundary
HASCC	Hydrogen Assisted Stress Corrosion Cracking
HAZ	Heat Affected Zone
HE	Hydrogen Embrittlement
HEAC	Hydrogen Environment Assisted Cracking
HEDE	Hydrogen Enhanced Decohesion
HELP	Hydrogen Enhanced Localized Plasticity
HSLA	High Strength Low Alloyed
H	Hardness
HV	Hardness Vickers
IPF	Inverse Pole Figure
IHAC	Internal Hydrogen Assisted Cracking
ISE	Ion-Induced Secondary Electrons
IQ	Image Quality
LAGB	Low Angle Grain Boundary
LEFM	Linear Elastic Fracture Mechanics
LI	Linear Intercept

LME	Liquid Metal Embrittlement
M	Martensite
M(L)	Lath Martensite
M(T)	Twin Martensite
M-A-C	Martensite-Austenite-Carbide
MVC	Microvoid Coalescence
NMI	Non Metallic Inclusion
OM	Optical Microscopy
P	Pearlite
PF	Primary Ferrite
PF(GB), PF(G)	Grain Boundary Primary Ferrite
PF(I)	Idiomorphic Ferrite
PF(NA)	Primary Ferrite Non Aligned
P-FC	Ferrite/Carbide Aggregate
P-FC(P)	Fine Colony Pearlite
RA	Retained Austenite
ROI	Region of Interest
SE	Secondary Electrons
SEM	Scanning Electron Microscope
SENB	Single-Edge Notched Beam
SMAW	Shielded Metal Arc Welding
SRIM	Stopping and Range of Ions into Matter
TEM	Transmission Electron Microscope
TRIM	Transport and Range of Ions into Matter

UCP	Unit Crack Path
W-AF	Widmanstätten Acicular Ferrite
WF	Widmanstätten Ferrite
WF(GB)	Grain Boundary Widmanstätten Ferrite
WF(I)	Intragranular Widmanstätten Ferrite
W-FP(I)	Intragranular Widmanstätten Ferrite Plates
W-FS(A)	Widmanstätten Ferrite with Aligned Microphase
W-FS(I)	Intragranular Widmanstätten Ferrite Sideplates
W-FS(NA)	Widmanstätten Ferrite with Non-Aligned Microphase
WIC	Welding Institute of Canada
WM	Weld Metal
WTIA	Welding Technology Institute of Australia

LIST OF SYMBOLS

A	projected area of indentation contact
a	notch depth of micro-beam
a_n	crack mouth opening
b	height of micro-beam
C	curvature of the indentation loading curve
C_H	hydrogen concentration for charging procedure
d	diameter
d_{hkl}	spacing of diffracting planes
d_p	size of the plastic zone
E	Young's modulus
E^*	reduced Young's modulus
E_P	ion energy
F	Faraday constant
F	dimensionless shape factor
G	crack extension force LEFM
H	WIC test plate thickness
h	indentation depth
h_W	height of weld metal throat
h_m	maximum indentation depth
I	moment of inertia
l	restraint length for WIC test
I(t)	oxidation current

$I_H(t)$	oxidation current for hydrogen charged specimen
$I_{ref}(t)$	oxidation current for uncharged specimen
J	crack extension force EPFM
K_c	fracture toughness
K_I	stress intensity factor
K_D	function for strengthening due to dislocations
$K_L\{L\}$	function for strengthening due to grain size
K_Q	conditional fracture toughness
K_{th}	threshold stress intensity factor
k_Y	Hall–Petch slope
M_1	mass of incident ion
M_2	mass of target atom
n	strain hardening exponent
P_m	maximum load
P_Q	applied load at a critical point
P_C	critical load at failure
P_{H_2}	hydrogen pressure
P	load
P_u	unloading force during indentation test
Q_H^{abs}	quantity of absorbed hydrogen
R	strength coefficient
$R_{p0.2}$	offset yield point
R_F	restrained intensity
R_p	projected range of implanted ions

R_l	lateral range of implanted ions
r_e	rotation factor
S_n	nuclear stopping power
U_S	surface binding energy
v	effective specimen volume
w	width of micro-beam
Y	sputter yield
z	number of electrons
α	ferrite
γ	austenite
γ_p	fracture energy
Δa	increase of crack length
$\Delta\theta$	allowable angular deviation
$\Delta\delta$	Increase in Crack Opening
δ_p	plastic component of CTOD
δ_e	elastic component of CTOD
ε	strain
θ_{hkl}	angle of incidence on the diffracting planes
λ	wavelength of electrons
ν	Poisson’s ratio
ρ_D	dislocation density
Σ	degree of fit between the structures of the two grains
σ_0	lattice friction stress
σ_C	strengthening due to carbon

σ_D	strengthening contributions due to dislocation density
σ_{Fe}	strength of pure annealed iron
σ_{GS}	strengthening contributions due to grain size
σ_{LS}	strengthening contributions due to lath size
σ_P	strengthening contributions due to cementite
σ_R	restraint stress for WIC test
σ_{SS_i}	substitutional solute strengthening
σ_Y	yield strength

CHAPTER 1

INTRODUCTION

1 Introduction

1.1 General Background

Shielded metal arc welding (SMAW) with cellulosic welding consumables is traditionally used for “stovepipe” welding of steel gas transmission pipelines in Australia. This manual metal arc welding technique, used with cellulosic welding electrodes, offers unique productivity advantages and is therefore part of a well-established process for pipeline girth weld production for small and medium pipeline diameters.

Pipelines are constructed from a variety of strength steel grades, and pipelines made from higher strength steels require the use of higher strength welding electrodes to match the pipe strength. For pipelines manufactured from API 5L Grade X70 pipe, this process involves the use of E6010 (cellulosic) electrodes usually without preheat for the root pass, and E8010 (cellulosic) electrodes for subsequent passes (Fletcher & Yurioka 2000). The high moisture content in the cellulosic flux of the electrode decomposes during welding and thereby produces a gaseous shield, rich in hydrogen. This hydrogen gas provides a high arc force which allows high welding speeds due to an improved penetration of the arc (Weaver & Ogborn 2005). However, hydrogen also dissolves in the molten weld pool and, as a result of its reduced solubility in steel after solidification, it can diffuse to various regions within the weld and degrade the fracture resistance leading to hydrogen assisted cold cracking (Yurioka & Suzuki 1990).

Hydrogen Assisted Cold Cracking (HACC), also referred to as delayed cracking or cold cracking, is a weld defect with unique characteristics. Failure typically occurs in the heat affected zone (HAZ) of the parent metal or in the weld metal (WM) after the deposited weld

has cooled down to temperatures below 200°C and can initiate within minutes to even days after welding (Yurioka & Suzuki 1990). Due to its time delayed nature the onset of HACC may remain undetected and could result in catastrophic failure. Therefore, from a structural integrity point of view HACC is perhaps the most serious of all pipeline welding problems (Barbaro 1999).

Prior to the utilization of modern high strength low-alloyed (HSLA) steels, HACC usually occurred in the HAZ of the parent metal. However, the trend to reduce the carbon content and carbon equivalent in these high strength steels has considerably reduced the risk of HAZ HACC (Yurioka & Suzuki 1990). Nevertheless, as illustrated in Figure 1, the advanced alloy design has also raised the austenite (γ-Fe) to ferrite (α-Fe) transformation temperature in the HAZ to a point where it is now believed that despite the direction of the temperature gradient, the decomposition of γ-Fe occurs first in the HAZ and not in the WM (Barbaro 1999).

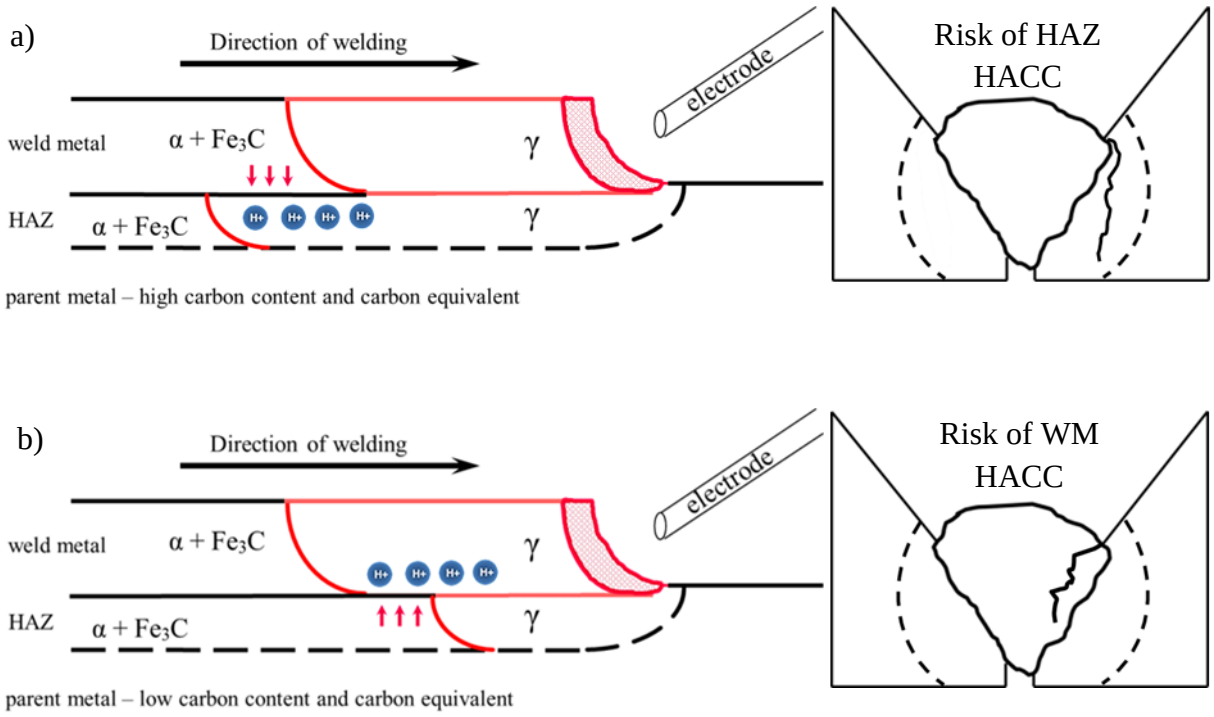

Figure 1: Schematic diagrams illustrating the redistribution of hydrogen when:

a) The γ-Fe /α-Fe transformation temp. is lower in the HAZ than in the WM,

b) The γ-Fe /α-Fe transformation temp. is higher in the HAZ than in the WM;

As shown in previous studies (Kuzmikova et al. 2012; Olson, D.L.R. et al. 1996), the difference in the γ-Fe → α-Fe transformation temperature between WM and HAZ determines the direction of the hydrogen diffusion within a particular temperature range as the deposited weld solidifies. This is mainly because in body centred cubic (bcc) α-Fe the hydrogen solubility is lower while the diffusivity is higher than in face centred cubic (fcc) γ-Fe. Therefore, in modern HSLA steels, during cooling hydrogen may be rejected from the HAZ (α-Fe) and diffuse towards the WM (γ-Fe), which acts as a hydrogen sink and thereby increases the risk of WM HACC (see Figure 1) (Barbaro 1999).

Extensive research work lead to the development of the WTIA Technical Note 1: The weldability of steels. This document outlines a methodology for selecting welding parameters so that HAZ HACC can be avoided when welding carbon steels, including pipeline steels. However, neither Technical Note 1 nor any of the current HACC management and avoidance strategies are capable of predicting and therefore providing comprehensive information on avoiding WM HACC in practice (Fletcher 1999).

Overall, there is very little information on the risk of weld metal hydrogen cracking which can provide a basis for the derivation of safe welding conditions. Therefore, currently significant research efforts are devoted to a better understanding of weld metal hydrogen cracking with the aim of developing guidance for industry, so that the risk of WM HACC can be minimized.

1.2 Motivation

There is a general agreement in the literature that HACC only occurs at temperatures below 200°C if all three of the following causal conditions are present simultaneously (Davidson, JL, Lynch & Majumdar 1997; Yurioka & Suzuki 1990):

i. Critical hydrogen concentration,

ii. Critical triaxial tensile stress,

iii. Crack susceptible microstructure.

The schematic illustration in Figure 2 depicts the main interactions that promote HACC if all of the above mentioned causal conditions are satisfied.

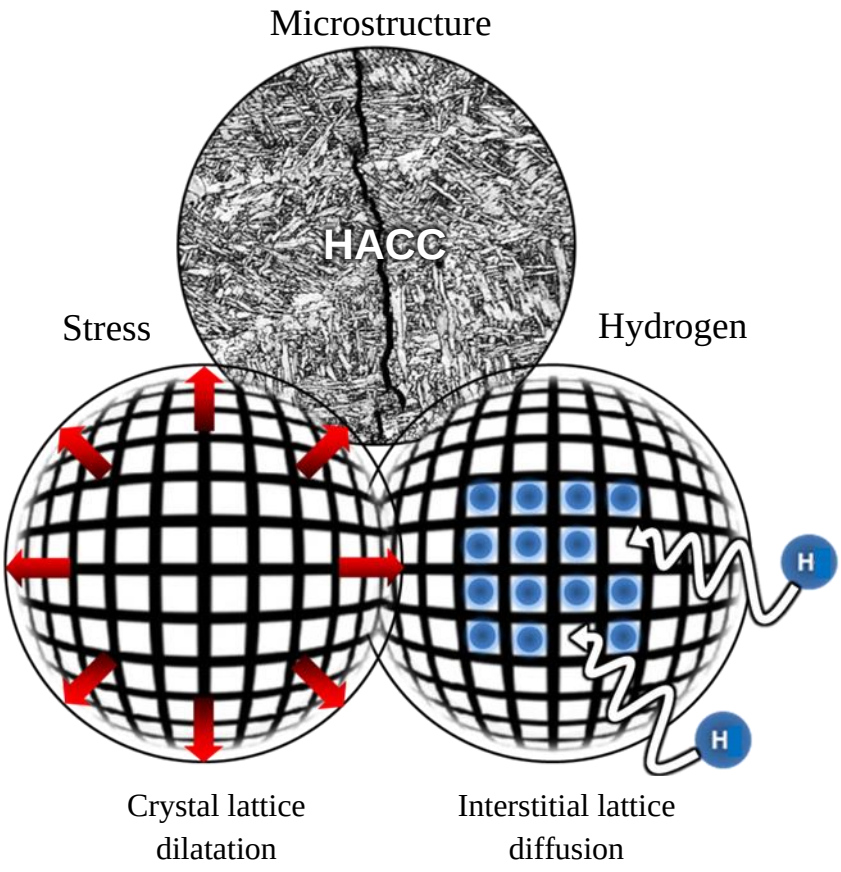

Figure 2: Simplified illustration describing the main interactions promoting HACC formation.

An important feature of the dissolved monoatomic hydrogen is its ability to diffuse through the lattice of most metals and alloys even at ambient temperatures (Yurioka & Suzuki 1990). Hydrogen atoms are small enough to fit into the interstitial lattice positions and can

therefore migrate from one empty interstitial site to another one, which at dilute concentrations does not require the formation of vacancies (Kirchheim 2004).

Since hydrogen atoms occupy a specific molar volume within interstitial lattice sites, they tend to migrate from compressed to expanded regions within the crystal lattice until an equilibrium concentration profile is established (Kirchheim 2004). Triaxial tensile stresses are hence a driving force for interstitial lattice diffusion of hydrogen towards the dilatation zone, where hydrogen may accumulate and thereby incrementally degrade the localised fracture resistance of the weld metal (Bernstein 1970).

Various, often controversial, views have been proposed to describe the physical mechanisms by which hydrogen affects plasticity and degrades the fracture resistance in metals (Birnbaum & Sofronis 1994; Lynch 1989; Troiano 1960). However, all these proposed hydrogen embrittlement mechanisms explain physical processes that operate at atomic scales and are mainly based on models that consider simple, ideal situations which are in many cases difficult to validate experimentally (Barnoush & Vehoff 2010).

Nevertheless, it is known that fracture occurs when the critical hydrogen concentration for either crack initiation or propagation is exceeded (Gangloff 2003). The critical hydrogen concentration will thereby depend on both, the local stress intensity and the susceptibility of the microstructure (Barbaro 1999).

Despite a vast number of theoretical and experimental studies it still remains unclear which particular aspects of the weld metal microstructure define its susceptibility to HACC (Alam et al. 1996; Davidson, JL, Lynch & Majumdar 1997; Wildash 1999). The weld metal microstructure is particularly complex and consists of diverse constituents with characteristic features and different mechanical properties (see Figure 3 a) and Figure 3 b)). However, such features only occur in small material volumes, within the micrometre regime in size and are not directly assessable with conventional macroscopic test methods. Because of these experimental

limitations, there is a lack of understanding of the microstructural factors that control properties such as strength, toughness and WM HACC resistance at the smallest microstructural dimensions.

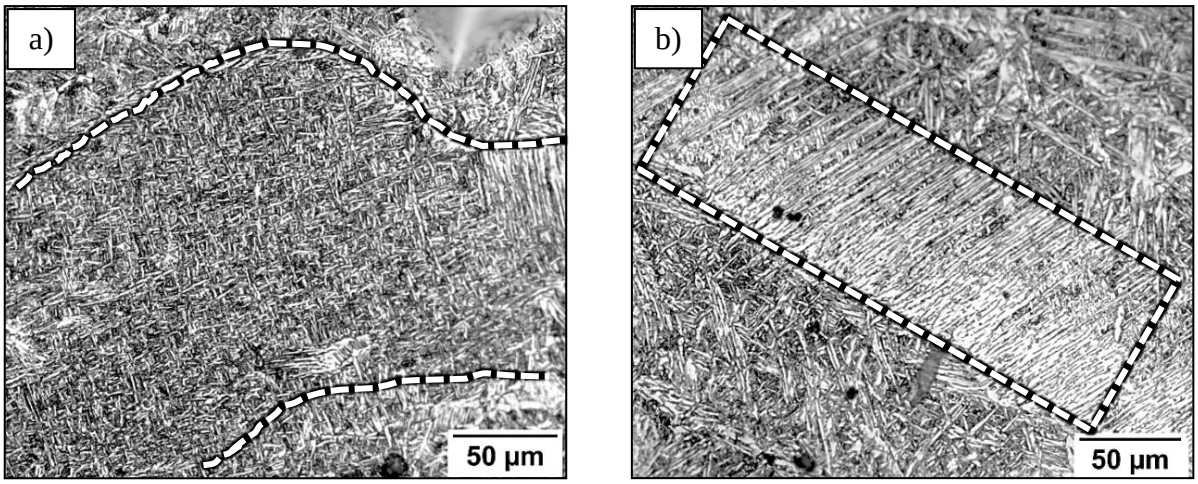

Figure 3: Optical micrographs obtained from a 2% Nital etched weld metal specimen deposited with E 6010 cellulosic consumables illustrating the unique architectures of discrete microstructural constituents. The microstructural constituents shown (regions encompassed by the broken lines) here are:

a) Acicular ferrite,
b) Upper bainite;

Recent developments in advanced characterisation and micro-mechanical testing techniques as allow to evaluate the fundamental link between microstructure, mechanical properties and HACC susceptibility for individual weld metal microstructural constituents.

1.3 Research Objectives

The main objective of the current research is to investigate the relationship between the microstructure, mechanical properties and HACC susceptibility of particular weld metal microstructural constituents. In this regard, two common microstructural constituents of ferritic

weld metal, acicular ferrite and upper bainite, will be examined. The main challenge is to establish an experimental procedure where the properties of such phases can be studied in isolation. However, since the production of weld metal solely comprised of a specific microstructural constituent is not feasible experimentally, the tests should be carried out in-situ on weld specimens fabricated conventionally, by employing micro-mechanical tests with the capability of isolating the microstructural constituents of interest. Therefore, to overcome this difficult challenge, the objectives are chronologically specified below:

i. To undertake a literature review to provide a comprehensive update on the body of knowledge on the microstructural factors that control strength, toughness and the susceptibility to WM HACC,

ii. To undertake a literature review to provide a comprehensive update on the body of knowledge on Hydrogen Embrittlement (HE) mechanisms,

iii. To provide an update on recent advances in micro-mechanical testing,

iv. To adapt and develop techniques that can be utilised as a tool to probe both the intrinsic mechanical properties as well as the WM HACC resistance of discrete microstructural constituents,

v. To employ these techniques to provide new insight into the fundamental microstructural aspects that control the mechanical properties as well as the WM HACC susceptibility,

vi. To evaluate the possible mechanisms that operate during the onset of WM HACC;

CHAPTER 2

LITERATURE REVIEW

2 Literature Review

2.1 Ferritic Weld Metal Microstructures

For ferritic weld metal, the decomposition of austenite typically results in a complex microstructure with diverse constituents. This section gives a brief overview of the most common principal microstructural constituents in the weld metal and provides some basic information on the particular nucleation sites as well as on the characteristic morphologies. In weld metal research difficulties were often encountered in comparing microstructural data by various authors, either due to differences in interpretation or simply due to inconsistent terminologies. In response to the problem, a number of schemes have been proposed to allow a consistent qualitative and quantitative assessment of weld metal microstructures (Dolby 1986; IIW 1988; Widgery 1976). In the current work, all the terminologies, abbreviations as well as the identification of individual microstructural constituents were based on a classification scheme proposed by Thewlis (Thewlis 2004).

2.1.1 Overview and Terminologies

On cooling from the molten state, after the transformation from δ-ferrite to γ-austenite, allotriomorphic ferrite is the first phase to form below the Ae_3 temperature where austenite becomes unstable and the decomposition begins. As illustrated in Figure 4, this phase nucleates at the austenite grain boundaries. At lower temperatures, ferrite may also begin to nucleate on inclusions within the austenite grains which is then referred to as idiomorphic ferrite (Thewlis 2004). The classification scheme of Thewlis refers to both phases as primary ferrite (see Table 1).

Abbreviations			Terminologies	Description
Overall	Main	Sub		
Primary Ferrite PF	PF(GB)	PF(GB)	Grain boundary primary ferrite, Allotriomorphic ferrite, Polygonal ferrite, Ferrite veins	*Ferrite veins or polygonal grains aligned with prior austenite grain boundaries.*
		PF(NA)	Polygonal primary ferrite non aligned	*Polygonal ferrite grains within the prior austenite grains, of a size approximately three times greater than the surrounding ferrite laths or grains. These are cross-sections of ferrite allotriomorphs that have grown from prior austenite grain boundaries below the plane of observation.*
	PF(I)	PF(I)	Idiomorphic ferrite	*Ferrite idiomorphs associated with intragranular nucleation sites (large oxide/sulphide inclusions).*

Table 1: Classification scheme for primary ferrite (Thewlis 2004).

Pearlite transformation may occur at the austenite grain boundaries or at inhomogeneities such as inclusions (Bhadeshia & Honeycombe 2011). At high transformation temperatures, pearlite forms nodules of alternate ferrite and cementite lamellae that may be quite coarse. As the transformation temperature is lowered, the lamellae become increasingly finer until the structure becomes irresolvable under the light microscope (Thewlis 2004). Alternatively, distorted lamellae may appear as virtually irresolvable ferrite/carbide aggregate (Thewlis 2004).

Abbreviations			Terminologies	Description
Overall	Main	Sub		
Pearlite P	P	FC(P)	Lamellar pearlite, Degenerated pearlite, Fine colony pearlite	*Nodules of alternate ferrite/cementite lamellae, which are often difficult to resolve under the optical microscope. The structure has a rapid etching response in 2% Nital and a generally low hardness. Pearlite may be present as a microphase.*
		FC	Ferrite/carbide aggregate	*Pearlite lamellae viewed in cross-section. Distorted pearlite lamellae may appear as a dark etching virtually irresolvable ferrite/carbide aggregate.*

Table 2: Classification scheme for Pearlite (Thewlis 2004).

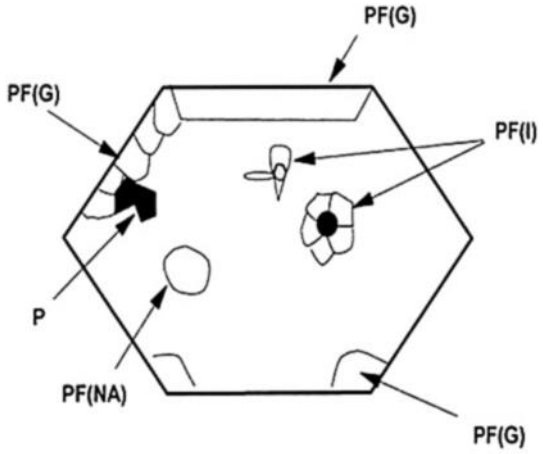

Figure 4: Schematic illustrates the different nucleation sites and morphologies for primary ferrite and pearlite. Adapted from (Thewlis 2004).

There are two types of Widmanstätten ferrite, primary and secondary. As illustrated in Figure 5, primary Widmanstätten ferrite plates grow directly from the prior austenite grain boundaries, whereas secondary Widmanstätten ferrite plates grow from allotriomorphic ferrite at the grain boundaries (Thewlis 2004). Primary Widmanstätten ferrite plates may also grow from inclusions, while secondary Widmanstätten ferrite plates can grow from intragranular idiomorphic ferrite (Thewlis 2004).

Acicular ferrite nucleates intragranularly from inclusions within the prior austenite grains and is characterised by fine ferrite plates (diameter typically < 5 μm) that form an interlocking morphology (see Figure 5) (Bhadeshia 2001). For a long time, acicular ferrite was considered to be a single transformation product. Early studies suggested that it was intragranularly nucleated Widmanstätten ferrite (Ricks, Howell & Barritte 1982). Later research provided evidence for intragranularly nucleated bainitic acicular ferrite (Bhadeshia 2001).

However, more recent investigations demonstrated that different reaction products may nucleate on intragranular inclusions at reconstructive (diffusion-based) and displacive (diffusionless) transformation temperatures during continuous cooling depending on the nature,

size and amount of inclusions (Thewlis 2004). Hence, acicular ferrite may be comprised of a mixture of different intragranular transformation products such as idiomorphic ferrite, intragranular Widmanstätten ferrite and intragranular bainite (Thewlis 2004). Alternatively, Widmanstätten acicular ferrite or bainitic acicular ferrite may form by itself (Bhadeshia 2001; Ricks, Howell & Barritte 1982). However, in the current study it was not possible to distinguish between Widmanstätten acicular ferrite and bainitic acicular ferrite. Therefore, the only distinction made was between acicular ferrite and other intragranular transformation products.

Abbreviations			**Terminologies**	**Description**
Overall	Main	Sub		
Widman-stätten ferrite WF	WF(GB)	FS(A)	Widmanstätten ferrite with aligned microphase, Widmanstätten ferrite sideplates	*Colonies of parallel ferrite laths (or sideplates) with microphases aligned between the laths ranging from pearlite to martensite. Lath boundaries are difficult to resolve. Primary Widmanstätten ferrite grows from the prior austenite grain boundaries, whereas secondary Widmanstätten ferrite grows from allotriomorphic ferrite at the boundary.*
		FS(NA)	Widmanstätten ferrite with non-aligned microphase	*Aggregate of microphase islands and Widmanstätten ferrite within the prior austenite grains. These are cross-sections of Widmanstätten ferrite sideplates that grow from prior austenite grain boundaries below the plane of observation.*
	WF(I)	FS(I)	Intragranular Widmanstätten ferrite sideplates	*Multiple coarse Widmanstätten ferrite plates (aspect ratio greater than 4:1) with aligned microphases, which grow from intragranular inclusions. Primary intragranular ferrite sideplates grow from inclusions, whereas secondary sideplates grow from ferrite idiomorphs associated with inclusions.*
		FP(I)	Intragranular Widmanstätten ferrite plates	*Individual coarse plates of Widmanstätten ferrite growing relatively unimpeded from intragranular inclusions.*
		AF	Widmanstätten acicular ferrite	*Fine interlocking structure formed by multiple impingements of individual Widmanstätten ferrite plates growing from intragranular inclusions.*

Table 3: Classification scheme for Widmanstätten ferrite (Thewlis 2004).

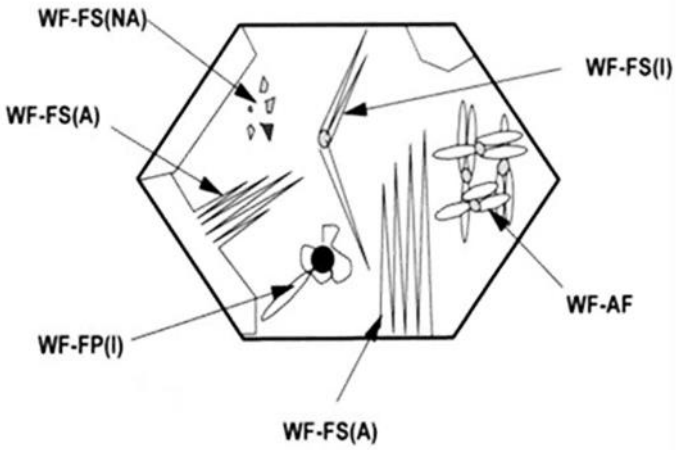

Figure 5: Schematic illustrates typical nucleation sites and morphologies for Widmanstätten ferrite. Adapted from (Thewlis 2004).

Bainite grows as individual plates or sub-units that can form sheaves of parallel ferrite laths which can be categorised as either upper or lower bainite, depending on the transformation temperature (Bhadeshia & Honeycombe 2011). As shown in Figure 6, in upper bainite, carbon precipitates as cementite (Fe_3C) between the bainitic ferrite plates. In lower bainite, the ferrite becomes supersaturated with carbon and some carbide precipitation occurs within the ferrite sub-units as well as between them (Bhadeshia & Honeycombe 2011). As illustrated in Figure 7, bainite may grow directly from prior austenite grain boundaries or from intragranular inclusions (Thewlis 2004).

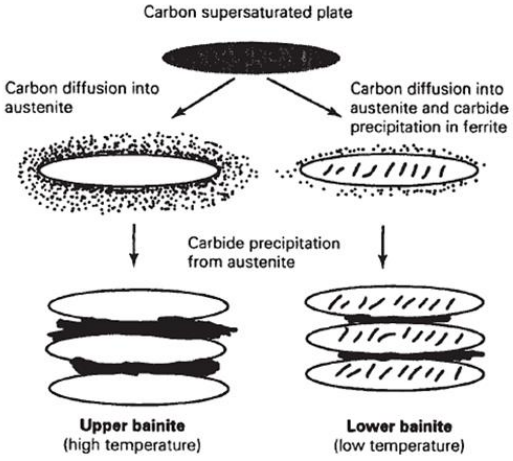

Figure 6: Schematic illustrates the formation of upper and lower bainite. Adapted from (Bhadeshia & Honeycombe 2011).

Abbreviations			Terminologies	Description
Overall	Main	Sub		
Bainite B	B(GB)	FS(A)	Bainitic ferrite with aligned carbide	*Sheaves of parallel ferrite laths (or sub-units) with Fe_3C particles aligned between the laths. Lath boundaries are generally irresolvable under the light microscope. Sheaves grow from prior austenite grain boundaries. A further distinction may be made where upper and lower bainite can be positively identified.*
		FS(NA)	Bainitic ferrite with non-aligned carbide	*Aggregate of coarse Fe_3C and bainitic ferrite within the prior austenite grains. These are cross-sections of bainite sheaves that grow from prior austenite grain boundaries (or existing sheaves) below the plane of observation.*
		FS(UB)	Upper Bainite	*Fe_3C particles are precipitated between the bainitic ferrite plates.*
		FS(LB)	Lower Bainite	*Fine Fe_3C particles precipitated within as well as between bainitic ferrite plates. Lower bainite has a generally darker etching response than upper bainite.*
	B(I)	FS(I)	Intragranular bainite sheaves	*Sheaves of fine bainitic ferrite plates with aligned Fe_3C, which grow from intragranular inclusions.*
		FP(I)	Intragranular bainite plates	*Individual fine plates of bainitic ferrite that grow relatively unimpeded from intragranular inclusions. No aligned Fe_3C.*
		AF	Bainitic acicular ferrite	*Very fine interlocking structure formed by multiple impingements of individual bainitic ferrite plates growing from intragranular inclusions. No aligned Fe_3C.*

Table 4: Classification scheme for Bainite (Thewlis 2004).

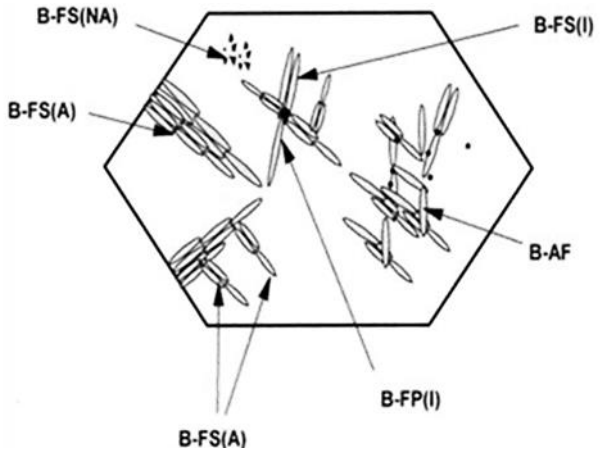

Figure 7: Schematic illustrates typical nucleation sites and morphologies for bainite. Adapted from (Thewlis 2004).

Martensite forms as a result of an extremely rapid, diffusionless transformations where carbon is retained in solution (Speich & Leslie 1972). Martensite can occur in the form of either laths or plates. The sub-structure of lath martensite is characterised by a high density of dislocations arranged in cells where each martensite lath is composed of many dislocation cells. The substructure of plate martensite consists of very fine twins. Hence, this form of martensite is also referred to as twinned martensite (Thewlis 2004).

Abbreviations			**Terminologies**	**Description**
Overall	Main	Sub		
Martensite M	M	M(L)	Lath martensite	*Low carbon martensite with a lath structure and heavily dislocated sub-structure. Lath martensite has a slow etching response in 2% Nital and a generally high hardness. Colonies of martensite may form within the prior austenite grains. Smaller colonies may be treated as microphases. Microphases may consist of martensite with retained austenite (M-A).*
		M(T)	Twinned martensite	*High carbon martensite with a plate structure and twinned sub-structure.*

Table 5: Classification scheme for martensite (Thewlis 2004).

Besides the above mentioned principal microstructural constituents, weld metal usually also contains second phase particles such as Non Metallic Inclusions (NMI's) or cementite as well as microphases like Retained Austenite (RA) and Martensite-Austenite-Carbide constituents (M-A-C) (Wildash 1999).

The flowcharts in Table 6 and Table 7 illustrate the standard procedure for the identification of the individual weld metal microstructural constituents, as proposed by Thewlis (Thewlis 2004). Where Table 6 describes the identification of constituents that typically form at the prior austenite grain boundaries and Table 7 that of intragranular constituents which usually form within the prior austenite grains.

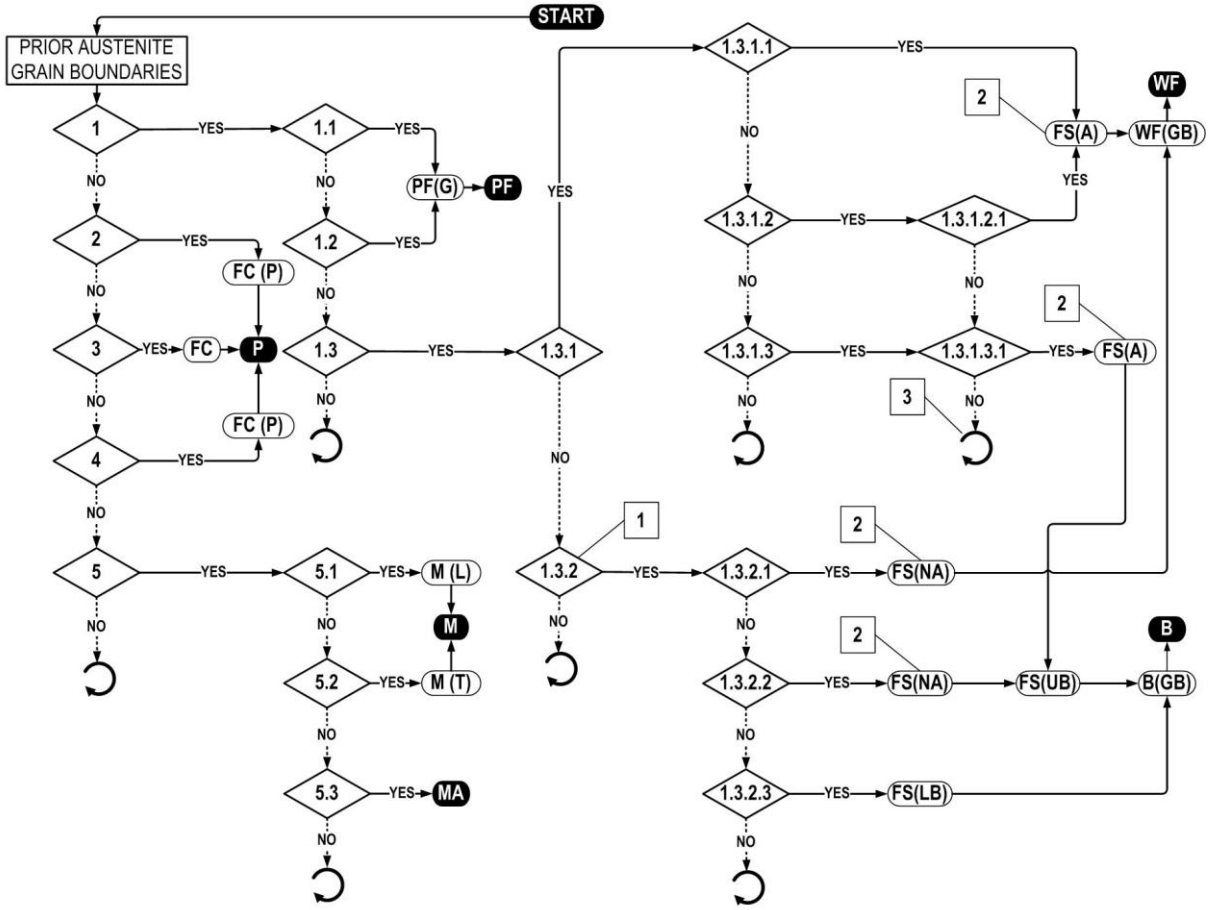

1: Is it ferrite?
- 1.1: Are the grains polygonal?
- 1.2: Are there veins of ferrite?
- 1.3: Is the ferrite constituent interspersed with second phase?
  - 1.3.1: Are there parallel ferrite plates or laths with aligned second phase?
    - 1.3.1.1: Are the ferrite plates coarse and grow from grain boundary ferrite allotriomorphs; are there sometimes faint low angle ferrite boundaries?
    - 1.3.1.2: Do the plates grow from prior austenite grain boundaries?
      - 1.3.1.2.1: Are there colonies of coarse ferrite plates with various microphases aligned between them; are there sometimes faint low angle ferrite boundaries?
    - 1.3.1.3: Do the plates grow sympathetically from existing plates?
      - 1.3.1.3.1: Are there sheaves of fine ferrite laths with particles aligned between them?
  - 1.3.2: Are there aggregates of ferrite and second phase within the austenite phase?
    - 1.3.2.1: Are there islands of various microphases in a matrix of ferrite; are there sometimes faint low angle ferrite boundaries?
    - 1.3.2.2: Are there course carbides in a matrix of ferrite?
    - 1.3.2.3: Are there fine carbides (aligned and non aligned) in a ferrite matrix with a generally dark etching response ?

2: Are there alternate ferrite/cementite lamellae?

3: Is it ferrite/ carbide aggregate and can be excluded from being bainite?

4: Is the constituent irresolvable; does it have a fast etching response and a low hardness?

5: Is the constituent irresolvable; does it have a slow etching response and a high hardness?
- 5.1: Is the constituent in form of laths with a heavily dislocated substructure?
- 5.2: Are there light etching ferrite plates with twinning?
- 5.3: Is the phase mixed martensite and retained austenite?

Table 6: Flowchart for the identification of grain boundary constituents. Adapted from (Thewlis 2004).

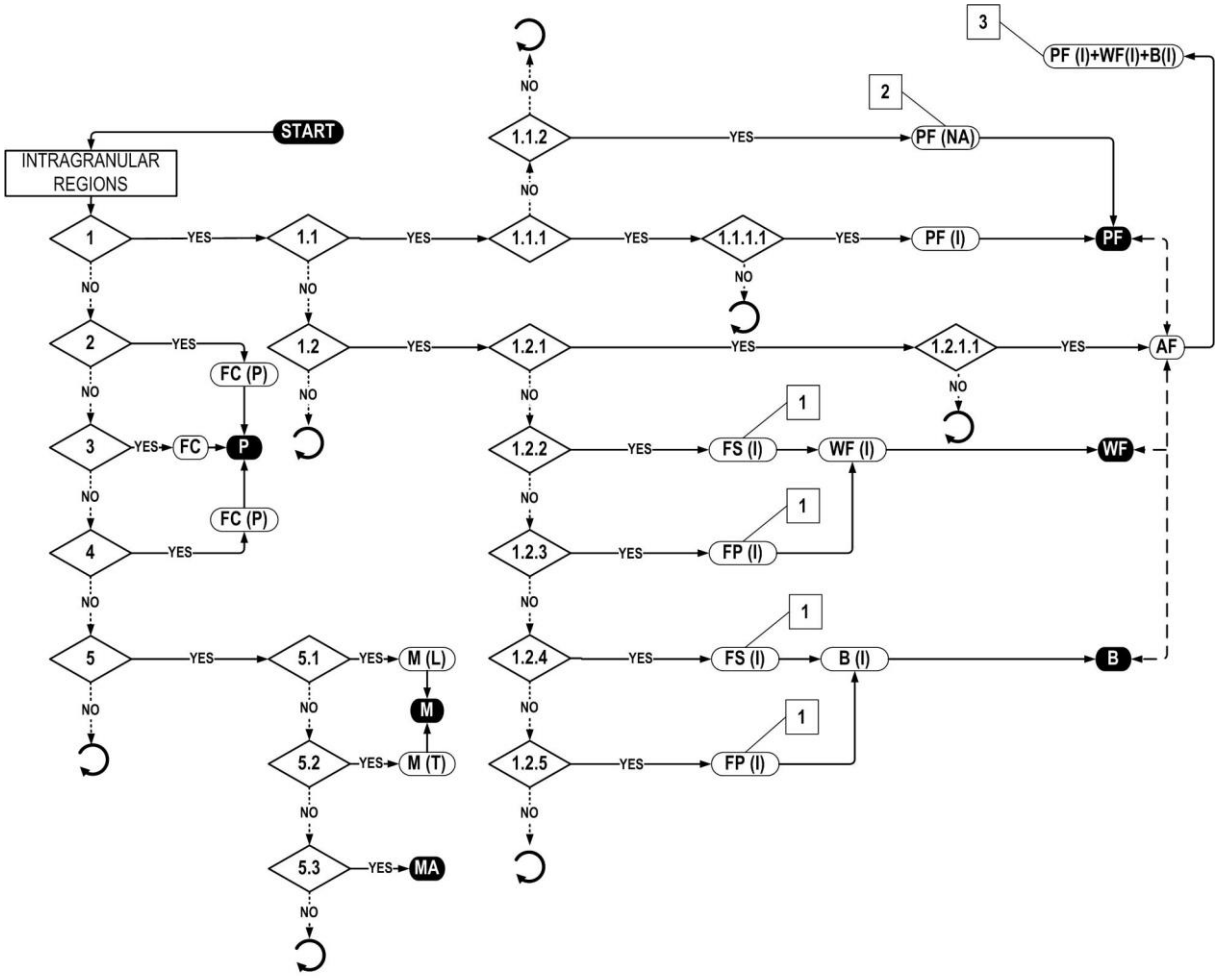

YES/NO decision based on the observation of a particular microstructure (see table below).

Return to start and check again or use other identification techniques.

Principal structure classification.

Main and sub-category classification.

1 Phases may be linked directly to the principal structures.

2 Cross-sections of primary ferrite allotriomorphs that have grown from that have grown from prior austenite grain boundaries below the surface of observation.

3 Very fine structure resulting from multiple hard impingements of intragranular ferrite grains or laths nucleated and growing from inclusions

1: Is it ferrite?
- 1.1: Are the grains polygonal?
  - 1.1.1: Is the ferrite associated with inclusions?
    - 1.1.1.1: Is the ferrite in form of blocks, loops, petals or rosettes?
  - 1.1.2: Is the constituent about three times greater in size than surrounding ferrite laths or grains?
- 1.2: Is the ferrite constituent interspersed with micro phase?
  - 1.2.1: Is the ferrite in form of very fine interlocking grains or laths of a size less than 5 μm?
    - 1.2.1.1: Does the ferrite constituent nucleate on inclusions and/or sympathetically from existing ferrite?
  - 1.2.2: Are there multiple coarse ferrite plates (aspect ratio greater than 4:1) with aligned microphase, which grow from inclusions?
  - 1.2.3: Are there individual coarse ferrite plates (aspect ratio greater than 4:1) that grow relatively unimpeded from inclusions?
  - 1.2.4: Are there sheaves of fine ferrite laths with aligned carbide particles that grow from inclusions?
  - 1.2.5: Are there individual fine plates that grow relatively unimpeded from inclusions?

2: Are there alternate ferrite/cementite lamellae?

3: Is it ferrite/ carbide aggregate and can be excluded from being bainite?

4: Is the constituent irresolvable; does it have a fast etching response and a low hardness?

5: Is the constituent irresolvable; does it have a slow etching response and a high hardness?
- 5.1: Is the constituent in form of laths with a heavily dislocated substructure?
- 5.2: Are there light etching ferrite plates with twinning?
- 5.3: Is the phase mixed martensite and retained austenite?

Table 7: Flowchart for the identification of intragranular constituents. Adapted from (Thewlis 2004).

2.2 Microstructure, Mechanical Properties and WM HACC Susceptibility

Due to the significant material and cost savings achieved through the reduction in wall thickness, pipeline construction is progressively moving towards the use of higher strength linepipe steel. This development requires certain weld metal properties i.e. an adequate strength to match the pipe, a certain toughness to ensure that in the event of girth weld failure fracture occurs by plastic collapse and not in a brittle manner and an appropriate resistance to WM HACC (Barbaro, Bowie & Holmes 2002). It is an ongoing challenge in weld metal research to find the optimum balance between these properties.

Early studies on WM HACC indicated that there appears to be a correlation between weld metal strength, hardness, toughness and HACC resistance (Hart & Watkinson 1975; Makara et al. 1971). These studies showed that the risk for WM HACC tends to be higher if the weld metal's strength and hardness are high but its toughness is low. However, Davidson et al (Davidson, JL, Lynch & Majumdar 1997) highlighted that neither strength, hardness nor toughness are reliable indicators for WM HACC susceptibility, by pointing to the inconsistencies in results contained in the published literature at that time. The contradicting results were largely associated with variations of the underlying weld metal microstructural constituents.

The weld metal's microstructural constituents are known to have characteristic features such as the grain size, second phase particles and grain boundaries contributing to their intrinsic mechanical properties, which in turn also affects the mechanical properties of the bulk material they constitute (Bhadeshia 1997). A number of workers suggested that the presence of particular microstructural constituents, used to achieve certain weld metal mechanical properties, may have a greater influence on the WM HACC susceptibility than the bulk material's mechanical properties per se (Albrecht, Thompson & Bernstein 1979; Cain & Troiano 1965; Chen, Thompson & Bernstein 1980; Davidson, JL, Lynch & Majumdar 1997).

Hence, in order to be able to efficiently implement microstructural design to optimise the weld metal's mechanical properties and HACC resistance, it's first necessary to understand how the characteristic features of individual microstructural constituents control their intrinsic mechanical properties and their role under conditions encountered during WM HACC.

2.2.1 Grain Size

It is well established that a finer grain size increases the yield strength (Hall 1951; Petch 1953). The most common mechanism to explain the relationship between grain size and yield strength is the dislocation pile up model based on the work of Hall (Hall 1951) and Petch (Petch 1953). The prerequisite for this model is that dislocations can only move along specific directions within slip planes and therefore have to change the direction of their motion in order to pass a grain boundary. This becomes more difficult as the crystallographic misorientation between two adjacent grains increases, leading to a pile up of dislocations at the grain boundaries, which act as barriers to the dislocation movement.

The dislocation pile-ups introduce stress concentrations ahead of their slip planes, which generate new dislocations in adjacent grains and thereby transmit plastic deformation across the grain boundaries (Bhadeshia 2001). A finer grain size implies a greater grain boundary density per unit volume which in turn may lead to an increased impediment of the dislocation motion and therefore result in a higher yield strength.

In the literature, most models used to describe the relationship between the grain size and yield strength are based on the Hall-Petch relation (Hall 1951; Petch 1953):

$$\sigma_Y=\sigma_0+k_Y d^{-1/2} \qquad (2\text{-}1)$$

Where σ_0 is the lattice friction stress required to move individual dislocations, k_Y is a material-dependent constant known as the Hall–Petch slope, and d is the average grain diameter. Since σ_0 and k_Y are constants, the proportionality between yield strength and grain size can be defined as $\sigma_Y \propto d^{-1/2}$.

Although, the Hall-Petch relation can be used to describe the grain size dependency of the yield strength for most of the weld metal's principal microstructural constituents, for bainite and martensite it was found that the slip plane dimensions may become too small to allow the existence of effective dislocation pile ups (Bhadeshia 2001). Langford and Cohen (Langford & Cohen 1969) were the first to observe that yielding is then determined by the stress necessary to expand a dislocation loop across a slip plane. Under such circumstance it was found that the yield strength tends to be proportional to the reciprocal of the lath diameter, $\sigma_Y \propto d^{-1}$ (Daigne, Guttmann & Naylor 1982; Naylor 1979).

Tabor (Tabor 1956) was the first to establish an empirical relationship between Vickers hardness (HV) and yield strength (σ_Y), which is defined as followed:

$$HV \sim 3\,\sigma_Y \qquad (2\text{-}2)$$

However, this rough approximation may vary significantly for different materials. Previous investigations showed that the ratio between hardness and strength, of different types of steel, varied between 2.03 and 3.65, while for ceramics this ratio was found to range between 28 and 183.23 (Zhang, Li & Zhang 2011). Regarding the ratio between hardness and strength, it has to be considered that HV is usually expressed as a number only, while the calculations of the HV/σ_Y ratios mentioned above where all based on SI units (Zhang, Li & Zhang 2011).

In general, the toughness describes a materials resistance to fracture and as such is measured as the energy needed to cause fracture. The ability of a material to undergo some plastic deformation is critical to the enhancement of its toughness, as this feature enables the

local dissipation of high stresses that would otherwise cause fracture. This is the reason that materials with a high yield strength and a high hardness tend to be rather brittle while materials with a lower yield strength are more ductile, can deform more readily and tend to be tougher (Ritchie 2011). Since yield strength, hardness and toughness are all interrelated, the grain size affects either directly or indirectly all three properties.

As discussed later in detail, the mechanisms by which hydrogen affects the fracture resistance are not yet completely understood. Furthermore, in the case of hydrogen assisted crack propagation, the fracture mode may vary for the same microstructure (i.e. microvoid coalescence, quasi-cleavage or intergranular fracture), depending on the stress intensity and hydrogen concentration ahead of the crack tip (Alam et al. 1996; Beachem 1972). Hence, for each particular fracture mode, the grain size may have different effects on the fracture resistance. Because of this complex, often unpredictable nature, the link between grain size and WM HACC susceptibility still remains unclear.

However, a number of fracture tests with different types of hydrogen charged steels showed that the critical stress intensity tends to increase as the average grain size decreases (Lessar & Gerberich 1976; Procter & Paxton 1969; Takasawa et al. 2010). It was therefore suggested that grain refinement may inhibit hydrogen assisted crack initiation.

2.2.2 Second Phase Particles

Second phase particles, such as NMI's or cementite precipitates, may directly affect the yield strength by impeding the movement of dislocations. An increase in the volume fraction of NMI's and/or cementite precipitates will therefore result in an increase of both, yield strength and hardness (Daigne, Guttmann & Naylor 1982; Wildash 1999).

The exact mechanisms by which second phase particles control the fracture toughness, if a significant amount of plastic deformation is involved, are not yet completely understood. However, it is well known that ductile fracture usually forms via the nucleation, growth and coalescence of microvoids. NMI's as well as cementite precipitates may thereby act as potential nucleation sites for microvoids. If the number density of the voids is large, then their mean separation distance (inter-void spacing) is reduced and coalescence may occur rapidly upon loading and decrease the amount of plastic deformation a material can accommodate before fracture occurs. In case of ductile fracture, a higher volume fraction of second phase particles is therefore believed to reduce the toughness (Bhadeshia 2001).

The hydrogen permeation experiments of Darken and Smith (Darken & Smith 1949) showed that hydrogen diffusion in steels is affected by imperfections in the lattice such as vacancies, solute atoms, dislocations, grain boundaries, voids and second phase particles. In these localised regions, the mean residence time of hydrogen can be considerably longer than in interstitial lattice sites. Therefore, the generic term for this phenomenon is referred to as hydrogen trapping (Pressouyre 1980). Hydrogen traps are generally classified as either irreversible or reversible traps. Irreversible traps act solely as hydrogen sinks whereas reversible traps can act as either hydrogen sinks or hydrogen sources.

By acting as hydrogen traps, second phase particles can affect the WM HACC resistance in two different ways. If a second phase particle is susceptible to HACC it may become a potential crack nucleation site and therefore increase the risk for HACC initiation. The crack formed by a fractured particle will only propagate into the adjacent ferrite matrix if the stress intensity factor at the newly formed crack tip is large enough. Such an event is more likely to occur as the particle size increases, since the crack will be longer and hence the stress intensity factor at the crack tip will be higher (Davidson, JL, Lynch & Majumdar 1997). On the other hand, by trapping hydrogen, second phase particles can reduce the amount of mobile residual hydrogen, thus reducing diffusion to more susceptible sites (i.e. other microstructural

constituents and/or the crack tip), thereby reducing the risk of HACC initiation and propagation (Olson, D.L.R. et al. 1996; Pressouyre 1980).

2.2.3 Grain Boundaries

As mentioned previously, the yield strength can be related to the grain boundary density per unit volume. Because of their physical relevance, grain boundaries are one of the most important microstructural features used to control the mechanical properties of polycrystalline materials (Watanabe 1994).

Grain boundaries are interfaces between adjacent grains with different orientations. The geometry of a grain boundary can be fully characterized by five degrees of freedom; three angles define the crystallographic orientation of the two grains with respect to one another, while two parameters describe the inclination of the grain boundary plane (Lejček 2010). Depending on the degree of misorientation between two adjacent grains, grain boundaries may be of the tilt type, when the rotation axis lies in the boundary plane, or of the twist type, when the rotation axis is normal to the boundary plane (see Figure 8).

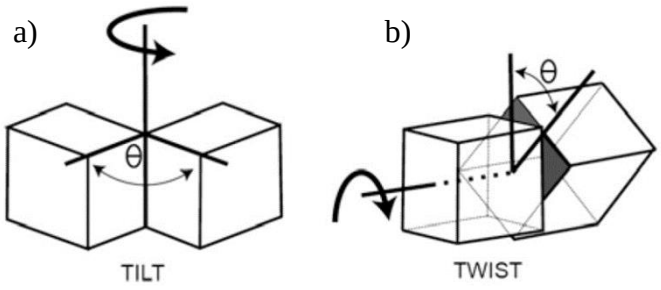

Figure 8: Schematic illustrations of:
a) Tilt boundary,
b) Twist boundary; Adapted from (Dohmen & Milke 2010).

When this misorientation angle θ between two grains is low, typically < 15°, then the interface between them is usually referred to as a small- (or Low-) Angle Grain Boundary (LAGB) (Lejček 2010). In this case the misorientation can be formed by an array of dislocations (Randle 1996). Tilt boundaries are typically formed by edge dislocations, while twist boundaries consist of an array of screw dislocations (Lejček 2010).

Orowan, Polanyi and Taylor (Orowan 1934; Polanyi 1934; Taylor 1934) were the first to introduce the concept of the edge dislocation. This type of dislocation is characterised by an "inserted" extra half-plane of atoms as illustrated in Figure 9 a). Within the region around the dislocation line there are some localized lattice distortions or elastic strain fields. The atoms above the dislocation line in Figure 9 a) are squeezed together which leads to a compressive strain field, while those below are pulled apart resulting in a tensile strain field. The magnitude of the distortion decreases with the distance away from the defect. The shift vector, or Burgers vector as it is now commonly referred to is perpendicular to the dislocation line.

The concept of the screw dislocation, was first introduced by Burgers (Burgers 1939). In contrast to the edge dislocation, the shift vector or "Burgers vector" is in this case parallel to the dislocation line as shown Figure 9 b).

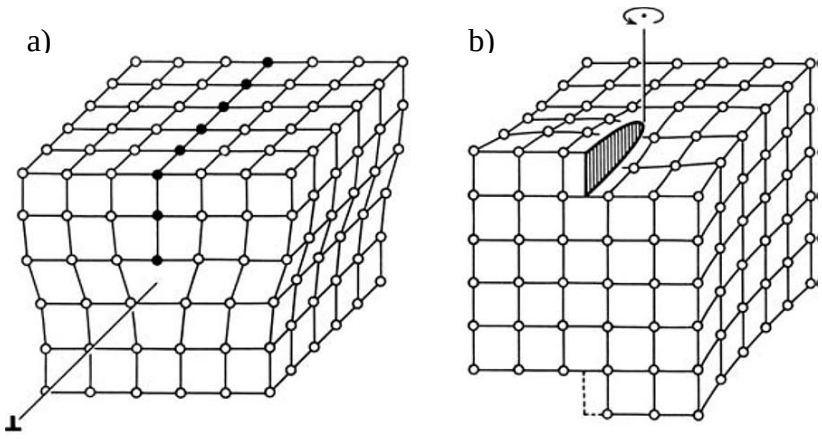

Figure 9: Schematic illustrations of:

a) Edge dislocation,

b) Screw dislocation; Adapted from (Messerschmidt 2010);

As the misorientation angle θ between two adjacent grains increases above approximately 15°, the dislocation cores start to overlap and individual dislocations are not distinguishable anymore (see Figure 10) (Lejček 2010). These types of boundaries are usually referred to as High Angle Grain Boundaries (HAGB's), where the atomic arrangement is usually described by structural unit models (Gleiter 1971).

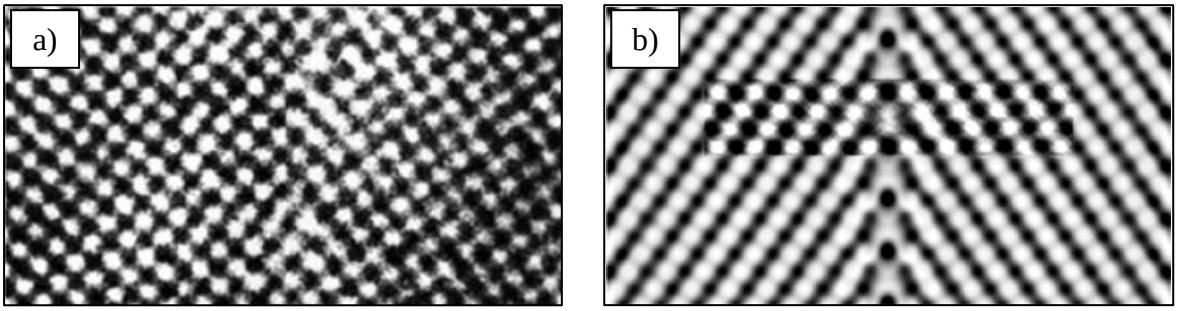

Figure 10: High-resolution transmission electron microscope images of:
a) Low angle grain boundary (tilt boundary formed by an array of edge dislocations),
b) High angle grain boundary (the bright belt in the centre of the image is the computer-simulated structure); Adapted from (Lejček 2010).

Kronberg and Wilson (Kronberg & Wilson 1949) were the first to discover that at certain misorientations, some HAGB's share a finite number of lattice sites on either side of a grain boundary which has led to the foundation of the concept of the Coincident Site Lattice (CSL) model with the characteristic notation Σ, where Σ is the reciprocal density of coincident lattice sites.

This model is based on the simple assumption that the grain boundary energy is low when the number of coincident sites in both adjacent grains is high because the number of bonds that are broken across the boundary is small. This is because the minimum Gibbs free energy of a system corresponds to the state of perfectly arranged atoms in a lattice. Therefore, a grain

boundary will possess a lower energy when more atoms are coincident with the positions of the perfect crystal than in a non-coincident state (Lejček 2010).

Grain boundaries can act as trapping sites for hydrogen (Oriani, R A 1970). The ability of a grain boundary to trap hydrogen thereby depends on its binding energy, which in turn depends on the Gibbs free energy (Maroef 2002). Therefore, it is believed that random HAGB's have a higher binding energy than CSL or LAGB's (Kane 2000).

Moreover, as shown in Figure 10 b), random HAGB's have relatively large gaps and can therefore accommodate a high number of hydrogen atoms, which makes them more susceptible to intergranular crack initiation and propagation than LAGB's and CSL boundaries (Matsumoto et al. 2010). However, as in the case of second phase particles, grain boundaries can either act as potential crack nuclei and increase the risk of WM HACC, or reduce the risk of WM HACC by reducing the available residual diffusible hydrogen, that may otherwise promote HACC initiation and/or propagation (Olson, D.L.R. et al. 1996; Pressouyre 1980).

The characteristic misorientation of grain boundaries has an additional crucial effect on the localised resistance to HACC. Fractographic observations showed that cleavage-like hydrogen assisted crack progression, through discrete crystal lattice planes, may only significantly deviate or arrest at HAGB's, which act as obstacles to the crack growth (Mazancová, Rucká & Mazanec 2007). In this case, the presence of HAGB's therefore may significantly improve the resistance to HACC propagation. The concept of the Unit Crack Path (UCP) is thereby a well-established method to quantitatively evaluate how particular types of grain boundaries contribute to the localised fracture resistance. This parameter is generally defined as the distance a crack can propagate through the surrounding microstructure in a nearly straight line (Brozzo et al. 1977). The shorter the UCP, the more frequent changes in direction and thus increased dissipation of energy from the crack driving force, which leads to an increase of the fracture resistance.

2.3 Models for the Prediction of Mechanical Properties and HACC Resistance

All of the different microstructural aspects discussed in the previous section described how particular features of individual microstructural constituents may contribute to their intrinsic mechanical properties and resistance to WM HACC. However, diverse additional factors which were not explicitly discussed such as composition, dislocation density and the intrinsic strength of iron may also have a crucial effect (Bhadeshia 1997; Lalam, Bhadeshia & MacKay 2000a, 2000b; Yurioka & Suzuki 1990).

The currently most advanced models that allow to predict the mechanical properties of particular microstructural constituents, were developed to evaluate the yield strength. The prerequisite for these models is that the yield strength can be factorised into a number of intrinsic components (Bhadeshia 1997):

$$\sigma_Y = \sigma_{Fe} + \sum_i x_i \sigma_{SS_i} + x_C \sigma_C + K_L \{L\} + K_D \rho_D^{0.5} \qquad (2\text{-}3)$$

Where σ_{Fe} is the strength of pure, annealed iron, σ_{SS_i} is the substitutional solute strengthening and x_i is the concentration of a substitutional solute which is represented here by a subscript i. σ_C is the strengthening due to carbon and x_C is the concentration of carbon. $K_L \{L\}$ and K_D are the function for strengthening due to the grain size and the coefficient for strengthening due to dislocations respectively, ρ_D represents the dislocation density. Additionally, for certain microstructures such as bainite, the strengthening contribution due to the presence of second phase particles i.e. cementite has to be considered as well (Bhadeshia 2001).

However, in weld metal diverse microstructural constituents, with often substantially different mechanical properties, coexist and interact with each other, which may cause plastic constraints that affect both, the strength of the individual microstructural constituents as well

as their contribution to the mechanical properties of the bulk material they constitute (Bhadeshia 1997). In order to predict the mechanical properties of weld metal, e.g. by using a rule of mixtures, it is necessary to have insight on the volume fraction the microstructural constituents as well as on their constraint and unconstraint properties (Bhadeshia 1997). Models such as in Equation (2-3) are particularly appealing because of the difficulty to directly probe the unconstraint, intrinsic mechanical properties of the weld metal's individual microstructural constituents, which only occur in microscopic material volumes. However, because of the experimental limitations, the validity of such models at the smallest microstructural scales still remains unclear.

Models that could be utilised to predict the HACC susceptibility of weld metal and its microstructural constituents can be divided into two categories (Wongpanya et al. 2009).

The first type of models was developed to evaluate the time required for hydrogen crack initiation as well as the stress-strain threshold of cracking, as those proposed by Gerberich and Chen (Gerberich & Chen 1988) as well as by Akhurst and Baker (Akhurst & Baker 1981). However, the adoption of these models to evaluate the WM HACC initiation resistance is rather difficult due to the unclear interaction of various factors, including the contribution of specific microstructural features (Wongpanya et al. 2009).

The second type of models focus on hydrogen crack propagation, as for example those proposed by Gerberich (Gerberich et al. 1988). Most of these analytical models are applicable to Hydrogen Environment Assisted Cracking (HEAC), such as Hydrogen Assisted Stress Corrosion Cracking (HASCC), which involves the conjoint action of mechanical loading and chemical reaction. However, these models cannot be easily transferred to evaluate the resistance to WM HACC propagation, which is classified as Internal Hydrogen Assisted Cracking (IHAC) and involves the redistribution of dissolved hydrogen from the surrounding microstructure to the crack tip in order to promote crack growth, as discussed in detail in the literature (Gangloff 2003; Wongpanya et al. 2009).

2.4 Microstructure, Mechanical Properties and HACC Resistance of Acicular Ferrite and Upper Bainite

As mentioned previously, weld metal consists of diverse constituents with unique microstructural features and distinctive mechanical properties. Two common microstructural constituents found in ferritic weld metal, that have substantially different features as well as mechanical properties, are acicular ferrite and upper bainite. EBSD investigations showed that while acicular ferrite is characterised by a chaotic arrangement of fine-grained plates with different orientations that are separated by HAGB's, upper bainite consists of sheaves of parallel ferrite laths (or sub-units) with largely similar crystallographic orientations that are separated by LAGB's, where cementite precipitates may decorate the lath boundaries (Díaz-Fuentes, Iza-Mendia & Gutiérrez 2003).

Numerous studies on the integrity of weld metal have demonstrated that both strength (Farrar & Harrison 1987) and fracture resistance (Farrar & Harrison 1987; Yang, J. R. et al. 1993) could be significantly improved by increasing the volume fraction of acicular ferrite. The enhanced mechanical properties were largely associated with the small grain size and the high density of HAGB's (Bhadeshia 2001; Díaz-Fuentes, Iza-Mendia & Gutiérrez 2003; Farrar & Harrison 1987; Wang et al. 2009). Medium and low carbon steels with high contents of acicular ferrite have been developed for automotive, pressure vessel and the pipeline industry (Shi et al. 2014; Wang, Shan & Yang 2009; Wang et al. 2009). These steels were reported to have a better strength, fracture toughness, H_2S and fatigue resistance compared to steels having a primary ferrite-pearlite microstructure (Wang, Shan & Yang 2009; Wang et al. 2009; Zhong et al. 2006). The yield strength and absorbed impact energy (which can be related to fracture toughness) of ferrous alloys with high contents of acicular ferrite have been reported to be respectively in the range of 480 MPa - 750 MPa and 140 J - 190 J (Díaz-Fuentes, Iza-Mendia & Gutiérrez 2003; Wang, Shan & Yang 2009; Wang et al. 2009; Yang, J. R. et al. 1993; Zhao, Yang & Shan 2003).

There is a general agreement that high strength and good fracture toughness can also be achieved in bainitic steels with extremely low carbon contents (Edmonds & Cochrane 1990). These small concentrations allow to eliminate the inter-lath cementite and thereby enhance the fracture toughness (Yang, J. R. et al. 1993). For bainitic steels the yield strength and absorbed impact energy has been reported to be respectively in the range between 500 MPa - 1000 MPa and 20 J - 70 J at ambient temperature (Grassl, Thompson & Krauss 1989; Yang, J. R. et al. 1993). Therefore, it can be concluded that bainitic steels normally have a higher strength compared to steels which consist predominantly of acicular ferrite. However, the fracture resistance of steels with high contents of acicular ferrite seem to be superior compared to bainitic steels.

The considerations above are largely based on the outcomes of testing bulk properties of materials where microscopic regions of acicular ferrite and bainite co-existed and physically interacted with other microstructural constituents. However, not much is currently known about the intrinsic mechanical properties of acicular ferrite and bainite, constituting the bulk material.

It has been reported that acicular ferrite seems to have a higher HACC propagation resistance than bainite (Alam et al. 1996; Mazancová, Rucká & Mazanec 2007). This was mainly associated with the high density of HAGB’s in acicular ferrite which apparently increases the resistance to cleavage-like fracture (Mazancová, Rucká & Mazanec 2007).

Due to their different characteristics, acicular ferrite and bainite, more specifically upper bainite, represent ideal candidates to investigate the fundamental link between microstructure, mechanical properties and WM HACC susceptibility.

2.5 Hydrogen Embrittlement Mechanisms

Johnson in 1875 (Johnson W.H. 1875) was the first to report about the deleterious effects of hydrogen on the mechanical properties of iron and steels. The phenomenon is historically referred to as Hydrogen Embrittlement (HE) because the presence of hydrogen in metals was generally associated with brittle failure due to a reduction in fracture resistance and ductility. The term Hydrogen Assisted Cracking (HAC) was later suggested by Beachem (Beachem 1972) who argued that hydrogen assisted crack propagation may imply microscopic deformation processes that are not necessarily the result of the cessation, restriction, or exhaustion of ductility. However, from a mechanistic point of view both designations refer to the same phenomenon.

HE has been studied in many different materials, and by a variety of experimental and theoretical approaches. The global objective of these studies was to understand the mechanisms of the hydrogen assisted degradation process in metals. Several theoretical models have been proposed over the years but only a few have stood up to scrutiny and remain in consideration (see Table 8).

Mechanisms	Description	Reference
Hydrogen Enhanced Decohesion (HEDE)	Hydrogen induced reduction of the cohesive strength between metal inter-atomic bonds results in a decrease of the local plasticity.	(Johnson & Troiano 1957; Oriani, R.A. 1972; Oriani, R.A. , Hirth & Smialowski 1985; Troiano 1960)
Adsorption Induced Dislocation Emission (AIDE)	Hydrogen adsorption weakens inter-atomic bonds at the crack tip and thereby facilitates the injection of dislocations which results in an extensive dislocation activity.	(Lynch 1979; Lynch 1989)
Hydrogen Enhanced Localized Plasticity (HELP)	Hydrogen atmospheres attached to dislocations decrease the barrier to dislocation movement which leads to an increase of the localised plasticity.	(Birnbaum & Sofronis 1994; Ferreira, Robertson & Birnbaum 1998)

Table 8: Overview of the currently most established models for Hydrogen Embrittlement.

There is a general agreement that different mechanisms are applicable in different material/environment systems and for different microstructures (Pundt & Kirchheim 2006), but little consensus has been reached regarding the applicability of mechanisms in particular systems and microstructures (Lynch 2008).

Continuous improvements to both modeling and experimental techniques have brought scientists closer to understanding the mechanism, but each of the approaches still has its disadvantages that must be overcome before a consensus can be reached. This chapter gives a general overview of the most common HE mechanisms as well as the experimental evidence to support or disprove the various hypotheses.

2.5.1 Hydrogen Enhanced Decohesion HEDE Model

The HEDE model was initially proposed by Johnson and Troiano in 1957 (Johnson & Troiano 1957), and further developed by Oriani and co-workers (Gerberich et al. 1991; Oriani, R.A. 1972). This mechanism suggests that dissolved monoatomic hydrogen tends to diffuse to regions of high triaxial tensile stresses, where they fill interstitial lattice sites and thereby weaken the cohesive strength of the inter-atomic bonds in the host metal, which reduces the critical stress at which a crack will initiate or propagate (Vehoff, H. & Rothe 1983). Initially the mechanism was solely based on hydrogen accumulation driven by the crystal lattice dilation due to elastic hydrostatic stresses (Li, Oriani & Darken 1966), while later work recognized that trapping is also a possible mechanism for hydrogen segregation (Pressouyre 1980).

The HEDE mechanism was initially founded on fractographic interpretations (Oriani, R.A. 1972). In this interpretation, it was assumed that any plasticity that occurred during fracture was a direct consequence of the actual embrittlement mechanism rather than being an integral component of it. However, over time, proponents of HEDE did recognize that plasticity

plays a part, but they argued that the primary effect is that the dislocations emanating from crack tips greatly enhance the localised stresses and thereby promote additional hydrogen accumulation in the vicinity of the crack tip, which then causes the decohesion event that allows the crack to propagate (Gerberich et al. 1991).

Another key component of the HEDE mechanism is that a critical hydrogen concentration is required to cause embrittlement. In a study on medium-carbon steel, for example, Oriani and Josephic (Oriani, R. A. & Josephic 1979) showed that with controlled cathodic charging at successively higher fugacity of hydrogen, a critical value was necessary to produce an abrupt increase in the load relaxation rate.

Probably the most significant experimental evidence for a decrease of the plasticity ahead of the crack tip due to the presence of hydrogen was provided from in-situ Scanning Electron Microscope (SEM) observations of stressed Fe-3 wt% Si single crystals, where the crack tip opening angle decreased progressively with increasing external hydrogen pressure as shown in Figure 11 (Vehoff, H & Neumann 1980).

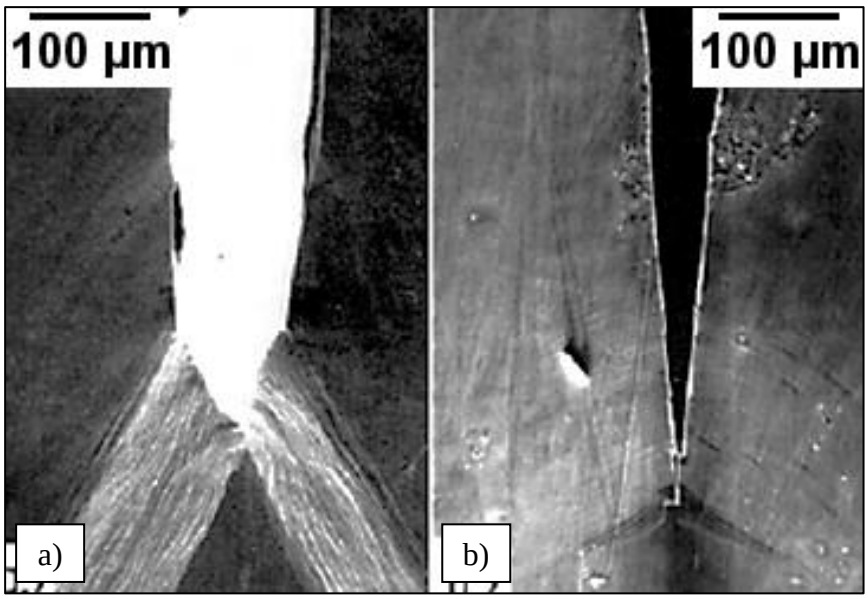

Figure 11: SEM images of the crack tip in Fe-3wt% Si single crystals after straining in:
a) Vacuum,
b) Hydrogen atmosphere; Adapted from (Vehoff, H & Neumann 1980).

The diagram in Figure 12 illustrates the dependency of the measured crack tip opening angle α on the hydrogen pressure P_{H_2} at several temperatures. Where the parameter a_n represents the ratio of incremental crack extension to crack mouth opening $a_n = \cot\frac{\alpha}{2}$. The horizontal-dashed line represents crack growth exclusively by crack tip slip, with α as the angle between active slip planes in the single crystal. The diagram shows that as the hydrogen pressure increases, the crack tip angle α decreases.

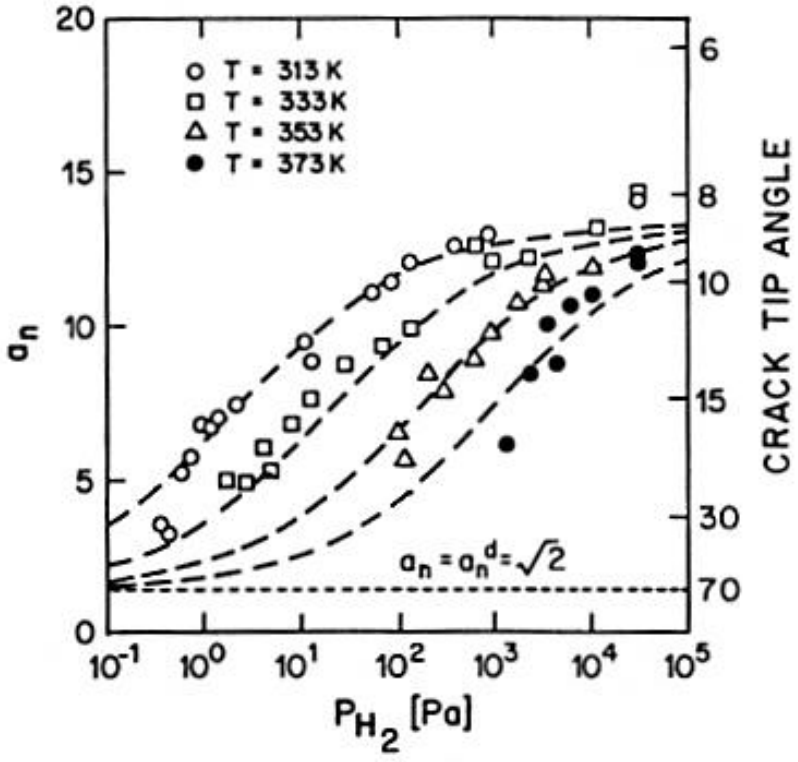

Figure 12: The diagram shows the dependency of the measured crack tip opening angle on the hydrogen pressure at several temperatures. Adapted from (Vehoff, H. & Rothe 1983).

Since the crack planes were always parallel to (100) and dimples were not resolved on these crack surfaces, the results were interpreted as evidence to prove that HEDE progressively replaced crack tip slip in the fracture process, as illustrated in Figure 13. Where Δδ is the

increase in crack opening after an increase of a crack length Δa, Δa_i^H and Δa_i^d are the microscopic growth steps produced either by hydrogen induced cleavage or by ductile rupture.

Contrary to classical HEDE, the mechanism proposed to explain this phenomenon involved both, hydrogen induced micro-cleavage and ductile rupture (Vehoff, H & Neumann 1980).

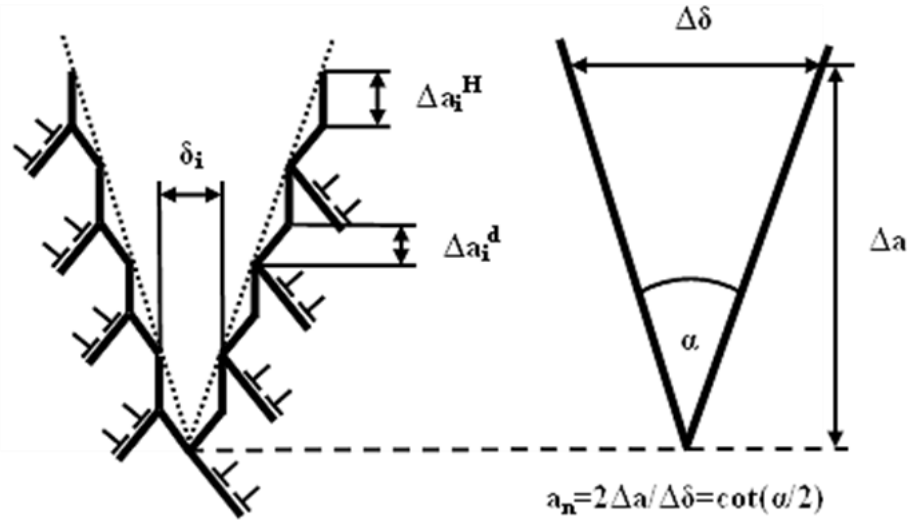

Figure 13: Schematic drawing of a crack tip produced by alternating micro cleavage and slip. Adapted from (Vehoff, H. & Rothe 1983).

However, a direct measurement of the reduction of the cohesive strength as a function of the hydrogen concentration is not possible due to analytical limitations (Martin et al. 2011). Therefore, the experimental evidence supporting the HEDE mechanism is based on the interpretation of macroscopic tests and observations rather than on direct measurements. Despite this weakness, HEDE is one of the most established models for HE (Gangloff 2003; Song & Curtin 2013).

2.5.2 Adsorption Induced Dislocation Emission (AIDE) Model

The AIDE model was first proposed by Lynch in 1979 (Lynch 1979) and has been later updated in 1989 (Lynch 1989). In the updated version of the AIDE model, adsorbed hydrogen on the crack surface as well as one or two atomic layers beneath it, weakens the interatomic bonds at the crack tip and thereby facilitates the nucleation of dislocations. The result is that extensive dislocation activity occurs ahead of the crack tip which promotes the crack propagation. In macroscopically brittle fracture this dislocation activity forms voids ahead of the cracks and the crack advances by the coalescence of voids, as illustrated in Figure 14 (Lynch 1989). Where the inset illustrates the dislocation injection from a crack tip, first on plane A and then on plane B which results in an increment of crack advance Δa. Voids are nucleated in the plastic zone ahead of the crack and the crack grows by alternate-slip and coalescence of the voids that formed along the line of prolongation ahead of the crack tip so that the macroscopic fracture plane bisects the active slip planes.

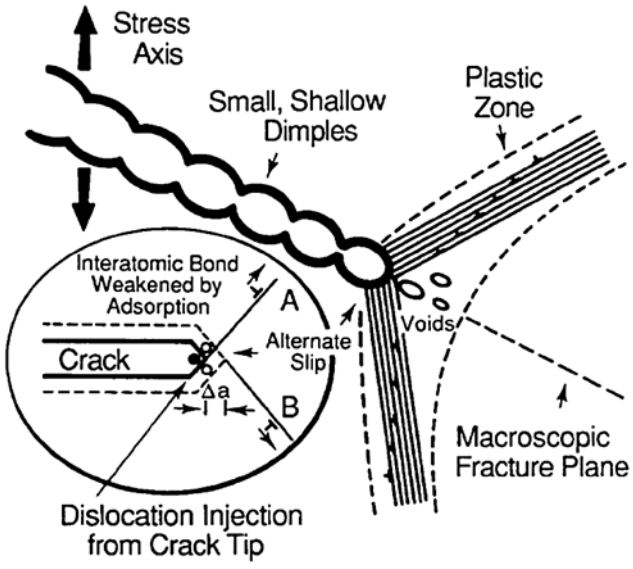

Figure 14: Diagrams illustrate the adsorption-induced localized-slip mechanism for cleavage-like cracking. Adapted from (Lynch 1989).

One of the key arguments in favour of this model is the remarkable similarity between the fracture surfaces of Liquid Metal Embrittlement (LME) specimens and HE specimens, as illustrated in Figure 15. The SEM images show a comparison of nickel single crystals that were embrittled by gaseous hydrogen (H_2) and in liquid mercury (Hg) (Lynch 1988). The fracture surfaces in both cases were defined by serrated steps and tear ridges. The similarity of the fracture morphology, suggests that a common mechanism might operate in both systems. This observation is important, because for the formation of hydrogen cracks it is unclear whether adsorbed or solute hydrogen is responsible for embrittlement (Lynch 1988). In LME, the liquid metal must come from adsorption at the crack tip, because it cannot diffuse through the bulk, therefore the similarities between LME and hydrogen embrittlement suggest the particular importance of adsorbed hydrogen, which is in agreement with the AIDE mechanism.

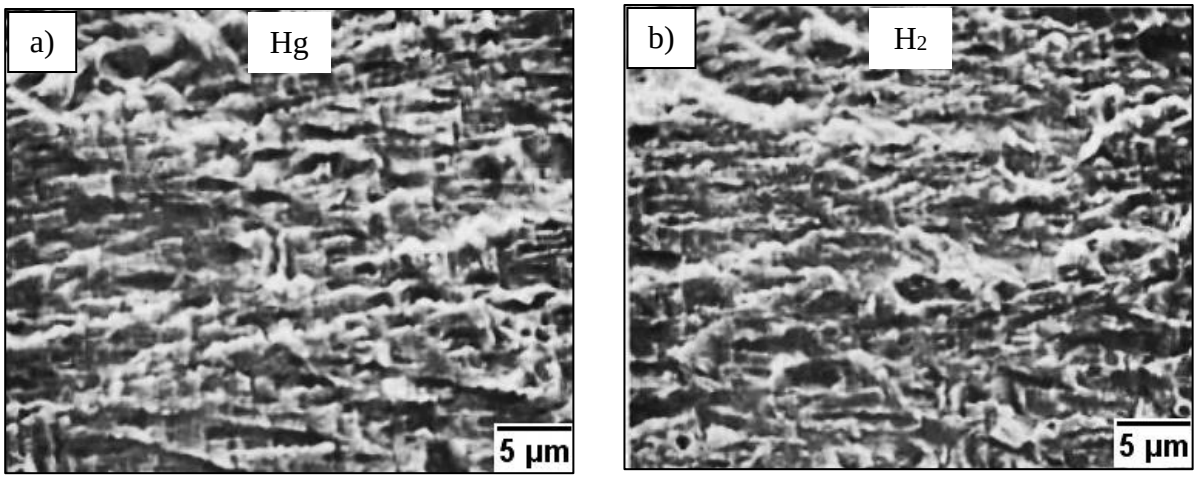

Figure 15: SEM images of single crystal nickel samples with identical orientations show:
a) Liquid mercury embrittlement,
b) Hydrogen embrittlement; Adapted from (Lynch 1988).

AIDE and HEDE both postulate a reduction in the cohesive force of the inter-atomic bonds due to the presence of hydrogen. As already mentioned previously, there is no direct evidence for this phenomenon. However, the mechanism of crack growth differs between the

two. In the HEDE mechanism the process is atomically brittle, while for the AIDE mechanism it is completely plastic (Lynch 2011).

2.5.3 Hydrogen Enhanced Localized Plasticity HELP

Beachem in 1972 (Beachem 1972) was the first to propose that despite the brittle macroscopic appearance of hydrogen cracks, highly localized deformation processes may constitute the fracture process. Based on this concept the HELP model was developed by Birnbaum and Sofronis (Birnbaum & Sofronis 1994) and other workers (Ferreira, Robertson & Birnbaum 1998; Robertson, I. M., Birnbaum, H. K. & Sofronis, P. 2009). It suggests that hydrogen atmospheres attached to dislocations decrease the barrier to dislocation movement resulting in a smaller localised flow stress.

The increased mobility of dislocations is due to a reduction of the elastic strain fields in their dilation zone as a result of the hydrogen accumulation in these regions (Birnbaum & Sofronis 1994). Providing the strain rate is low enough and the temperature high enough to enable the hydrogen to move with the kinetically faster dislocations, the reduction of the elastic strain fields reduces the interaction of dislocations with other dislocations or obstacles enabling dislocations to move at lower stress levels. This suggests that the characteristic loss of ductility associated with hydrogen embrittlement on the macroscopic scale does not preclude localised plasticity on a micro scale (Birnbaum & Sofronis 1994; Ferreira, Robertson & Birnbaum 1998).

While it has proven very difficult to show direct experimental evidence for HEDE and AIDE, there is an abundance of direct evidence for the HELP model. One of the most important pieces of evidence in favour of this mechanism comes from in-situ TEM observations. Experiments have been performed for different materials, in which a TEM foil was strained in

situ in a specialized TEM with an environmental cell, allowing the sample to be exposed to hydrogen gas while under strain (Ferreira, Robertson & Birnbaum 1998; Robertson 2001).

The experiment operated by holding the stage displacement constant, so that dislocations piled up against a grain boundary remained stationary and then hydrogen was introduced into the cell. As shown in Figure 16, the introduction of hydrogen reduced the separation distance between the dislocations, indicating that the presence of hydrogen has in fact reduced the elastic strain fields and hence the repulsive forces between the dislocations which lead to a reduction of the threshold stress level for dislocation motion (Ferreira, Robertson & Birnbaum 1998; Robertson 2001).

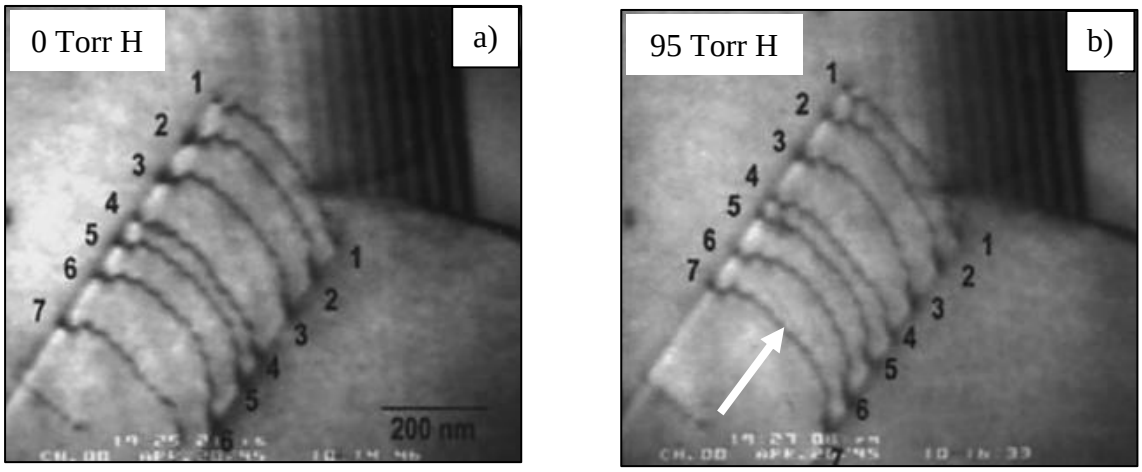

Figure 16: Bright field images captured from a video tape showing the change in the dislocation arrangement as a function of hydrogen content in 310 S stainless steel.
a) Dislocations piled up against a grain boundary,
b) Reduction of the separation distance after introduction of hydrogen gas; Adapted from (Ferreira, Robertson & Birnbaum 1998).

Another attempt to provide experimental evidence for the HELP model focused on a common feature of hydrogen embrittled fracture surfaces, known as quasi-cleavage (Martin et al. 2011). Compact tension tests in a high-pressure (5 MPa - 100 MPa) hydrogen gas environment were conducted on API 5L X60 pipeline steel. The resulting fracture surface

morphologies included regions that were classified as quasi-cleavage, characterized by the presence of striations also referred to as tear ridges or river markings (see Figure 17a)). It was reported that these tear ridges most likely formed in the grain interior and typically matched ridge-to-ridge on opposing fracture surfaces. TEM observations revealed extensive dislocation structures and the formation of intense slip bands directly beneath these features (see Figure 17b)), which was associated with failure mechanisms due to highly localised deformation processes assisted by HELP (Martin, Robertson & Sofronis 2011).

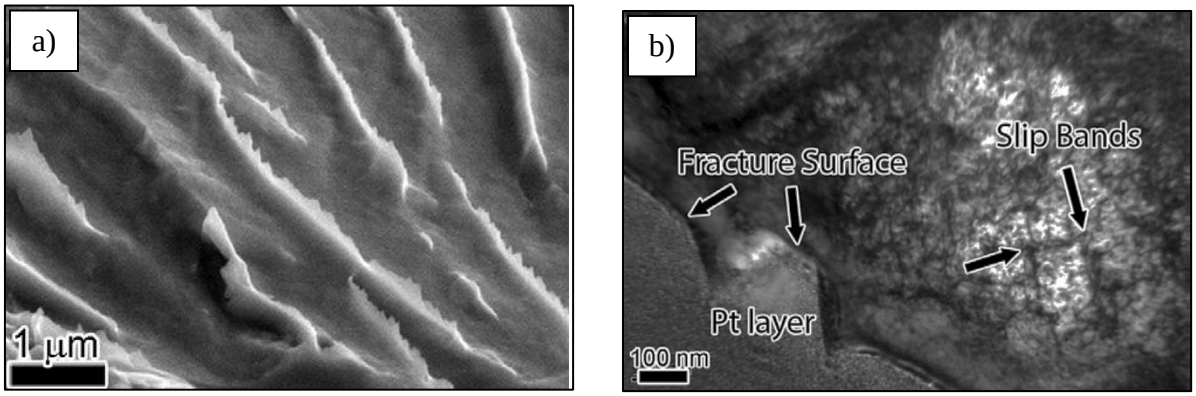

Figure 17: a) SEM image shows tear ridges which in some cases had saw-teeth features, b) Bright-field image shows extensive dislocation structures and the formation of intense slip bands; Adapted from (Martin, Robertson & Sofronis 2011).

While there is significant controversy as to which of the proposed mechanisms is the correct explanation for the observed phenomena, it is likely that several of them play some role and that different mechanisms might dominate in different material systems, microstructures and environments. There is little consensus as to the extent each mechanism plays a role. In addition, new models continue to be proposed and evaluated against these currently best explanations (Kirchheim 2010; Nagumo, Nakamura & Takai 2001).

2.6 Fracture Mechanics Concepts

2.6.1 Material Behaviour in Fracture Testing

The behaviour of metallic materials during a fracture test can be described by the following three main aspects (Zhu & Joyce 2012):

i. Fracture behaviour,
ii. Strength and deformation behaviour,
iii. Constraint effect of the geometry;

Understanding these three aspects is imperative to successfully evaluate fracture related properties such as the fracture toughness. Thus, care should be taken so that the proper fracture parameters and characterisation procedures are used in the fracture test for the material of interest.

The fracture behaviour describes the micro-mechanism of fracture and is usually defined as being brittle or ductile. Brittle fracture behaviour results in the development of rapid and unstable crack extension, which usually corresponds to cleavage or cleavage-like fracture. A material demonstrating such a fracture mode has usually a unique and well-defined point of crack initiation, corresponding to a sudden drop in load, which allows to evaluate the fracture resistance using Linear Elastic Fracture Mechanics (LEFM). On the contrary, ductile fracture behaviour results in slow and stable crack extension, usually caused by the nucleation and coalescence of micro-voids, which tends to absorb more energy. Such a fracture mode implies a continuous process of ductile tearing rather than point fracture and requires therefore special considerations to evaluate the fracture resistance, as provided by different methods of Elastic-Plastic Fracture Mechanics (EPFM).

The deformation behaviour during fracture can be characterised as being linear elastic, nonlinear elastic, or elastic–plastic (Zhu & Joyce 2012). In general, a material's deformation behaviour determines which fracture parameter and test method can be used to evaluate its fracture resistance.

The prerequisite for the application of fracture mechanics methods for engineering and structural analysis purposes is that the fracture toughness is a material property that can be transferred from the laboratory test to structural applications. However, the crack-tip constraint caused by thickness, size and configuration of fracture test specimens can have a strong effect on the measured values of the fracture toughness. In general, high constraint results in higher crack-tip stresses with less crack tip yielding, which promotes a more brittle fracture. On the other hand, low constraint results in lower crack-tip stresses with more crack-tip yielding and tends to reduce the possibility of brittle fracture (Bhadeshia 1997; Zhu & Joyce 2012).

2.6.2 Linear Elastic Fracture Mechanics

Based on the work of Griffith (Griffith 1921) and Orowan (Orowan 1949), Irwin (Irwin 1948) was the first to develop LEFM in terms of energy. He defined the elastic energy released for an increase in crack area, the crack extension force, G. A fracture would initiate when G reached a critical value $G_c = 2\gamma_p$, where γ_p is the fracture energy (Orowan 1949). Kies (Kies & Smith 1955) observed that the critical stress for a given crack size depended only on G_cE, where E is the elastic modulus. Boeing engineers, who had initiated the work on hot stretching, used $(G_cE)^{1/2}$ as their fracture parameter, which they termed the fracture toughness, K_c, in recognition of Kies (Rossmanith 1997). Irwin (Irwin 1957), related G to the stress field at the crack tip and introduced the stress intensity factor $K = (GE)^{1/2}$, which was also named in honour of Kies. For any symmetrical geometry, K can be expressed as:

$$K = \sigma\sqrt{\pi a} F\left(\frac{a}{W}\right) \quad (2\text{-}4)$$

Where σ is a representative stress, a is the crack length, and $F(a/W)$ is a function of the geometry.

LEFM is one of the most successful concepts of continuum mechanics and can be applied to many fields including fatigue crack growth, dynamic fracture mechanics, creep- and visco-elastic fracture, stress-corrosion cracking as well as hydrogen cracking (Cotterell 2002; Gangloff 2003).

LEFM provides the basis for incorporating HE or HAC into structural integrity management (Rotfe & Barsom 1977). In accordance with this theory a single parameter, the stress intensity factor, K, governs the crack initiation and crack growth rates. This concept was confirmed by many studies over the past 60 years (Gangloff 2003; Gerberich & Chen 1973; Loginow & Phelps 1975; Olden, Alvaro & Akselsen 2012). From a structural integrity point of view, three parameters have to be identified experimentally:

i. Threshold stress intensity factor, K_{th}, below which a crack does not propagate,
ii. Crack growth rates (da/dt) at $K>K_{th}$,
iii. Fracture toughness K_c;

Effective laboratory methods have been developed and standardised as in ASTM E-1681 (ASTM 1999) to determine the threshold and kinetics for hydrogen assisted cracking, which are necessary for the safe design of structures subjected to the risk of HAC. The testing procedures may involve a fracture specimen, typically fatigue pre-cracked, which can be stressed under either constant or rising load, crack mouth opening displacement or constant K. These procedures are substantially more complex and time consuming compared to standard fracture testing. For example, the identification of the threshold stress intensity factor, K_{th}, may require several thousand hours of testing time (ASTM 1999).

The values for K_{th} in case of an API X70 pipeline steel welded joint, were reported to be 149 MPa $m^{1/2}$, 147 MPa $m^{1/2}$ and 143 MPa $m^{1/2}$ for the base metal ($R_{p0.2}$=485 MPa), weld metal ($R_{p0.2}$=579 MPa) and heat affected zone ($R_{p0.2}$=812 MPa) respectively (Olden, Alvaro & Akselsen 2012). In medium carbon steels, with yield strengths between 580 MPa and 830 MPa, K_{th} was measured under various testing conditions to range between 42 MPa $m^{1/2}$ and 88 MPa $m^{1/2}$ (Gerberich & Chen 1973; Loginow & Phelps 1975). For low carbon steels, with yield strengths between 310 MPa and 760 MPa, K_{th} ranged between 37 MPa $m^{1/2}$ and 78 MPa $m^{1/2}$ (Homrossukon, Mostovoy & Todd 2009; Yu et al. 1997).

For low and medium carbon steels, the lower bound values of subcritical crack growth near the threshold level were reported to be around 10^{-9} ms^{-1} (Homrossukon, Mostovoy & Todd 2009; Loginow & Phelps 1975).

Due to a wide range of parameters affecting HAC, (such as the rate and mode of loading, constraint conditions, hydrogen charging method, temperature, specimen size and diverse microstructural factors) the outcomes of conventional HAC tests often demonstrate a large scatter (Barnoush & Vehoff 2010). In the development of experimental methods to characterise HAC over the past 50 years, a great effort has been directed to eliminate the diverse parameters influencing the reproducibility of the test results (Barnoush & Vehoff 2010). In addition, the utilisation of the stress intensity factor and plane strain conditions as well as controlled hydrogen charging allowed an accurate measure of the mechanical stress and environmental conditions, two main factors affecting HAC (Gangloff 2003).

However, for a wide range of materials, the microstructure, which is the third main factor affecting HAC, consist of diverse constituents with specific features and mechanical properties that only occur in microscopic volumes, as in the case of weld metal. One specific manifestation of HAC is HACC, a weld defect that may occur after the deposited weld has cooled down to temperatures below 200°C, as discussed in detail previously. In order to investigate the intrinsic HACC susceptibility of particular microstructural constituents in weld

metal, it is necessary to reduce the dimensions of fracture specimens, down to the typical size of individual microstructural constituents within the bulk material.

Di Maio and Roberts (Di Maio & Roberts 2005) were the first to introduce fracture testing at such small scales, to measure the fracture toughness of thin brittle coatings, by employing sharply notched micro-beams and LEFM.

2.6.3 Elastic Plastic Fracture Mechanics

Irwin (Irwin 1958) was the first who, by simple equilibrium arguments, estimated the size of the plastic zone, d_p, at a crack tip in a material with yield strength of σ_y to be:

$$d_p = \frac{1}{n\pi}\left(\frac{K}{\sigma_y}\right)^2 \tag{2-5}$$

Where n=1 for plane stress and n=3 for plane strain. Provided the stress field outside of the plastic zone is dominated by the K-field, then LEFM can be applied, which means that d_p must be small compared to the dimensions of the specimen. In this regime, Irwin (Irwin 1958) showed that LEFM could still be used provided that an effective crack length equal to $d_p/2$ was added to the actual crack length. However, as the plastic zone becomes large LEFM is not applicable and plastic deformation has to be considered in detail.

Wells (Wells 1961) was the first to introduce the crack opening displacement concept, also referred to as the crack tip opening displacement (CTOD), to evaluate fracture under conditions of large plastic deformation. The assumption thereby was that, in order for fracture to occur there must be a critical crack tip opening. For complete yielding of a deep notch bend specimen, the CTOD could be obtained from slip line theory and the rotation of the arms since, according to slip line theory, the deformation is essentially that of rigid arms rotating about a

rigid circular core. For small scale yielding Wells proposed an approximation where the CTOD, δ, is given by:

$$\delta = \frac{4}{\pi} \frac{K^2}{E \sigma_y} \tag{2-6}$$

Which is very close to the more exact approximation obtained by Burdekin and Stone (Burdekin & Stone 1966), based on the analysis of Dugdale (Dugdale 1960).

Rice (Rice 1968) was the first who introduced the J-integral to the fracture community. The J-integral, the EPFM equivalent to the crack extension force, G, in LEFM, is the energy that is extracted through the crack tip singularity. The J-integral has been very successfully applied to determine the initiation of fracture in the presence of significant plastic deformation. However, its application to fracture propagation is rather difficult. The standard method adopted by ASTM E 1152 (ASTM 1987) calculates the propagation value, J_R, by assuming that the material is non-linear elastic using the work of Ernst (Ernst, Paris & Landes 1981).

Wurster (Wurster, Motz & Pippan 2012) was the first to develop a procedure for the evaluation of the J-integral for micro-sized test specimens, based on the ASTM E-1820 standard (ASTM 2013). The study utilised sharply notched micro-beams to determine the fracture mechanical parameters of monocrystalline tungsten.

Due to the large plastic zone in relation to the small sample size, LEFM was not applicable and an EPFM approach had to be applied. The conditional fracture toughness values J_Q were calculated from corrected force vs. displacement diagrams. The crack growth was measured by direct observations as well as with the help of unloading compliances. Another option to determine the fracture toughness of micro-fracture specimens is to employ the CTOD (Wurster, Motz & Pippan 2012).

2.7 Fracture Testing at the Micro-Scale

2.7.1 Indentation Techniques

Indentation testing is the most common method to determine the mechanical properties of small material volumes. These tests are quick, easy to perform, repeatable and inexpensive. The technique has its origins in Mohs' hardness scale of 1822 (Mohs 1822) in which materials that are able to leave a permanent scratch in another material were ranked harder with diamond assigned the maximum value of 10 on the scale. Almost a century later, Johan Brinell introduced the first widely used and standardised hardness test in engineering and metallurgy. Brinell's test involves the indentation of a material with a hard sphere (Chandler 1999). Many people such as Knoop (Knoop, Peters & Emerson 1939), Smith and Sandly from Vickers Ltd. (Smith & Sandly 1922), and Rockwell (Rockwell & Rockwell 1919) have all modified this test, but the principle has remained the same.

Besides properties such as hardness, elastic modulus, strain-hardening exponent and yield strength it is also possible to evaluate the fracture toughness of brittle materials from the crack lengths at the indentation corners when a sharp indenter tip (Berkovich, Knoop or cube corner tip) is applied (Ponton & Rawlings 1989).

This method was originally proposed by Evans and Charles (Evans & Charles 1976) who related the stress intensity factor for Vickers indentation cracks to the observed crack lengths in the vicinity of the indentation area. The evaluation of the fracture toughness largely relies thereby on linear-elastic solutions readily available for the observed crack morphologies (Ponton & Rawlings 1989).

However, such an approach is not applicable for materials where failure is accompanied by relatively large plastic deformations, or in other words, when the indentation process does

not produce brittle cracks. Therefore, it seems, that for relatively ductile materials, such as weld metal, a more viable option to directly evaluate the fracture resistance at micro- and nano-scales is to use notched or pre-cracked miniaturised mechanical test specimens.

2.7.2 Fracture Testing of Miniaturised Mechanical Test Specimens

Recent advances in the miniaturisation of mechanical tests were mainly attributed to development of Focused Ion Beam (FIB) micro-fabrication techniques. The increasing efficiency and accuracy of modern FIB workstations allow a reproducible, site-specific fabrication of micro and nano- scaled mechanical test specimens with diverse complex shapes. Mechanical loading of such small samples requires the application of nano-indentation techniques or micro-manipulators.

The first experiments of this kind were introduced by Uchic et al (Uchic et al. 2004) and involved compression tests on FIB machined micro-pillars. The results revealed that as the specimen dimensions decreased the measured strength seemed to increase. This extrinsic size effect becomes obvious as the specimen dimensions approach sub-micron scales and is not yet completely understood but a topic of rigorous investigations (Greer & De Hosson 2011).

Since these first experiments were introduced approximately a decade ago, many researchers adapted and evolved micromechanical testing of FIB machined specimens to perform tensile (Gianola et al. 2011), deflection (Armstrong, Wilkinson & Roberts 2009) and fracture tests (Di Maio & Roberts 2005) in various materials.

As mentioned previously, Di Maio and Roberts (Di Maio & Roberts 2005) were the first to deflect notched micro-beams via nano-indentation to measure the fracture toughness of thin brittle coatings. Similar techniques were later employed to examine the localised fracture

toughness in brittle and semi-brittle materials (Wurster, Motz & Pippan 2012). However, none of the studies focused on the evaluation of the fracture resistance in ductile materials. Moreover, the technique has not yet been employed as a tool to study the effects of hydrogen on fracture. The aim of this overview is to focus on the main difficulties that may be encountered for micro-fracture tests in weld metal, in addition to the possible effects of the hydrogen charging procedure.

2.7.3 Size Effects

Reducing the dimensions of fracture tests from the macro to the micro-scale may alter the fracture behaviour for semi-brittle and ductile materials (Wurster, Motz & Pippan 2012). The fracture process for such materials is usually governed by plastic deformation in front of the crack tip, which can spread out over a certain length. This may change the fracture behaviour if the sample size is small compared to the plastic zone ahead of the crack tip.

This phenomenon was observed for micro-fracture tests conducted on a single crystal tungsten specimen, as shown in Figure 18 a). Backscattered electron investigations clearly revealed a remarkable degree of plastic deformation, indicated by the formation of slip lines adjacent to the crack path (see Figure 18 b)). In contrast to these test results, at macro scales tungsten is known to fail by brittle fracture at ambient temperatures (Kiener et al. 2009).

However, it is not clear if such size effects can also be observed in ductile, polycrystalline materials. A strategy to reduce or avoid these effects for investigations of the fracture behaviour of single microstructural constituents in weld metal is to select micro-beam dimensions that are as small as necessary but as large as possible to reduce size effects.

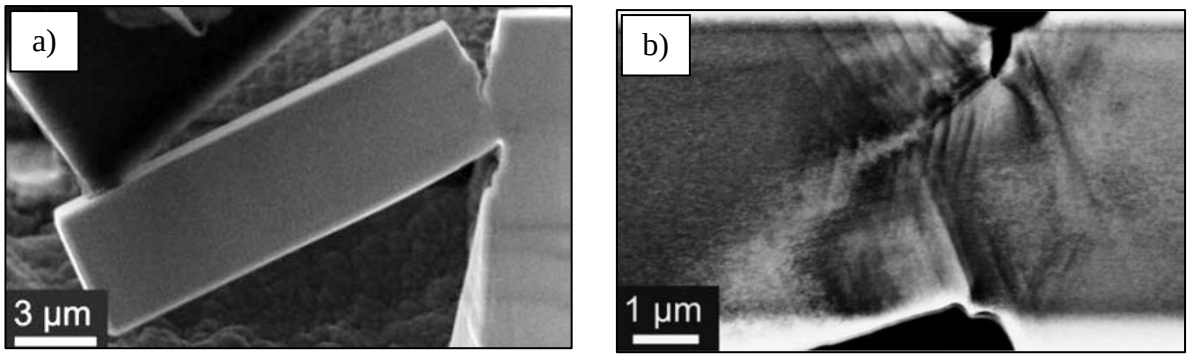

Figure 18: a) SEM image shows deflected micro-beam,
b) Backscattered electron image shows the formation of slip lines along the crack path; Adapted from (Kiener et al. 2009).

2.7.4 Surface Damage

Early studies of the effects of solute hydrogen on the deformation of solids often gave conflicting results. It has been suggested that this inconsistency was primarily caused by the hydrogen charging procedure and its effect on the defect population (Robertson, I.M., Birnbaum, H.K. & Sofronis, P. 2009).

Hydrogen is typically introduced from high-fugacity sources, either from the gas phase or from electrolytic solutions by cathodic charging. A consequence of high-fugacity charging may be ‘‘near surface damage’’, such as the formation of voids and pressurized H_2 gas bubbles (Robertson, I.M., Birnbaum, H.K. & Sofronis, P. 2009). In some cases, such defects seemed to cause a decrease in the flow stress and an increase of the ductility also referred to as softening (Asano & Otsuka 1976).

Another consequence of high-fugacity charging is that the large lattice expansion that accompanies the high hydrogen concentrations in the near surface regions may generate a stress gradient and thereby introduce residual stresses (Narita, Altstetter & Birnbaum 1982). This may also facilitate high dislocation densities in the near surface region which can lead to surface

hardening (Robertson, I.M., Birnbaum, H.K. & Sofronis, P. 2009). The high dislocation densities and the residual stresses generally lead to an increase in the flow stress.

Depending on the material system different effects can result from high-fugacity hydrogen charging. Particularly for small specimen dimensions these effects may have a critical impact on the mechanical properties. It is therefore, necessary to verify that after hydrogen charging the surface integrity of the micro-beams remains largely unchanged. However, subsurface defects may only be detected via TEM examination.

2.8 Experimental Techniques for the Characterisation of Chemical Composition, Microstructure and Mechanical Properties

2.8.1 Glow Discharge Optical Emission Spectrometry

Glow Discharge Optical Emission Spectroscopy (GD-OES) was developed in the 1970s, based on a Grimm type of source (Grimm 1968) and the spectrometer design of Rowland (Rowland 1882). This method can be used for the analysis of the chemical composition for a wide range of solid materials, including metals, alloys, semiconductors, polymers, glass and ceramics. It is thereby possible to analyse the bulk material as well as to conduct depth profiling.

In glow discharge, cathodic sputtering is used to remove the material from the specimen surface. The atoms, removed from the surface, migrate into the plasma where they collide with electrons or metastable carrier gas atoms. A characteristic X-ray spectrum is emitted by these excited atoms and can be measured with a spectrometer, in order to qualitatively and quantitatively evaluate the corresponding composition. More detailed information on this technique can be found in the literature (Broekaert 2003).

2.8.2 Dual Beam Platform

Dual beam platforms incorporate both a SEM and a Focused Ion Beam (FIB) in a single system as illustrated in Figure 19. However, most facilities are usually equipped with various additional analytical tools. The first commercial systems began to appear in the early 1990's (Young & Moore 2005). Since then dual beam platforms gained widespread use in material science, electronics and life sciences because of their capability to offer both high-resolution imaging and site-specific micromachining at length scales ranging from a few nanometres to hundreds of microns (Volkert & Minor 2007).

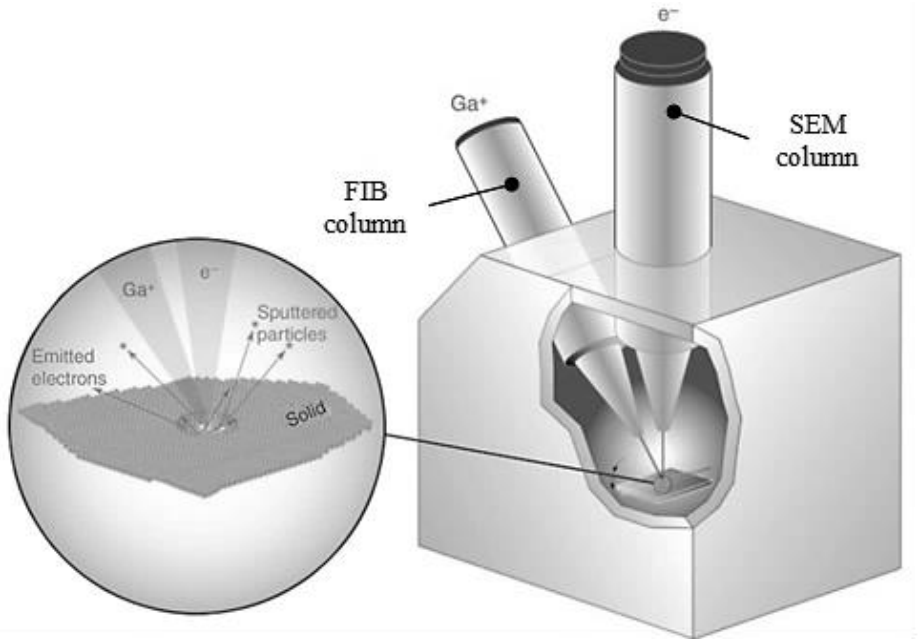

Figure 19: Schematic illustration of a dual-beam SEM–FIB instrument. Expanded view shows the electron and ion beam sample interaction. Adapted from (Volkert & Minor 2007).

The prime function of the SEM is to accelerate and focus a beam of electrons onto the surface of a sample where the incident electrons interact with the atoms in the material and

thereby generate a variety of electron induced signals (see Figure 20) which can be utilised for both, imaging and analytical purposes.

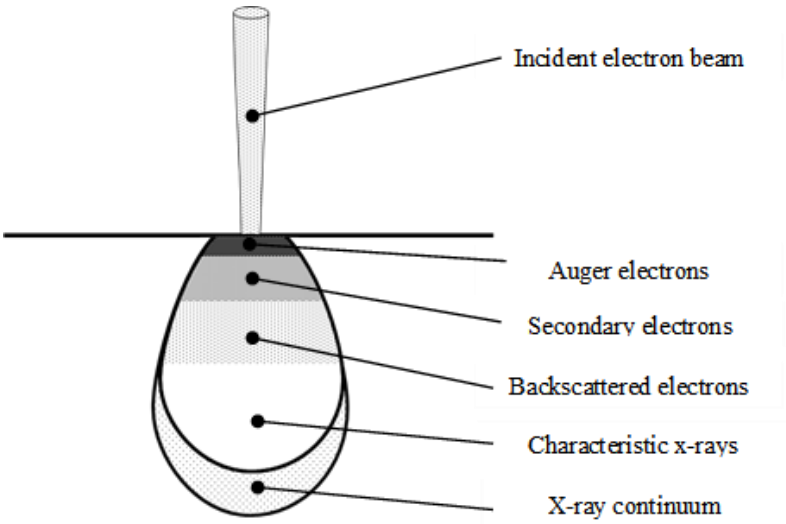

Figure 20: Examples of signals generated in the interaction volume at the sample surface.

The most common signals used for the micro-characterisation of materials are:

i. Secondary Electrons (SE's),
ii. Backscattered Electrons (BSE's),
iii. Characteristic X-rays;

SE's are typically used to create an image of a scanned surface. These electrons are emitted as a result of inelastic collisions where the incident electrons interact with the electrons of the atoms in the sample. As SE's have a relatively low energy (< 50 eV) they can only escape from a region within a few nanometres of the sample surface (Zhou et al. 2007). The relative number of detected SE's from a specific spot depends on both the inclination of the surface and the relative position of the SE detector. Both factors lead to the topographical contrasts in a SE image.

BSE's are another common signal used for imaging. These electrons are formed due to elastic collisions with the nucleus of the atoms in the sample and undergo single or multiple scattering events before they escape from the surface with a relatively high energy (>50 eV) (Zhou et al. 2007). The likelihood for elastic scattering events depends thereby on the atomic number of the atoms in the scanned region. The higher the atomic number the more electrons will be elastically scattered and detected. Therefore, a BSE image can provide both, topographic and compositional information. However, BSE's are typically emitted from deeper regions beneath the surface than SE's and are therefore less sensitive to topographic features.

Another class of signals produced by the interaction of the incident electron beam with the specimen are characteristic X-rays which contain information about the chemical composition of the analysed regions. When an electron in the inner shell of an atom is ejected by an incident electron through collision events, an outer shell electron may fall into the inner shell to re-establish the proper charge balance in its orbitals (Zhou et al. 2007). The difference in energy between the higher-energy shell and the lower energy shell may be released in the form of an X-ray photon which enables the atom to return to its ground state.

Further electron induced signals which can be used to analyse the microstructure are Auger electrons, cathodoluminescence and transmitted electrons. However, this brief introduction was limited to the interactions and signals that were relevant for the interpretation of the micrographs in the current work. More detailed information on electron induced signal formation and scanning electron microscopy in general can be found in literature (Goldstein et al. 2013; Reimer 1985).

The main function of the FIB is to accelerate and focus a beam of ions (typically Gallium) onto the surface of a sample where the interactions of the ion beam with atoms in the sample allow both, imaging and the selective removal of small material volumes. The illustration in Figure 21 shows some of the possible interactions that may occur when an ion impinges on the surface of a sample.

An incident ions kinetic energy is transferred to the atoms in the sample through inelastic and elastic interactions until it is dissipated. Consequently, the incident ion comes to rest and remains implanted at some depth R_P (projected range) below the sample surface (Giannuzzi, Prenitzer & Kempshall 2005).

Inelastic interactions occur if the electrons of the incident ion interact with the electrons of the atoms in the sample. Such events may generate phonons, plasmons (in metals), and the emission of SE's (Giannuzzi, Prenitzer & Kempshall 2005). These Ion-Induced Secondary Electrons (ISE's) can be used for imaging purposes. Typically, 1–10 ISE's with energies below 10 eV are generated per incoming 5–30 keV Ga^+ ion (Volkert & Minor 2007).

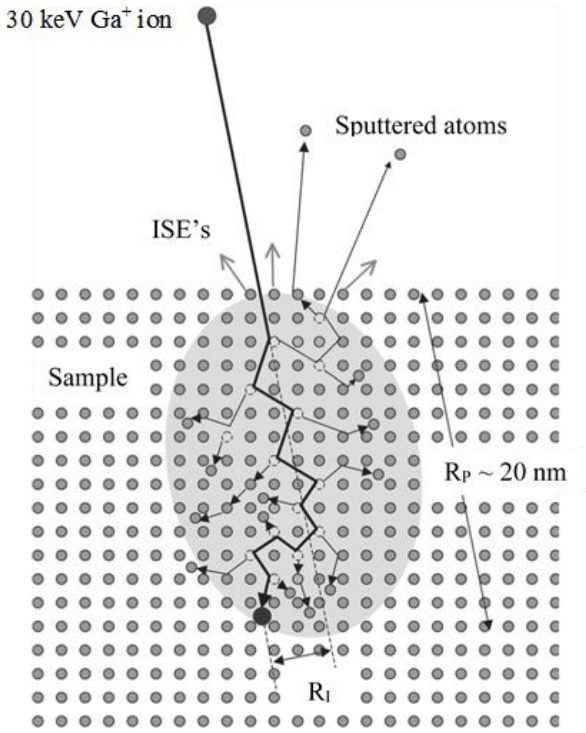

Figure 21: Schematic illustration of a collision cascade generated by a 30 keV Ga+ ion incident on a crystal lattice, showing the damage created in the collision cascade volume and the projected range R_P and lateral range RI of the implanted ion. Adapted from (Volkert & Minor 2007).

Ion beams are not as finely focused as electron beams and, partly for this reason, they generally offer lower resolution. However, the contrast mechanisms for ISE generation are different from those for SE generation and can offer complementary information about a sampled region. SE and ISE images of the same region are shown in Figure 22. Both the SE (Figure 22 a)) and the ISE (Figure 22 b)) images show contrasts due to the surface topography.

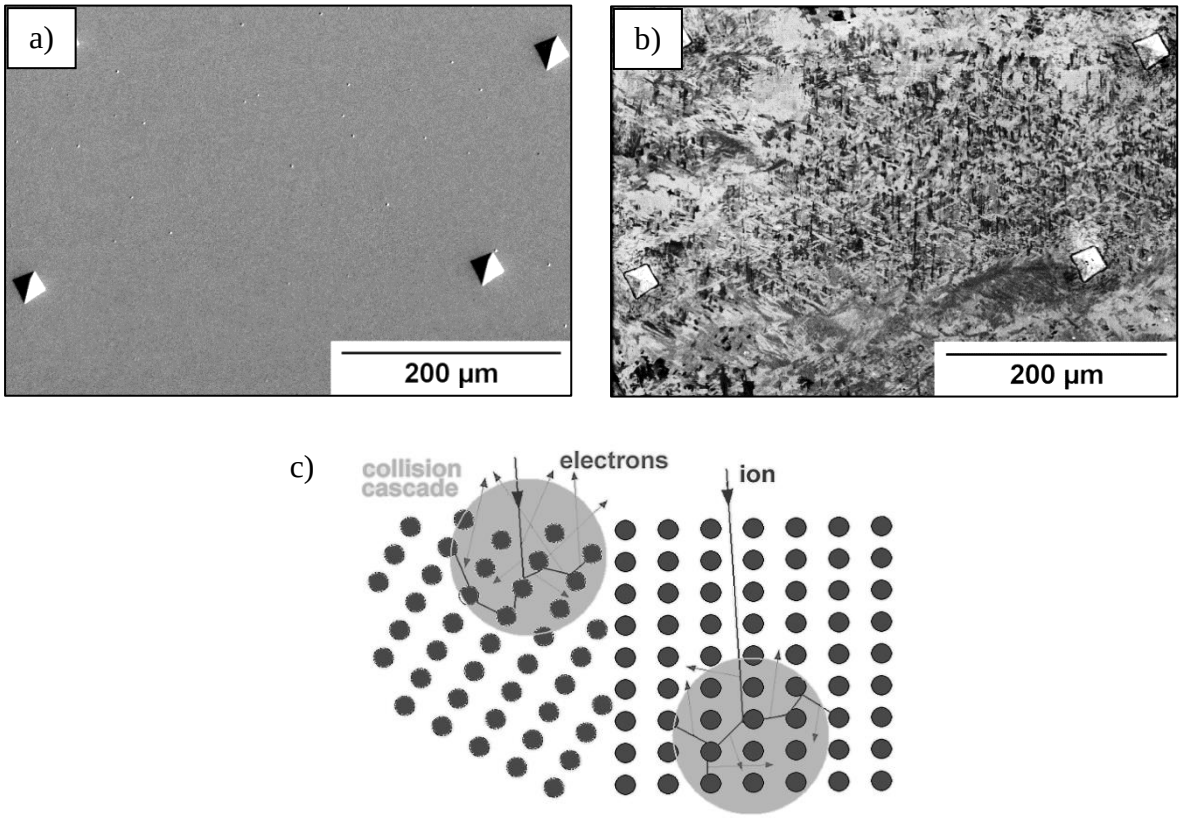

Figure 22: a) SE image of a selected region in a polished weld metal sample,
b) ISE image of same region reveals the weld metal microstructure due to the channelling contrast,
c) Schematic illustrates the formation of the channelling contrast;

However, the ISE image provides additionally ion channelling contrasts which reveal the microstructural constituents without chemical etching. These ion channelling contrasts are a result of the varying secondary electron yield caused by different crystallographic orientations as described in Figure 22 c). A particular crystallographic region (i.e., a grain in a

polycrystalline sample) will appear darker if its orientation allows an incident ion to "channel" along the crystal planes. This is because there are fewer ion interactions with sample atoms near the surface and thus fewer ISE's can be emitted (Giannuzzi, Prenitzer & Kempshall 2005).

Elastic interactions within a collision cascade occur when kinetic energy is transferred from the incident ion to the nucleus of the atoms in the sample. The atoms in the sample are usually referred to as target atoms. A target atom may be ejected from the surface of a sample as a sputtered particle if it receives a component of kinetic energy that is sufficient to overcome the surface binding energy of the material (Giannuzzi, Prenitzer & Kempshall 2005). Because of this sputtering phenomenon focused ion beams can be used to selectively remove material in highly localised regions. The quantitative aspects of sputtering are complicated and depend on the energy of the ion beam, the mass of the incident ions and the target atoms, the surface binding energy of the target atoms, the crystallographic orientation of the sputtered material, the incidence angle of the ion beam, and the extent of redeposition (Giannuzzi, Prenitzer & Kempshall 2005).

A characteristic parameter of the sputtering process is the sputter yield Y, i.e. the average number of target atoms emitted per impinging incident ion:

$$Y = \frac{\text{number of target atoms sputtered}}{\text{number of incident ions impinging}} \tag{2-7}$$

Sigmund (Sigmund 1969) developed the most widely used formula to obtain Y for amorphous and polycrystalline materials at perpendicular ion incidence. It can be written in the following form (Benninghoven, Rüdenauer & Werner 1987):

$$Y = \frac{4.2\times10^{14}[\text{cm}^{-2}]\,\alpha\left(\frac{M_2}{M_1}\right) S_n(E_P,M_1,M_2)[\text{eV cm}^2]}{U_S\,[\text{eV}]} \tag{2-8}$$

Where α is an empirical universal function that depends on the ratio between the mass of the target atom M_2, and the incident ion M_1, S_n is the nuclear stopping power of the incident ion in the sputtered sample and depends on the ion energy E_P as well as on the incident ions and target atoms mass, and U_S is the surface binding energy of the sputtered material.

However, Sigmund's theory may provide less accurate predictions of the sputter behaviour in polycrystalline materials, since the sputter yield also depends on the crystallographic orientation and may therefore vary between different grains (Nastasi 1996). In grains where the crystallographic orientation promotes channelling, the incident ions experience only inelastic glancing-angle collisions and hence travel deeper into the crystal before elastic collisions may occur. Consequently, fewer atoms can be sputtered from the surface (Volkert & Minor 2007).

As the incidence angle of the ion beam increases, the number of sputtered atoms increases. However, at the same time, the fraction of backsputtered ions also increases. Backsputtering occurs when an incident ion is scattered either directly, or after multiple collisions, out of the sample instead of being implanted (Sigmund 1981). The combination of these two effects leads to a maximum sputter yield at an incidence angle of approximately 75–80° (Lehrer et al. 2001; Volkert & Minor 2007).

The direction and velocity of a sputtered particle will be altered if it collides with another particle or an exposed surface. Depending on the impact energy and the sticking coefficient of the material, the sputtered particle may be redeposited if it strikes a surface. The sticking coefficient is a statistical measure of a material's affinity to adhere to a surface (Giannuzzi, Prenitzer & Kempshall 2005). Redeposition decreases the effective sputter yield because sputtered atoms may be redeposited at active milling sites and must be therefore removed a second time (Volkert & Minor 2007).

FIB micro-machining is often used to create features with high aspect ratios such as holes or deep narrow trenches (see Figure 23 b)). As the aspect ratio of such features increases during the fabrication process, the number of sputtered atoms and backsputtered ions which can escape without being redeposited continuously decreases, which typically results in a "V-shaped" sputter profile (Orloff, Swanson & Utlaut 2003).

Another factor that affects the overall sputter profile is the current density of the ion beam (Lehrer et al. 2001). A FIB generated ion beam exhibits a nearly Gaussian profile. The width of the profile is thereby proportional to the beam current (Lugstein et al. 2002). Lower beam currents result in a narrower beam profile and allow therefore to mill at a glancing angle relatively vertical sidewalls as illustrated in Figure 23 a). A narrower beam also reduces the redeposition because the sputtered atoms and backsputtered ions have a wider angle to escape as depicted in Figure 23 b). However, a reduction of the beam current also significantly increases the required sputter time to remove a specific material volume. A common practice is therefore to use high beam currents for coarse milling procedures to remove relatively large amounts of material and lower currents for fine details or to polish the machined features.

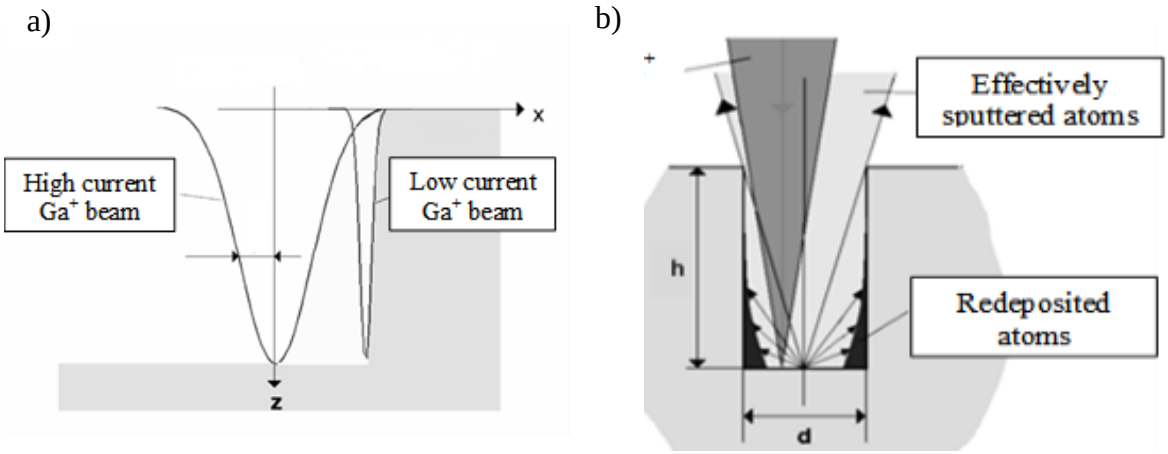

Figure 23: a) Illustration shows the relationship between an ion beams current density, its beam profile and the steepness of a sidewall milled at a glancing angle,
b) Illustration shows the relationship between redeposition, effective sputter rate and the width of the ion beam profile;

The sputter profiles also depend on the exact sequence in which the ion beam is scanned over the surface. As shown in Figure 24, the sputter profile of a ring cut by rapid “multi-pass” scanning differs from that obtained by a slow “single-pass” scan over the same area.

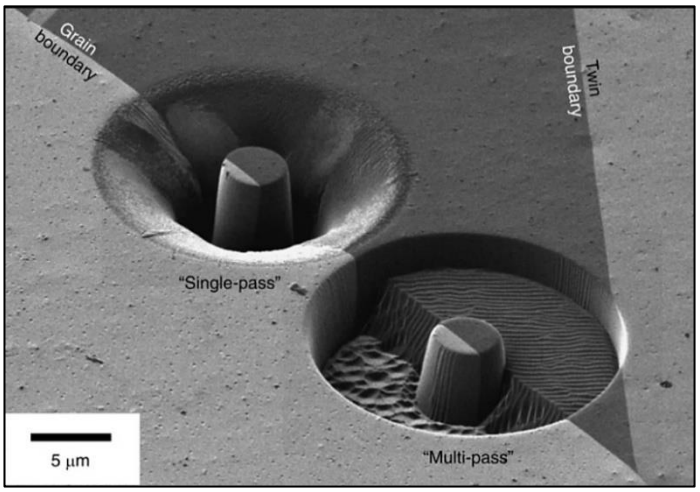

Figure 24: ISE image of rings milled at a grain boundary in Cu. The single-pass ring shows an enhanced sputter yield and redeposition while the multi-pass ring shows channelling effects and surface roughening. Adapted from (Volkert & Minor 2007).

An important factor to consider, particularly for analytical purposes and the FIB based micro-fabrication of mechanical test specimens, is the lattice damage created by the ion beam. As a result of the intrinsic nature of the sputter process, ions are always going to be implanted into the lattice of a sputtered sample as illustrated in Figure 25. Depending on the sample material and temperature, the ion beam can additionally cause amorphisation, point defects, dislocations, phase formations, grain modifications and other artefacts which may impair or prevent the microstructural characterisation and change the localised mechanical properties (Kiener et al. 2009).

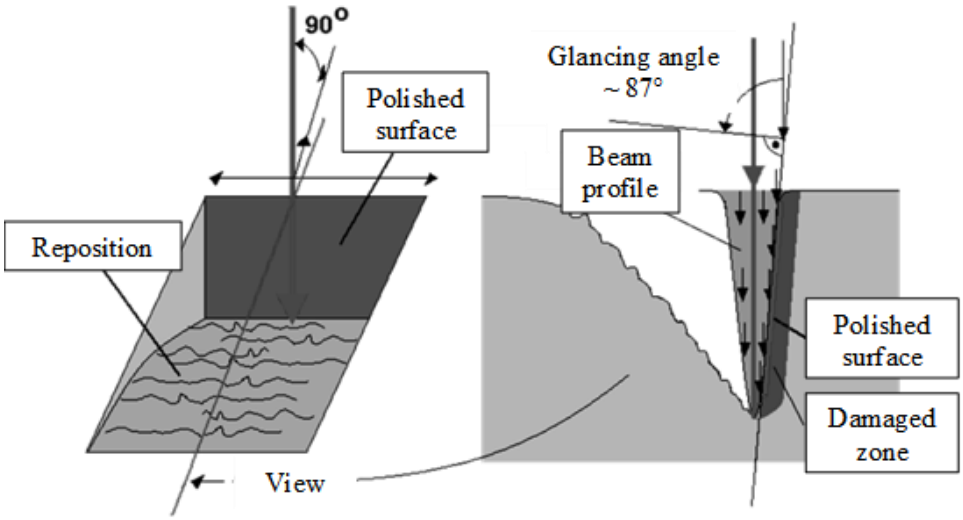

Figure 25: Schematic illustrates lattice damage at a milling site due to the fabrication process.

As the size of a FIB machined mechanical test specimen decreases, the proportion of the damaged volume due to the fabrication process increases as depicted in Figure 26. The effects of lattice damage on the mechanical properties can be especially critical for specimens with dimensions in the nanometre regime (Kiener et al. 2009). The depth of the lattice damage beneath the sample surface can be evaluated either empirically, for example, due to TEM observations or via modeling by Transport of Ions in Matter (TRIM) simulations (Ziegler, J.F., Biersack & Littmark 1985).

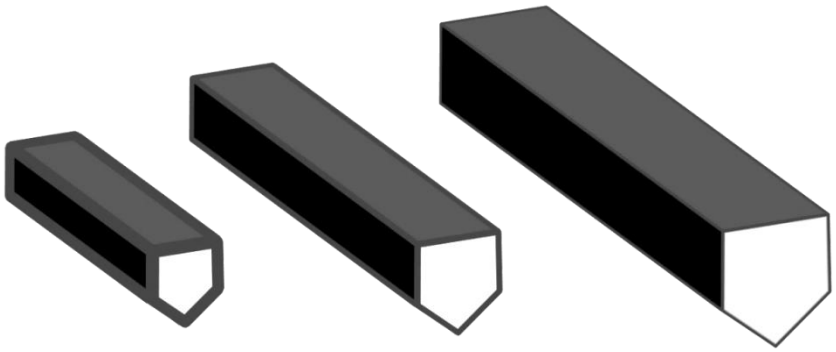

Figure 26: Schematic illustrates for FIB machined micro-beams the increasing proportion of the damaged volume as the sample size decreases.

2.8.3 Electron Backscattered Diffraction

The earliest observation of a diffraction pattern from backscattered electrons was reported in 1928 by Nishikawa and Kikuchi (Kikuchi & Nishikawa 1928). The researchers directed a beam of 50 keV electrons onto a thin mica crystal and recorded the diffraction pattern on photographic plates. The first commercial SEM's became available in 1965. By 1967, the first paper was published describing the SEM based observation of "Kikuchi like" patterns (Coates 1967).

The typical experimental setup of a modern Electron Backscattered Diffraction (EBSD) system consists of a SEM and an EBSD camera as illustrated in Figure 27. This technique provides quantitative information about the microstructure and crystallographic nature of most inorganic crystalline materials such as metals, minerals, semiconductors, and ceramics (Schwartz et al. 2009).

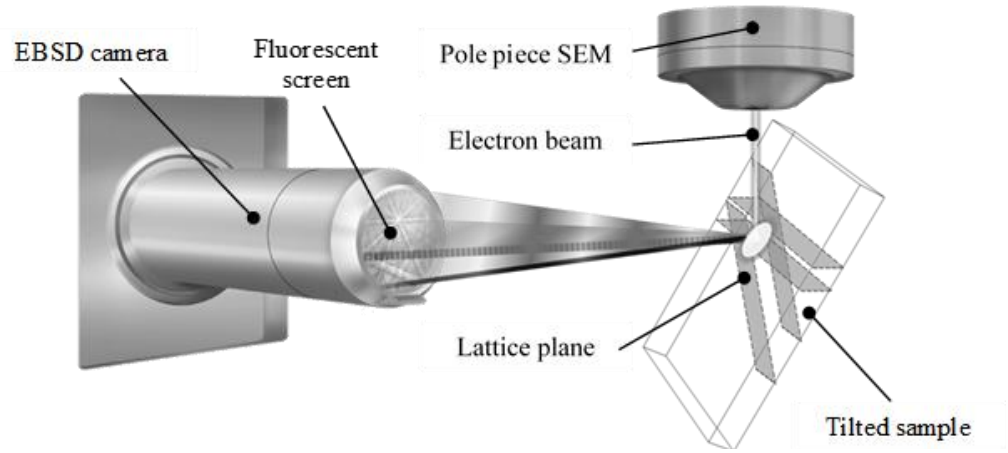

Figure 27: Schematic shows the pole piece of the SEM, the incident electron beam, the tilted sample and its lattice planes as well as the phosphor screen.

EBSD can be utilised to reveal, for example, grain size, grain boundary character (misorientation), grain orientation, texture, and phase identity. The nominal angular resolution

limit is approximately 0.5° and the spatial resolution mainly depends on the resolution of the SEM. For modern Field Emission SEM's (FE-SEM's), 20 nm grains can be measured with a reasonable accuracy (Maitland & Sitzman 2007).

In order to obtain EBSD pattern, a shallow angle, usually 20°, is required between the incident electron beam and the sample surface (Schwartz et al. 2009). The SEM stage is often used to tilt the plane of the sample to this shallow angle, the stage tilt is thereby typically 70° (Maitland & Sitzman 2007). Another option is to use a pre-tilted specimen holder.

The main function of the SEM is to generate an electron beam and to accelerate it towards the surface of the tilted sample. A fraction of the electrons that impinge the surface are incident on lattice planes at angles which satisfy the Bragg equation:

$$n\lambda = 2d_{hkl} \sin\theta_{hkl} \tag{2-9}$$

Where n is an integer representing the order of reflection, λ is the wavelength of the electrons, d_{hkl} is the spacing of the diffracting plane, and θ_{hkl} is the angle of incidence on the diffracting plane. These electrons can be scattered elastically and undergo constructive interference to form, corresponding to each diffracting plane, a pair of large angle cones as illustrated in Figure 28 a).

If these cones are projected to a fluorescent screen they form a pair of "Kikuchi" lines, the regions of enhanced electron intensity between the cones produce bright "Kikuchi" bands. Since, crystalline structures generally consist of several intersecting lattice planes they typically produce a network of intersecting Kikuchi bands which is usually referred to as Electron Backscatter Diffraction Pattern (EBSP), as shown in Figure 28 b).

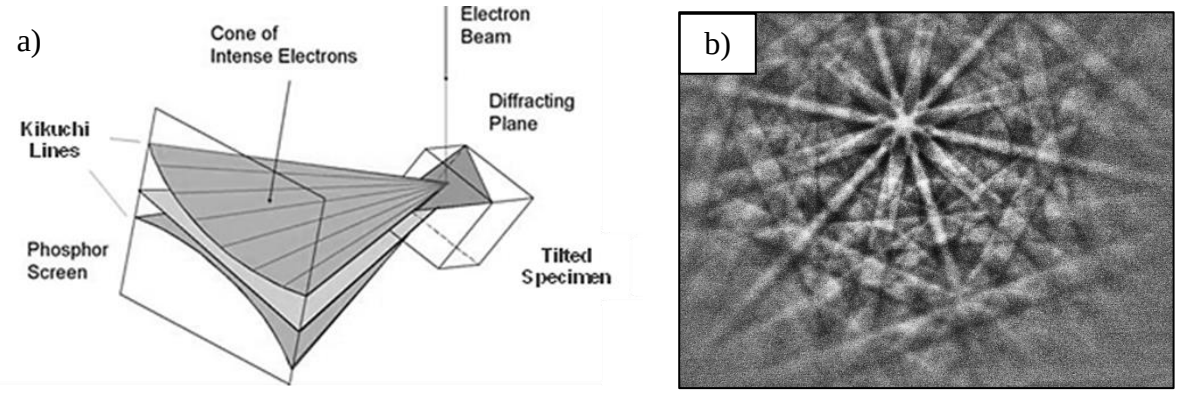

Figure 28: a) Schematic of the diffracting cones with respect to the reflecting plane, the specimen, and the phosphor screen, adapted from (Schwartz et al. 2009),
b) EBSP obtained from a ferritic phase in weld metal at 30 keV;

The geometry of an EBSP is unique for a particular crystal structure and lattice orientation (Schwartz et al. 2009). The angular width of a Kikuchi band is $2\theta_{hkl}$ and therefore, according to Bragg's equation, directly related to the interplanar spacing d_{hkl} . The centre lines of individual bands are the projection of the diffracting lattice planes. The interplanar angles can therefore be obtained from the positions of centre lines in the pattern. Once the position and width of the individual bands in the pattern have been identified, the crystal orientation can be evaluated.

Early EBSD systems required an operator skilled in crystallography to manually identify features in a captured pattern in order to determine the corresponding orientation. However, modern automated systems use image-processing techniques to identify the features needed to determine the crystallographic orientation from diffraction patterns without any operator intervention (Schwartz et al. 2009). The expected phases have to be pre-selected from a database. Each of the collected patterns is indexed based on its correlation with the structure parameters and reflectors of the candidate phases. Detailed algorithms for the automated indexing of EBSP's have been published by many authors, including a complete description by Wright (Wright 2000).

2.8.4 Nanoindentation

The nanoindentation technique was developed in the mid-1970s to characterise the mechanical properties of small volumes of material at length scales in the nanometre regime (Ternovskii et al. 1974). Apart from the displacement scale involved, the distinguishing feature of nanoindentation testing is the indirect measurement of the contact area, which is the area of contact between the indenter and the specimen.

In conventional indentation tests, the area of contact is calculated from direct measurements of the dimensions of the residual impression left in the specimen surface upon the removal of load (Fischer-Cripps 2011). In nanoindentation tests, the size of the residual impression, particularly at very low loads, is too small to be accurately measured with conventional optical techniques. Thus, it is customary to determine the area of contact by measuring the depth of penetration of the indenter into the specimen surface. This, together with the known geometry of the indenter, provides an indirect measurement of contact area at full load (Fischer-Cripps 2011).

Nanoindentation tests can be conducted with either pyramidal or spherical indenters. The Berkovich indenter, (see Figure 29 a)) is generally used in small-scale indentation studies and has the advantage that the edges of the pyramid are more easily constructed to meet at a single point. The face angle of the Berkovich indenter normally used for nanoindentation testing is 65.27° (Berkovich 1951). The tip radius for a typical new Berkovich indenter is on the order of 50–100 nm which may increase to about 200 nm with use. The Knoop indenter, (see Figure 29 b)), is a four-sided pyramidal indenter with two different face angles. Measurement of the unequal lengths of the diagonals of the residual impression is very useful for investigating anisotropy of the surface of the specimen. This tip was originally developed to allow the testing of very hard materials where a longer diagonal line could be more easily measured for shallower depths of residual impression (Knoop, Peters & Emerson 1939). The cube corner indenter (see

Figure 29 c)), is similar to the Berkovich indenter but has a semi-angle at the faces of 35.26° (Fischer-Cripps 2011).

Spherical indenters are particularly suitable to conduct deflection experiments on micro-beams as the penetration into the material is reduced and the measurements reflect predominantly the beam deflection rather than the surface indentation. As shown in Figure 30, the indenter tip is typically a spherocone. Only the very tip of the indenter is used to penetrate the specimen surface. Diamond spherical indenters with a radius of less than 1 µm can be routinely fashioned (Fischer-Cripps 2011).

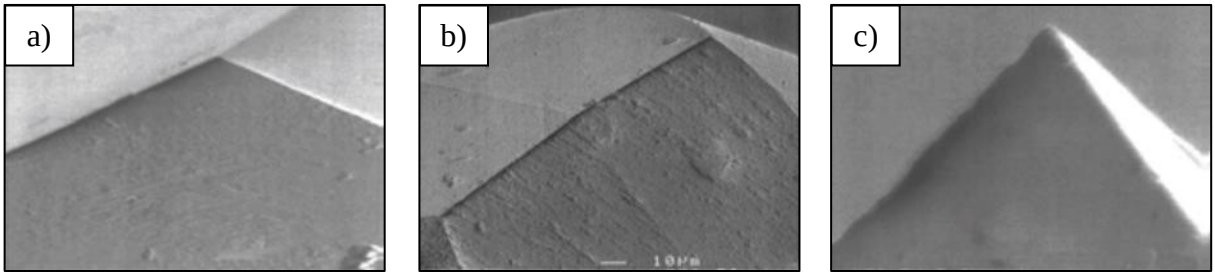

Figure 29: SEM images of the tips of:
a) Berkovich indenter,
b) Knoop indenter,
c) Cube-corner indenter. Adapted from (Fischer-Cripps 2011);

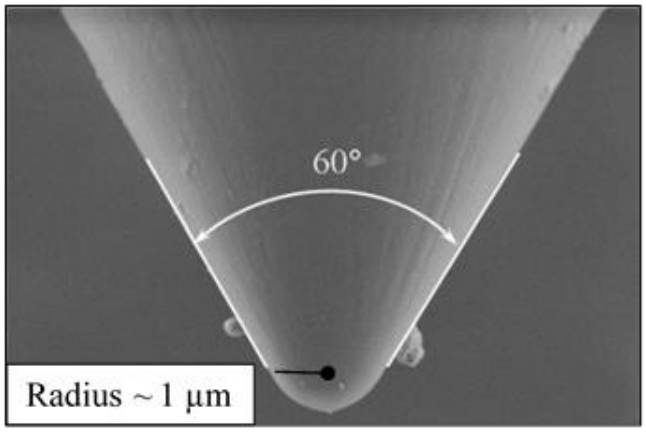

Figure 30: SEM image of a conical indenter with a spherical diamond tip. Adapted from (Zaafarani et al. 2008).

The loading conditions for fracture tests on notched micro-beams can be either load or displacement controlled. It is generally accepted that up to the point of the initiation of crack growth the measured values should be independent of the loading conditions (Kolednik 1992). However, if a ductile material reaches its ultimate strength in a load-controlled situation, it will continue to deform, with no additional load application, until it ruptures. If the loading is displacement-controlled, the deformation of the material may relieve the load, preventing rupture. The recorded load-displacement data is in both cases used to evaluate the relevant properties for the tested material.

CHAPTER 3

RESEARCH GAPS

3 Research Gaps

This chapter provides a summary of the identified gaps in the current knowledge on the relationship between microstructure, mechanical properties and WM HACC susceptibility.

i. Many important properties of weld metal such as strength, toughness and the resistance to WM HACC are a function of its microstructure, comprised of diverse constituents with characteristic features and different mechanical properties, which co-exist and interact at the smallest microstructural dimensions. Hence, conventional test methods used to determine the bulk material's properties are not suitable to evaluate the intrinsic properties of its individual microstructural constituents. Because of these experimental limitations, there is a lack of understanding of microstructural aspects that control the mechanical properties and the resistance to HACC at the micro-scale,

ii. For weld metal there seems to be a rough correlation between strength, toughness and HACC resistance. However, it still remains unclear if such a correlation also exists at the micro-scale, for the weld metal's individual microstructural constituents,

iii. Although several models have been proposed that describe the physical mechanisms of hydrogen embrittlement or hydrogen assisted cracking, which is the underlying phenomenon that leads to the formation of WM HACC, there seems to be no agreement on which of the proposed models provides the correct explanation. Additionally, none of the proposed methods used to investigate the effects of hydrogen on plasticity and fracture resistance is capable of directly evaluating the effects of hydrogen on the onset of crack initiation in particular microstructural constituents,

iv. Nanoindentation in combination with micro-fracture tests were identified as a potential technique to overcome the experimental limitations, in order to provide new insight on

the fundamental microstructural aspects that control the intrinsic mechanical properties and WM HACC susceptibility at the micro-scale,

v. Micro-scale fracture tests have not yet been employed to evaluate the fracture properties of complex, ductile microstructures or as a tool to study the effects of hydrogen on fracture. Hence, there is a lack of knowledge of the applicability and limitations of this technique in this area,

vi. Due to their distinctive characteristics, acicular ferrite and upper bainite were identified as ideal candidates to verify if site-specific micro-mechanical tests are applicable to investigate the fundamental link between microstructure, mechanical properties and HACC susceptibility,

vii. Due to its reportedly high resistance to WM HACC, acicular ferrite was identified as the ideal candidate to verify if micro-fracture tests can be utilised as a tool to conduct site-specific HACC tests,

CHAPTER 4

RESEARCH METHODOLOGY

4 Research Methodology

In order to achieve the research goals, it was necessary to employ proper manufacturing techniques and test procedures. The following sections provide information on the different techniques and procedures applied to attain the results that are presented in Chapter 5.

4.1 Experimental Procedure

The following paragraphs provide a brief overview of the three-tiered experimental approach to evaluate the relationship between the microstructure, mechanical properties and HACC susceptibility of acicular ferrite and upper bainite in weld metal.

This first part of the work examined the microstructure and mechanical properties of acicular ferrite and upper bainite in weld metal. Two localised microstructural regions, one acicular ferrite and the other one upper bainite, were first selected and then characterised using a high-resolution SEM in combination with EBSD. Semi-empirical models, based on microstructural aspects and physical principles, were used to determine the theoretical yield strengths of both microstructures. Different tests were then conducted within each of the initially selected microstructural regions to characterise the intrinsic mechanical properties. Conventional nanoindentation and an advanced characterisation procedure were employed to obtain the yield strength, hardness, elastic modulus and strain hardening exponent. Micro-fracture tests in combination with linear and non-linear approaches of fracture mechanics were used to evaluate the deformation behaviour, fracture behaviour and fracture resistance.

The second part of the work examined the microstructure and HACC propagation resistance of acicular ferrite and upper bainite in weld metal. A modified version of the Welding

Institute of Canada (WIC) weldability test was employed to generate WM HACC under controlled conditions (Kurji, R.N. & Coniglio 2015). The hydrogen crack propagation through selected microstructural regions of acicular ferrite and upper bainite was then characterised using EBSD. The UCP was utilised as a parameter to evaluate the HACC propagation resistance of both microstructures (Brozzo et al. 1977). Fractographic observations were conducted with a high resolution SEM, to characterise the fracture behaviour in the selected microstructural regions.

The third part of the work examined the microstructure and HACC initiation resistance of acicular ferrite in weld metal. A selected microstructural region of acicular ferrite was characterised using a high-resolution SEM in combination with EBSD. Micro-fracture tests were then conducted at different loads on a hydrogen pre-charged specimen, that was fabricated into the selected region with a FIB. LEFM was applied to determine the range for the threshold stress intensity factor, K_{th}, to initiate HACC. The microstructure, deformation behaviour as well as the fracture behaviour were examined and compared with the data obtained from first part of the work, where a micro-fracture test was conducted on an uncharged specimen, that was fabricated into the same region of acicular ferrite.

Because of the high production costs due to the time-consuming fabrication of the microscopic test specimens (approximately 30-40 hours/specimen), the investigation was in this case limited to only one microstructure. The main purpose was to test the feasibility of the experimental approach described in the previous paragraph. Hence, a microstructure had to be selected where failure formation was expected to be particularly difficult to achieve. Acicular ferrite was preferred to upper bainite due to its reportedly beneficial contribution to the HACC resistance of the bulk material it constitutes (Alam et al. 1996).

4.1.1 Overview of Experimental Procedure

The chart in Figure 31 outlines the experimental procedure. The methods and techniques used to conduct the different tasks are detailed in the following sections.

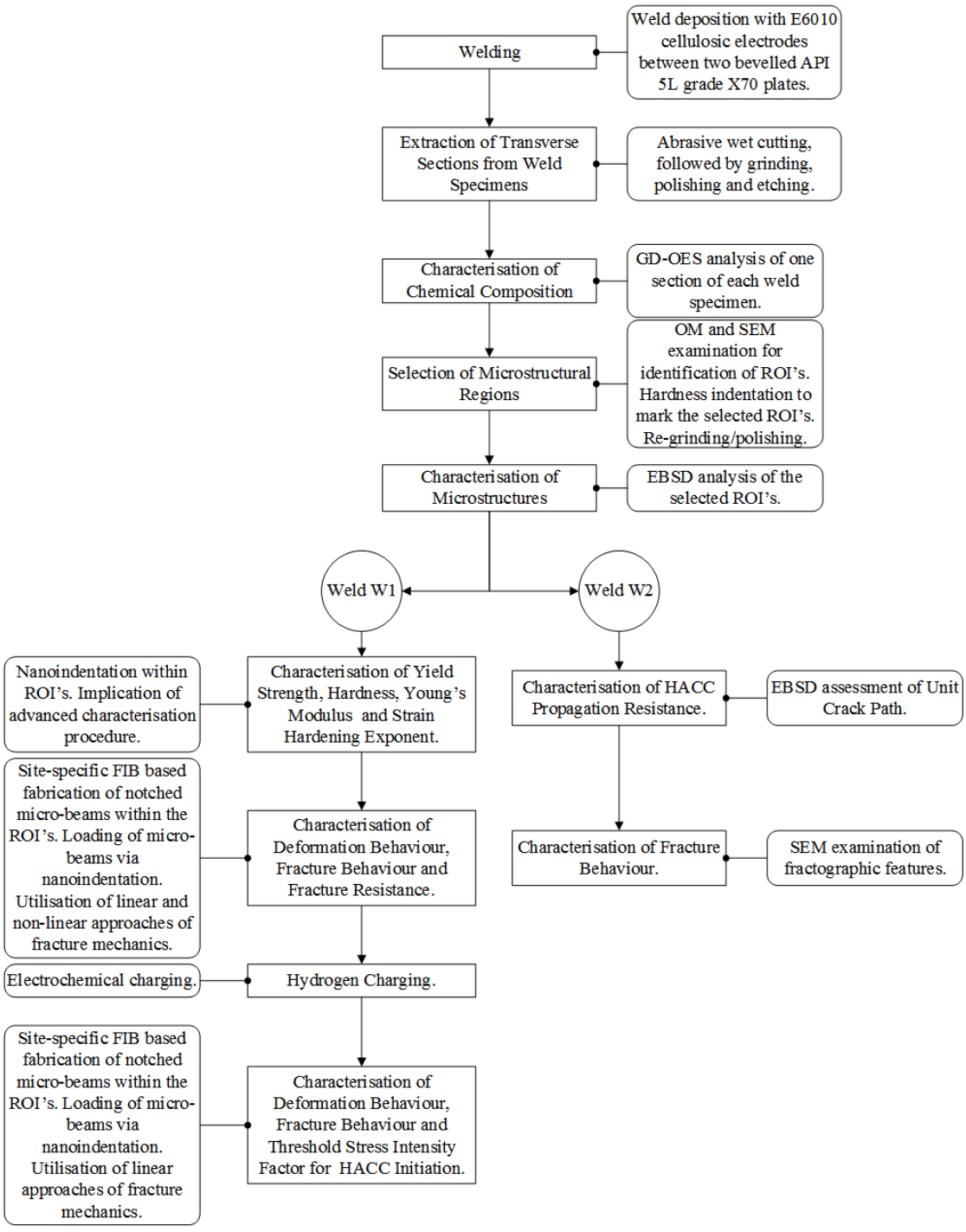

Figure 31: Chart provides an overview of the experimental procedure.

4.1.2 Fabrication of Weld Specimens

The weld specimens were deposited with 4 mm diameter E6010 cellulosic electrodes between two bevelled, hot rolled API 5L grade X70 test plates with 20mm thickness that were restraint by anchor welds on top of the backing plate of the modified WIC test rig, as detailed in the next section. The electrodes batch chemistry and the test plates chemical composition are listed in Table 9 and Table 10 respectively. The typical microstructure of the test plates in the as received condition are shown in Figure 32.

C	Mn	Si	S	P	Ni	Mo	Cr	V
0.16	0.62	0.19	0.009	0.009	0.2	0.01	0.02	<0.01

Table 9: Electrode batch chemical composition in weight % (from manufacturer).

C	Mn	Si	S	P	Nb	Ti	Cu	Ni	Mo	Cr	Ca	Al	V
0.05	1.55	0.21	0.001	0.01	0.04	0.01	0.15	0.19	0.18	0.026	0.0016	0.04	0.03

Table 10: Chemical composition of test plates in weight % (from manufacturer).

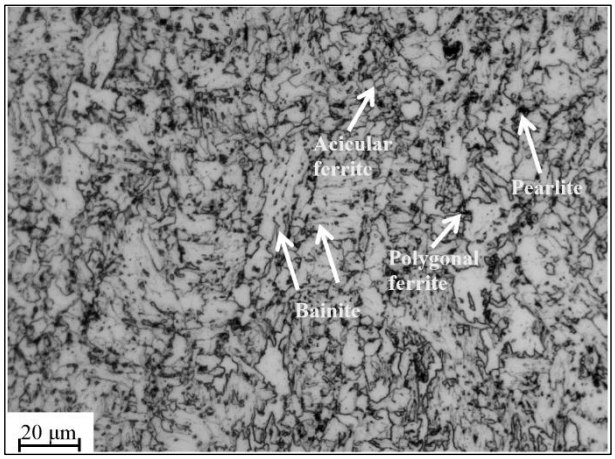

Figure 32: Optical micrograph of polished and 2% Nital etched API 5L X70 test plates (Alipooramirabad et al. 2016).

The welding procedure involved a unidirectional, mechanized SMA welding machine with a specimen-holding plate moving vertically upwards during welding, at a controlled velocity, thus simulating vertical-down (stovepipe) welding conditions. A constant force and an angle of 20° normal to the plate were maintained between the electrode and the work piece. All these specifications (see Table 11) had the main purpose to replicate field conditions, as encountered when laying the root pass of a girth weld.

The weld specimens, W1 and W2, were produced with similar heat inputs but different post weld cooling conditions, as detailed in Table 11, to achieve equivalent microstructures but different final hydrogen levels. Welding of specimen W1 implied a preheat treatment of 100°C which resulted in a slower cooling rate, particularly below 200°C. Hence, most of the residual diffusible hydrogen could effuse out from the weld region and the specimen remained free of WM HACC. On the contrary, the welding parameters for specimen W2 were specifically selected to generate WM HACC.

Welding Specifications		**Welding Parameters**		
Direction:	Vertical Down (5G)	**Weld:**	**W1**	**W2**
Electrode Size:	Ø 4.0 [mm]	Current [A]:	178	155
AWS Class:	A5.1	Voltage [V]:	22.9	26
Specification:	E6010	Travel Speed [mm/min]:	456.7	420
Polarity:	DC+	Preheat [°C]:	100	0
		Heat Input [kJ/mm]	0.536	0.576

Table 11: Welding specifications and parameters used to deposit the weld specimens W1 and W2.

4.1.3 Modified Welding Institute of Canada test

The original WIC test was first introduced in the 1980's as a small scale, intrinsic, qualitative weldability test that can be utilised to assess the HACC susceptibility of a weld (Kurji, R N et al. 2013). The main components of the test rig are illustrated schematically in Figure 33 a). It basically consists of a T profile (backing plate with stiffener) and two test plates that are restraint on top of the backing plate by anchor welds. The test weld has to be deposited into a single V groove preparation to join the restraint plates. The restrained length refers thereby to the unrestrained part between the plates and its main function is to control the intensity of transverse stresses on the deposited weld. The resultant stress for a selected restrained length is referred to as restraint stress σ_R and can be expressed by (Kurji, R N et al. 2013):

$$\sigma_R = \frac{SR_F}{h_W} \tag{4-1}$$

Where S is the total contraction and h_W is the height of the weld metal throat. The tensile restraint intensity R_F is given by (Kurji, R N et al. 2013):

$$R_F = \frac{Eh}{l} \tag{4-2}$$

Where E is the Young's modulus, h is the test plate thickness and l is the restraint length. The equations (4-1) and (4-2) indicate that a longer restraint length results in smaller restraint intensities and therefore smaller transverse stresses in the weld metal.

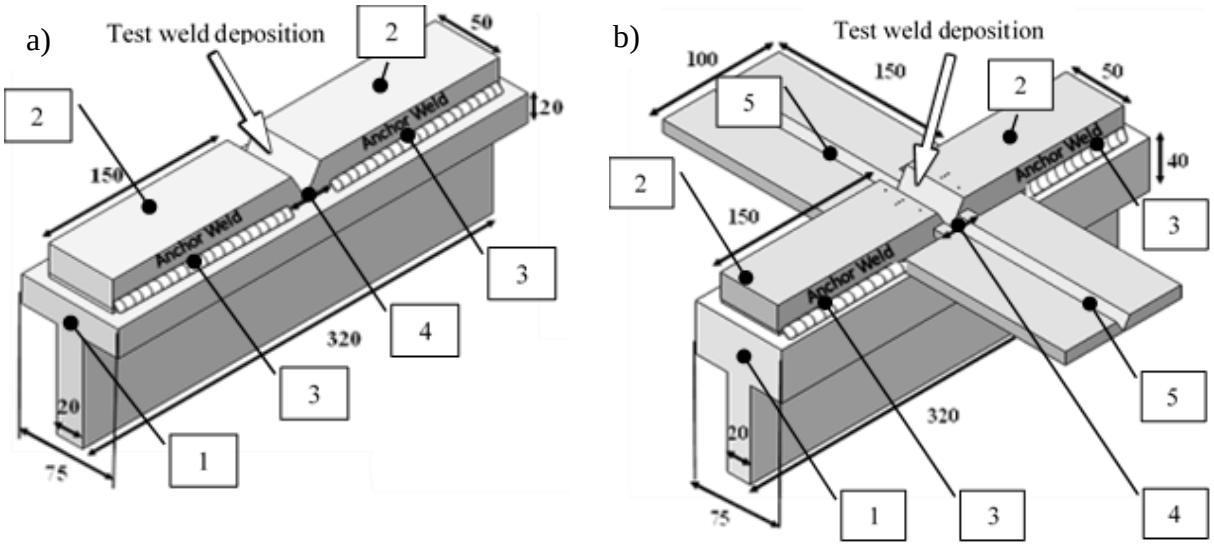

Figure 33: a) Schematic of standard WIC test: *1: Backing plate with stiffener, 2: Test plate, 3: Anchor weld, 4: Restraint length;*
b) Schematic of modified WIC test: *1: Backing plate with stiffener, 2: Test plate, 3: Anchor weld, 4: Restraint length, 5: Run on, run off tabs;* Adapted from (Kurji, R N et al. 2013).

The standard WIC test setup used to fabricate the specimens was modified to improve the quality of the deposited weld at lower heat inputs (see Figure 33 b)). The modifications as well as the specifications for this test are described elsewhere in literature (Kurji, R N et al. 2013).

4.1.4 Extraction of Weld Specimens

The deposited test welds W1 and W2 were extracted from the WIC test rig 24 hours after deposition, by milling the test assembly just inside the restrained length. Abrasive wet cutting was then used to cut the welds into four transverse sections, as illustrated in Figure 34 a) and Figure 34 b). For each test weld, the 2nd section in welding direction was used to

determine the chemical composition by GD-OES. All the other investigations were carried out on the 3rd section in welding direction.

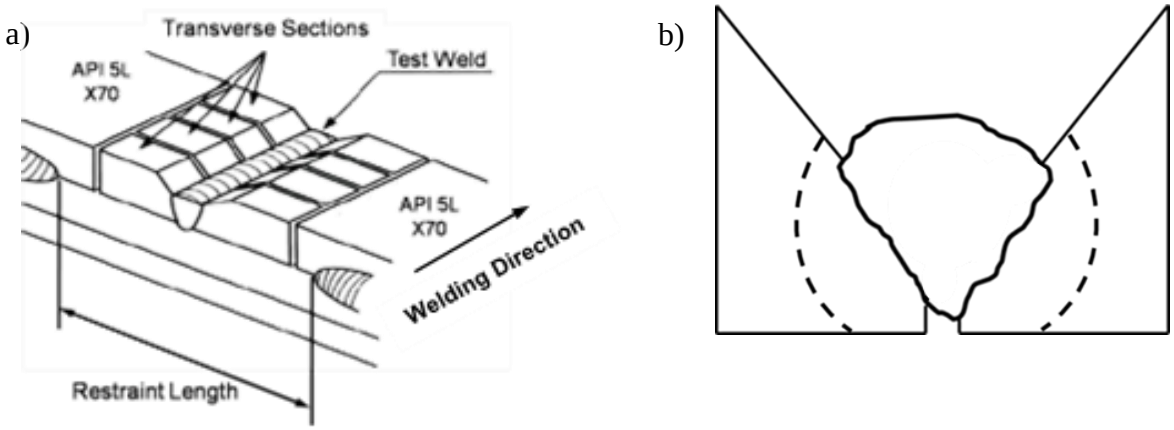

Figure 34: a) Extraction of test weld. Adapted from (Cannon 2009),
b) Schematic of transverse section of weld specimen.

4.1.5 Characterisation of Chemical Composition

The chemical compositions of the weld specimens W1 and W2 (2nd section in welding direction) were determined by GD-OES, using a HORIBA GD-Profiler 2™. A 4 mm anode was utilised to conduct the measurements, at 70W and a pressure of 850 Pa, to assure the maximum sensitivity. All elements of interest were calibrated prior to the analysis. The quantifications obtained with the 4 mm anode represent an average of the signal over the surface and in volume.

4.1.6 Selection of Microstructural Regions

The selected regions of interest (ROI's) in the current work were acicular ferrite and upper bainite, which are known to have substantially different microstructures, with particular intrinsic mechanical properties and HACC susceptibility (Alam et al. 1996; Bhadeshia 1997). However, in the bulk material they usually co-exist and interact with other microstructural constituents. Therefore, the relationship between the microstructure, mechanical properties and HACC susceptibility of acicular ferrite and upper bainite in weld metal still remains unclear.

Because of the relatively large field of view at low magnifications, optical microscopy was employed to locate the individual ROI's, in each of the weld specimens, using a Zeiss Axio Imager 2^{TM} optical microscope. More detailed examinations were conducted with the high resolution SEM (FEI Helios Nanolab 600 Dual Beam^{TM} platform).

The sample preparation procedure for the optical examinations is summarised in Table 12. The transverse sections (3rd section in welding direction) of the specimens were hot mounted in Bakelite. Afterwards, a Struers Tegra-pol-35 advanced preparation system was utilised to grind and polish the mounted samples, which were subsequently etched with 2% Nital to reveal their microstructures.

Two localised microstructural regions, acicular ferrite and upper bainite, were selected for the investigations conducted on the 3rd section in weld W1, through detailed inspection of the entire surface, as shown in Figure 35. It was thereby necessary to choose regions with a sufficiently large area to accommodate all micro-mechanical tests. Once the individual regions were identified and selected, hardness indentations were used to mark their locations for further analysis (see Figure 36, Figure 37 and Figure 38).

Step	Plane Grinding	Fine Grinding	Diamond Polishing	Etching
Surface	SiC Paper 320	MD-Largo	MD-Dac	2% Nital
Suspension		DiaPro 9 µm	DiaPro 1 µm	
rpm	300	150	150	
Force [N]	30	30	10	
Time [sec.]	60	600	300	5

Table 12: Preparation procedure for the identification of the ROI's in the weld specimens. Ultrasonic cleaning in a 10% detergent solution (Triton™ X-100) in water was required after each step.

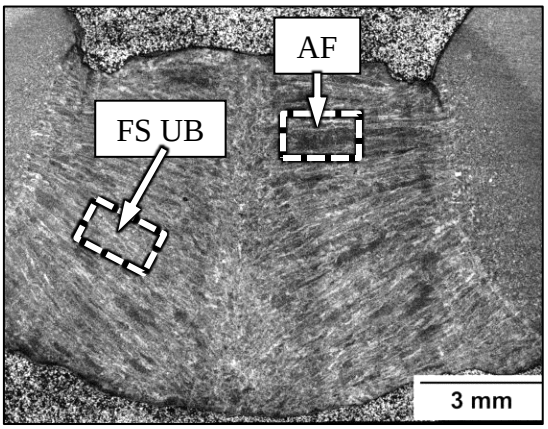

Figure 35: Optical micrograph of the 2% Nital etched 3rd section of weld W1 shows the selected microstructural regions for the micro-mechanical tests. Higher magnifications of these regions are shown in Figure 36, Figure 37 and Figure 38.

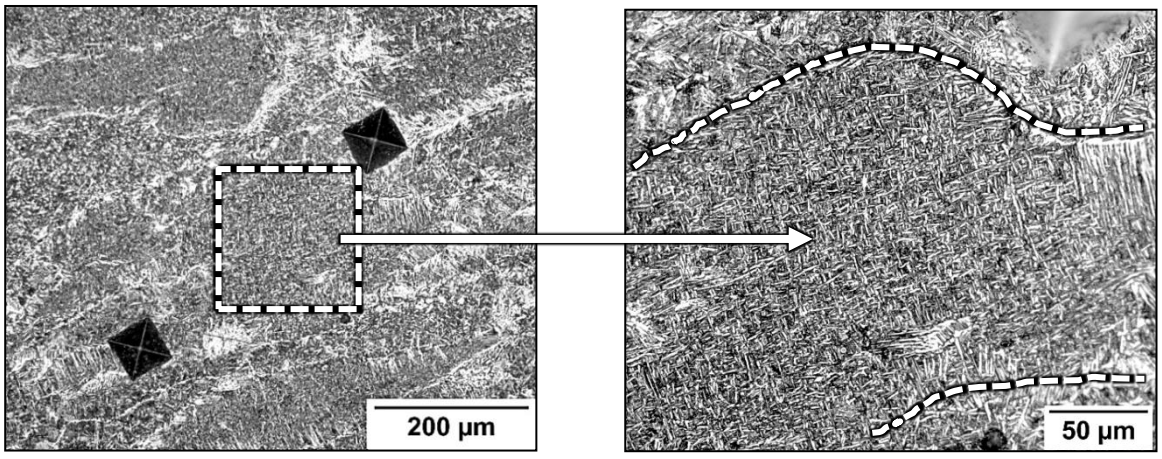

Figure 36: Optical micrographs of the 2% Nital etched section of weld W1 show acicular ferrite defined by the interlocking arrangement of fine-grained ferrite plates.

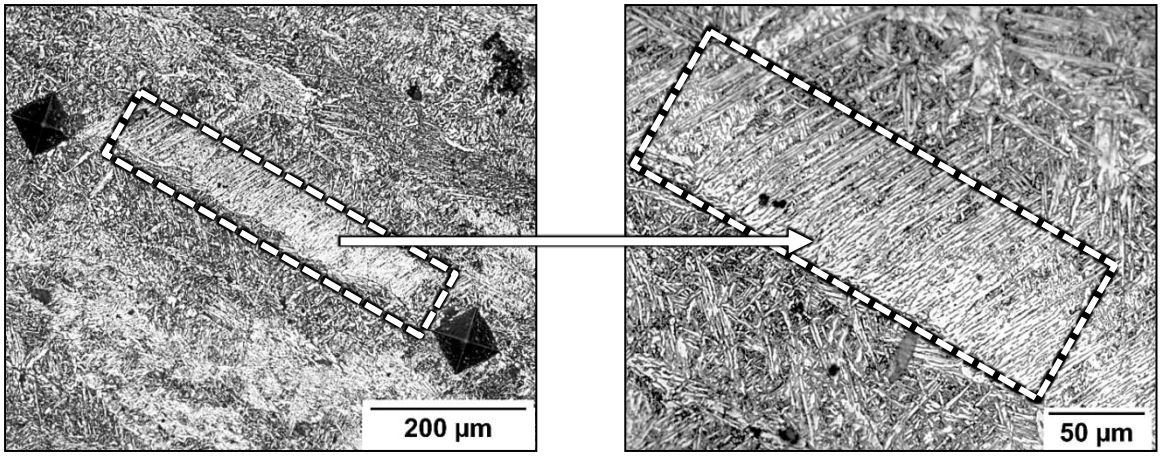

Figure 37: Optical micrographs of the 2% Nital etched section of weld W1 show adjacent ferrite laths of upper bainite.

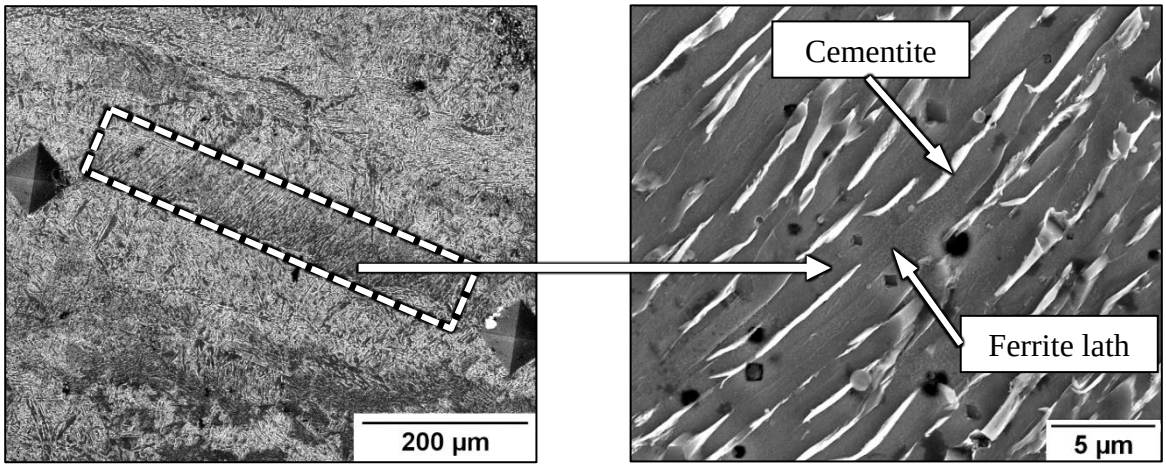

Figure 38: SE images of upper bainite reveal individual ferrite laths with elongated cementite particles between their boundaries.

The optical assessment of weld W2 showed that WM HACC initiated from the root of an undercut (see Figure 39 a) and Figure 39 b)). Such weld discontinuities are usually associated with excessive currents and high travel speeds (Alam et al. 1996). Triaxial tensile stresses resulting from the weld thermal cycle and restraint conditions are concentrated in these regions which have therefore a high affinity for hydrogen accumulation and are hence common WM HACC initiation sites (Alam et al. 1996).

The hydrogen crack propagated across the columnar prior austenite grains, including microscopic regions of acicular ferrite and upper bainite, as highlighted in Figure 39 b). Once these regions were identified and selected, hardness indentations were used to mark their locations.

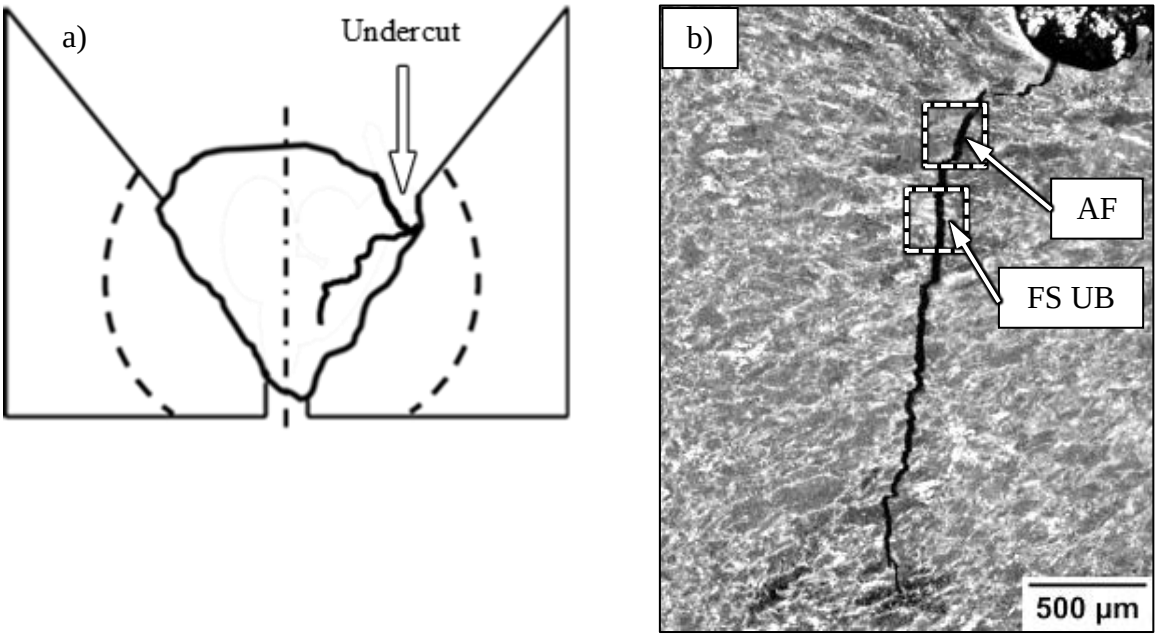

Figure 39: a) Schematic of HACC location,
b) Optical micrograph of a 2% Nital etched section of weld W2 shows WM HACC initiating from the root of an undercut followed by crack propagation across the columnar prior austenite grains. The highlighted regions show the location of hydrogen crack propagation through microscopic regions of acicular ferrite and upper bainite.

The optical micrographs in Figure 40 represent higher magnifications of the selected regions in weld W2 (see Figure 39 b)) and indicate that the hydrogen crack in acicular ferrite followed a rather intricate path, while the crack propagation in upper bainite occurred along a nearly straight line.

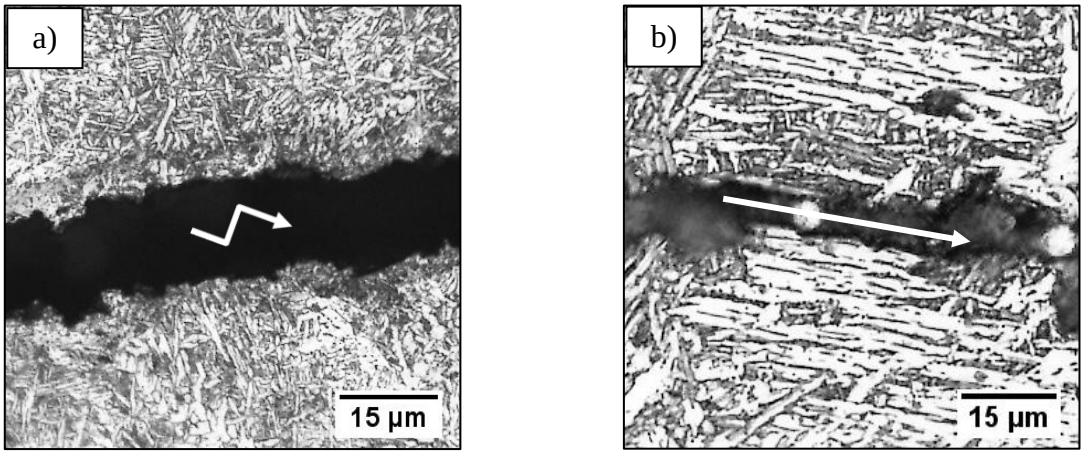

Figure 40: Optical micrographs show the highlighted regions in Figure 39 b), where the hydrogen crack propagated through microscopic regions of:

a) Acicular ferrite,

b) Upper bainite;

4.1.7 Characterisation of Microstructures

The topographic contrasts, resulting from the 2% Nital etch, are detrimental for the EBSD investigations as they introduce intensity gradients within the EBSP's and therefore impede a correct indexing (Nowell, Witt & True 2005).

EBSD is a particularly surface-sensitive technique since the diffraction signal containing the crystallographic information is typically collected from the top few nanometres of the crystal lattice (Schwartz et al. 2009). Therefore, it is essential that this top layer remains free from damage and also free from contamination or oxidation. Consequently, an appropriate sample preparation is absolutely critical in order to obtain good EBSD data. The preparation procedure used for the weld specimens is summarised in Table 13.

It is thereby important to keep the grinding time as short as possible in order to maintain a visible indentation. Additionally, it has to be considered that both, indentation depth as well as abrasive behaviour, may vary between different microstructural constituents.

Step	Plane Grinding	Fine Grinding	Diamond Polishing	Oxide Polishing
Surface	N/A	MD-Largo™	MD-Dac™	MD-Chem™
Suspension		DiaPro™ 9 µm	DiaPro™ 1 µm	OP-U™ 0.04 µm
rpm		150	150	150
Force [N]		30	10	10
Time [sec]		15	180	600

Table 13: Table shows the required preparation procedure for the EBSD analysis of the ROI's in weld W1 and W2. Ultrasonic cleaning in a 10% detergent solution (Triton™ X-100) in water was required after each step.

Due to the hardness indents, the ROI's in weld W1 and W2 could be located after re-grinding and polishing the specimens. The locations of the individual EBSD scans are shown in Figure 41 and Figure 42.

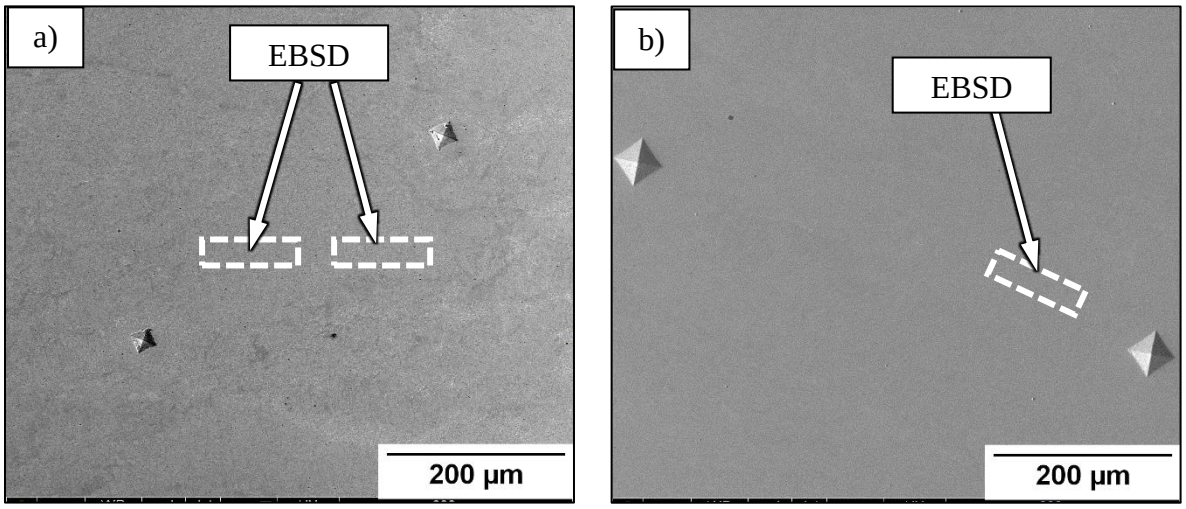

Figure 41: SE images show the locations of the EBSD scans in weld W1 for:
a) Acicular ferrite,
b) Upper bainite;

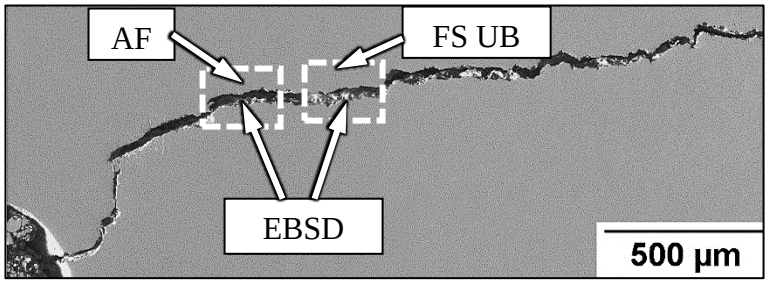

Figure 42: SE image shows the locations of the EBSD scans in weld W2 for acicular ferrite and upper bainite.

Although the initial optical examination was suitable to identify the ROI's in weld W1 and W2, EBSD was required for a detailed quantitative characterisation. The general settings for the EBSD data collection are summarised in Table 14.

Beam Settings	Step Size	Scan Grid	SEM	EBSD Camera
20 kV/ 2.1 nA	20 nm	Hexagonal	FEI Helios NanoLab™ 600	EDAX Hikari™

Table 14: Settings for EBSD data collection from the ROI's in weld W1 and W2.

The EBSD data can be used to generate various types of maps to visualise different aspects of the microstructure. One common map constructed from EBSD data is the Image Quality (IQ) map. The IQ is a metric that describes the quality of a diffraction pattern, which in turn depends on the "perfection" of the crystal lattice within the diffracting volume from which it originated (Wright & Nowell 2006). An IQ map typically represents undisturbed crystallographic regions in a brighter tone and imperfections such as grain boundaries in a darker tone. The resulting greyscale images provide a useful visualisation of the microstructure, as shown in Figure 43.

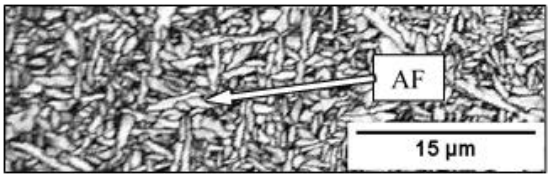

Figure 43: IQ map of acicular ferrite in weld metal.

A common map to represent the texture of a microstructure is the Inverse Pole Figure (IPF) map. These types of maps show the distribution of crystallographic orientations relative to a selected reference direction. For example, the selected reference direction for the superimposed IQ and IPF map in Figure 44 was [001], which was defined as the direction perpendicular to the sample surface for all IPF maps in the current work. The colour in each point of the map is assigned to a specific crystallographic direction according to a colour coded unit triangle.

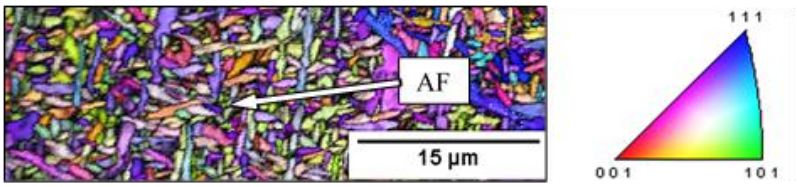

Figure 44: Superimposed IQ and [001] IPF map of acicular ferrite in weld metal.

While the concept of a grain in conventional metallography is well known, the definition of a grain in an EBSD scan is slightly different. Grains in EBSD are formed by an algorithm that groups sets of connected and similarly oriented points into "grains". For each point in an EBSD scan, the neighbours are checked to see if they are within a specific grain tolerance angle relative to the given point. If a neighbouring point is found to be within the tolerance angle, then the neighbours of that point are checked to verify if they are within the tolerance angle. The procedure is repeated over and over again until a set of connected grains is bounded by

points, which exceed the tolerance angle to their neighbours. Using this approach, the point to point misorientation in a “grain” will be quite small but the spread of orientations among all points in the “grain” can be relatively large. The number of points required to decide whether a given group of points should be considered a “grain” can be specified by the user along with the grain tolerance angle. Thus, the definition of a grain in EBSD can vary depending on user defined values.

The grain size in EBSD can be simply specified as the number of data points contained within a grain. Alternatively, the grain size may be specified by an area. The area is calculated by summing up the number of points in a grain multiplied by the product of the square of the step size and a factor depending on the type of scanning grid. For square grids the factor is 1 and for hexagonal grids the factor is $1.5\sqrt{3}$ (EDAX 2007). The grain size may also be specified by the diameter, which can be calculated by first determining the area and then Equivalent Circular Area Diameter (ECAD). Another common method to evaluate the grain size the mean Linear Intercept (LI). More detailed information on the quantitative aspects of grain size measurements can be found in the literature (Muirhead et al. 2000).

In conventional metallography, a grain boundary denotes the line separating two grains. Generally, in EBSD a grain boundary refers to a line segment separating two measurement points in a scan. To completely describe a grain boundary, 5 parameters are needed, two to describe the orientation of the boundary plane normal and three to describe the misorientation. The boundary plane cannot be recovered directly from the EBSD data. Since the EBSD data is collected from a plane, only one trace of the boundary can be observed. Thus, serial sectioning or other stereological approaches are needed to extract the complete boundary normal information. However, since the orientations at both points separated by the line segment are known, the misorientation associated with a line segment can be calculated (EDAX 2007). For the grain boundary maps in the current work, the minimum number of points to define a grain was 2 and the grain tolerance angle was 0.5°. The allowable angular deviation to define the

CSL boundaries was based on the Brandon criterion (Brandon 1966) which can be formulated as:

$$\Delta\theta \leq 15\ \Sigma^{-1/2} \quad (4\text{-}3)$$

Where $\Delta\theta$ is the allowable angular deviation and Σ is the sigma notation of the CSL boundary.

4.1.8 Site-Specific Fabrication of Notched Micro-Beams

The localised fracture properties of ductile materials cannot be characterised with conventional nano-indentation techniques. Indeed, these rely on the measurement of the crack length formed at the indentation corners (Evans & Charles 1976) and can therefore only be applied to test rather brittle materials. Thus, it seems that for inherently ductile materials, such as for example weld metal, the only viable option to directly evaluate localised fracture related properties, at micro- and nano-scales, is to conduct tests on miniaturised fracture specimens, as demonstrated in the current work.

A FIB (FEI Helios Nanolab 600 Dual Beam^{TM}) was utilised for the site-specific fabrication of the notched micro-beams. The locations for the material removal in the selected microstructural regions of weld W1 are shown in Figure 45. The aim was to micro-machine fracture specimens from the martial beneath the regions that were previously analysed with EBSD. It has to be noted that the dimensions of the mapped regions were similar, in order to be able to compare particular microstructural features of a certain area. It was thereby expected that the analysed regions were, at least for a certain depth and volume, representative for the material underneath. The ISE image in Figure 45 b), reveals that the colony of upper bainite consisted of crystallographic packets with particular orientations. The EBSD scan as well as

the fabrication of the micro-beam were conducted in such a crystallographic packet. The length of the individual ferrite laths did approximately correlate with the width of both, the scanned region and the micro-beam, that was fabricated into upper bainite.

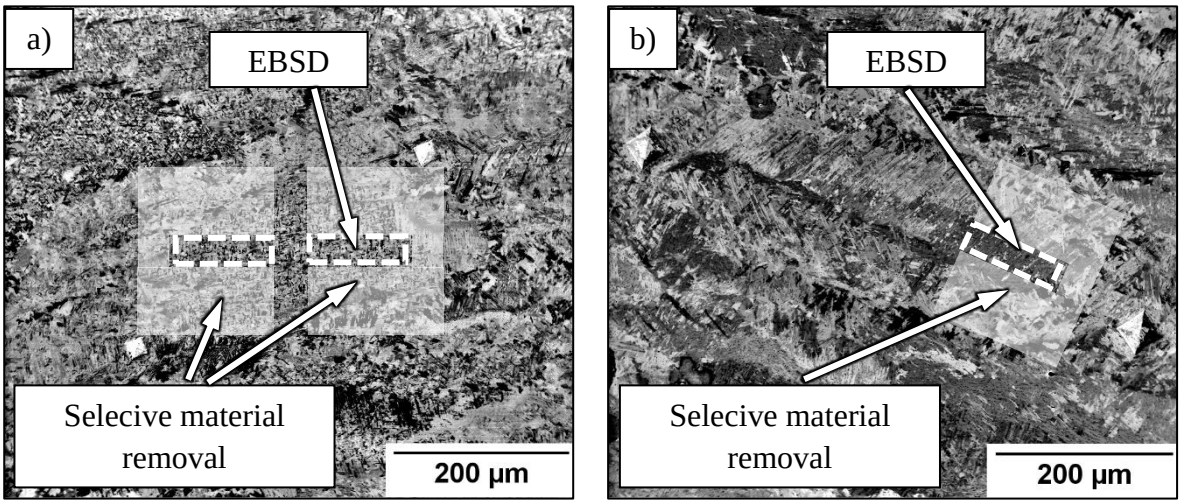

Figure 45: ISE images show the locations of the EBSD scans and the fabrication of the notched micro-beams in weld W1 for.

a) Acicular ferrite,

b) Upper bainite;

The selected shape for the micro-beams was a pentagonal profile as shown in Figure 46. If the specimens are fabricated in the vicinity of free edge, it is also possible to machine micro-beams with a rectangular profile as it was demonstrated by Motz et al. (Motz, Schöberl & Pippan 2005). Such specimen profiles are more commonly used in conventional fracture testing (e.g. Single-Edge Notched Beam or SENB).

However, for the objective of the current work, the fabrication of the specimens had to be very site-specific, to target particular microstructural constituents. Hence, such an approach was not feasible.

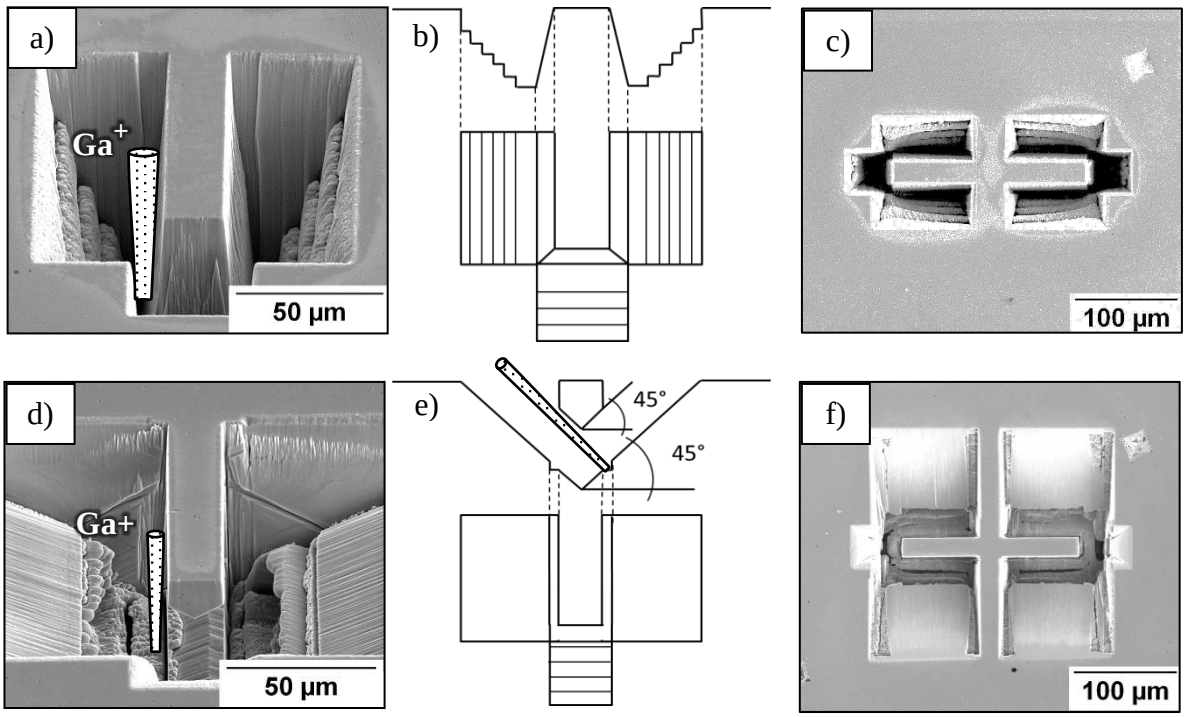

Figure 46: SE images and schematics illustrate the fabrication procedure for the micro-beams. The milling of the sidewalls was conducted at a glancing angle.

The first step of the fabrication process was to mill for each micro-beam three trenches with stair step patterns as illustrated in Figure 46 a) b) c). The ratio between final specimen length and trench depth had to be selected appropriately to ensure that the deflected beams did not touch the bottom of the trench during testing. In this case the trench depth was 50 µm and the final beam length was 75 µm.

As highlighted in Figure 46 a), for the first fabrication step, a large amount of material had to be removed. Therefore, a beam with an intense current density (21 nA/30 kV) was used to increase the sputter rate and to reduce the required milling time. The sample was thereby tilted 90° respectively to the incident ion beam (see Figure 47 a)).

The second step of the fabrication process is illustrated in Figure 46 d) e) f). A beam with a less intense current density (2.8 nA/30 kV) was selected to mill (polish) the sidewalls. The sample was then tilted 45° respectively to the incident ion beam to cut the bottom of the

micro-beam (see Figure 46 e) and Figure 47 b)). The operation was then repeated on the other side to create a symmetric cross-section with a pentagonal profile.

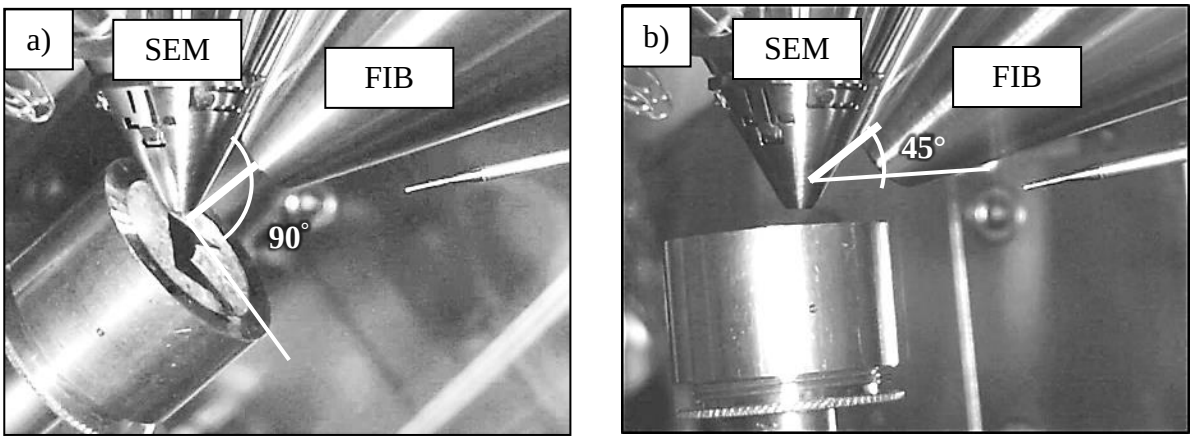

Figure 47: Images show the specimen chamber of the FEI Helios Nanolab 600 Dual Beam™:
a) Specimen tilt for milling the sidewalls,
b) Specimen tilt for milling the bottom of the micro-beam;

The final specimen dimensions of the micro-beams are shown in Figure 48. The deviations between the dimensions of the individual micro-beams were in a range within ±100 nm, measured with a high resolution SEM.

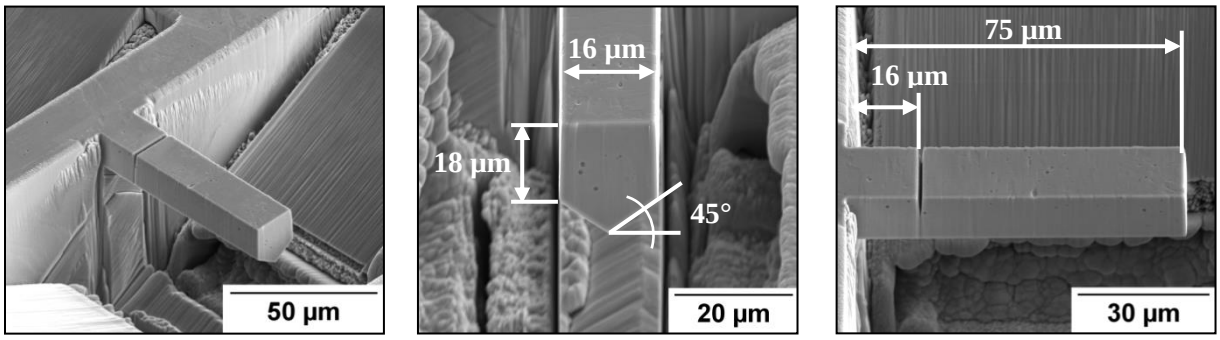

Figure 48: SE images show the final micro-beam dimensions.

Particularly for ductile materials an appropriate notch geometry and notch depth are essential, since the evaluation of the fracture toughness is directly related to the critical (plastic) displacements at the notch tip (Ritchie & Thompson 1985).

For each of the specimens, a stair step pattern and an ion beam with a very low intensity (0.46 nA/30 kV) were employed to fabricate a sharp notch (6° tip angle and 8 µm deep) 16 µm away from the beam support, as shown in Figure 48 and Figure 49.

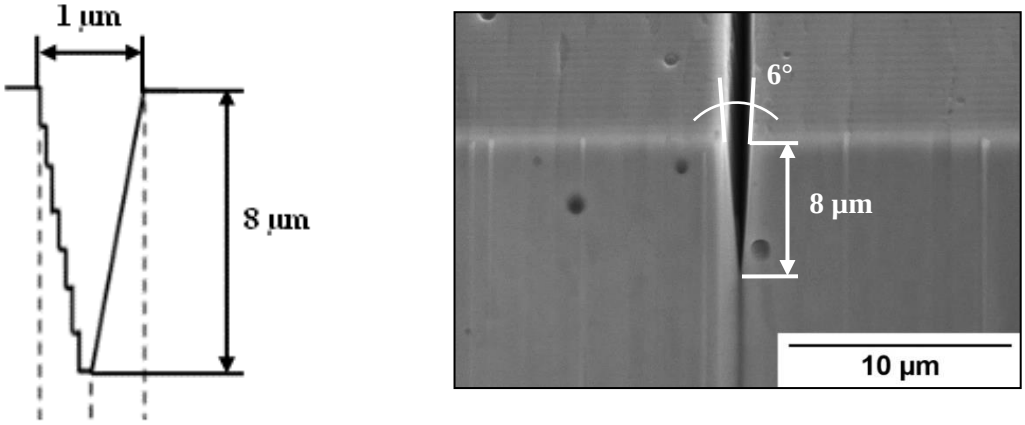

Figure 49: Schematic and SE image show the notch dimensions.

4.1.9 Evaluation of Lattice Damage

As mention earlier, a certain lattice damage is always involved when an ion-beam is used to remove material (see Figure 25). The effects of the lattice damage on the mechanical properties of a test specimen become more prevalent as the specimen dimensions decrease. Hence, detailed information on the depth of the damaged layer is essential, particularly for very small specimen dimensions (see Figure 26).

Stopping and Range of Ions into Matter (SRIM) is a group of programs that were first introduced by Ziegler, Biersack and Littmark in 1985 (Ziegler, J.F., Biersack & Littmark 1985). These programs are capable to calculate the stopping and range of ions into matter using a quantum mechanical treatment of ion-atom collisions. The software package used for the calculations in the current work was SRIM 2013, where the particular program used to simulate the ion/recoil distribution and to estimate the lattice damage distribution was TRIM 2013. Retrieved from http://www.srim.org (12th of September 2015).

Simulations were generated for 30 keV Ga^{+} ions impinging at in incidence angle of 0° (imaging) and 89° (milling of the sidewalls at a glancing angle) onto the surface of an iron target (see Figure 50). The distributions were calculated for 1000 ions for each of the incidence angles.

The ion distribution plots show the distributions for all ions stopped within the target. The ion/recoil distribution plots show both the ion distributions as well as all target atom redistributions. The lattice damage plots represent the distribution of the atomic displacements in the target material, due to the ion solid interactions.

It is thereby apparent that the lattice damage due to the imaging was approximately 300 Å or 30 nm whereas the damage due to milling at a glancing angle was about 200 Å or 20 nm, which is negligible when compared to the dimensions of the micro-beams. No significant effects on the mechanical properties caused by the lattice damage due to the fabrication process were therefore expected. More detailed information on TRIM simulation can be found in literature (Ziegler, James F & Biersack 2008).

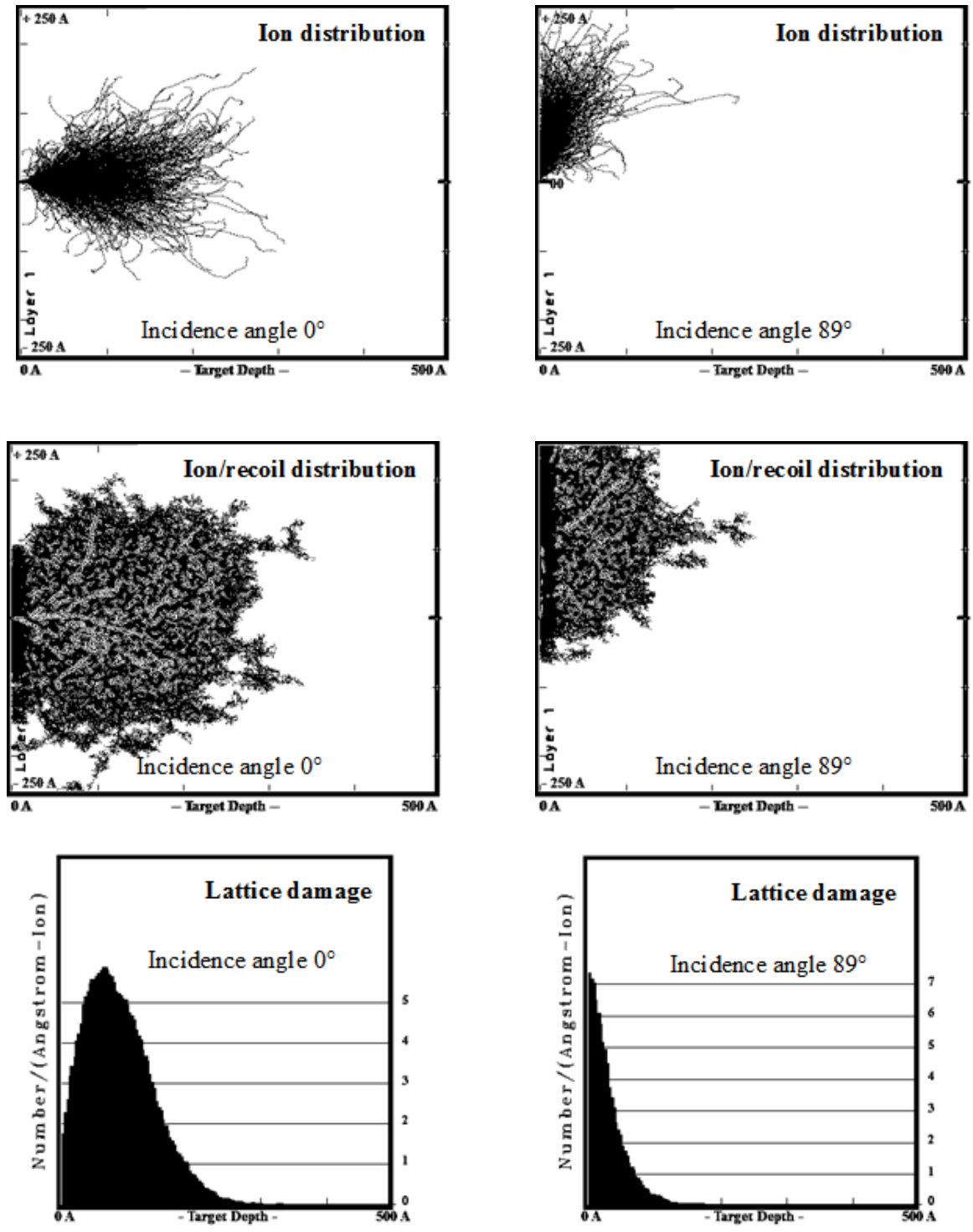

Figure 50: Overview of TRIM simulations for 30 keV Ga^+ ions impinging at incidence angles of 0° and 89°onto the surface of an iron target.

4.1.10 Characterisation of Mechanical Properties

A commercial nanoindenter (IBIS, Fischer-Cripps Laboratories) with a closed loop motorized sample stage (accuracy 0.25 µm), equipped with a Berkovich diamond tip was used to evaluate the mechanical properties of selected microstructures. Three indentation tests were conducted, in each of the microstructural regions, at a maximum load of 50 mN. The locations for the indentation tests are highlighted in Figure 51. The yield strength, Young's modulus and the strain hardening exponent were derived from the load-displacement diagrams according to an advanced characterisation procedure proposed by Dao (Dao et al. 2001). The hardness values were also extracted from the recorded diagrams.

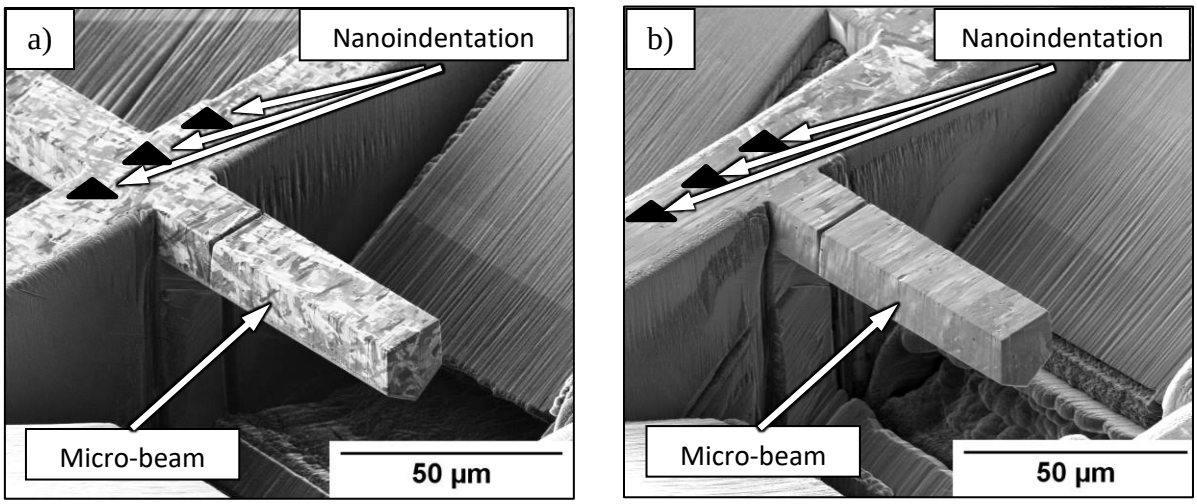

Figure 51: ISE Images highlight the locations for micro-mechanical tests conducted in:
a) Acicular ferrite,
b) Upper bainite;

The fracture tests were conducted on the notched micro-beams, that were fabricated into the selected microstructural regions (see Figure 51). The exposed surfaces in Figure 52 indicate that the entire volume of the specimens was comprised of either acicular ferrite or upper bainite.

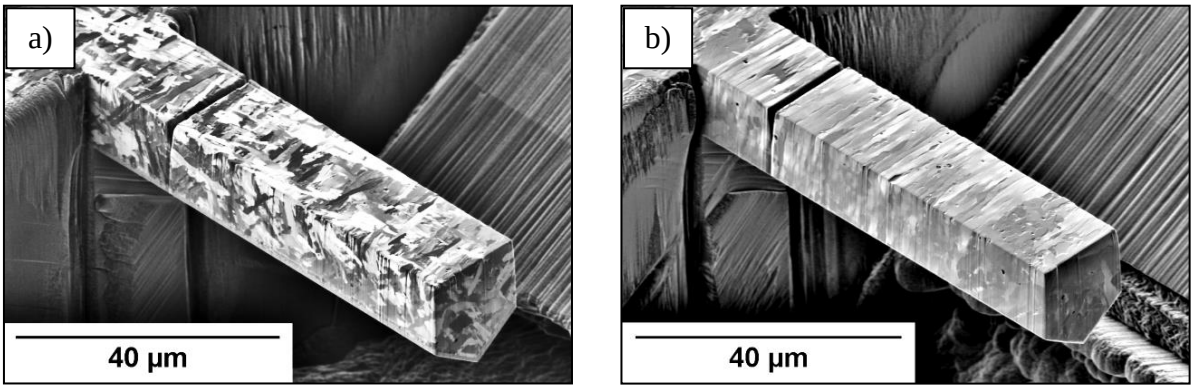

Figure 52: ISE images indicate that the entire volume of the micro-beams was comprised of:

a) Acicular ferrite,

b) Upper bainite;

The nanoindenter was also used to apply a bending load at a distance of 55 µm from the notch (see Figure 53), while recording the resulting load-deflection curves. The loading was displacement-controlled with a load displacement rate of 0.02 µm s^{-1} and a maximum displacement (beam deflection) of 18.5 µm, because of the limitations of the instrument.

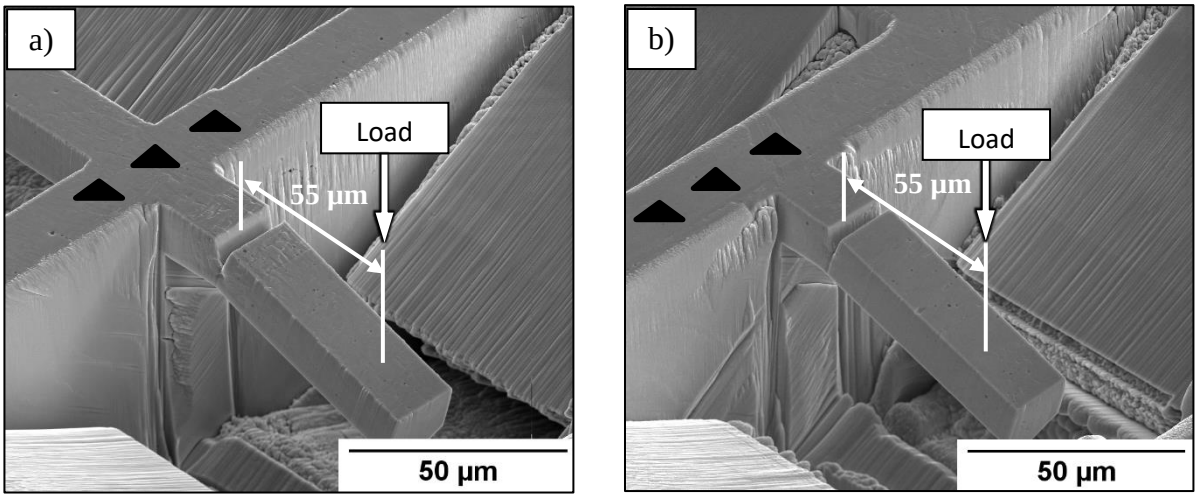

Figure 53: SE images show the deflected micro-beams in the selected region of:

a) Acicular ferrite,

b) Upper bainite;

The selected indenter tip was spherical, with a relatively large diameter of 40 µm, to avoid penetration and to minimise the local deformation in the contact area. Therefore, the measured displacements were dominated by the beam deflection rather than the deformation in the contact area. All micro-mechanical tests were conducted at room temperature.

4.1.11 Characterisation of HACC Propagation Resistance

Because of the physical significance and the possibility of direct measurements, the UCP was utilised as a parameter to evaluate the HACC propagation resistance of the selected microstructural regions in weld W2. The EBSD data of the hydrogen crack propagation through acicular ferrite and upper bainite (see Figure 54) was used to determine the UCP's for each of the microstructural constituents. The corresponding fracture surfaces were examined using a high-resolution SEM.

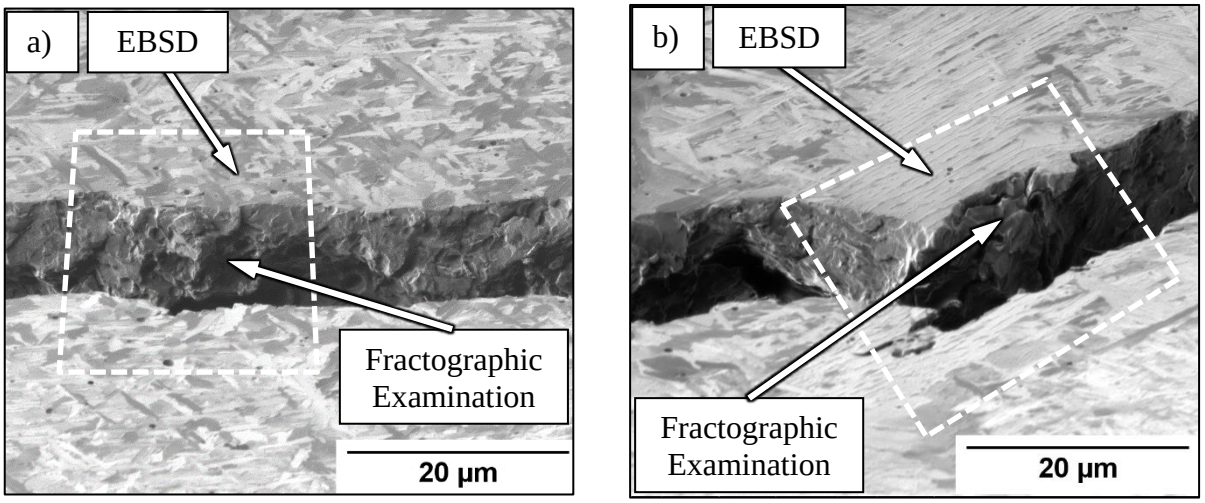

Figure 54: ISE images illustrate the locations for the EBSD scans and fractographic examinations of:

a) Acicular ferrite,

b) Upper bainite;

In order to preserve delicate morphological features, the specimen was only tilted to expose the fracture surface instead of inducing artificial fracture after exposing the specimens to liquid nitrogen, as it is a common practice for similar types of investigations (Martin, Robertson & Sofronis 2011).

4.1.12 Characterisation of HACC initiation Resistance

Micro-fracture tests were conducted at different loads (5 mN and 14 mN) on a hydrogen charged specimen, fabricated into the selected region of acicular ferrite in weld W1. The purpose of these tests was to determine the range for the threshold stress intensity factor to initiate HACC. A spherical tip with a diameter of 40 µm was used to apply the loads at a distance of 55 µm from the notch, as shown in Figure 55. The loading was displacement-controlled with a load displacement rate of 0.02 µm s^{-1} and a maximum displacement of 18.5 µm.

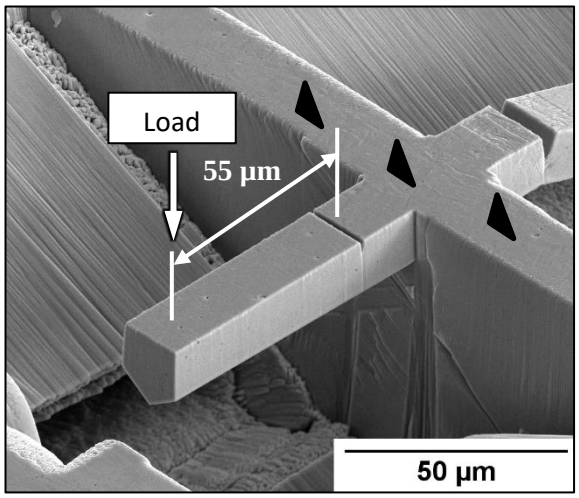

Figure 55: SE image illustrates the loading of the hydrogen charged micro-beam, fabricated into the selected microstructural region of acicular ferrite, in weld W1.

The exposed surfaces in Figure 56 indicate that the entire volume of the specimen was comprised of acicular ferrite.

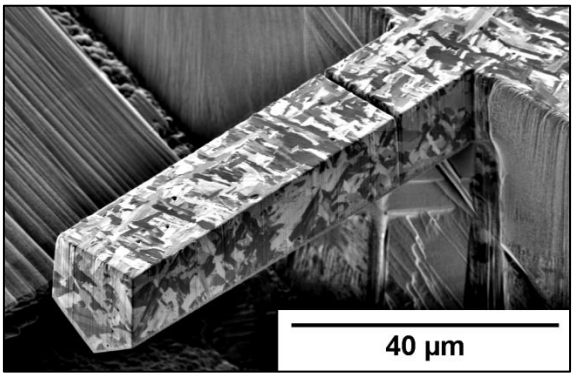

Figure 56: ISE image indicates that the entire volume of the micro-beam was comprised of acicular ferrite.

Prior to each test, the specimen was electrochemically charged with hydrogen for 90 minutes by applying a current density of -20 mA cm^{-2} in a 0.05 M H_2SO_4 solution. It was thereby possible to largely conserve the surface integrity after charging, as shown in Figure 57.

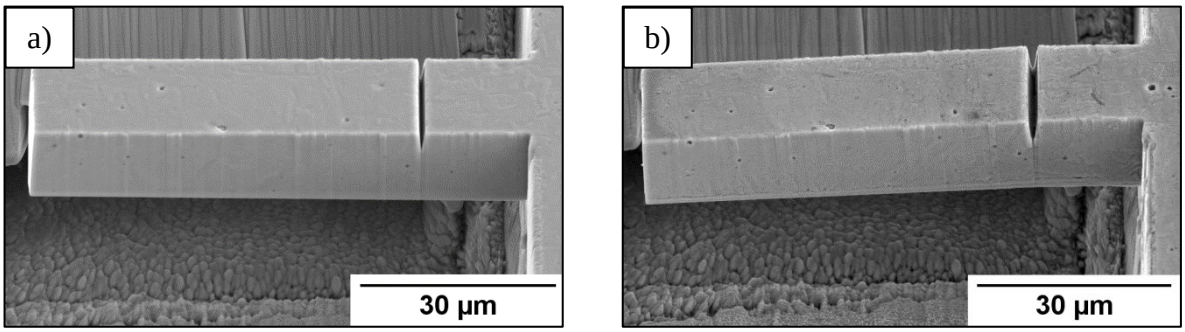

Figure 57: SE images show the micro-beam fabricated within of the acicular ferrite region of the weld:

a) Prior to the hydrogen charging and testing,

b) After hydrogen charged twice and tested at 5mN and 14 mN;

The hydrogen electrochemical oxidation method (Capelle et al. 2013; Nam, Kim & Choi 2013; Yan & Weng 2006) was applied to an adjacent weld section (4th section in welding direction) to estimate the total amount of hydrogen absorbed during the charging procedure.

The oxidation currents were obtained by keeping the specimens at a potential of +168 $mV_{Ag/AgCl}$ in a deaerated 0.2 M NaOH solution for 2 hours. This potential, which is higher than the hydrogen equilibrium potentials and lower than the passive film breakdown potential of the metal, allowed the oxidation reaction of the metal to be limited in this solution (see the uncharged reference curve in Figure 58, and the oxidation reaction of hydrogen to be induced simultaneously. The total quantity of the hydrogen absorbed (Q_H^{abs}) by the weld metal can be thus expressed as:

$$Q_H^{abs} = \int_0^t [I_H(t) - I_{ref}(t)]dt \,, \quad \text{at} \quad E_{anodic} = \text{const.} \tag{4-4}$$

Where $I_H(t)$ is the oxidation current for the hydrogen charged specimen and $I_{ref}(t)$ is the oxidation current for the specimen without hydrogen (see reference curve in Figure 58). According to Faraday's law, the hydrogen concentration C_H, is related to Q_H^{abs} as followed:

$$C_H = \frac{Q_H^{abs}}{zFv} \tag{4-5}$$

Where F is the Faraday constant (=96487 C mol^{-1}), v is the effective volume of the specimen (in this case 0.5754 cm^3) and z is the number of electrons ($z = 1$). With the charging parameters presented above, the hydrogen concentration in the specimen was thus calculated as 1.038×10^{-6} mol cm^{-3}, which corresponds to 0.132 ppm.

A load of 5 mN was applied within five minutes after completion of the hydrogen charging and held constant for 12 hours to simulate the delayed nature of HACC. Due to the small specimen dimensions, most of the hydrogen effused from the micro-beam during the prolonged test, which is generally indicated by a recovery of the mechanical properties (Katz,

Tymiak & Gerberich 2001). Consequently, the whole procedure, including hydrogen charging, was repeated for 14 mN.

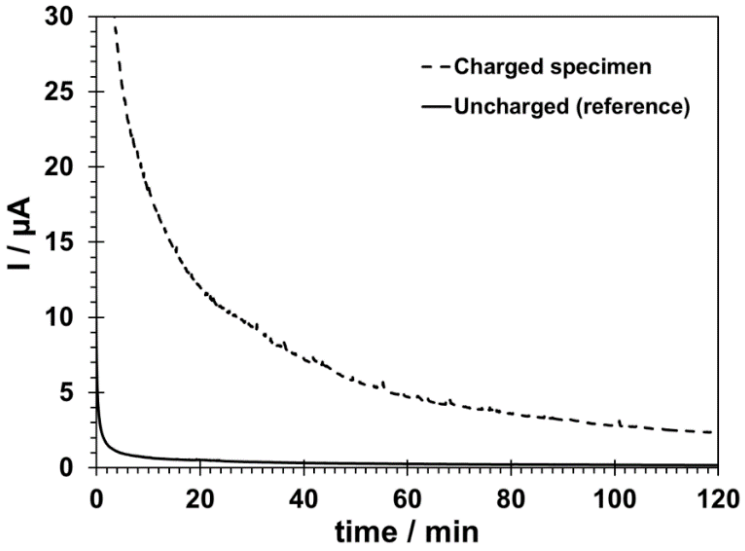

Figure 58: Hydrogen discharging process (oxidation current) under anodic polarisation (+168 $mV_{Ag/AgCl}$) in 0.2 M NaOH for the electrochemically charged specimen (at 20 mA cm^{-2} for 90 min in 0.05 M H_2SO_4 solution) and the reference specimen (uncharged).

All electrochemical tests were conducted with a Gamry interface 1000^{TM}, using the specimens as the working electrode, a platinum mesh as the counter electrode and a silver/silver chloride electrode as the reference. The experiments were all performed at room temperature.

CHAPTER 5

RESULTS

5 Results

5.1 Microstructure and Mechanical Properties of Acicular Ferrite and Upper Bainite in Weld Metal

5.1.1 Characterisation of Microstructures

The EBSD data was collected from the planes on top of the micro-beams that were fabricated into microscopic regions of acicular ferrite and upper bainite, as shown in Figure 45 in Section 4.1.8. The size of the mapped regions was 16µm×75µm.

The IQ maps in Figure 59 provide a visualisation of the unique microstructures of acicular ferrite and upper bainite. It is apparent that acicular ferrite consists of multiple fine interlocking ferrite plates or "grains" and upper bainite of a colony of parallel ferrite laths.

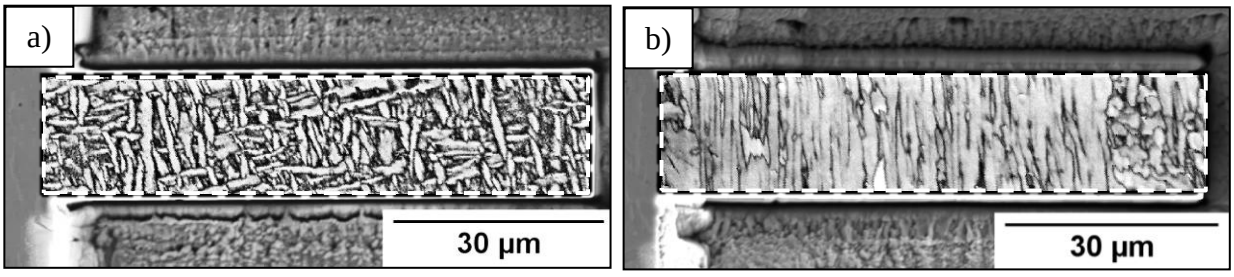

Figure 59: IQ maps reveal the microstructures of:
a) Acicular ferrite,
b) Upper bainite;

The superimposed IPF and IQ map in Figure 60 a) shows that the ferrite grains constituting acicular ferrite have divergent crystallographic orientations. On the contrary, upper bainite appears to form a single crystallographic packet, consisting of parallel ferrite laths with almost similar orientations (see Figure 60 b)).

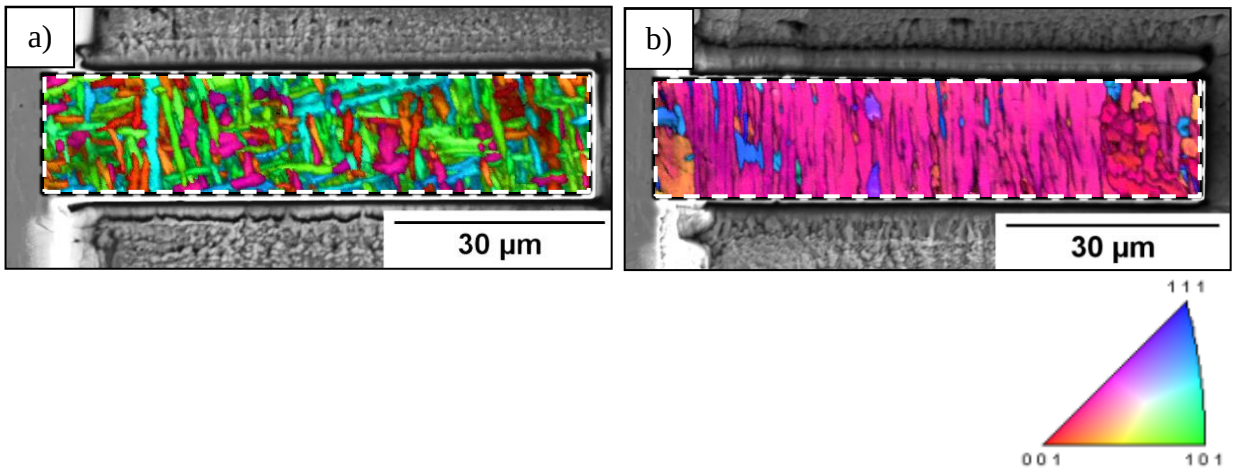

Figure 60: Superimposed [001] IPF and IQ map illustrate:
a) Acicular ferrite,
b) Upper bainite;

The chart in Figure 61 represents the total length of boundaries with misorientations between 0.5° and 180° for acicular ferrite and upper bainite.

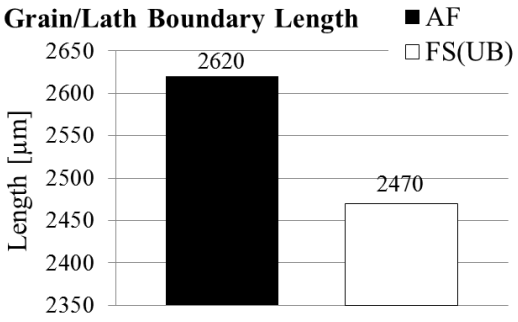

Figure 61: Chart shows the total length of boundaries for the mapped regions (area=1200 μm^2) of acicular ferrite and upper bainite.

The resulting grain/lath boundary densities are 2.18 µm/µm^2 for acicular ferrite and 2.05µm/µm^2 for upper bainite as shown in Figure 62.

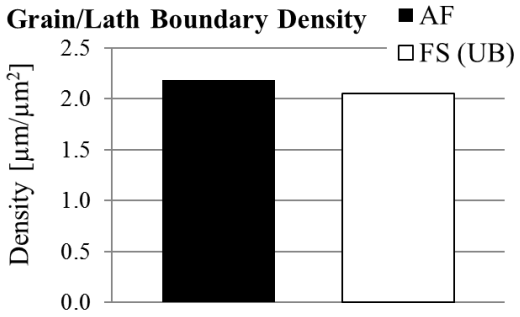

Figure 62: Chart shows grain boundary density of acicular ferrite and the lath boundary density of upper bainite.

The superimposed grain/lath boundary and IQ maps (see Figure 63 a) and Figure 64 a)) as well as the misorientation distribution charts in Figure 63 b) and Figure 64 b) show that the boundaries found within acicular ferrite had a large proportion of misorientations >15° while for the same area the misorientation of the boundaries of upper bainite were mainly < 15°. There seem to be no boundaries with misorientations between 20° to 47° in any of the microstructures.

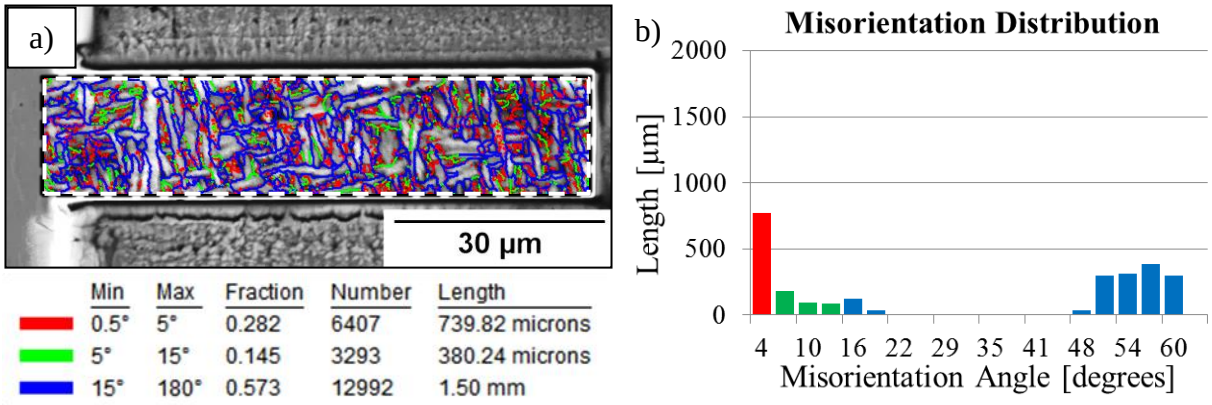

Figure 63: a) Superimposed grain boundary and IQ map for acicular ferrite,
b) Chart illustrates the misorientation distribution for acicular ferrite;

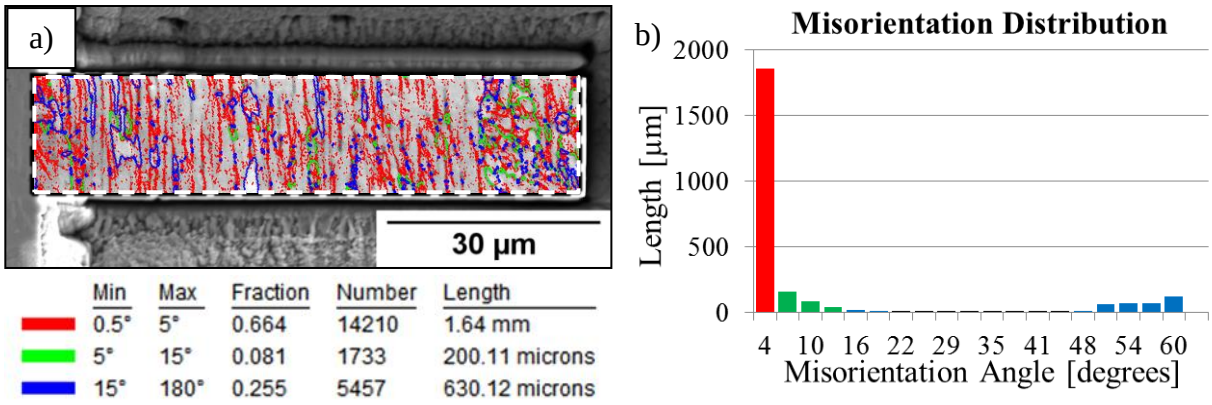

Figure 64: a) Superimposed grain boundary and IQ map for upper bainite,
b) Chart illustrates the misorientation distribution for upper bainite;

The chart in Figure 65 is a quantitative illustration of the grain/lath boundary character distributions of acicular ferrite and upper bainite. Boundaries with misorientations ranging from 0.5° to 15° were in this case classified as LAGB's and the ones with misorientation between 15° and 180° as HAGB's. Some of the HAGB'S found in both microstructures shared a finite number of lattice sites on either side of a grain boundary and can therefore be classified as CSL boundaries with a relatively high ratio of Σ3 boundaries (see CSL boundary distribution chart in Figure 66).

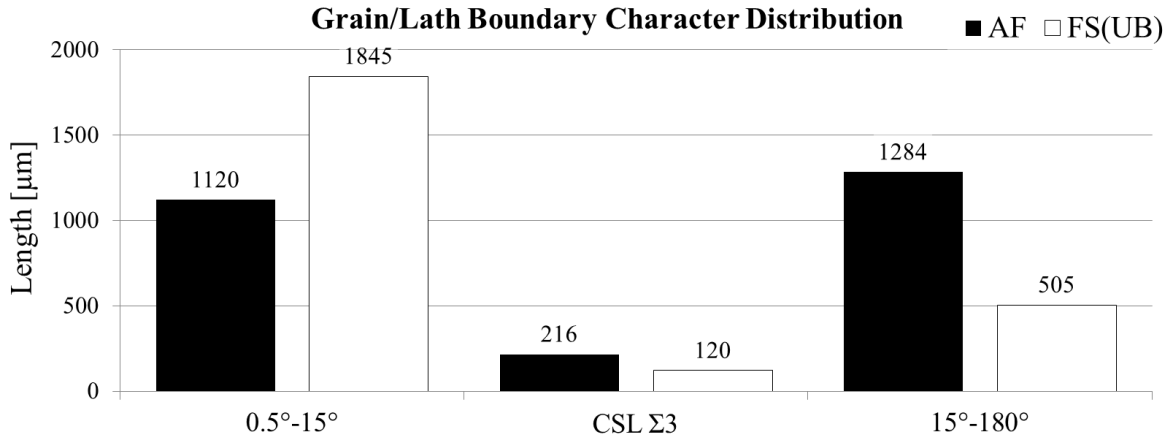

Figure 65: Grain/lath boundary character distribution of acicular ferrite and upper bainite.

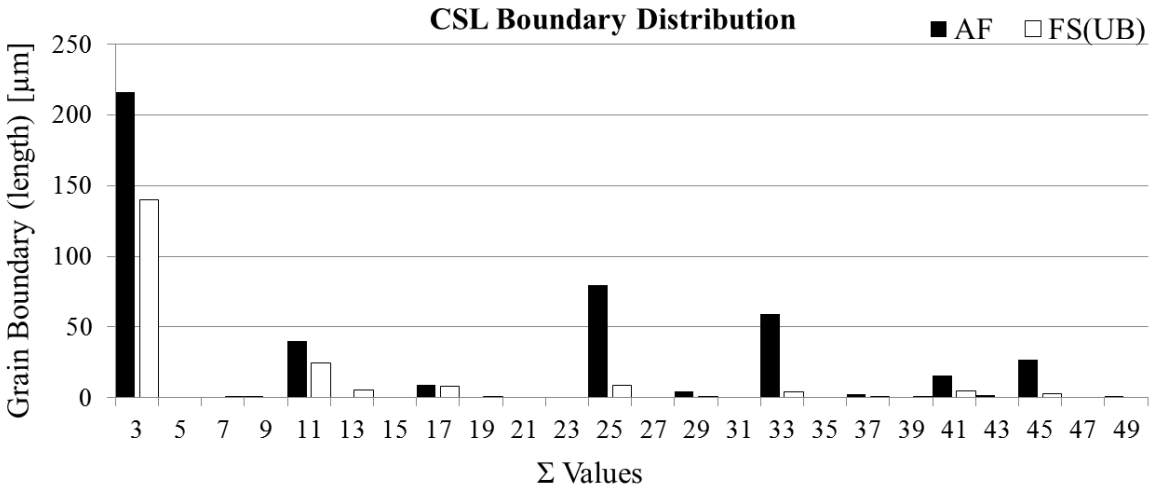

Figure 66: Chart illustrates the CSL boundary distribution of acicular ferrite and upper bainite.

Acicular ferrite is often interspersed with different intragranular transformation products of primary ferrite, PF(I), Widmanstätten ferrite, WF(I) and bainite, B(I) (Thewlis 2003; Thewlis, Whiteman & Senogles 1997). However, since the plate or "grain" diameter of acicular ferrite is typically finer (< 5 µm) than most of the other intragranular transformation products (≥ 5µm) (Thewlis 2004), it is possible to distinguish between AF and PF(I)+WF(I)+B(I) by evaluating the grain diameter distribution. Where the grain diameter here refers to the diameter of a circle having the same area as the grain being measured, i.e. the Equivalent Circular Area Diameter (ECAD).

The Grain Diameter map in Figure 67 a) highlights individual grains according to their diameter as either green (<5 µm) or red (≥ 5 µm). Figure 67 b) illustrates the distribution of the different grain diameters within the AF+PF(I)+WF(I)+B(I) aggregate. This data was used to determine the ratio between AF and PF(I)+WF(I)+B(I) (see Figure 68). The average ECAD of the aggregate is 3.25 ± 1.17 µm.

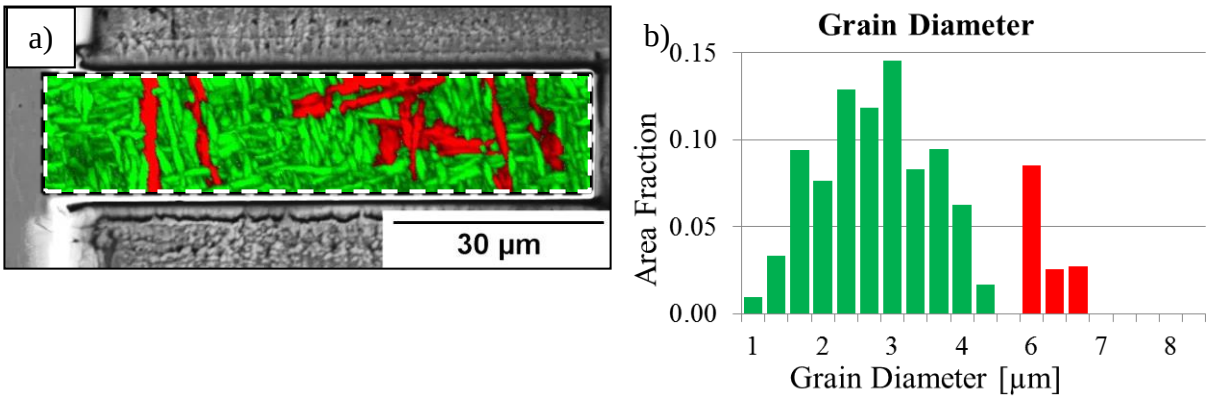

Figure 67: a) Superimposed Grain Diameter and IQ map highlights the distribution of acicular ferrite (green) and PF(I)+WF(I)+B(I) (red),
b) The chart illustrates the grain diameter distribution. Adjacent data points with misorientations <5° were considered to be part of the same grain;

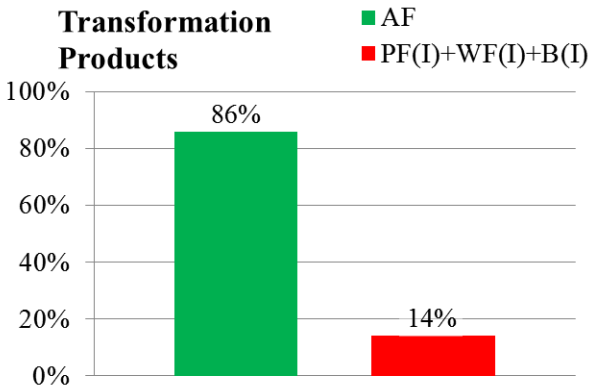

Figure 68: Chart shows the ratio between acicular ferrite and other phase transformation products of the aggregate. Quantitative criteria such as grain diameter or aspect ratio were not applicable to distinguish between the individual transformation products of PF(I)+WF(I)+B(I).

The ECAD of the upper bainite packet was 34 µm as illustrated in Figure 69. Areas where adjacent data points had misorientations < 5° were considered to be part of the same packet or "grain". The region highlighted green in Figure 69 a) represents such an area and was used to determine the crystallographic packet diameter of upper bainite, as shown in Figure 69 b).

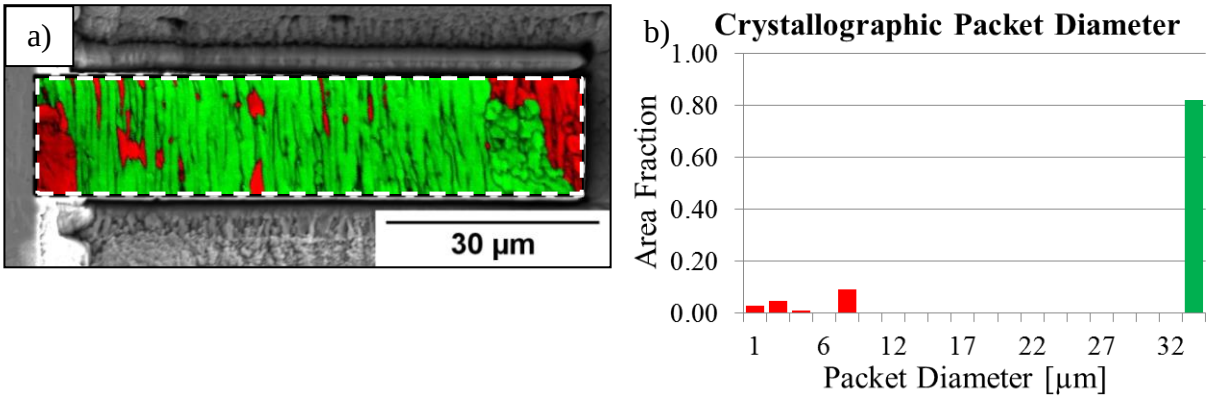

Figure 69: a) Superimposed Grain Diameter and IQ map highlights the crystallographic packet of upper bainite in green,
b) The chart shows the diameter of the highlighted crystallographic packet (green column);

The ECAD of the ferrite laths can be calculated using the following equation:

$$d=2\sqrt{\frac{(A=lath_{length}\times lath_{width})}{\pi}} \qquad (5\text{-}1)$$

Where the width of the individual ferrite laths was in this case obtained from SEM observations of the etched microstructure, prior to the EBSD analysis but within the same region as shown in Figure 70 a). The lath width, averaged over 20 different measurements, was 0.6 ± 0.09 µm. The lath length can be expressed by the width of the mapped area (16 µm), which correlates well with the length of the laths in the original upper bainite packet, as shown in Figure 45 b) in Section 4.1.8. The resulting mean lath diameter is approximately 3.5 µm.

As shown in Figure 70 a), the boundaries of the ferrite laths of upper bainite are often decorated with cementite precipitates. Figure 70 b) is a binary representation of Figure 70 a) and was created with an image analysis software (Image J v1.48) in order to differentiate between the proportion of ferrite and cementite. The resulting ratio between the two phases is approximately 90% ferrite and 10% cementite.

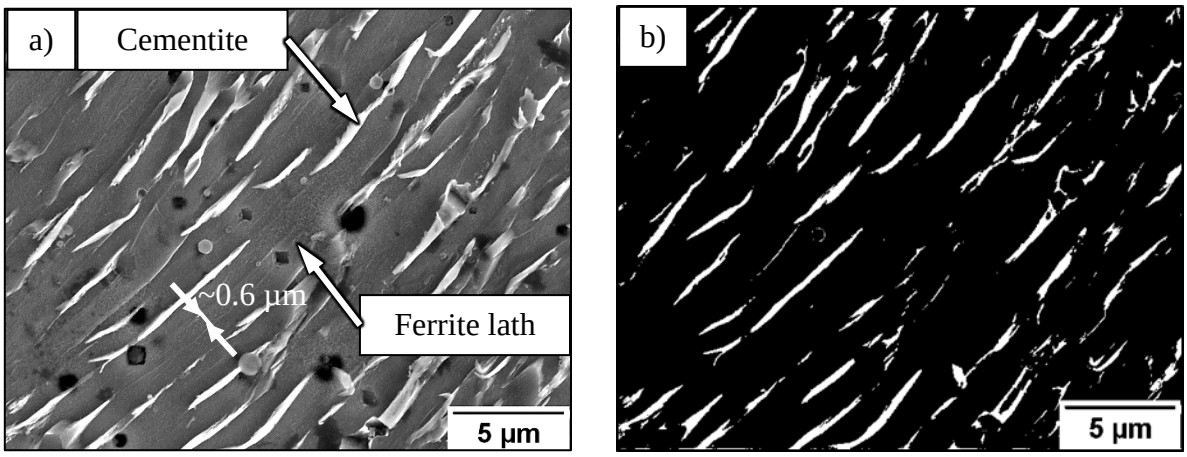

Figure 70: a) SE image reveals the main components of upper bainite (2% Nital etched surface) and shows the average width of a ferrite lath,
b) The binary representation of the SE image highlights ferrite (black pixels) and cementite (white pixels);

The grain/lath shape aspect ratios of both, acicular ferrite and upper bainite are presented in Figure 71. In case of acicular ferrite, the calculation of the individual grains aspect ratios was based on the EBSD data. In order to determine the aspect ratios for upper bainite, the lath length was considered to be 16µm, corresponding to the width of the micro-beam. The individual lath widths were obtained from Figure 70 a).

The standard deviations for the grain/lath shape aspect ratios were 0.04 and 0.009 for acicular ferrite and upper bainite respectively. Both diagrams indicate that the grains/laths are not circular and considering solely the ECAD may be inaccurate. Hence, for calculations that imply the grain/lath size, other parameters such as the mean Linear Intercept (LI) should be considered.

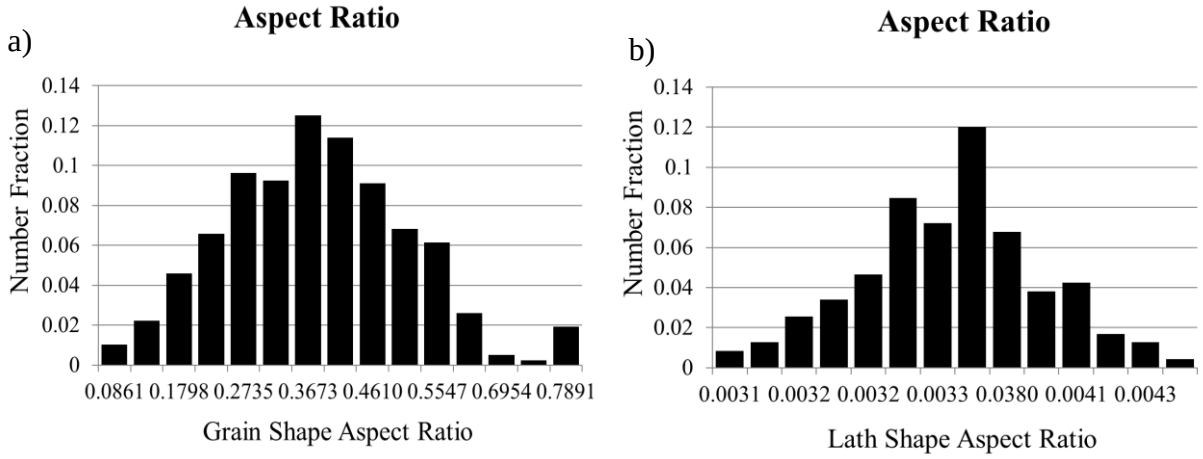

Figure 71: a) Grain shape aspect ratios of acicular ferrite,
b) Lath shape aspect ratios of upper bainite;

5.1.2 Evaluation of Yield Strength based on Microstructural Aspects and Physical Principles

From a theoretical point of view, the yield strength of acicular ferrite can be factorised into a number of intrinsic components with specific contributions (Bhadeshia 1997):

$$\sigma_{Y} = \sigma_{Fe} + \sum_i x_i \sigma_{SS_i} + \sigma_D + \sigma_{GS} \quad (5\text{-}2)$$

Where σ_{Fe} is the strength of pure, annealed iron, which is about 219 MPa at 300 K (Bhadeshia 1997). σ_{SS_i} is the substitutional solute strengthening and x_i is the concentration of each substitutional solute which is represented here by a subscript i (Bhadeshia 1997). σ_D and σ_{GS} are the strengthening contributions related to the dislocation density and the grain size, respectively.

A quantitative analysis of the chemical composition of weld specimen W1 was required to determine σ_{SS_i}. For this purpose, GD-OES was utilised, using a HORIBA GD-Profiler 2™. The results of this analysis are listed in Table 15.

i	Si	Mn	Ni	Mo	Cr	V	Co
x_i [wt.%]	0.20	1.03	0.13	0.08	0.02	0.02	0

Table 15: Concentration of the substitutional solutes x_i in the weld specimen W1 determined by GD-EOS.

The second row in Table 16 shows the strengthening contribution of each solute as a function of its concentration (see Table 15), using the proportional ratio from the data in the first row of Table 16, as reported by (Bhadeshia 1997). The total strengthening contribution due to solid solution was approximately 74 MPa. Although implied in Equation (2-3), the effect of carbon was here not considered since its solubility in ferrite is negligible (Bhadeshia 1997).

	Si	Mn	Ni	Mo	Cr	V	Co	$\sum_i x_i \sigma_{SS_i}$
for x_i=1 wt.%	105	45	37	18	5.8	4.5	4.9	220.2
for x_i=see Table 15	21	46.4	4.8	1.4	0.1	0.1	0	73.8

Table 16: The first row of the table shows the solid solution strengthening terms (in MPa) for ferrite, for 1 wt.% of solute. This data was determined for a strain rate of 0.0025 s^{-1} at 23°C (Bhadeshia 1997). The second row represents the solid solution strengthening contributions for the weld metal, using the proportional ratio.

For acicular ferrite in weld metal, the strengthening contribution due to dislocations, σ_D was estimated to be approximately 145 MPa, for a dislocation density of 10^{14} m^{-2}, determined by transmission electron microscopy (Yang, J.R. & Bhadeshia 1990).

Based on the Hall-Petch relation (Hall 1951; Petch 1953), the grain size strengthening σ_{GS} can be expressed as (Kamikawa et al. 2015):

$$\sigma_{GS}=210\ d^{-1/2} \quad (5\text{-}3)$$

Where d (≈ 1.51 μm) is the average spacing of boundaries with misorientations above 2°, determined by the LI method with random test lines using EBSD. According to Equation (5-3), σ_{GS} is around 171 MPa.

Adding up all the intrinsic contributions results in an overall strength of approximately 609 MPa for acicular ferrite.

For upper bainite, the strength can also be factorised into individual components (Bhadeshia 2001):

$$\sigma_{Y} = \sigma_{Fe} + \sum_{i} x_i \sigma_{SS_i} + \sigma_D + \sigma_{LS} + \sigma_P \quad (5\text{-}4)$$

Where σ_{Fe}, σ_{SS_i} and σ_D have the same meaning as it was the case for acicular ferrite. σ_{LS} and σ_P are the strengthening contributions of the lath size and the cementite precipitates, respectively.

Similar to acicular ferrite, the strengthening contributions of pure annealed iron σ_{Fe} and solid solution σ_{SS_i} are about 219 and 74 MPa respectively.

The dislocation strengthening contribution σ_D can be expressed as (Bhadeshia 1997):

$$\sigma_D=k_D\ \rho_D^{1/2} \quad (5\text{-}5)$$

Where $k_D=7.34\times10^{-6}$ MPa m (Bhadeshia 1997) and the dislocation density ρ_D is reported to be for bainite in the range between 10^{14} m^{-2} and 10^{15} m^{-2} (Bhadeshia 2001). Taking a mid-range value for ρ_D of 5×10^{14} m^{-2}, results in $\sigma_D\approx$ 164 MPa.

In the case of upper bainite, the evaluation of σ_{LS} requires special considerations since the classical grain size effect theories cannot be directly applied to its microstructural parameters (Bhadeshia 2001). For very fine lath widths, as encountered in bainite, the

dimensions of the slip planes are too small to allow the formation of dislocation pile-ups as required for the classic Hall-Petch formulation (Bhadeshia 2001). Yielding is then determined by the stress, which is necessary to expand a dislocation loop across the slip plane according to the Langford-Cohen relationship (Naylor 1979). In such cases the strength is related to the reciprocal of the average lath diameter by the following relationship:

$$\sigma_{LS}=k_{\varepsilon}(d)^{-1} \quad (5\text{-}6)$$

Where k_{ε} is approximately 115 MPa m and d (≈ 1.62 μm) was the mean LI measured on random sections using EBSD. The resulting σ_{LS} is around to 71 MPa.

The contribution of cementite precipitates σ_P to the overall strength of upper bainite can be expressed as followed (Bhadeshia 2001):

$$\sigma_P=k_p\Delta^{-1} \quad (5\text{-}7)$$

Where k_p is approximately 0.52 V_θ MPa m, V_θ is the volume fraction of cementite and Δ the average distance between a cementite particle and its two or three nearest neighbours. For V_θ 10% and Δ= 1.4 μm, σ_P results in 37 MPa.

Adding up the contributions of all the intrinsic components considered for upper bainite results in an overall yield strength of approximately 565 MPa.

5.1.3 Characterisation of Yield Strength, Hardness, Young's Modulus and Strain Hardening Exponent

Three nano-indentation tests were conducted in the vicinity of the micro-beams in each of the selected regions of acicular ferrite and upper bainite as described in detail in Section 4.1.10. An advanced characterisation procedure, for ductile materials subjected to instrumented

sharp indentation (Dao et al. 2001), was then used to extract the yield strength, Young's modulus and strain hardening exponent from the load-displacement diagrams shown in Figure 72.

The hardness was determined with conventional methods for instrumented indentation tests as described in detail elsewhere in literature (Fischer-Cripps 2011).

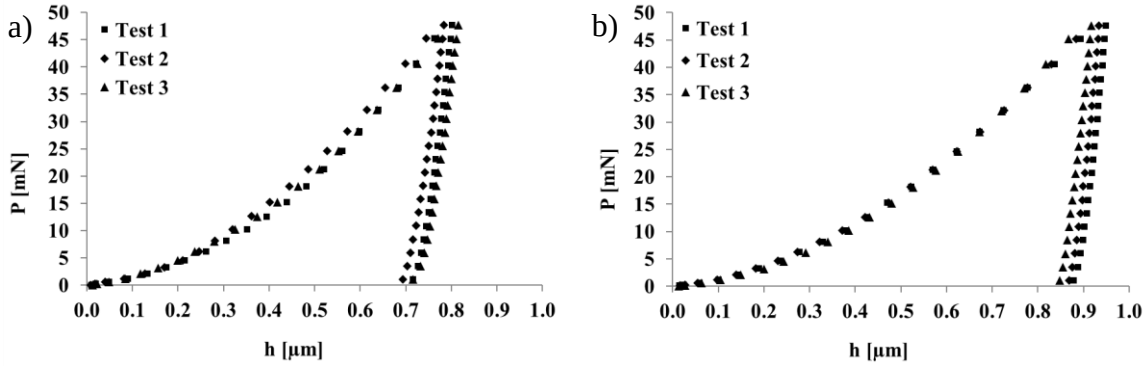

Figure 72: Load – displacement (depth of indentation) diagrams for:
a) Acicular ferrite,
b) Upper bainite;

The characterisation of the yield strength, Young's modulus and strain hardening exponent from the load-displacement curves was conducted according to the following procedure proposed by Dao et al. (Dao et al. 2001).

The plastic behaviour can be estimated by a power law description. A simple elastic-plastic, true stress–true strain behaviour is thereby assumed to be:

$$\sigma = \begin{cases} E\varepsilon, & \text{for } \sigma \leq \sigma_y \\ R\varepsilon^n, & \text{for } \sigma \geq \sigma_y \end{cases} \quad (5\text{-}8)$$

Where E is the Young's modulus, R a strength coefficient, n the strain hardening exponent, σ_y the initial yield stress and ε_y the corresponding yield strain, which leads to:

$$\sigma_y = E\varepsilon_y = R\varepsilon_y^{\,n} \tag{5-9}$$

Here the yield stress σ_y is defined at zero offset strain. The total effective strain, ε, consists of two parts, ε_y and ε_p:

$$\varepsilon = \varepsilon_y + \varepsilon_p \tag{5-10}$$

Where ε_p is the nonlinear part of the total effective strain accumulated beyond ε_y. With Equation (5-9) and Equation (5-10), when $\sigma > \sigma_y$, the nominal stress σ can be defined as:

$$\sigma = \sigma_y \left(1 + \frac{E}{\sigma_y}\,\varepsilon_p\right)^n \tag{5-11}$$

The applied engineering stress, or true stress $\sigma_{0.033}$ at a deformation ε_p of 0.033 can be determined as followed:

$$\frac{C}{\sigma_{0.033}} = -1.131\left[\ln\left(\frac{E^*}{\sigma_{0.033}}\right)\right]^3 + 13.635\left[\ln\left(\frac{E^*}{\sigma_{0.033}}\right)\right]^2 - 30.594\left[\ln\left(\frac{E^*}{\sigma_{0.033}}\right)\right] + 29.267 \tag{5-12}$$

Where C is the curvature of the loading curve and can be determined by solving Equation (5-13):

$$P = Ch^2 \tag{5-13}$$

Where P is the load and h is the indentation depth. E* is the reduced Young's modulus which combines the elasticity effects of an elastic indenter and an elastic-plastic solid and can be expressed as:

$$E^* = \frac{1}{2.12}\frac{\sqrt{\pi}}{\sqrt{A}}\frac{dP_u}{dh}\bigg|_{h_m} \tag{5-14}$$

Where P_u is the unloading force, h_m is the maximum indentation depth and A is the projected area of contact, which for a Berkovich indenter is typically defined as:

$$A=24.56h_m^2 \tag{5-15}$$

By determining the slope of the unloading curve at the maximum load depth, $\frac{dP_u}{dh}\Big|_{h_m}$, the strain hardening exponent can be obtained by using the following equation:

$$\begin{aligned}\frac{1}{E^* h_m}\frac{dP_u}{dh}\Big|_{h_m} = {} & (-1.40557n^3+0.77526n^2+0.1583-0.06831)\left[\ln\left(\frac{E^*}{\sigma_{0.033}}\right)\right]^3 \\ & +17.93006n^3-9.22091n^2-2.37733n+0.86295)\left[\ln\left(\frac{E^*}{\sigma_{0.033}}\right)\right]^2 \\ & +(-79.99715n^3+40.5562n^2+9.00157n-2.54543)\left[\ln\left(\frac{E^*}{\sigma_{0.033}}\right)\right] \\ & +(122.65069n^3-63.88418n^2-9.58936n+6.20045)\end{aligned} \tag{5-16}$$

The yield strength can then be determined as followed:

$$\sigma_{0.033}=\sigma_y\left(1+\frac{E}{\sigma_y}\,0.0033\right)^n \tag{5-17}$$

The Young's modulus E can be calculated by solving the equation below, where $\frac{(1-\nu_i^2)}{E_i}$ = 0.001264:

$$\frac{1}{E^*}=\frac{(1-\nu^2)}{E}+\frac{(1-\nu_i^2)}{E_i} \tag{5-18}$$

Where E_i and ν_i are the Young's modulus and Poisson's ratio of the indenter. The universal hardness H, can be determined using Equation (5-19), as reported in the literature (Fischer-Cripps 2011):

$$H=\frac{P_m}{A} \tag{5-19}$$

Where P_m is the maximum load. The resulting Vickers hardness, HV can be calculated as followed:

$$HV=0.094495\ H \tag{5-20}$$

The values derived for C, $\sigma_{0.033}$, E^*, A, $\left.\frac{dP_u}{dh}\right|_{h_m}$ obtained from three tests in each of the microstructures are shown in Table 17. The corresponding values for hardness (HV), Young's Modulus (E), Yield strength (σ_Y) and strain hardening exponent (n) are listed in Table 18.

		C [N/m^2]	$\sigma_{0.033}$ [MPa]	E^* [GPa]	A [m^2]	$\left.\frac{dP_u}{dh}\right\|_{h_m}$ [N/m]
AF	Test 1	78.3×10^9	986	174.8	1.59×10^{-11}	837×10^3
	Test 2	85.2×10^9	1123	167.2	1.44×10^{-11}	785×10^3
	Test 3	79.0×10^9	985	181.8	1.40×10^{-11}	841×10^3
FS UB	Test 1	59.1×10^9	685	177.5	2.54×10^{-11}	1107×10^3
	Test 2	60.0×10^9	694	181.4	2.38×10^{-11}	1096×10^3
	Test 3	61.2×10^9	724	169.3	2.22×10^{-11}	986×10^3

Table 17: The table shows values for C, $\sigma_{0.033}$, E^*, A, $\left.\frac{dP_u}{dh}\right|_{h_m}$ obtained from three nano-indentation tests in acicular ferrite and upper bainite.

		HV	E [GPa]	σ_y [MPa]	n
AF	Test 1	314	204	631	0.193
	Test 2	330	193	814	0.157
	Test 3	308	215	418	0.314
	Mean	317	204	621	0.221
	Stdev.	11	11	198	0.082
FS UB	Test 1	220	208	560	0.083
	Test 2	228	214	522	0.113
	Test 3	237	196	534	0.25
	Mean	228	206	539	0.149
	Stdev.	8	9	19	0.089

Table 18: The table shows HV, σ_Y, E and n for acicular ferrite and upper bainite.

5.1.4 Characterisation of Deformation Behaviour, Fracture Behaviour and Fracture Resistance

The micro-beams, fabricated into the selected microstructural regions of acicular ferrite and upper bainite, were deflected via nano-indentation to promote failure ahead of the notch tip, as described in Section 4.1.10. The resulting load-deflection curves are illustrated in Figure 73. The linearity of the load-deflection curves at low loads confirms that the measured displacements were dominated by the beam deflection rather than by the contact deformation or penetration of the indenter. A qualitative analysis of the load-deflection diagrams indicates that the yield strength of acicular ferrite is higher than of upper bainite since the deviation from the linear behaviour occurred much earlier for the micro-beam comprised of upper bainite. The load-deflection curves additionally illustrate that the values for the Young's modulus of the two microstructures seem to be quite close as the slopes of the linear parts of the load-deflection diagrams are notably similar.

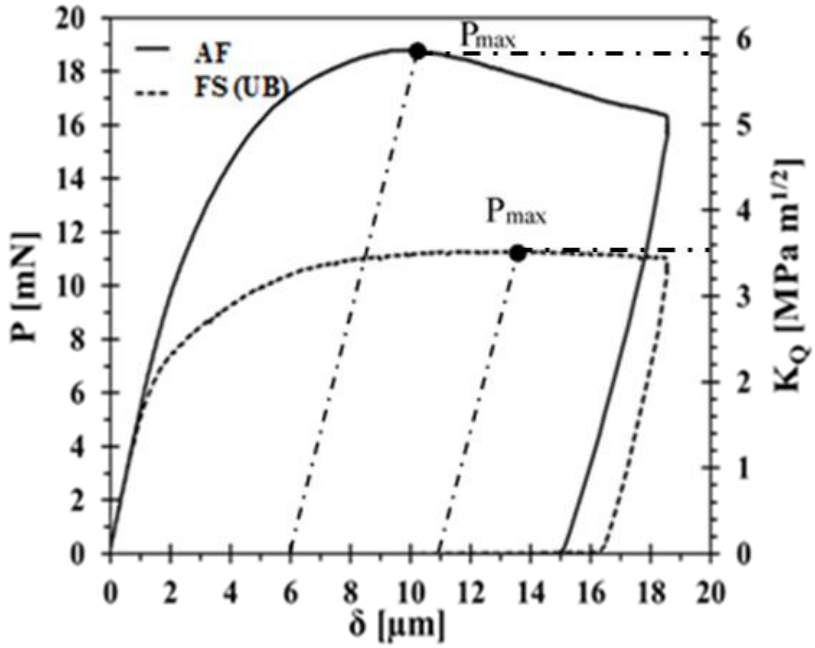

Figure 73: Load-deflection curves obtained from micro-fracture tests conducted in acicular ferrite and upper bainite.

After testing, the area in the vicinity of the notch tip was inspected using a high resolution SEM. Figure 74 shows relatively small crack growth with approximately 1.3 µm and 0.6 µm for acicular ferrite and upper bainite respectively. Figure 74 a) and Figure 74 b) also reveal that the fracture propagation in acicular ferrite is characterised by the formation and coalescence of micro-voids, while in the case of upper bainite fracture was accompanied by homogeneous deformations.

For both microstructures, the elastic-plastic deformation behaviour indicated by the load-deflection curves in Figure 73 as well as the ductile fracture behaviour and the formation of relatively a large plastic zone observed in Figure 74 a) and Figure 74 b) imply that a Linear Elastic Fracture Mechanics (LEFM) approach cannot provide correct values for the fracture toughness. However, LEFM can deliver a lower bound for fracture toughness.

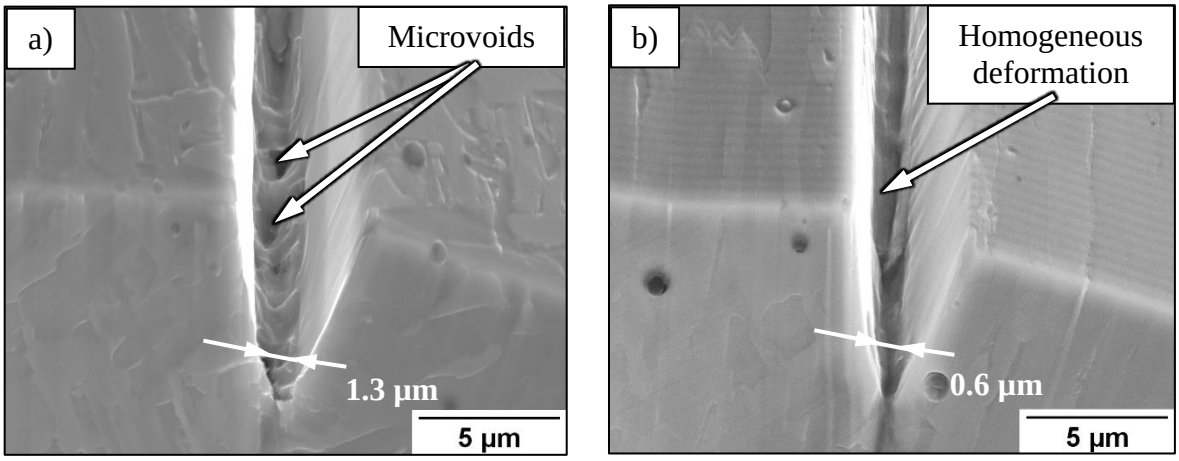

Figure 74: SE images show small crack growth in the vicinity of the notch tip after loading for:
a) Acicular ferrite,
b) Upper bainite;

The conditional fracture toughness (K_Q) at a critical point, can be found for each of the specimens, using the following approach adopted from (Di Maio & Roberts 2005):

$$K_Q = \frac{P_Q L y}{I} \sqrt{\pi a}\, F\left(\frac{a}{b}\right) \tag{5-21}$$

Where a is the notch depth (8 µm) (see Figure 49 in Section 4.1.8) and F(a/b) is a dimensionless shape factor, which is related to the specimen geometry, P_Q is the applied load at a critical point determined according to ASTM E-399 (ASTM 2009), L is the distance between the notch and the point of loading on the micro-beam (55µm) (see Figure 53 a) and Figure 53 b) in Section 4.1.10), I is the moment of inertia of the beam cross section and y is the vertical distance between the upper surface and the neutral plane. I and y can be calculated using the following equations (Di Maio & Roberts 2005):

$$I = \frac{wb^3}{12} + \left(y - \frac{b}{2}\right)^2 bw + \frac{w^4}{288} + \left[\frac{b}{6} + (b-y)\right]^2 \frac{w^2}{4} \tag{5-22}$$

$$y = \frac{\frac{b^2 w}{2} + \frac{w^2}{4}\left(b + \frac{w}{6}\right)}{bw + \frac{w^2}{4}} \tag{5-23}$$

Where b is the height of the parallel vertical face (18 µm) and w is the width of the micro-beam (16 µm) (see Figure 48 in Section 4.1.8). For these specimen geometries the resulting values for I and y are 1.5545×10^{-8} mm^4 and 0.01112 mm respectively.

The equation for the dimensionless shape factor F was proposed by DiMaio et al. (Di Maio & Roberts 2005) and is based on extensive finite element simulations for a wide range of specimen geometries. For $0.3 \leq (a/b) \leq 0.5$ following equation can be applied:

$$F\left(\frac{a}{b}\right) = 1.85 - 3.38\left(\frac{a}{b}\right) + 13.24\left(\frac{a}{b}\right)^2 - 23.26\left(\frac{a}{b}\right)^3 + 16.8\left(\frac{a}{b}\right)^4 \tag{5-24}$$

This results in F(a/b) =1.58 at a/b=0.44, for the specimen and notch dimensions used in this study.

The load-deflection diagrams in Figure 73 show the variation of K_Q as a function of the applied loading. These plots do not take into account any crack growth or large plastic

deformations. They only demonstrate the reaction of the specimens to the applied load, which allows the evaluation of the lower limits of the fracture toughness at the maximum load P_{max}. resulting in 5.9 and 3.5 MPa $m^{1/2}$ for acicular ferrite and upper bainite, respectively.

The presence of the large yielding ahead of the crack tip requires non-linear approaches to evaluate the fracture resistance. In this case, the Crack Tip Opening Displacement (CTOD) was selected as a parameter to describe the fracture toughness of the individual microstructural constituents. A plastic hinge model, originally proposed by British Standards Institution in 1972 (British Standards Institution 1972), was used to evaluate the CTOD of both micro-beams. In this model, the Centre of Rotation (CR) was assumed to be at a depth of $r_e(d-a)$, where r_e the rotation factor and d is the total height of the micro-beam (26 µm). r_e depends on the shape of the cross sectional area of the beam and varies for different material properties and loading conditions. It was reported to be within the range of 0.3 – 0.5 (Druce & Eyre 1979). From direct measurements, the CR can be located at approximately 2.4 µm and 3.5 µm from the lower lateral edge of the specimen (see Figure 75). This corresponds to 10.4 µm from the bottom of the specimen (vertex point) in the case of acicular ferrite and 11.5 µm for upper bainite. resulting in r_e = 0.42 and 0.36 for acicular ferrite and upper bainite respectively.

At high levels of loading the deformations and displacements in beams are largely associated with the rotation of the unsupported part of the beam around the CR. However, for the current tests it is apparent that the CR had a slight shift from the notch tip towards the beam support. This can be explained by the approximate nature of the plastic hinge concept as well as the fact that the beam is quite short and the notch is quite shallow, so high levels of shear stresses were generated as a result of the applied bending load. These factors have an influence on the deformation mechanisms and affect the position of the plastic hinge.

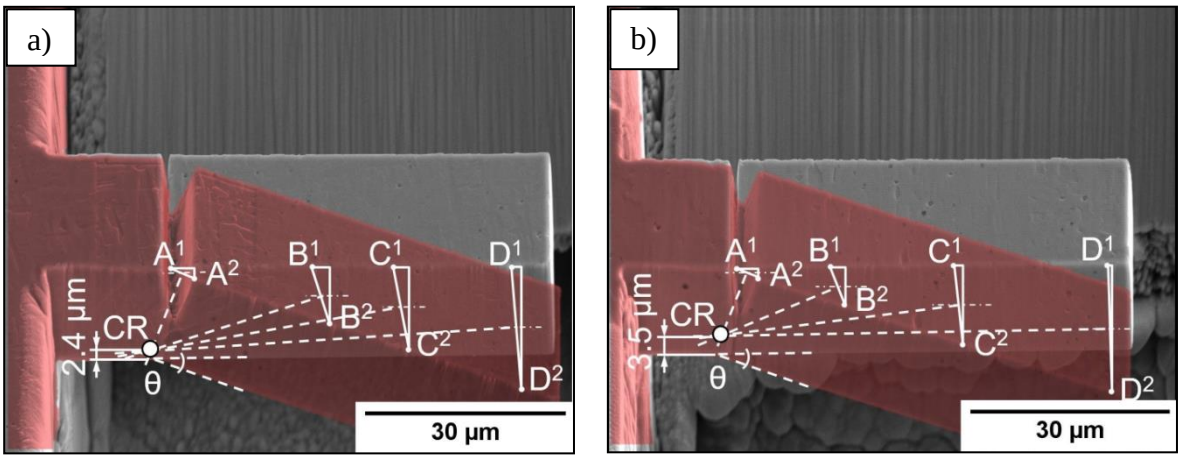

Figure 75: Superimposed, tilt corrected SE images of micro-beams before and after testing show the location of the CR for:
a) Acicular ferrite,
b) Upper bainite;

The evaluation of the CTOD can be represented as a sum of two components, elastic, δ_e, and plastic, δ_p (British Standards Institution 1972):

$$CTOD = \frac{J}{\sigma_Y} = \delta_e + \delta_p = \frac{K^2(1-\nu^2)}{2\sigma_Y E} + \frac{r_e(d-a)V_p}{r_e(d-a)+a} \quad (5\text{-}25)$$

Where K is in this case K_Q at the maximum load P_{max} as defined in Equation (5-21) and ν is the Poisson's ratio (0.3). The yield strength σ_Y and Young's modulus E for acicular ferrite and upper bainite can be found in Table 18. V_p is the plastic component of crack opening displacement at the lateral surface of the specimen and can be determined by measuring the distances between crack opening before (B^1) and after loading (B^2), which are approximately 3.68µm and 3.2µm (see Figure 76) at the maximum deflections 15.4µm and 16.4µm (see Figure 73) for acicular ferrite and upper bainite respectively.

r

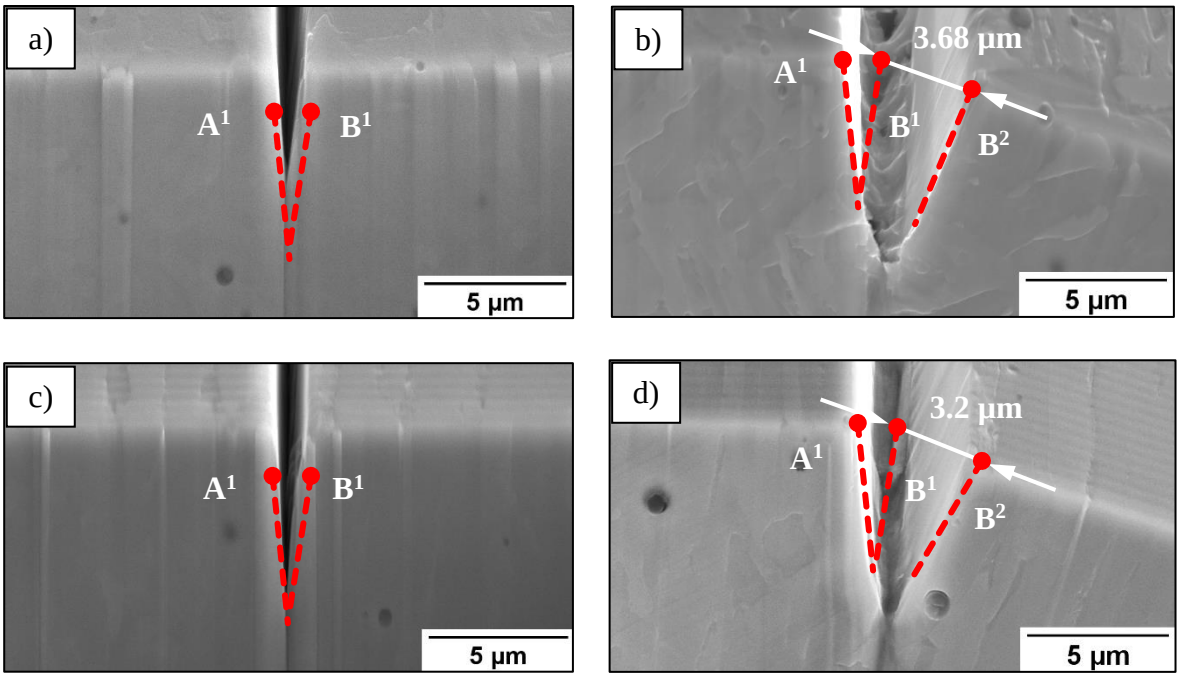

Figure 76: SE images show the notch tip for:
a) Acicular ferrite before loading,
b) Acicular ferrite after loading,
c) Upper bainite before loading,
d) Upper bainite after loading;

The corresponding values of V_p for the deflections at P_{max}, which are 6µm for acicular ferrite and 11µm for upper bainite (see Figure 73), can be calculated using the proportional ratios leading to 1.43 µm and 2.14 µm respectively. The resulting elastic components δ_e are 0.125 µm and 0.05 µm, while the plastic components δ_p are 0.69µm and 0.96 µm for acicular ferrite and upper bainite respectively.

The values for the conditional fracture toughness $K_{Q,\,CTOD}$ can be determined by first calculating the individual $CTOD_Q$'s (see Equation (5-25)) corresponding to the maximum load P_{max} and then substituting them into following equation (Wurster, Motz & Pippan 2012):

$$K_{Q,\,CTOD} = \sqrt{\frac{E^*}{d_n}\sigma_y CTOD_Q} \tag{5-26}$$

The $CTOD_Q$'s for P_{max} are approximately 0.82 µm and 1 µm for acicular ferrite and upper bainite, respectively. $\bar{E}$ is the reduced modulus defined as $E^* = E/(1-\nu 2)$ and d_n is the Shih factor which is 0.78 for plane strain conditions (Di Maio & Roberts 2005). The resulting fracture toughness values for acicular ferrite and upper bainite are 12.1 and 12.5 MPa $m^{1/2}$ respectively.

5.2 Microstructure and HACC Propagation Resistance of Acicular Ferrite and Upper Bainite in Weld Metal

5.2.1 Characterisation of Microstructures and HACC Propagation Resistance

EBSD data was collected from two selected microstructural regions where a hydrogen crack propagated in one case through acicular ferrite and in the other one through upper bainite as illustrated in Figure 40 in Section 4.1.6.

As evident in the superimposed IQ and IPF maps in Figure 77 a) and Figure 77 c), the hydrogen crack in acicular ferrite propagated transgranularly across the interlocking ferrite plates or grains, while in upper bainite the crack propagated along the boundary between two ferrite laths which were part of a crystallographic packet of several aligned laths with largely similar orientations.

The misorientation profile in Figure 77 b) shows that in acicular ferrite the majority of grain boundaries adjacent to the crack path range between approximately 45° to 60° and can thus be classified as HAGB's. As highlighted in Figure 77 a), in the case of acicular ferrite, the fine grain size and the HAGB's forced the crack to frequently change the microscopic propagation plane in order to accommodate the new crystallographic orientation, which resulted

in a relatively short UCP of 2.3 µm (average of 10 measurements). According to Figure 77 a), for acicular ferrite, the UCP corresponds to the distance between two neighbouring HAGB's.

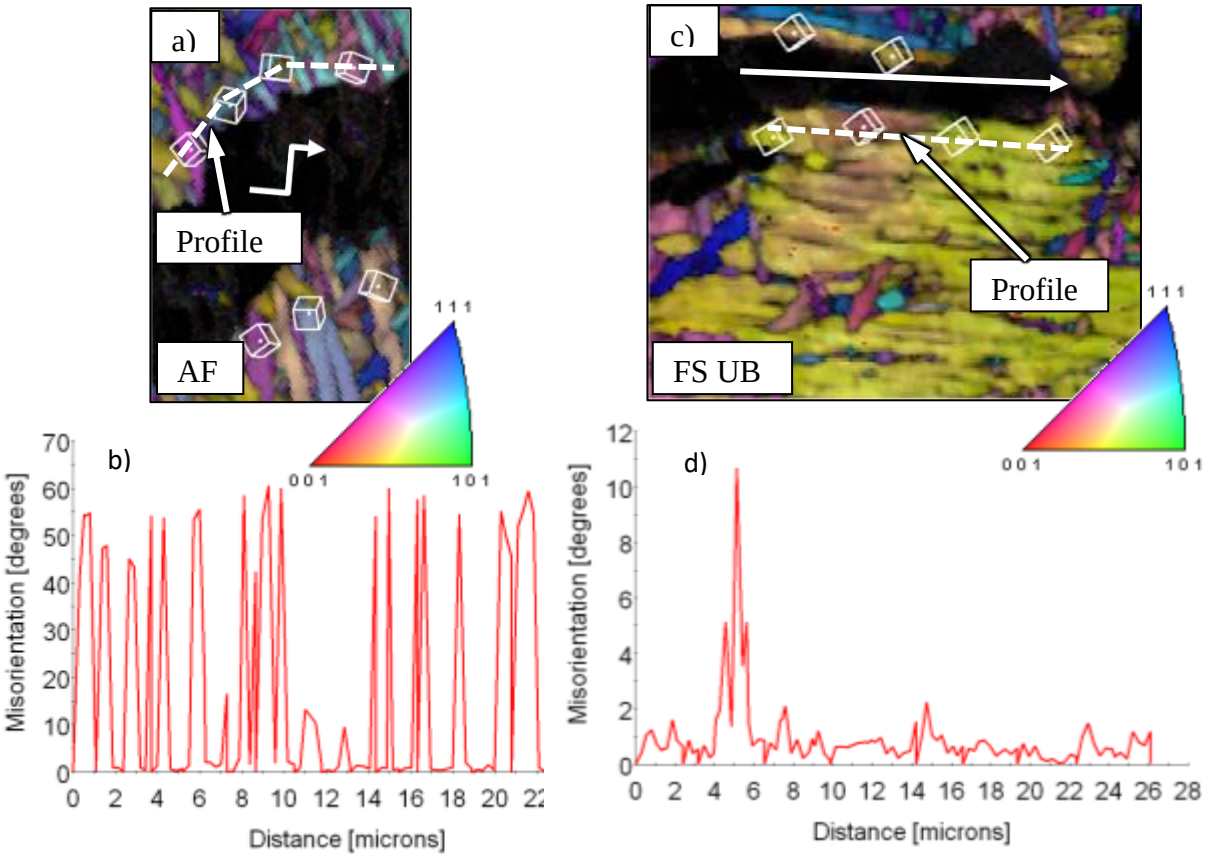

Figure 77: a) Superimposed [001] IPF and IQ map of HACC propagation through acicular ferrite,
b) Misorientation profile of the highlighted region in acicular ferrite,
c) Superimposed [001] IPF and IQ map of HACC propagation through upper bainite,
d) Misorientation profile of the highlighted region in upper bainite;

Misorientations below 15° as mainly found in upper bainite can be classified as LAGB's and were reported to have no significant effect on the UCP of a propagating hydrogen crack (Mazancová, Rucká & Mazanec 2007). In the current case, the crack propagated in a nearly straight line along the inter-lath boundaries without intersecting any misorientations above 10° (see Figure 77 c) and Figure 77 d)), the UCP depends therefore mainly on the average lath

length which is around 26.2 µm (average of 10 measurements). However, for a random crack propagation direction, the UCP in bainite is usually associated with the diameter of the entire crystallographic packet (Medina et al. 2014), which is in this case 32.2 µm for the ECAD.

5.2.2 Characterisation of Fracture Surface

The SE images in Figure 78 a) and Figure 78 b) illustrate the typical fractographic features found in acicular ferrite and upper bainite, which were mainly defined by clusters of coplanar cleavage facets, often found in the vicinity of NMI's. The topology of the cleavage facets was in both cases not completely flat but characterised by the presence of shallow dimples, indicating cleavage-like failure that involved some limited micro-plasticity (Beachem & Pelloux 1965; Martin et al. 2011).

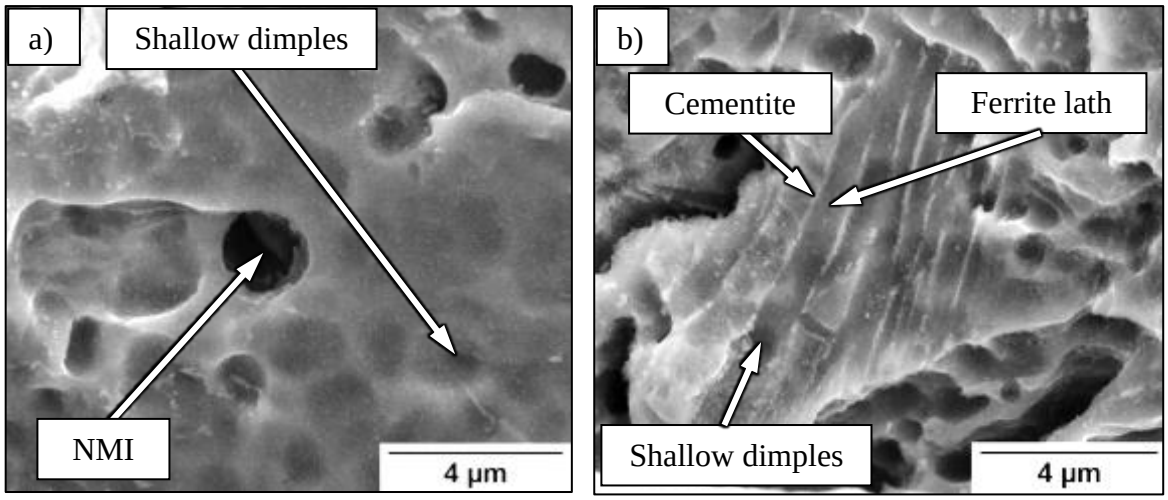

Figure 78: a) SE image shows the typical fractographic features found in acicular ferrite, b) SE image shows the typical fractographic features found in upper bainite;

5.2.3 Characterisation of Chemical Composition

The results from the GD-OES analysis of weld specimen W2 are listed in Table 19.

i	Si	Mn	Ni	Mo	Cr	V	Co
x_i [wt.%]	0.20	1.03	0.13	0.08	0.02	0.02	0

Table 19: Concentration of the substitutional solutes x_i in the weld specimen W2 determined by GD-EOS.

5.3 Microstructure and HACC Initiation Resistance of Acicular Ferrite

5.3.1 Characterisation of Microstructures

The EBSD data was collected from the plane on top of a micro-beam, fabricated into a selected microstructural region of acicular ferrite, as detailed in Figure 45 a) in Section 4.1.8.

The superimposed grain boundary and IQ map (see Figure 79 a)) as well as the misorientation distribution chart in Figure 79 b) show that the main proportion of boundaries in the analysed region can be classified as HAGB's, with a large proportion of misorientations >15°, which correlates well with the data obtained from the uncharged acicular ferrite specimen, as shown in Figure 63 a) and Figure 63 b) in Section 5.1.1.

The chart in Figure 80 is a quantitative illustration of the grain boundary character distributions for the uncharged and hydrogen pre-charged specimens.

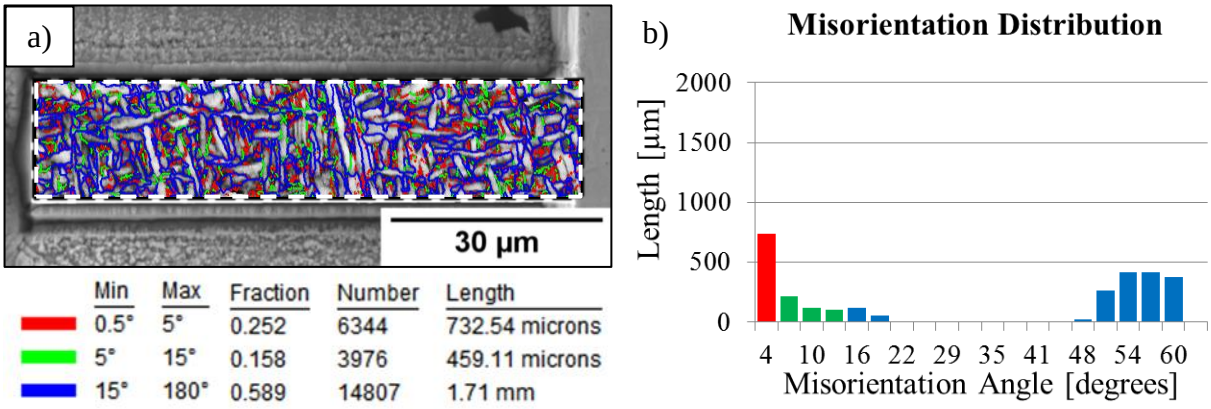

Figure 79: a) Superimposed grain boundary and IQ map obtained from the acicular ferrite specimen tested after hydrogen charging,
b) Chart illustrates the according misorientation distribution;

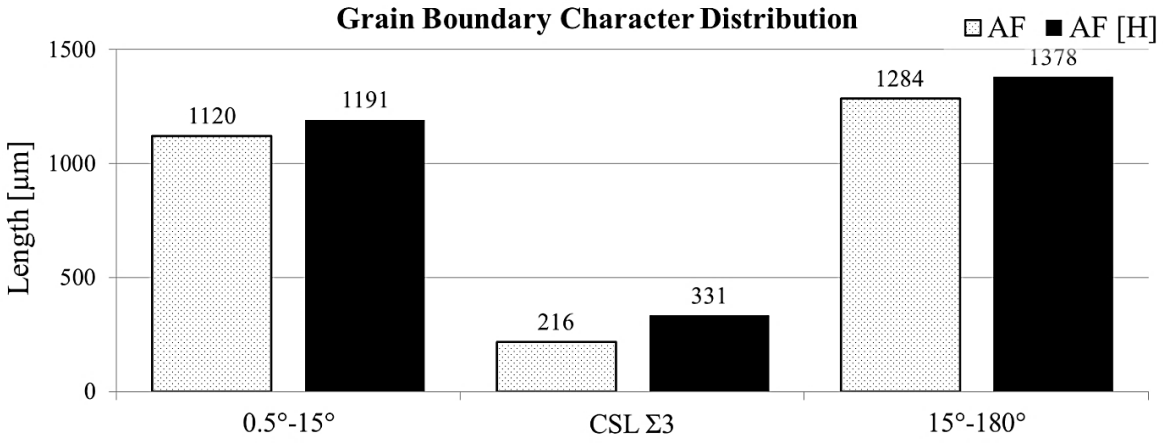

Figure 80: Chart illustrates the grain boundary character distribution for the uncharged and hydrogen pre-charged [H] specimens.

The Grain Diameter map in Figure 81 highlights for the hydrogen charged micro-beam the individual grains according to their diameter as either green (<5µm) or red (≥5 µm). The chart illustrates the distribution of the different grain diameters within the aggregate. The data was additionally used to determine the ratio between acicular ferrite and PF(I)+WF(I)+B(I) (see Figure 82 a)) as well as the average grain diameter of the aggregate (see Figure 82 b)).

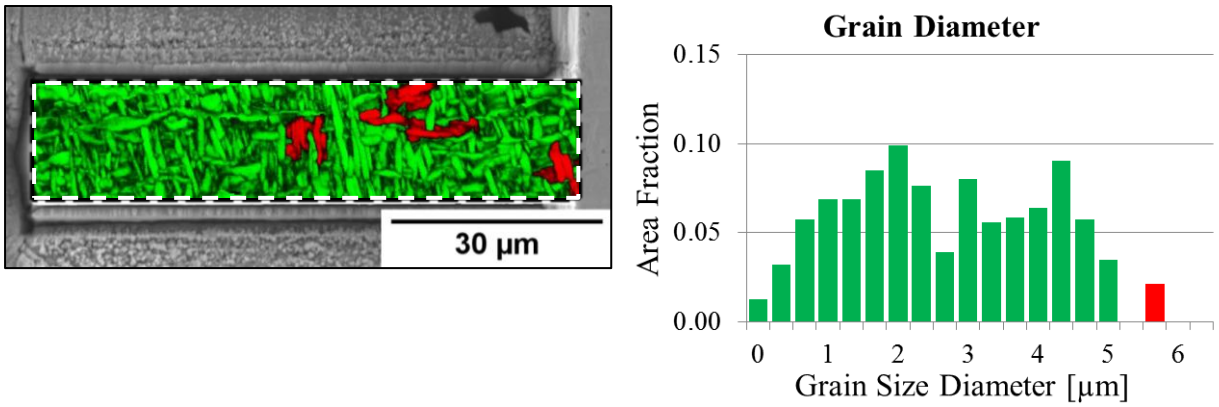

Figure 81: Superimposed Grain Diameter and IQ map highlights the distribution of acicular ferrite (green) and PF(I)+WF(I)+B(I) (red). The chart illustrates the grain diameter distribution. Adjacent data points with misorientations <5° were considered to be part of the same grain.

The results show that for the charged specimen the proportion of acicular ferrite is slightly higher and the average grain diameter consequently lower than for the uncharged specimen. Where the diameter refers here to the ECAD. The corresponding grain sizes determined by the LI method are 1.42 µm and 1.51 µm for the charged and uncharged specimens respectively.

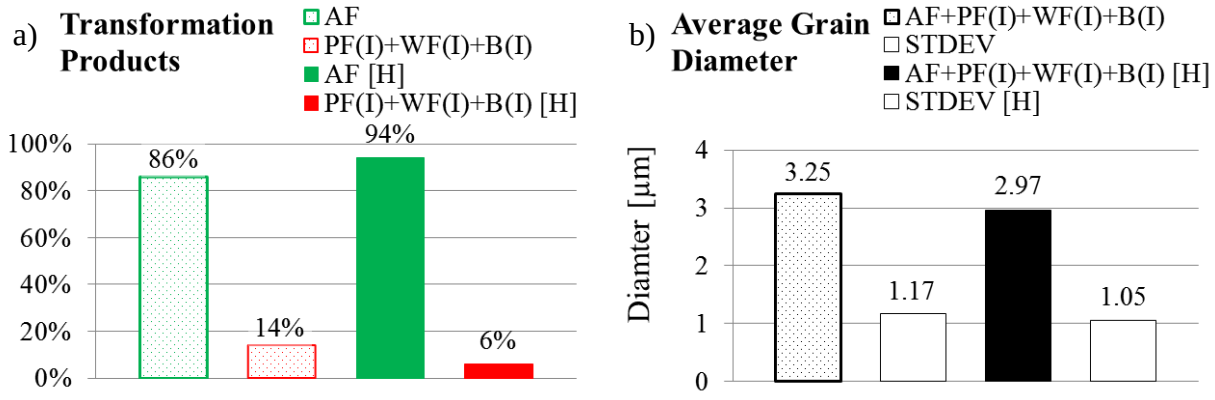

Figure 82: a) Chart shows the ratio between the transformation products of the uncharged and the pre-charged [H] specimens,

b) Chart shows the average grain diameter of the uncharged and the pre-charged [H] specimens;

5.3.2 Characterisation of Deformation Behaviour, Fracture Behaviour and Stress Intensity Factors

For each test, the micro-beam was first charged with hydrogen and then deflected via nano-indentation to promote HACC initiation, as described in detail in Section 4.1.12. The resulting load-deflection curves are illustrated in Figure 83, together with the load-deflection curve of the uncharged micro-beam (see Figure 73).

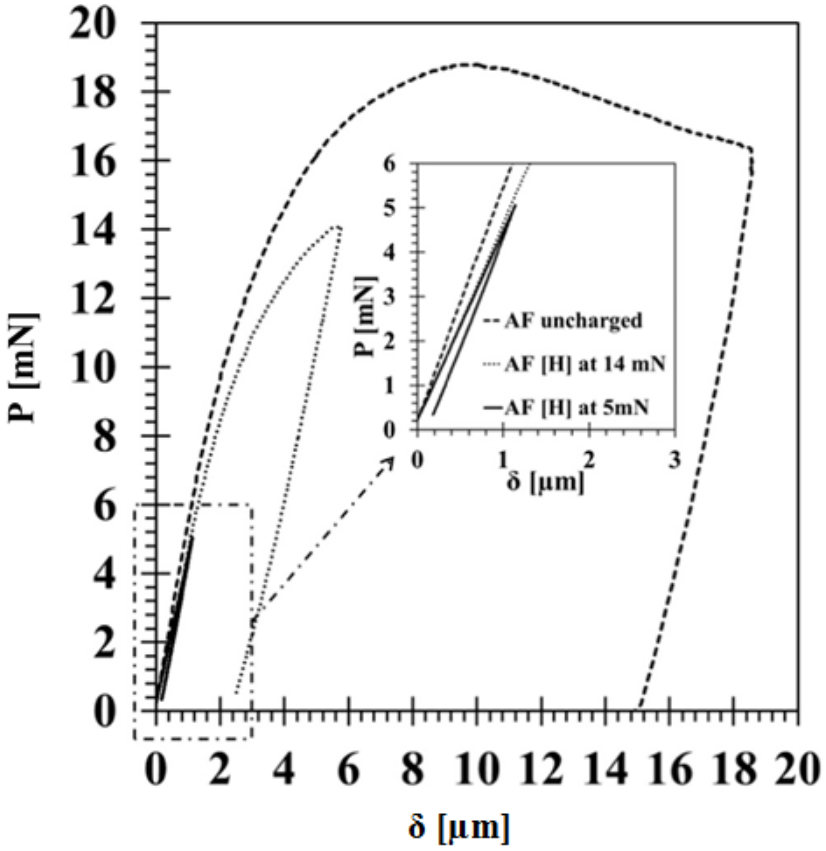

Figure 83: Load-deflection curves for the tests conducted on the uncharged and pre-charged [H] specimens.

The tests on the hydrogen charged specimen were conducted at 5 mN and 14 mN, corresponding to approximately 25% and 75% of the critical load (P_{max}) obtained for the uncharged specimen (see Figure 73). The loads were applied within five minutes after

completion of the hydrogen charging procedure and held constant for 12 hours to simulate the delayed nature of HACC.

The respective stress intensity factors K_I can be calculated using the following equation (Di Maio & Roberts 2005):

$$K_I = \sigma\sqrt{\pi a}\, F\left(\frac{a}{b}\right) \tag{5-27}$$

Where σ is the nominal stress, a is the notch depth (8 µm) (see Figure 49 in Section 4.1.8) and F(a/b) =1.58 at a/b=0.44, as discussed previously (see Equation (5-24)). For a micro-beam subjected to a bending load, P, σ can be calculated as followed:

$$\sigma = \frac{PLy}{I} \tag{5-28}$$

Where P is the applied load, L is the distance between the notch and the point of loading on the micro-beam (55 µm) (see Figure 55 in Section 4.1.12), I is the moment of inertia of the beam cross section (1.5545×10^{-8} mm^4) and y is the vertical distance between the upper surface and the neutral plane (0.01112 mm). Both can be calculated using Equations (5-22) and (5-23) as detailed in Section 5.1.4. The resulting stress intensity factors for 5 mN and 14 mN were 1.56 MPa $m^{1/2}$ and 4.36 MPa $m^{1/2}$ respectively.

The Young's modulus as well as the yield strength were notably lower for the tests conducted on the hydrogen charged specimen, indicated by the gradient of the slopes in the linear part of the load-deflection curves and the deviation from linear behaviour which occurred much earlier for the test conducted at 14 mN, as shown in Figure 83. However, during unloading, the Young's modulus has fully recovered to the corresponding value of the uncharged specimen (see detailed plot of 5 mN test in Figure 83). This suggests that the hydrogen diffused almost entirely out of the sample during the 12-hour tests. Nevertheless, as the Young's modulus changed during the prolonged tests, conventional crack monitoring based

on the measurement of specimen compliance was not possible. Therefore, the crack growth had to be derived from optical observations, using a high-resolution SEM.

After completion of each test, the areas at the vicinity of the notch tips were observed and compared. The fracture behaviour in case of the uncharged specimen was ductile and resulted in severe blunting at the vicinity of the notch tip (see Figure 84 a)), while an apparently brittle crack initiated from the notch tip of the hydrogen pre-charged micro-beam tested at 14 mN (see Figure 84 b) and Figure 84 c)). The crack length of 1.55 µm seemed thereby to be insufficient to cause cross-sectional failure. The corresponding mean crack growth rate for the 12-hour test was 3.59×10^{-11} m s^{-1}.

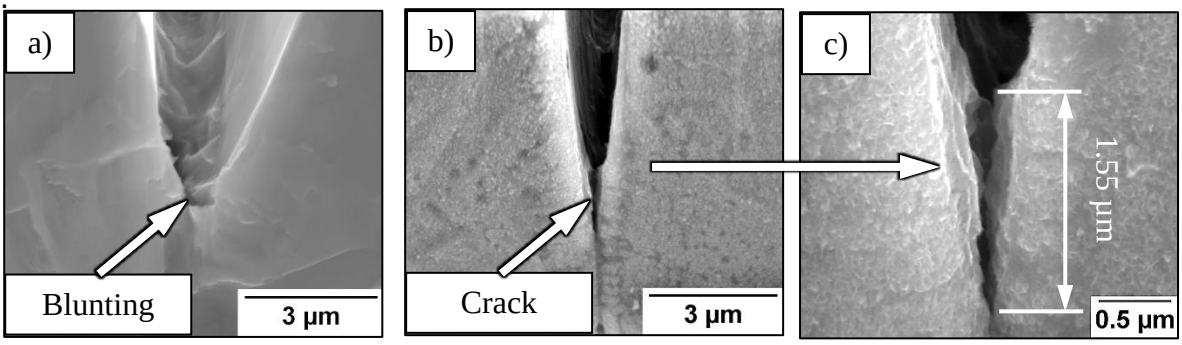

Figure 84: SE images show notch tip after testing for:
a) Uncharged micro-beam,
b) Pre-charged micro-beam tested at 14 mN,
c) Higher magnification of pre-charged micro-beam tested at 14 mN;

The fracture morphology of the hydrogen crack was defined by tear ridges that followed the direction of the crack propagation as shown in Figure 85 a), Figure 85 b) and Figure 85 c). The opposing fracture surfaces matched thereby ridge to ridge, indicating that minor plastic deformations may have constituted the crack growth. The SE images in Figure 85 also reveal that the hydrogen charging introduced some minor surface damage as evident in the regions adjacent to the crack path.

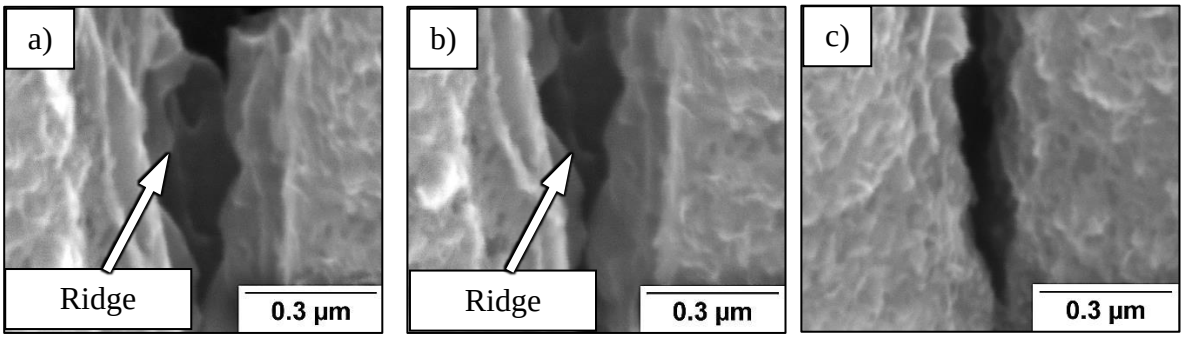

Figure 85: SE images show the fracture surface morphologies at:
a) HACC initiation,
b) HACC propagation,
c) HACC arrest;

No cracks, plastic deformations or deflection were observed for the test conducted at 5 mN, as shown in Figure 86 a) and Figure 86.b).

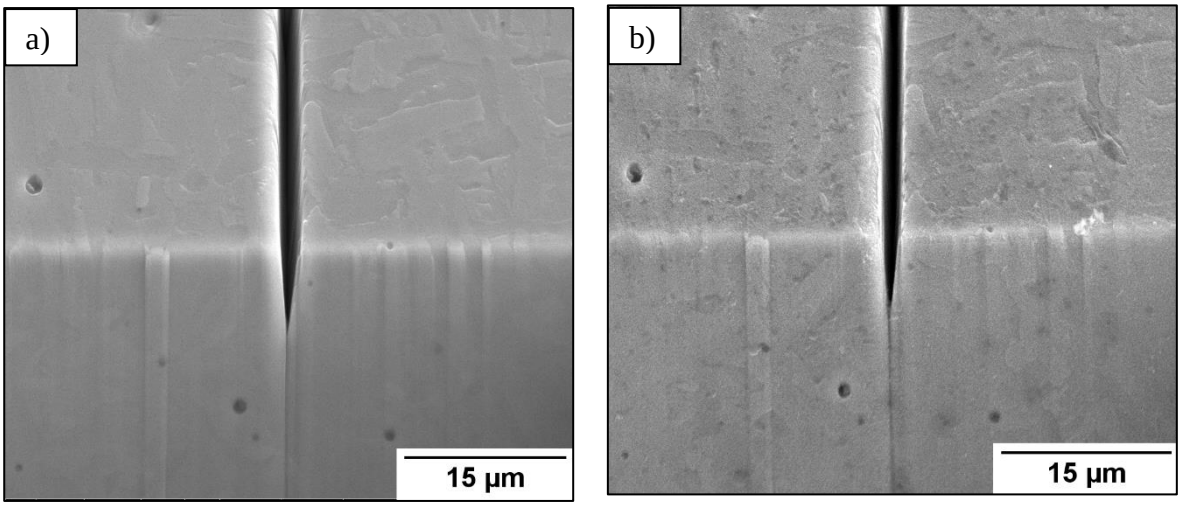

Figure 86: a) SE image shows the notch of the micro-beam prior to hydrogen charging and testing,
b) SE image shows the notch of the pre-charged micro-beam, after testing at 5 mN;

CHAPTER 6

DISCUSSION

6 Discussion

6.1 Relationship between the Microstructure and Mechanical Properties of Acicular Ferrite and Upper Bainite in Weld Metal

The microstructure of ferritic weld metal consists of diverse constituents which typically only form in very small material volumes, within the micrometer regime in size. Acicular ferrite and upper bainite are such highly localised constituents, known to have substantially different microstructural features contributing to their intrinsic mechanical properties (Bhadeshia 1997). However, in weld metal acicular ferrite and upper bainite usually co-exist and interact with other microstructural constituents. Therefore, the link between their microstructure and mechanical properties is difficult to assess with conventional test methods and still remains unclear. This part of the work utilised advanced characterisation and micro-mechanical testing techniques to evaluate this fundamental link.

The EBSD analysis of selected microstructural regions of acicular ferrite and upper bainite revealed vastly different characteristics, although they form within an almost similar temperature range, by the same type of transformation mechanisms (Bhadeshia 2001). This is mainly because acicular ferrite nucleates intragranulary from inclusions inside the prior austenite grains which prevents the formation of parallel ferrite plates and simultaneously restricts their growth due to multiple impingements (Bhadeshia 2001; Thewlis 2003). All these factors produce an interlocking microstructure that consists of fine ferrite plates with divergent crystallographic orientations, as shown in Figure 60 a) in Section 5.1.1. Contrary to acicular ferrite, upper bainite nucleates at the prior austenite grain boundaries and forms crystallographic packets consisting of parallel ferrite laths with almost similar orientations and cementite precipitates that decorate the lath boundaries (Bhadeshia 2001), as shown in Figure 60 b) and

Figure 70 in Section 5.1.1. Upper bainite is therefore expected to exhibit a more anisotropic behaviour than acicular ferrite, where the orientations vary between the individual grains.

The results correlate well with previous EBSD investigations conducted on acicular ferrite and bainite (Díaz-Fuentes, Iza-Mendia & Gutiérrez 2003).

A common feature of acicular ferrite and upper bainite is their orientation relationship with the parent austenite grain in which they nucleated (Kudrjumov & Sachs 1930; Nishiyama 1934; Wassermann 1935). This is because the transformation of austenite into acicular ferrite or upper bainite only occurs on particular planes and in particular directions. As a result of these orientation relationships, the different ferrite grains or laths formed within the same austenite grain cannot be related by misorientations in the approximate range of 20° to 47° (Díaz-Fuentes, Iza-Mendia & Gutiérrez 2003) as evident in the misorientation distribution charts in Figure 63 b) and Figure 64 b) in Section 5.1.1.

The chart in Figure 87 a) shows a quantitative comparison of the observed microstructural differences between acicular ferrite and upper bainite. The mean values for the grain size of acicular ferrite and the lath size of upper bainite were quite similar, set apart by less than 8%. This similarity was consistent, regardless if the ECAD or LI method was used to determine the size.

It is well established that the mean grain/lath size is closely related to the grain/lath boundary density. Hence, the difference between the grain/lath boundary densities was also relatively low (less than 6%), but their characteristics were distinctive for each of the microstructures.

The proportion of LAGB's (0°-15°) was 42% for acicular ferrite and 75% for upper bainite. The proportion of HAGB's (15°-180°) was 50% and 21% for acicular ferrite and upper bainite respectively. Approximately 8% of the HAGB's of acicular ferrite could be classified as CSL Σ3 boundaries and 4% in the case of upper bainite.

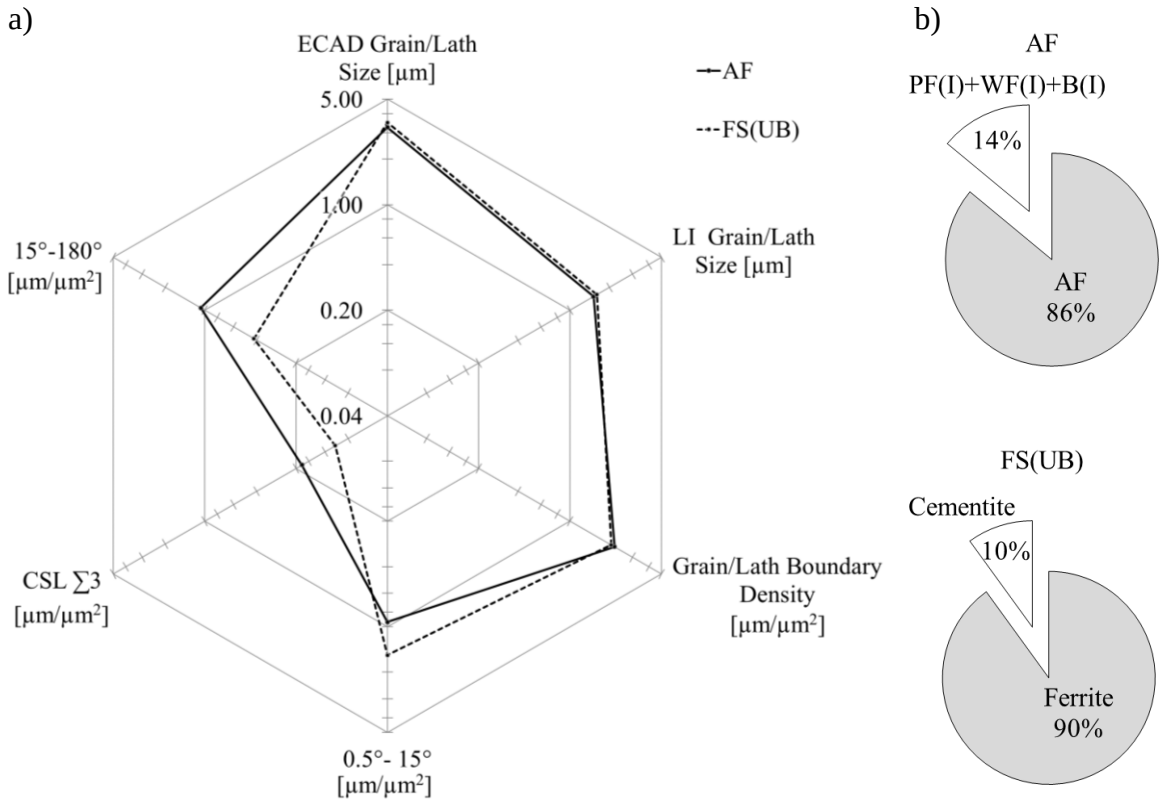

Figure 87: Charts illustrate for acicular ferrite and upper bainite:

a) Quantitative comparison between average grain/lath size, density of grain/lath boundaries and the grain boundary characteristics,

b) The proportion of the different microstructural components;

It can be quite difficult to achieve a consistent microstructure within a finite volume, even at very small scales. In weld metal, the individual microstructural constituents usually form aggregates with multiple components (Thewlis 2004). The chart in Figure 87 b) shows the proportion of the different microstructural components found in the selected microscopic regions of acicular ferrite and upper bainite. Although not explicitly discussed here, but both microstructures can additionally contain different types of NMI's and micro-phases (Thewlis 2004).

Each of the microstructural features listed in Figure 87 a) and Figure 87 b) may contribute to some extend to the intrinsic mechanical properties of the examined microstructures. For acicular ferrite and bainite, the currently most advanced models that imply

a direct link between particular microstructural features and mechanical properties are used to predict the yield strength (Bhadeshia 1997). By employing these semi-empirical models, it is possible to determine the individual contributions of the theoretical yield strength's intrinsic components, as illustrated in Figure 88 a) and Figure 88 b). The charts reveal that the most important contribution, other than the intrinsic strength of featureless iron, solid solution strengthening and the dislocation density, is due to the grain/lath size.

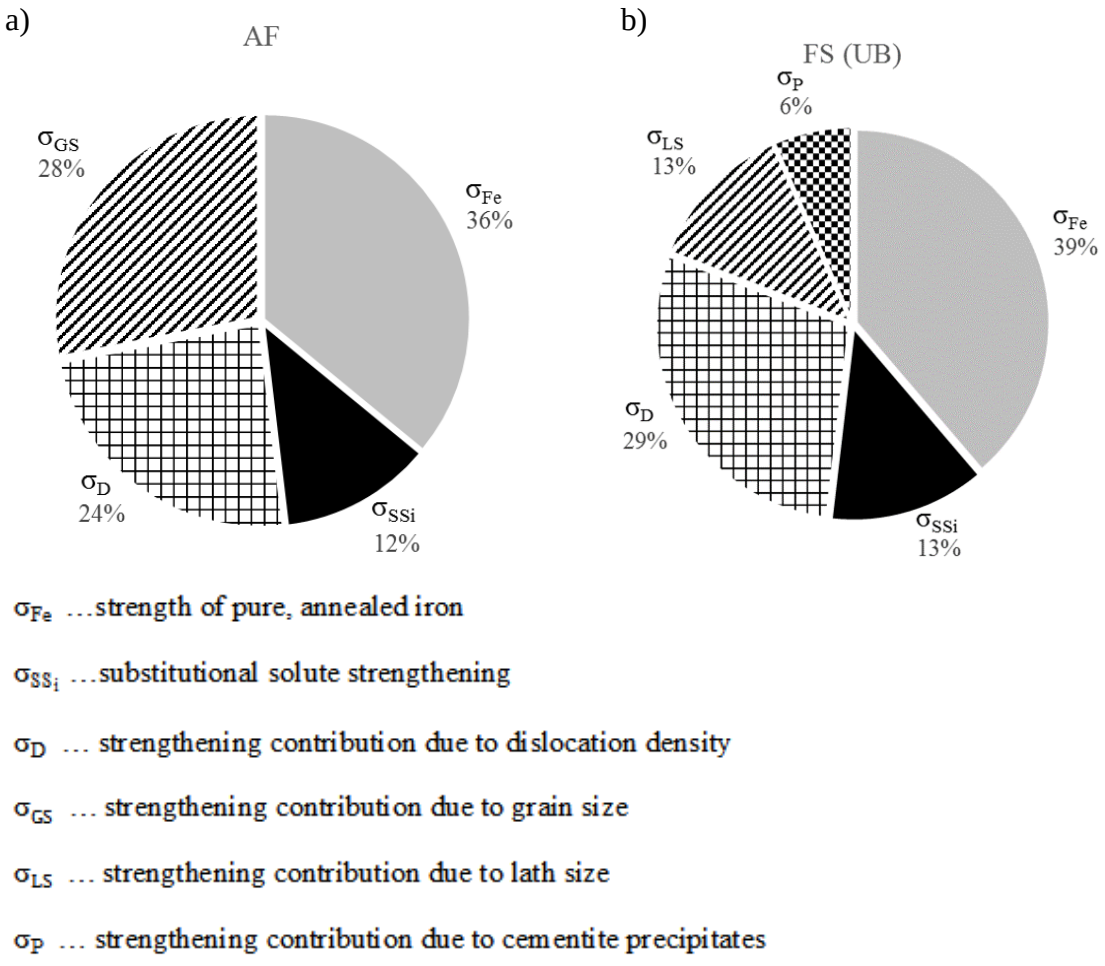

Figure 88: Charts show the individual contributions of the intrinsic components of the theoretical yield strength for:
a) Acicular ferrite,
b) Upper bainite;

Where the grain and lath size used to determine σ_{GS} and σ_{LS} respectively refers here to mean linear intercept. It is thereby apparent that the corresponding strengthening contribution is significantly higher for acicular ferrite. This can be explained by the discrete strengthening mechanisms operating in acicular ferrite and upper bainite, which lead to different strengthening contributions, despite the similarity of the grain/lath sizes (see Equation (5-3) and Equation (5-6)).

The strengthening contribution due to specific grain boundary characteristic is more difficult to evaluate. While it's well established that HAGB's act as barriers to the dislocation movement and thereby increase the yield strength (Hall 1951; Petch 1953), the exact role of LAGB's and particular CSL boundaries in contributing to the yield strength remains unclear.

Second phase particles also impede the movement of dislocations and can therefore cause an increase in the yield strength (Daigne, Guttmann & Naylor 1982; Wildash 1999). However, the contribution of cementite precipitates to the yield strength (σ_P) of upper bainite was comparatively low as illustrated in Figure 88 b).

The chart in Figure 89 shows the close correlation between the theoretical and experimental yield strengths of acicular ferrite and upper bainite (difference <5%).

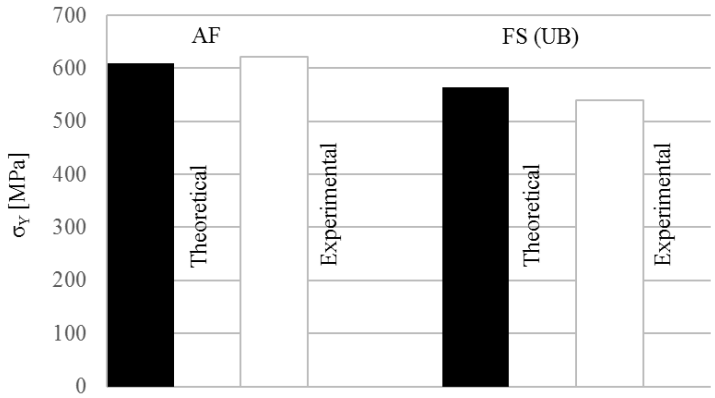

Figure 89: Diagram illustrates the theoretical and experimental yield strengths for acicular ferrite and upper bainite.

The chart in Figure 90 gives an overview of the intrinsic mechanical properties of acicular ferrite and upper bainite, obtained from mechanical tests that were conducted within the selected microstructural regions.

Conventional nano-indentation and an advanced characterisation procedure were employed to obtain the yield strength, hardness, elastic modulus and strain hardening exponent.

The yield strength of acicular ferrite was higher than of upper bainite. The difference between the two values was approximately 15%. Where the mean grain/lath size has been identified as the microstructural feature with the most significant contribution to the yield strength, as discussed earlier.

The Vickers hardness and the yield strength are usually proportional (Tabor 1956). Hence, the hardness of acicular ferrite was also higher than of upper bainite. Where the HV/σ_Y ratios were 5 and 4.15 for acicular ferrite and upper bainite respectively, which is in both cases higher than predicted by the 3 times approximation rule of Tabor (Tabor 1956). The deviations can be explained by a decrease of plastic constraints which usually implies a decrease in strength (Bhadeshia 1997), since all tests were conducted in regions that were largely isolated from the surrounding microstructure as shown in Figure 51 in Section 4.1.10.

The values for the Young's modulus were almost similar for both microstructures (difference <3%) and correlate well with typical values measured for low carbon steels (Brandes & Brook 1992). This similarity for the two substantially different microstructures is nevertheless quite surprising. Indeed, the Young's modulus is expected to be affected by the anisotropy (Armstrong, Wilkinson & Roberts 2009), which was more significant in the case of upper bainite, due to the unidirectional orientation of the laths.

In general, the strain-hardening exponent increases with increasing grain/lath size (Fan, Mingzhi & Deke 1989). Since the grain/lath sizes were quite similar for both microstructures, the higher strain-hardening exponent of acicular ferrite was presumably due to higher

proportion of HAGB's which have encouraged dislocation pile up, while the fine slip planes of upper bainite prevented dislocation pile up. Both strain-hardening exponents were within the range reported for low carbon steels (Fan, Mingzhi & Deke 1989).

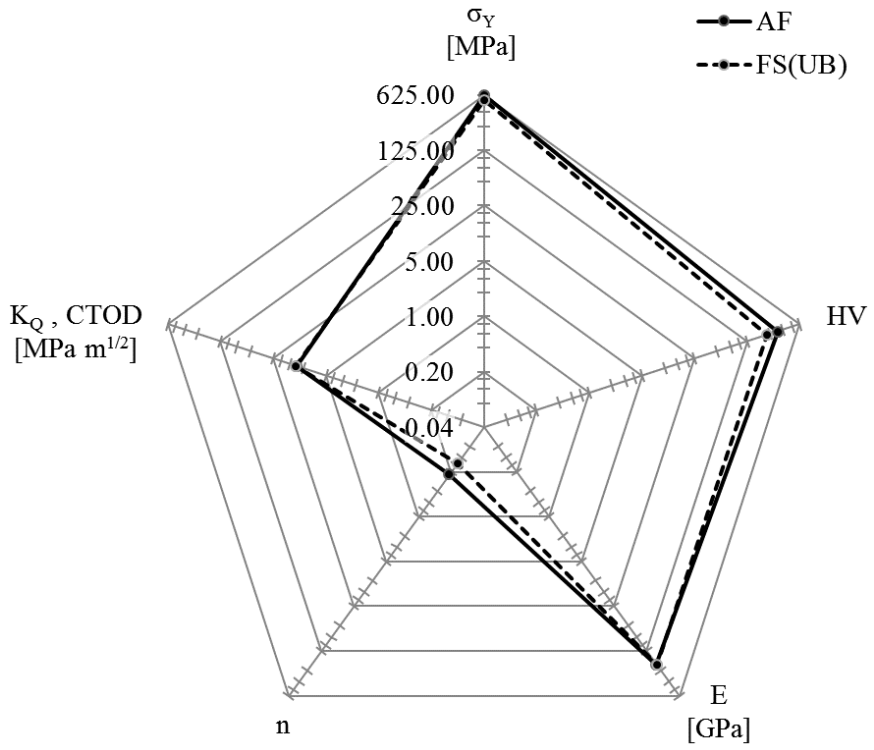

σ_Y ..... yield strength

HV ..... Vickers hardness

E ..... Young's Modulus

n ..... strain hardening exponent

$K_{Q,CTOD}$ ... conditional fracture toughness

Figure 90: Chart gives an overview of the intrinsic mechanical properties of acicular ferrite and upper bainite.

Micro-beams were fabricated with a FIB into the selected microscopic regions of acicular ferrite and upper bainite to be subsequently tested. The resulting load-deflection diagrams (see Figure 73 in Section 5.1.4) indicated in both cases elastic-plastic deformation

behaviour and that the yield strength of acicular ferrite was higher than of upper bainite, while the values for the Young's modulus seemed to be quite similar for both microstructures. All these observations are consistent with the results obtained from the nano-indentation tests in these regions.

Both microstructures showed ductile fracture behaviour. However, in the case of acicular ferrite the fracture propagation was characterised by the formation and coalescence of micro-voids, while in upper bainite fracture was accompanied by homogeneous deformations (see Figure 74 a) and Figure 74 b) in Section 5.1.4). This is mainly because the width of the ferrite laths in upper bainite is usually too small to allow the formation of dislocation pile ups that are able to give rise to localised slip. It is therefore expected that the deformation behaviour of the individual laths is relatively homogeneous (Bhadeshia 2001).

Various approaches can be selected to evaluate the fracture resistance. However, for the current tests it can be stated that a LEFM approach cannot provide correct values for fracture toughness due to the formation of relatively large plastic zones, compared to the small specimen dimensions, which fail to fulfil the conditions given in the testing standards by about three orders of magnitude (Wurster, Motz & Pippan 2012).

The most popular non-linear criteria, which are widely used to evaluate the fracture resistance are based on either J-integral, Crack Tip Opening Displacement (CTOD) or Crack Opening Angle (COA). The actual ASTM standards rely on the very detailed knowledge of the crack extension. However, in the present tests only a very limited crack growth was observed in the both samples (see Figure 74 a) and Figure 74 b) in Section 5.1.4). Moreover, fracture standards for the evaluation of critical J-values J_C such as E-813 (ASTM 1981) restrict the initial ligament size and thickness, which have to be larger than 25 J_C/σ_y. This standard also specifies an offset value for crack extension (typically 0.2 mm), which is not possible to achieve for experiments at this length scale.

Beside the opportunity to measure critical J-values, it is also possible to use the CTOD as a parameter to describe the fracture resistance. Methods based on the measurement of the CTOD are particularly appealing because of their readily-grasped physical significance and the possibility of direct measurements. Using this method allowed to identify that the conditional fracture toughness ($K_{Q,\,CTOD}$) of acicular ferrite was slightly lower than of upper bainite, where the difference between the two values was quite small (approximately 3%).

In general, the fracture toughness tends to decrease as the strength or hardness increases (Ritchie 2011). This is because plastic deformation, which is the major energy absorption mechanism during fracture, becomes more difficult as the strength or hardness increases (Bhadeshia 1997). The general relationship between fracture toughness, strength and hardness is consistent with the results obtained from the tests in the selected microstructures, where acicular ferrite had a lower fracture toughness but a higher strength and hardness than upper bainite. The evaluation of the elastic and plastic components of the CTOD's confirm that the proportion of plastic deformations during fracture was higher in upper bainite which may have led to the higher fracture toughness (see Figure 91 a) and Figure 91 b)).

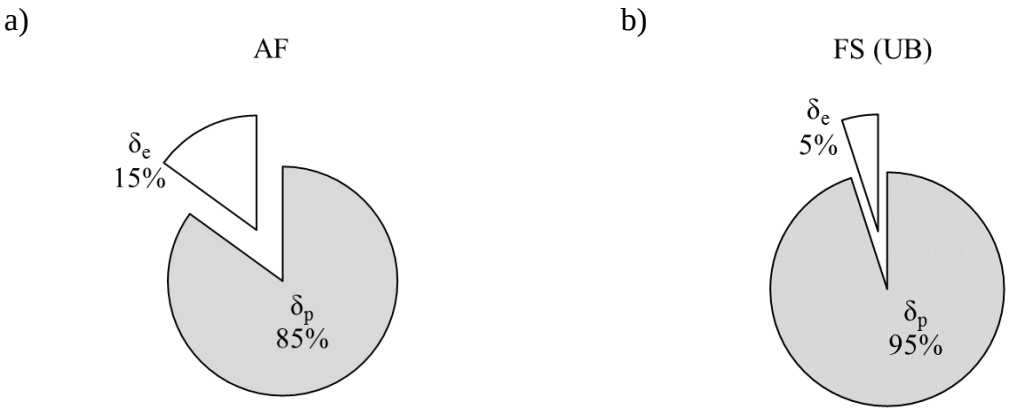

Figure 91: Charts represent the ratios between the elastic (δ_e) and plastic (δ_p) components of the CTOD's of:
a) Acicular ferrite,
b) Upper bainite;

For ductile fracture, where extensive plastic deformations may take place, the exact relationship between fracture toughness and microstructure is not well understood. However, all microstructural features that contribute to the yield strength, indirectly also influence the fracture toughness. Besides their contribution through the yield strength, by impeding the dislocation movement, second phase particles often also act as nucleation sites for micro-voids. If the number density of the voids is large, then their mean separation is reduced and coalescence occurs more rapidly, which decreases the amount of plastic deformation that can be accommodated before fracture occurs and simultaneously reduces the fracture toughness (Bhadeshia 2001).

It should be considered that the fracture toughness values presented in this study were at least by an order of magnitude lower than the ones typically reported for steels, which range from 480-1000 MPa (Díaz-Fuentes, Iza-Mendia & Gutiérrez 2003; Wang, Shan & Yang 2009; Wang et al. 2009; Yang, J. R. et al. 1993; Zhao, Yang & Shan 2003). This can be explained by the small specimen dimensions, which could cause a confinement of plastic deformations that may contribute significantly to the fracture resistance. Another important explanation for the low fracture toughness is that at the micro-scale not all fracture toughening mechanisms may be activated. These mechanisms may include crack bridging and deflection as well as further toughening associated with the subcritical crack growth. The obtained values correspond rather to the toughness at crack initiation, which can significantly increase with the crack extension as observed in conventional fracture tests (Druce & Eyre 1979). Nevertheless, it is worth noting that the fracture toughness values determined in this work for a relatively ductile material are higher than those reported for brittle and semi-brittle materials (between 0.63 and 8.5 MPa $m^{1/2}$) tested with similar methods at the micro-scale (Ast et al. 2014; Di Maio & Roberts 2005; Jaya, Kirchlechner & Dehm 2015; Wurster, Motz & Pippan 2012). In the current literature, at such small scales, no empirical data is available on the fracture toughness of specific microstructural constituents in weld metal. Therefore, it was not possible verify the results.

6.2 Relationship between the Microstructure, Mechanical Properties and HACC Propagation Resistance of Acicular Ferrite and Upper Bainite in Weld Metal

Several studies have reported that the HACC susceptibility of weld metal tends to generally increase with increasing strength (or hardness) and decreasing toughness (Davidson, JL, Lynch & Majumdar 1997). However, the question remains if such a correlation also exists at the micro-scale, for the weld metals individual microstructural constituents.

The analytical options to probe the mechanical properties of microstructural constituents in weld metal were outlined in the previous section. An established method to evaluate their contribution to the HACC susceptibility of the bulk material is to characterise their micro-fractographic behaviour along the hydrogen crack path (Alam et al. 1996). Once a hydrogen crack propagates through the surrounding microstructure and achieves a critical length, catastrophic failure is a likely outcome. The probability for such an event to occur depends, besides the hydrogen concentration and stress intensities in the vicinity of the crack tip, on the localised HACC propagation resistance of the weld metals different microstructural constituents. Insight on the HACC propagation resistance at the smallest microstructural scales is therefore essential in order to predict and control the WM HACC susceptibility of the bulk material.

Besides their contribution to the mechanical properties, the characteristic microstructures of acicular ferrite and upper bainite also govern their intrinsic resistance to HACC propagation (Davidson, JL, Lynch & Majumdar 1997; Mazancová, Rucká & Mazanec 2007). This part of the work utilised EBSD as well as the concept of the UCP to evaluate the HACC propagation resistance of both microstructures and to identify the microstructural features with the most significant contributions.

As illustrated in Figure 92, the UCP was significantly shorter for acicular ferrite than for upper bainite. The large difference between the UCP's can be attributed to specific microstructural aspects. The UCP in acicular ferrite mainly depends on the distance between two HAGB's within a fine interlocking microstructure with a high density of HAGB's. All these factors prevent straight crack growth and promote frequent deflections, resulting in a short UCP and thus a high HACC propagation resistance. On the other hand, the UCP in upper bainite depends on the diameter of the entire crystallographic packet, which is typically several times larger than the average distance between two HAGB's in acicular ferrite (Díaz-Fuentes, Iza-Mendia & Gutiérrez 2003). The large UCP of upper bainite implies a comparatively low HACC propagation resistance.

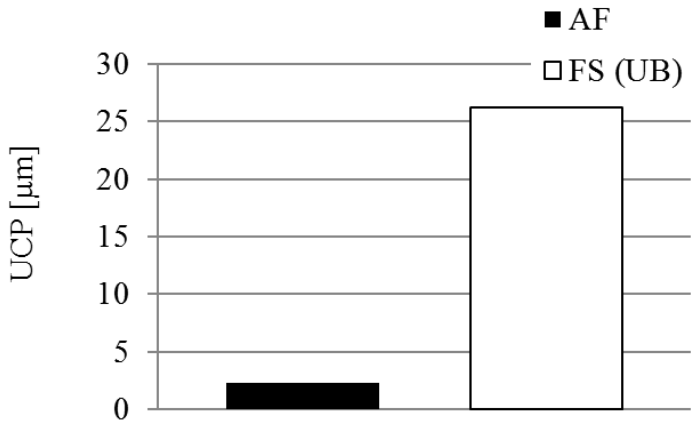

Figure 92: Diagram illustrates the ratio between the UCP's measured for a hydrogen crack propagating through:
a) Acicular ferrite,
b) Upper bainite;

The remarkable difference between the HACC propagation resistance of acicular ferrite and upper bainite correlates well with previous EBSD observations in different types of steel (Mazancová, Rucká & Mazanec 2007).

As shown in Figure 90, acicular ferrite has a higher strength, hardness and a lower fracture toughness than upper bainite. And yet, the micro-fractographic observations strongly

suggest that acicular ferrite is superior to upper bainite in terms of HACC propagation resistance. The reason is that the dissipation of energy during ductile fracture occurred mainly due to plastic deformations (see Figure 74 a) and Figure 74 b) in Section 5.1.4 as well as Figure 91) and in the case of HACC due to the impediment of brittle, cleavage-like crack propagation at HAGB's (see Figure 77 in Section 5.2.1 as well as Figure 78 a) and Figure 78 b) in Section 5.2.2).

The chemical compositions of weld W1 and W2 were quite similar, as shown in Table 15 in Section 5.1.2 and Table 19 in Section 5.2.3. Hence, significant variations of the mechanical properties due to compositional differences can be ruled out.

The results of this investigation suggest that macroscopic observations of the correlation between mechanical properties and HACC susceptibility are not applicable at the micro-scale. Which also implies that mechanical properties per se are not a good indicator of absolute HACC susceptibility and in fact may be misleading in terms of the intrinsic susceptibility of particular microstructural constituents. However, it should be considered that all the interpretations of the HACC propagation resistance are solely based on micro-fractographic observations. Neither the localised hydrogen concentration nor the stress intensity ahead of the crack tip were considered in the evaluation.

6.3 Relationship between the Microstructure, Mechanical Properties and HACC Initiation Resistance of Acicular Ferrite

As discussed earlier, microstructural constituents in weld metal usually form aggregates with multiple components. Some of these components, specifically second phase particles such as NMI's and carbides, may act as potential HACC initiation sites (Davidson, JL, Lynch & Majumdar 1997; Pressouyre 1980). The risk for crack formation in the adjacent matrix depends

thereby on the hydrogen concentration, stress intensity, and the HACC initiation resistance of the microstructure surrounding the initiation site.

Acicular ferrite is often considered to be the most beneficial microstructure for improving both, the weld metal's mechanical properties and HACC susceptibility (Alam et al. 1996; Mazancová, Rucká & Mazanec 2007). The mechanical properties and the HACC propagation resistance of this microstructure were discussed in detail in the previous sections. However, the HACC initiation resistance of acicular ferrite in weld metal has not been quantitatively evaluated yet. This is mainly due to the difficulty of probing the highly localised hydrogen concentration and threshold stress intensity required to initiate fracture in particular microstructural constituents of the bulk material. This part of the work utilised micro-fracture tests at different loads, on a hydrogen pre-charged specimen, comprised of acicular ferrite, to evaluate the range for the threshold stress intensity required initiate HACC. The microstructure, mechanical properties, deformation behaviour as well as the fracture behaviour were compared with the data obtained from the micro-fracture test conducted on an uncharged specimen also comprised of acicular ferrite as detailed in Section 5.1.

The chart in Figure 93 a) illustrates a quantitative comparison between the microstructures of the specimens tested under hydrogen charged and uncharged conditions. The average grain diameter was slightly higher for the uncharged specimen, where the difference was approximately 9%. The larger grain diameter can be explained by the higher proportion of larger intergranular transformation products, as shown in Figure 93 b). The larger grain diameter also implies a lower grain boundary density, where the difference between the uncharged and hydrogen charged specimen was around 10%.

As discussed in Section 6.1, a deviation in the grain size and grain boundary density results in different contributions to the theoretical yield strength, which in turn also has an influence on other mechanical properties. In the current case, the contribution due to the grain

size was 171 MPa (d≈ 1.51 µm) for the uncharged specimen and 176 MPa (d≈ 1.42 µm) for the hydrogen charged specimen (see Equation (5-3)). The close correlation suggests that the microstructural variations caused only minor differences between the intrinsic mechanical properties of both specimens, which allows to isolate the effects of hydrogen.

The deviation between the proportion of HAGB's was less than 6% and between the LAGB's less than 7%. The largest deviation was found for the CSL Σ3 boundaries with approximately 35%.

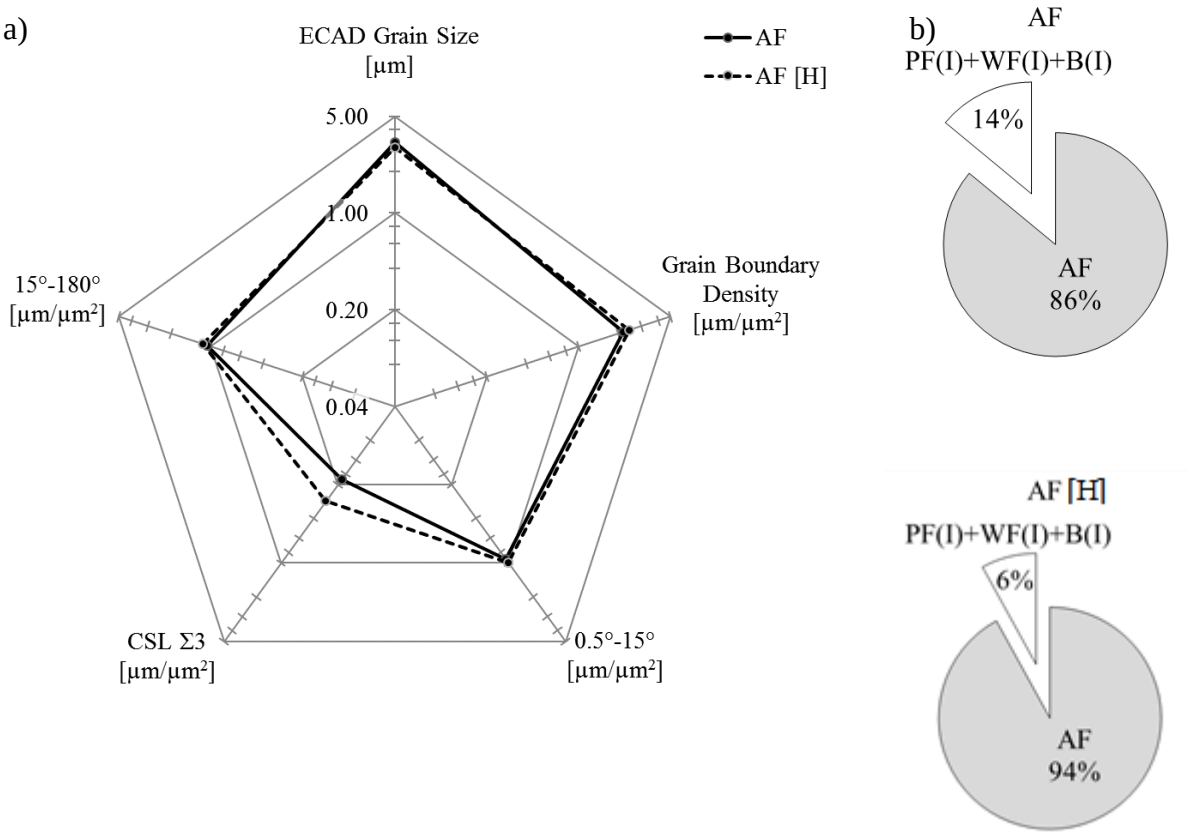

Figure 93: Charts illustrate for the uncharged and hydrogen pre-charged [H] acicular ferrite specimens:

a) Average grain size, grain boundary density and the grain boundary characteristics,

b) The proportion of the different microstructural components;

Besides their role as barriers to crack propagation, grain boundaries can also act as trapping sites for hydrogen (Oriani, R A 1970). Due to the higher binding energy, the ability of HAGB's to trap hydrogen is higher than of LAGB or CSL boundaries (Kane 2000). Moreover, HAGB's have relatively large gaps and can therefore accommodate a higher number of hydrogen atoms, making them more susceptible to intergranular crack initiation than LAGB's or CSL boundaries (Matsumoto et al. 2010). On the other hand, a higher density of HABG:'s may also reduce the risk of HACC initiation by reducing the available residual hydrogen that may otherwise diffuse to more susceptible crack initiation sites, such as different types second phase particles and micro-phases (Olson, D L R 1996).

Among all the CSL boundaries, the contribution of Σ3 boundaries to the improvement of the fracture resistance was reported to be the most significant (Watanabe 1994). This phenomenon is associated with the extremely low energy of Σ3 boundaries which makes them less susceptible to impurity or solute segregation, grain boundary sliding and intergranular degradation (Randle 1996). All these factors may be beneficial for an improvement of the HACC initiation resistance.

A qualitative analysis of the load-deflection curves (see Figure 83 in Section 5.3.2) showed that upon loading, the Young's modulus and yield strength of the hydrogen pre-charged specimen were lower. This implicates that hydrogen caused a notable decrease of both properties, indicated by the lower gradient of the slope in the linear part of the load-deflection curve and the earlier deviation from linear behaviour. In general, a decrease of the yield strength is associated with an increase of the fracture toughness since plastic deformations can occur more easily, as discussed previously. However, the presence of hydrogen seems to abolish this fundamental relationship, as fracture occurred in the hydrogen charged specimen at significantly lower loads, despite the lower yield strength.

This phenomenon can be evaluated by employing different theoretical models, developed to explain the fundamental mechanisms of hydrogen embrittlement. The HELP model provides a rational explanation for the simultaneous decrease of the yield strength and fracture resistance (Beachem 1972; Birnbaum & Sofronis 1994). This model postulates a hydrogen enhanced dislocation mobility, which in turn may promote microscopic plastic deformation at lower stress levels, leading eventually to fracture. Also, the AIDE model suggests that the hydrogen induced weakening of the inter-atomic bonds at the crack tip facilitates the injection of dislocations, which leads to an extensive dislocation activity at the vicinity of the crack tip and therefore results in a reduction of both, the localised yield strength and the fracture resistance (Lynch 1989). The observed decrease of the Young's modulus is also consistent with most of the data in the literature (Homrossukon, Mostovoy & Todd 2009; Ortiz & Ovejero-Garcia 1992; Psiachos, Hammerschmidt & Drautz 2011) and was attributed to a reduction of the cohesive energy of the iron lattice (Ortiz & Ovejero-Garcia 1992).

At an applied load above 10 mN, the load deflection curves of the uncharged and charged specimens demonstrated non-linear behaviour (see Figure 83 in Section 5.3.2), which indicates that in conjunction with the small specimen size, the plastic zone in the vicinity of the crack tip was significant. In this case non-linear fracture mechanics parameters, such as J-integral or crack opening displacement are more appropriate for the characterisation of stress state near the crack tip. However, in the current study, the stress intensity factor was employed as a measure of the intensity of the stress/strain field ahead of the notch tip to allow a comparison with corresponding values obtained from conventional (macroscopic) tests on the bulk material.

From the conducted experiments it was not possible to identify precisely the value for the threshold stress intensity factor K_{th}. However, it can be stated that for localised regions of acicular ferrite in weld metal the threshold value ranges between 1.56 MPa $m^{1/2}$ and 4.36 MPa $m^{1/2}$, as illustrated in Figure 94.

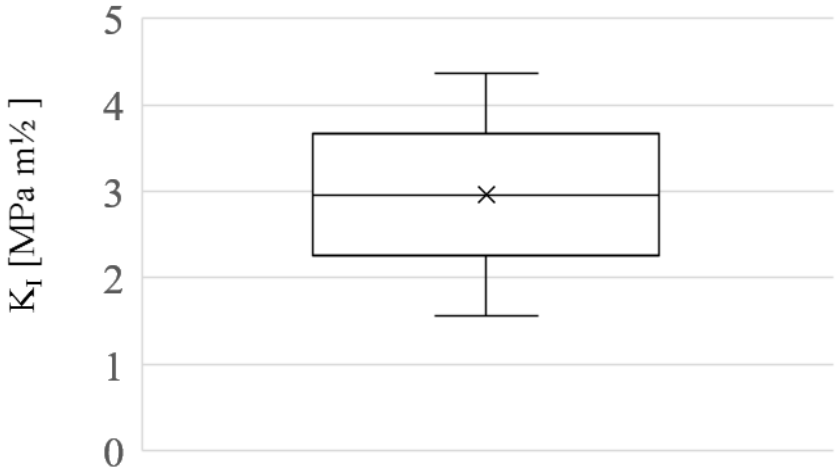

Figure 94: Diagram illustrates the range for the threshold stress intensity factor K_{th} to initiate HACC in a microscopic region of acicular ferrite with a hydrogen concentration of 0.132 ppm.

The identified range is significantly below the typical values for K_{th} of low and medium carbon steels. Indeed, the threshold stress intensity for API X70 pipeline steel welded joint, charged with a similar concentration of hydrogen, was reported to be around 147 MPa $m^{1/2}$ (Olden, Alvaro & Akselsen 2012). In medium and low carbon steels with yield strengths close to that measured for acicular ferrite in the examined region (see Section 5.1.3), the K_{th} ranged between 37 MPa $m^{1/2}$ and 88 MPa $m^{1/2}$ (Gerberich & Chen 1973 Guang-Hua, 1997 #616; Homrossukon, Mostovoy & Todd 2009; Loginow & Phelps 1975). However, it should be considered that all these observations were based on the results of tests conducted on the bulk material rather than on isolated microstructural regions, where the specimen size may play a crucial role. Hence, it was not possible to directly verify the results.

Since dissolved monoatomic hydrogen occupies a specific volume within interstitial lattice sites, it tends to migrate from compressed to expanded regions within the crystal lattice until an equilibrium concentration profile is established (Kirchheim 2004). Hydrostatic tensile stresses are hence a driving force for interstitial lattice diffusion of hydrogen towards the dilatation zone, which is located at the notch (crack) tip, where hydrogen may accumulate and

thereby incrementally degrade the localised fracture resistance of the microstructure (Bernstein 1970). A sufficient hydrogen concentration for failure formation may thus only occur periodically, in highly localised regions, explaining the slow crack growth rate. In these microscopic regions, failure may then occur either due to the formation of micro-voids (Beachem 1972; Birnbaum & Sofronis 1994; Lynch 1989), or due to the formation of miniscule cracks (Oriani, R.A. 1972; Troiano 1960). In both cases the crack would propagate gradually due to ductile tearing if the remaining ligaments are too weak to accommodate the stresses. The crack growth rate was measured to be several orders of magnitudes lower than typically obtained from macroscopic test, conducted on the bulk material. Indeed, the lower bound values of subcritical crack growth near the threshold level were reported at around 10^{-9} m s^{-1} (Homrossukon, Mostovoy & Todd 2009; Loginow & Phelps 1975), and for the current test the crack growth rate averaged over 12 hours was as low as 3.59×10^{-11} m s^{-1}.

CHAPTER 7

CONCLUSIONS AND FUTURE WORK

7 Conclusions and Future Work

7.1 Conclusions

7.1.1 Relationship between the Microstructure and Mechanical Properties of Acicular Ferrite and Upper Bainite in Weld Metal

i. Advanced characterisation and micro-mechanical testing techniques were employed to evaluate the fundamental link between the microstructure and mechanical properties of acicular ferrite and upper bainite in weld metal,

ii. For both microstructures, semi-empirical models were utilised to determine the individual contributions of the theoretical yield strength's intrinsic components. The analysis of the data revealed that, from a microstructural point of view, the size of the grains in acicular ferrite and of the laths in upper bainite, caused the most significant contributions to the yield strength. The close correlation between the theoretical and experimental yield strengths verified the validity of the models,

iii. Besides the yield strength, the grain/lath size has also an impact on other mechanical properties. It is well established that, as the grain/lath size becomes smaller both, yield strength and hardness increase, while the strain hardening exponent decreases. However, the results obtained from nanoindentation tests showed that, the yield strength, hardness and strain hardening exponent of acicular ferrite was notably higher than of upper bainite, although the grain/lath sizes were quite similar. This is mainly because the strengthening mechanisms were different for both microstructures and the corresponding strengthening contributions depended not only on the size of the grains/laths but also on their aspect ratio. The different yield strengths also implied

different hardness values for acicular ferrite and upper bainite, since both properties are usually proportional. The higher strain hardening exponent of acicular ferrite was presumably due to higher proportion of HAGB's which have encouraged dislocation pile up, while the fine slip planes of upper bainite prevented dislocation pile up. The nanoindentation tests additionally showed that the difference between the values for the Young's modulus of both microstructures was negligible and within the measurement error,

iv. Micro-fracture tests, conducted in acicular ferrite and upper bainite, indicated elastic-plastic deformation behaviour for both microstructures and that the yield strength of acicular ferrite was higher than of upper bainite, while the values for the Young's modulus seemed to be quite similar. All these observations were consistent with the results obtained from the nano-indentation tests in these regions.

v. Both microstructures showed ductile fracture behaviour, where the fracture propagation in acicular was characterised by the formation and coalescence of micro-voids, while in upper bainite fracture was accompanied by homogeneous deformations, since the width of the ferrite laths was too small to allow the formation of dislocation pile ups that were able to give rise to localised slip,

vi. The small specimen dimensions restricted the application of both linear and non-linear approaches of fracture mechanics. The conditional values of the critical stress intensity factors, K_Q, were obtained based on LEFM, which can be considered as a lower bound of the actual fracture toughness. A plastic hinge model was employed to evaluate the CTOD's and the corresponding values for the fracture toughness of acicular ferrite and upper bainite. The results indicated that the fracture toughness of acicular ferrite was slightly lower than of upper bainite. However, both values were well below the usually reported values for the fracture toughness of ferrous alloys at corresponding room

temperatures. The difference between the fracture toughness at the smallest microstructural-scales and in the bulk material could be due to many reasons, which are still not completely understood, such as the confinement of plastic deformations in small-scale specimens.

vii. It is well known that plastic deformation is the major energy absorption mechanism during ductile fracture. Furthermore, the proportion of plastic deformations decreases as the yield strength and hardness increase The evaluation of the elastic and plastic components of the CTOD's, showed that the proportion of plastic deformations during fracture was lower in acicular ferrite than in upper bainite. This finding correlates well with the observation that acicular ferrite had a higher strength and hardness but a lower fracture toughness than upper bainite;

7.1.2 Relationship between the Microstructure, Mechanical Properties and HACC Propagation Resistance of Acicular Ferrite and Upper Bainite in Weld Metal

i. For weld metal, where diverse microstructural constituents coexist and interact, an increasing strength (or hardness) and decreasing toughness often indicate an increase of the HACC susceptibility. However, uncertainty remains if such a correlation also exists at the micro-scale, for the weld metals individual microstructural constituents,

ii. EBSD observations combined with the concept of the UCP were used to evaluate the HACC propagation resistance of acicular ferrite and upper bainite as well as to identify the microstructural features with the most significant contributions,

iii. The investigations showed that HACC propagates along a path of least resistance through the surrounding microstructure, where the UCP was significantly shorter for

acicular ferrite than for upper bainite, thereby implying more frequent changes in direction and thus increased dissipation of energy from the crack driving force. These results strongly suggest that acicular ferrite, possessing fine interlocking grains and HABG's, increases the localised resistance to HACC propagation more than upper bainite, despite higher strength, hardness and lower fracture toughness. The main reason for this discrepancy is that the dissipation of energy during ductile fracture occurred mainly due to plastic deformations and in the case of HACC due to the impediment of brittle, cleavage-like crack propagation at HAGB's,

iv. The results suggest that mechanical properties per se are not a good indicator of absolute HACC susceptibility and in fact may be misleading in terms of the intrinsic susceptibility of particular microstructural constituents, which rather depends on microstructural aspects than on the localised mechanical properties;

7.1.3 Relationship between the Microstructure, Mechanical Properties and HACC Initiation Resistance of Acicular Ferrite in Weld Metal

i. Micro-fracture tests were conducted at different loads on a hydrogen charged specimen, fabricated into a selected region of acicular ferrite. The main purpose of these tests was to determine the range for the threshold stress intensity factor K_{th} to initiate HACC,

ii. The obtained range for the threshold stress intensity factor of acicular ferrite was well below the threshold values for weld metal as well as low and medium carbon steels with similar yield strengths. This indicates that, at the micro-scale, hydrogen cracks can grow at stress intensity factors well below the threshold values measured with conventional tests at the macro-scale. It seems that critical fracture toughening mechanisms may not be activated if the specimen dimensions are very small. These may include roughness

or plasticity induced closure, which cannot be developed in micro-samples due to the limited crack growth length,

iii. The crack growth rate in acicular ferrite, also appeared to be significantly lower than for the bulk material,

iv. Besides the "macroscopic" plastic deformations during fracture and the threshold stress intensity to initiate fracture, the yield strength and the Young's modulus also decreased due to the presence of hydrogen, which correlates well with previous observations and proposed HE models;

v. This study was limited to acicular ferrite, as the main purpose was to demonstrate the possibility of site-specific HACC fracture tests in particular microstructural constituents of weld metal. The comparison of HACC initiation resistance of different microstructural constituents was beyond the scope of the current work;

7.2 Future Work

i. The experimental approach presented in this thesis can be applied to different microstructural constituents in weld metal to gain more insight on the relationship between microstructure, mechanical properties and HACC susceptibility,

ii. These studies will contribute to a better understanding of the microstructural factors that control the mechanical properties and HACC susceptibility at the smallest microstructural scales. Such insight will help to design more HACC resistant materials with superior mechanical properties, by avoiding detrimental microstructural constituents and promoting beneficial ones;

8 References

Akhurst, KN & Baker, TJ 1981, 'The threshold stress intensity for hydrogen-induced crack growth', *METALLURGICAL TRANSACTIONS A*, vol. 12, no. 6, pp. 1059-1070.

Alam, N, Li, H, Chen, L, Dunne, D, Feng, B, Squires, I & Barbaro, FJ 1996, 'Fracture-microstructure relationships of hydrogen assisted cracking in steel weldments', *Materials Research 96.*, vol. 3, pp. 74-78.

Albrecht, J, Thompson, AW & Bernstein, IM 1979, 'The role of microstructure in hydrogen-assisted fracture of 7075 aluminum', *METALLURGICAL TRANSACTIONS A*, vol. 10, no. 11, pp. 1759-1766.

Alipooramirabad, H, Ghomashchi, R, Paradowska, A & Reid, M 2016, 'Residual stress-microstructure-mechanical property interrelationships in multipass HSLA steel welds', Journal of Materials Processing Technology, vol. 231, pp. 456-467.

Armstrong, DEJ, Wilkinson, AJ & Roberts, SG 2009, 'Measuring anisotropy in Young's modulus of copper using microcantilever testing', *Journal of Materials Research*, vol. 24, no. 11, pp. 3268-3276.

Asano, S & Otsuka, R 1976, 'The lattice hardening due to dissolved hydrogen in iron and steel', *Scripta Metallurgica*, vol. 10, no. 11, 11//, pp. 1015-1020.

Ast, J, Przybilla, T, Maier, V, Durst, K & Göken, M 2014, 'Microcantilever bending experiments in NiAl – Evaluation, size effects, and crack tip plasticity', *Journal of Materials Research*, vol. 29, no. 18, pp. 2129-2140.

ASTM 1981, *Standard Test Method for JIc, a Measure of Fracture Toughness,* (E-813-81), ASTM International, West Conshohocken, .

ASTM 1987, *Standard test method for determining JR curves, American Society for Testing and Materials, Philadelphia,* (E 1152-87), ASTM International.

ASTM 1999, *Standard test method for determining a threshold stress intensity factor for environment-assisted cracking of metallic materials,* (E1681-99), ASTM International, West Conshohocken.

ASTM 2009, *Standard test method for linear-elastic plane-strain fracture toughness KIc of metallic materials,* (E-399), ASTM International.

ASTM 2013, *Standard Test Method for Measurement of Fracture Toughness,* (E-1820), ASTM International.

Barbaro, FJ 1999, 'Types of hydrogen cracking in pipeline girth welds', paper presented at WTIA/APIA/CRC-WS International Conference on Weld Metal Cracking in Pipeline Girth Welds, Wollongong, NSW, Australia.

Barbaro, FJ, Bowie, GF & Holmes, W 2002, 'Welding the First ERW X80 Grade Pipeline', *International Conference on Pipeline Construction Technology,* Wollongong, NSW, Australia.

Barnoush, A & Vehoff, H 2010, 'Recent developments in the study of hydrogen embrittlement: Hydrogen effect on dislocation nucleation', *Acta Materialia*, vol. 58, no. 16, pp. 5274-5285.

Beachem, CD 1972, 'A new model for hydrogen-assisted cracking (hydrogen "embrittlement")', *Metallurgical Transactions*, vol. 3, no. 2, 1972/02/01, pp. 441-455.

Beachem, CD & Pelloux, RMN 1965, 'Electron fractography—a tool for the study of micromechanisms of fracturing processes', *Fracture toughness testing and its applications, ASTM STP*, vol. 381, p. 210.

Benninghoven, A, Rüdenauer, FG & Werner, HW 1987, *Secondary Ion Mass Spectrometry: Basic Concepts, Instrumental Aspects, Applications, and Trends*, J. Wiley.

Berkovich, ES 1951, 'Three-faceted diamond pyramid for micro-hardness testing', *Ind. Diamond Rev*, vol. 11, no. 127, pp. 129-133.

Bernstein, IM 1970, 'The role of hydrogen in the embrittlement of iron and steel', *Materials Science and Engineering*, vol. 6, no. 1, pp. 1-19.

Bhadeshia, HKDH 1997, 'Models for the elementary mechanical properties of steel welds', *BOOK-INSTITUTE OF MATERIALS*, vol. 650, pp. 229-284.

Bhadeshia, HKDH 2001, *Bainite in Steels : transformations, microstructure and properties*, 2nd edn, London : IOM Communications

Bhadeshia, HKDH & Honeycombe, R 2011, *Steels Microstructure and Properties*, Butterworth-Heinemann.

Birnbaum, HK & Sofronis, P 1994, 'Hydrogen-enhanced localized plasticity--a mechanism for hydrogen-related fracture', *Materials Science and Engineering: A*, vol. 176, no. 1-2, pp. 191-202.

Brandes, EA & Brook, GB 1992, *Smithells Metals Reference Book*, 7 edn, Butterworth-Heinemann, Oxford.

Brandon, DG 1966, 'The structure of high-angle grain boundaries', *Acta Metallurgica*, vol. 14, no. 11, 11//, pp. 1479-1484.

British Standards Institution 1972, *Methos for Crack Opening Displacement (COD) testing,* (DD19), London.

Broekaert, JAC 2003, 'Optical Emission Spectrometry with Glow Discharges', *Glow Discharge Plasmas in Analytical Spectroscopy*, John Wiley & Sons, Ltd, pp. 15-69.

Brozzo, P, Buzzichelli G., Mascanzonii, A & Mirabile, A 1977, 'Microstructure and cleavage resistance of low-carbon bainitic steels', *Met. Sci.,*, pp. 122-129.

Burdekin, FM & Stone, DEW 1966, 'The crack opening displacement approach to fracture mechanics in yielding materials', *The Journal of Strain Analysis for Engineering Design*, vol. 1, no. 2, pp. 145-153.

Burgers, JM 1939, *Some considerations on the fields of stress connected with dislocations in a regular crystal lattice. I*, Koninklijke Nederlandse Akademie van Wetenschappen.

Cain, WM & Troiano, AR 1965, 'Steel structure and hydrogen embrittlement', *Petroleum Engineer*, vol. 37, no. 5, pp. 78-82.

Cannon, B 2009, *WIC Test*, Bluescope Steel.

Capelle, J, Dmytrakh, I, Azari, Z & Pluvinage, G 2013, 'Evaluation of electrochemical hydrogen absorption in welded pipe with steel API X52', *International Journal of Hydrogen Energy*, vol. 38, no. 33, 11/4/, pp. 14356-14363.

Chandler, H 1999, *Hardness testing*, ASM international.

Chen, C., Thompson, A.W. & Bernstein, I.M. 1980, 'The correlation of microstructure and stress corrosion fracture of HY-130 steel weldments', *METALLURGICAL TRANSACTIONS A*, vol. 11, no. 10, pp. 1723-1730.

Coates, DG 1967, 'Kikuchi-like reflection patterns obtained with the scanning electron microscope', *Philosophical Magazine*, vol. 16, no. 144, 1967/12/01, pp. 1179-1184.

Cotterell, B 2002, 'The past, present, and future of fracture mechanics', *Engineering Fracture Mechanics*, vol. 69, no. 5, pp. 533-553.

Cuadrado, N, Casellas, D, Anglada, M & Jiménez-Piqué, E 2012, 'Evaluation of fracture toughness of small volumes by means of cube-corner nanoindentation', *Scripta Materialia*, vol. 66, no. 9, 5//, pp. 670-673.

Daigne, J, Guttmann, M & Naylor, JP 1982, 'The influence of lath boundaries and carbide distribution on the yield strength of 0.4% C tempered martensitic steels', *Materials Science and Engineering*, vol. 56, no. 1, 10//, pp. 1-10.

Dao, M, Chollacoop, N, Van Vliet, KJ, Venkatesh, TA & Suresh, S 2001, 'Computational modeling of the forward and reverse problems in instrumented sharp indentation', *Acta Materialia*, vol. 49, no. 19, 11/14/, pp. 3899-3918.

Darken, LS & Smith, RP 1949, 'Behaviour of hydrogen in steel during and after immersion in acid', *Corrosion*, vol. 5, p. 1.

Davidson, JL, Lynch, SP & Majumdar, A 1997, 'The relationship between hydrogen-induced cracking resistance, microstructure and toughness in high strength weld metal', Published by the Organising Committee of the Joint Seminar on behalf of Defence Science and Technology Association and Welding Technology Institute of Australia.

Davidson, MW & Abramowitz, M 2002, 'Optical Microscopy', *Encyclopedia of Imaging Science and Technology*, John Wiley & Sons, Inc.

Di Maio, D & Roberts, SG 2005, 'Measuring fracture toughness of coatings using focused-ion-beam-machined microbeams', *Journal of Materials Research*, vol. 20, no. 02, pp. 299-302.

Díaz-Fuentes, M, Iza-Mendia, A & Gutiérrez, I 2003, 'Analysis of different acicular ferrite microstructures in low-carbon steels by electron backscattered diffraction. Study of their toughness behavior', *Metallurgical and Materials Transactions A*, vol. 34, no. 11, 2003/11/01, pp. 2505-2516.

Dohmen, R & Milke, R 2010, 'Diffusion in Polycrystalline Materials: Grain Boundaries, Mathematical Models, and Experimental Data', *Reviews in Mineralogy and Geochemistry*, vol. 72, no. 1, pp. 921-970.

Dolby, RE 1986, 'Guidelines for the classification of ferritic steel weld metal microstructural constituents using the light microscope', *Welding in the World*, vol. 24, no. 7, pp. 144-148.

Druce, SG & Eyre, BL 1979, 'A critical assessment of elasto-plastic fracture mechanics', *Journal of Nuclear Materials*, vol. 80, no. 1, 1979/03/01, pp. 1-12.

Dugdale, DS 1960, 'Yielding of steel sheets containing slits', *Journal of the Mechanics and Physics of Solids*, vol. 8, no. 2, pp. 100-104.

EDAX 2007, 'OIM™ Analysis 5.2 manual'.

Edmonds, DV & Cochrane, RC 1990, 'Structure-property relationships in bainitic steels', *METALLURGICAL TRANSACTIONS A*, vol. 21, no. 6, 1990/06/01, pp. 1527-1540.

Ernst, HA, Paris, PC & Landes, JD 1981, 'Estimations on J-integral and tearing modulus T from a single specimen test record', *Fracture mechanics*, ASTM International.

Evans, AG & Charles, EA 1976, 'Fracture Toughness Determinations by Indentation', *Journal of the American Ceramic Society*, vol. 59, no. 7-8, pp. 371-372.

Fan, Z, Mingzhi, H & Deke, S 1989, 'The relationship between the strain-hardening exponent n and the microstructure of metals', *Materials Science and Engineering: A*, vol. 122, no. 2, 1989/12/20, pp. 211-213.

Farrar, RA & Harrison, PL 1987, 'Acicular ferrite in carbon-manganese weld metals: An overview', *Journal of Materials Science*, vol. 22, no. 11, pp. 3812-3820.

Ferreira, PJ, Robertson, IM & Birnbaum, HK 1998, 'Hydrogen effects on the interaction between dislocations', *Acta Materialia*, vol. 46, no. 5, pp. 1749-1757.

Fischer-Cripps, AC 2011, *Nanoindentation*, Springer New York.

Fletcher, L 1999, 'Weld Metal Cracking in Pipeline Girth Welds', *WTIA/APIA/CRC-WS International Conference,* n.p., Wollongong.

Fletcher, L & Yurioka, N 2000, 'A holistic model of hydrogen cracking in pipeline girth welding', *WELDING IN THE WORLD -LONDON-*, vol. 44, pp. 23-30.

Frazer, D, Abad, M, Back, C, Deck, C & Hosemann, P 2014, *Multi-scale characterization of SiC SiC composite materials*, vol. 173, John Wiley & Sons, Inc., Hoboken, NJ.

Gangloff, RP 2003, 'Hydrogen-assisted Cracking', *Comprehensive Structural Integrity*, Pergamon, Oxford, pp. 31-101.

Gerberich, WW & Chen, S 1988, 'Environment-induced cracking of metals', in RP Gangloff & MB Ives (eds), *EICM* pp. 167-186.

Gerberich, WW & Chen, YT 1973, 'A threshold stress intensity concept for environmental cracking', *International Journal of Fracture*, vol. 9, no. 3, pp. 369-371.

Gerberich, WW, L1vne, T, Chen, XF & Kaczorowski, M 1988, 'Crack growth from internal hydrogen—temperature and microstructural effects in 4340 steel', *METALLURGICAL TRANSACTIONS A*, vol. 19, no. 5, pp. 1319-1334.

Gerberich, WW, Oriani, RA, Lji, MJ, Chen, X & Foecke, T 1991, 'The necessity of both plasticity and brittleness in the fracture thresholds of iron', *Philosophical Magazine A*, vol. 63, no. 2, 1991/02/01, pp. 363-376.

Giannuzzi, LA, Prenitzer, B & Kempshall, BW 2005, 'Ion - Solid Interactions', in L Giannuzzi & F Stevie (eds), *Introduction to Focused Ion Beams*, Springer US, pp. 13-52.

Gianola, DS, Sedlmayr, A, Mönig, R, Volkert, CA, Major, RC, Cyrankowski, E, Asif, SAS, Warren, OL & Kraft, O 2011, 'In situ nanomechanical testing in focused ion beam and scanning electron microscopes', *Review of Scientific Instruments*, vol. 82, no. 6.

Gleiter, H 1971, 'The structure and properties of high-angle grain boundaries in metals', *physica status solidi (b)*, vol. 45, no. 1, pp. 9-38.

Goldstein, J, Newbury, DE, Joy, DC, Lyman, CE, Echlin, P, Lifshin, E, Sawyer, L & Michael, JR 2013, *Scanning Electron Microscopy and X-ray Microanalysis: Third Edition*, Springer US.

Grassl, K, Thompson, SW & Krauss, G 1989, *New options for steel selection for automotive applications*, no. 0148-7191, SAE Technical Paper.

Greer, JR & De Hosson, JTM 2011, 'Plasticity in small-sized metallic systems: Intrinsic versus extrinsic size effect', *Progress in Materials Science*, vol. 56, no. 6, 8//, pp. 654-724.

Griffith, AA 1921, 'The phenomena of rupture and flow in solids', *Philosophical transactions of the royal society of london. Series A, containing papers of a mathematical or physical character*, vol. 221, pp. 163-198.

Grimm, W 1968, 'Eine neue glimmentladungslampe für die optische emissionsspektralanalyse', *Spectrochimica Acta Part B: Atomic Spectroscopy*, vol. 23, no. 7, 1968/06/01, pp. 443-454.

Gubeljak, N, Legat, J & Kocak, M 2002, 'Effect of fracture path on the toughness of weld metal', *International Journal of Fracture*, vol. 115, no. 4, 2002/06/01, pp. 343-359.

Hall, EO 1951, 'The Deformation and Ageing of Mild Steel: III Discussion of Results', *Proceedings of the Physical Society. Section B*, vol. 64, no. 9, p. 747.

Hart, PHM & Watkinson, E 1975, 'Weld metal implant test ranks Cr-Mo hydrogen cracking resistance', *Welding Journal*, vol. 54, pp. 288s-295s.

Homrossukon, S, Mostovoy, S & Todd, JA 2009, 'Investigation of hydrogen assisted cracking in high and low strength steels', *Journal of Pressure Vessel Technology*, vol. 131, no. 4, p. 041405.

IIW 1988, *Guide to the light microscope examination of ferritic steel weld metals*, International Institute of Welding, IIW Doc. IX-1533-88.

Irwin, GR 1948, 'Fracture dynamics, Fracturing of Metals. American Society of Metals', Cleveland.

Irwin, GR 1957, 'Analysis of stresses and strains near the end of a crack traversing a plate', *Spie Milestone series MS*, vol. 137, no. 167-170, p. 16.

Irwin, GR 1958, 'Encyclopedia of physics', *VI, Springer-Verlag, Heidelberg*.

Jaya, BN, Kirchlechner, C & Dehm, G 2015, 'Can microscale fracture tests provide reliable fracture toughness values? A case study in silicon', *Journal of Materials Research*, vol. 30, no. 05, pp. 686-698.

Johnson, HH & Troiano, AR 1957, 'Crack Initiation in Hydrogenated Steel', *Nature*, vol. 179, no. 4563, pp. 777-777.

Johnson W.H. 1875, 'On Some Remarkable Changes Produced in Iron and Steel by the Action of Hydrogen and Acids', *Nature (London)*, vol. 11, no. 281.

Kamikawa, N, Sato, K, Miyamoto, G, Murayama, M, Sekido, N, Tsuzaki, K & Furuhara, T 2015, 'Stress–strain behavior of ferrite and bainite with nano-precipitation in low carbon steels', *Acta Materialia*, vol. 83, 1/15/, pp. 383-396.

Kane, RD 2000, *Environmentally Assisted Cracking: Predictive Methods for Risk Assessment and Evaluation of Materials, Equipment, and Structures*, vol. 1401, ASTM International.

Katz, Y, Tymiak, N & Gerberich, WW 2001, 'Nanomechanical probes as new approaches to hydrogen/deformation interaction studies', *Engineering Fracture Mechanics*, vol. 68, no. 6, 4//, pp. 619-646.

Kiener, D, Motz, C, Dehm, G & Pippan, R 2009, 'Overview on established and novel FIB based miniaturized mechanical testing using in-situ SEM', *International Journal of Materials Research*, vol. 100, no. 8, 2009/08/01, pp. 1074-1087.

Kies, JA & Smith, HL 1955, 'Toughness testing of hot-stretched acrylics', *Proc Aircraft Industries Association and Air Development Command Joint Conference, Dayton, OH*.

Kikuchi, S & Nishikawa, S 1928, 'Diffraction of Cathode Rays by Mica', *Japanese Journal of Physics*, vol. 5, no. 2, pp. 83-96.

Kirchheim, R 2004, 'Solid solutions of hydrogen in complex materials', *Solid State Physics*, vol. Volume 59, Academic Press, pp. 203-291.

Kirchheim, R 2010, 'Revisiting hydrogen embrittlement models and hydrogen-induced homogeneous nucleation of dislocations', *Scripta Materialia*, vol. 62, no. 2, 1//, pp. 67-70.

Knoop, F, Peters, CG & Emerson, WB 1939, 'A sensitive pyramidal-diamond tool for indentation measurements', *Journal of Research of the National Bureau of standards*, vol. 23, no. 1, pp. 39-61.

Kolednik, O 1992, 'Loading conditions may influence the shape of J-δa curves', *Engineering Fracture Mechanics*, vol. 41, no. 2, 1//, pp. 251-255.

Kronberg, ML & Wilson, FH 1949, 'Secondary recrystallization in copper', *AIME TRANS*, vol. 185, pp. 501-514.

Kudrjumov, G & Sachs, G 1930, 'The mechanism of hardening of steel', *Zeitschrift für Physik*, no. 64, pp. 325-343.

Kurji, RN & Coniglio, N 2015, 'Towards the establishment of weldability test standards for hydrogen-assisted cold cracking', *The International Journal of Advanced Manufacturing Technology*, vol. 77, no. 9-12, pp. 1581-1597.

Kurji, RN, Griggs, J, Linton, V, Barbaro, F, Kotousov, A, Gamboa, E, Ghomashchi, R & Coniglio, N 2013, 'An improved Welditg Institute of Canada test for evaluation of high-strength pipeline steel weldability', paper presented at 6th International Pipeline Conference, Thermae Palace Hotel, Ostend, Belgium.

Kuzmikova, L, Barbaro, FJ, Norrish, J & Huijun, I 2012, 'Weld metal hydrogen assisted cold cracking in high strength low alloy steels', paper presented at SEAISI Conference & Exhibition, Bali, Indonesia.

Lalam, SH, Bhadeshia, HKDH & MacKay, DJC 2000a, 'Estimation of mechanical properties of ferritic steel welds. Part 1: Yield and tensile strength', *Science and Technology of Welding & Joining*, vol. 5, no. 3, pp. 135-147.

Lalam, SH, Bhadeshia, HKDH & MacKay, DJC 2000b, 'Estimation of mechanical properties of ferritic steel welds. Part 2: Elongation and Charpy toughness', *Science and Technology of Welding & Joining*, vol. 5, no. 3, pp. 149-160.

Langford, G & Cohen, M 1969, 'Strain hardening of iron by severe plastic deformation', *ASM Trans Quart*, vol. 62, no. 3, pp. 623-638.

Lehrer, C, Frey, L, Petersen, S & Ryssel, H 2001, 'Limitations of focused ion beam nanomachining', *Journal of Vacuum Science and Technology B*, vol. 19, no. 6, pp. 2533-2538.

Lejček, P 2010, 'Grain Boundaries: Description, Structure and Thermodynamics', *Grain Boundary Segregation in Metals*, vol. 136, Springer Berlin Heidelberg, pp. 5-24.

Lessar, JF & Gerberich, WW 1976, 'Grain Size Effects in Hydrogen-Assisted Cracking', *METALLURGICAL TRANSACTIONS A*, vol. 7, no. 7, 1976/07/01, pp. 953-960.

Li, JCM, Oriani, RA & Darken, LS 1966, 'The Thermodynamics of Stressed Solids', *Zeitschrift für Physikalische Chemie*, vol. 49, no. 3_5, 1966/05/01, pp. 271-290.

Loginow, AW & Phelps, EH 1975, 'Steels for Seamless Hydrogen Pressure Vessels', *Corrosion*, vol. 31, no. 11, pp. 404-412.

Lugstein, A, Basnar, B, Hobler, G & Bertagnolli, E 2002, 'Current density profile extraction of focused ion beams based on atomic force microscopy contour profiling of nanodots', *Journal of Applied Physics*, vol. 92, no. 7, pp. 4037-4042.

Lynch, SP 1979, 'Mechanisms of hydrogen-assisted cracking', *Met. Forum*, vol. 2, pp. 189-200.

Lynch, SP 1988, 'Environmentally assisted cracking: Overview of evidence for an adsorption-induced localised-slip process', *Acta Metallurgica*, vol. 36, no. 10, 10//, pp. 2639-2661.

Lynch, SP 1989, 'Metallographic contributions to understanding mechanisms of environmentally assisted cracking', *Metallography*, vol. 23, no. 2, pp. 147-171.

Lynch, SP 2008, 'Towards understanding mechanisms and kinetics of environmentally assisted cracking', in Shipilov, Jones & Olive (eds), *Environment-Induced Cracking of Materials*, Elsevier, Amsterdam, pp. 167-177.

Lynch, SP 2011, 'Interpreting hydrogen-induced fracture surfaces in terms of deformation processes: A new approach', *Scripta Materialia*, vol. 65, no. 10, pp. 851-854.

Maitland, T & Sitzman, S 2007, *Electron backscatter diffraction (EBSD) technique and materials characterization examples*, vol. 14, Springer Berlin.

Makara, AM, Gordonny, VG, Dibets, AT, Grabin, VF & Denisenko, AV 1971, 'Cold transverse cracks in low-alloy high-strength welds', *AVTOMAT SVARKA, NOV. 1971,--11--, 1-4*.

Maroef, I 2002, 'Hydrogen trapping in ferritic steelweldmetal', *International Materials Reviews*, vol. 47, no. 4.

Martin, ML, Fenske, JA, Liu, GS, Sofronis, P & Robertson, IM 2011, 'On the formation and nature of quasi-cleavage fracture surfaces in hydrogen embrittled steels', *Acta Materialia*, vol. 59, no. 4, 2//, pp. 1601-1606.

Martin, ML, Robertson, IM & Sofronis, P 2011, 'Interpreting hydrogen-induced fracture surfaces in terms of deformation processes: A new approach', *Acta Materialia*, vol. 59, no. 9, pp. 3680-3687.

Matsumoto, R, Riku, M, Taketomi, S & Miyazaki, N 2010, 'Hydrogen–Grain Boundary Interaction in Fe, Fe–C, and Fe–N Systems', *Progress in Nuclear Science and Technology*, vol. 2, pp. 9-15.

Mazancová, E, Rucká, Z & Mazanec, K 2007, 'Comparison of microfractographic behaviour of acicular ferrite and bainite and hydrogen cracking resistance', *Arch. Mater Sci*, vol. 28, no. 1-4, pp. 95-99.

McClintock, FA 1968, *International Journal Fracture Mechanics*, vol. 4, no. 101.

Medina, SF, Rancel, L, Gómez, M, Cabrera, JM & Gutierrez, I 2014, 'Microstructural Unit Controlling Cleavage Crack Propagation in High Strength Bainitic Steels', *Key Engineering Materials,* Trans Tech Publ, vol. 622, pp. 846-853.

Messerschmidt, U 2010, *Dislocation dynamics during plastic deformation*, Springer.

Mohs, F 1822, *Grund-Riss der Mineralogie*, Arnold.

Motz, C, Schöberl, T & Pippan, R 2005, 'Mechanical properties of micro-sized copper bending beams machined by the focused ion beam technique', *Acta Materialia*, vol. 53, no. 15, 9//, pp. 4269-4279.

Muirhead, J, Cawley;, J, Strang;, A, English, CA & Titchmarsh, J 2000, 'Quantitative aspects of grain size measurement', *Materials Science and Technology*, vol. 16, no. 10, pp. 1160-1166.

Nagumo, M, Nakamura, M & Takai, K 2001, 'Hydrogen thermal desorption relevant to delayed-fracture susceptibility of high-strength steels', *Metallurgical and Materials Transactions A*, vol. 32, no. 2, pp. 339-347.

Nam, TH, Kim, JG & Choi, YS 2013, 'Electrochemical hydrogen discharge of high-strength low alloy steel for high-pressure gaseous hydrogen storage tank: Effect of discharging temperature', *International Journal of Hydrogen Energy*, vol. 38, no. 2, 1/24/, pp. 999-1003.

Narita, N, Altstetter, CJ & Birnbaum, HK 1982, 'Hydrogen-related phase transformations in austenitic stainless steels', *METALLURGICAL TRANSACTIONS A*, vol. 13, no. 8, 1982/08/01, pp. 1355-1365.

Nastasi, M 1996, *Ion-solid interactions: Fundamentals and applications*, Cambridge University Press.

Naylor, JP 1979, 'The influence of the lath morphology on the yield stress and transition temperature of martensitic- bainitic steels', *METALLURGICAL TRANSACTIONS A*, vol. 10, no. 7, 1979/07/01, pp. 861-873.

Nishiyama, Z 1934, 'X-ray investigation on the mechanism of the transformation from face-centered cubic lattice to body-centered cubic lattice', *Science Report of the Tohoku Imperial University*, no. 23, pp. 637-664.

Nowell, MM, Witt, RA & True, B 2005, 'EBSD Sample Preparation: Techniques, Tips, and Tricks', *Microscopy and Microanalysis*, vol. 11, no. SupplementS02, pp. 504-505.

Olden, V, Alvaro, A & Akselsen, OM 2012, 'Hydrogen diffusion and hydrogen influenced critical stress intensity in an API X70 pipeline steel welded joint – Experiments and FE simulations', *International Journal of Hydrogen Energy*, vol. 37, no. 15, 8//, pp. 11474-11486.

Olson, DLR 1996, 'Hydrogen Managment in Steel', in Davidson & Olson (eds), *Joint Seminar,* WTIA.

Olson, DLR, Maroef, I, Lensing, C, Smith, RD, Wang, WW, Liu, S, Wildeman, T & Eberhart, M 1996, 'Hydrogen management in high strength steel weldments', *Proceedings of the joint seminar, Melbourne,* pp. 1-19.

Oriani, RA 1970, 'The diffusion and trapping of hydrogen in steel', *Acta Metallurgica*, vol. 18, no. 1, pp. 147-157.

Oriani, RA 1972, 'Testing of the decohesion theory of hydrogen induced crack propagation', *Scripta Metallurgica*, vol. 6, pp. 681-688.

Oriani, RA, Hirth, JP & Smialowski, M 1985, 'Hydrogen Degradation of Ferrous Alloys', William Andrew Publishing/Noyes, pp. 271-288,641-685.

Oriani, RA & Josephic, PH 1979, 'Hydrogen-enhanced load relaxation in a deformed medium-carbon steel', *Acta Metallurgica*, vol. 27, no. 6, 6//, pp. 997-1005.

Orloff, J, Swanson, L & Utlaut, M 2003, *High Resolution Focused Ion Beams: FIB and its Applications: Fib and Its Applications: The Physics of Liquid Metal Ion Sources and Ion Optics and Their Application to Focused Ion Beam Technology*, Springer.

Orowan, E 1934, 'Zur kristallplastizität. iii', *Zeitschrift für Physik*, vol. 89, no. 9-10, pp. 634-659.

Orowan, E 1949, 'Fracture and strength of solids', *Reports on progress in physics*, vol. 12, no. 1, p. 185.

Ortiz, M & Ovejero-Garcia, J 1992, 'Effect of hydrogen on Young's modulus of AISI 1005 and 1070 steels', *Journal of Materials Science*, vol. 27, no. 24, pp. 6777-6781.

Petch, NJJ 1953, 'The Cleavage Strength of Polycristals', *The Journal of the Iron and Steel Institute*, vol. 174, pp. 25-28.

Polanyi, M 1934, 'Über eine Art Gitterstörung, die einen Kristall plastisch machen könnte', *Zeitschrift für Physik*, vol. 89, no. 9-10, pp. 660-664.

Ponton, CB & Rawlings, RD 1989, 'Vickers indentation fracture toughness test Part 1 Review of literature and formulation of standardised indentation toughness equations', *Materials Science and Technology*, vol. 5, no. 9, pp. 865-872.

Pressouyre, GM 1980, 'Trap theory of Hydrogen embrittlement', *Acta Metallurgica*, vol. 28, no. 7, pp. 895-911.

Procter, R & Paxton, H 1969, 'Hydrogen Embrittlement of Stainless Steel and carbon steel', *Trans. ASM*, vol. 62, p. 989.

Psiachos, D, Hammerschmidt, T & Drautz, R 2011, 'Ab initio study of the modification of elastic properties of α-iron by hydrostatic strain and by hydrogen interstitials', *Acta Materialia*, vol. 59, no. 11, 6//, pp. 4255-4263.

Pundt, A & Kirchheim, R 2006, 'Hydrogen in metals: microstructural aspects', *Annu. Rev. Mater. Res.*, vol. 36, pp. 555-608.

Randle, V 1996, *The role of the coincidence site lattice in grain boundary engineering*, Institute of Materials London.

Reimer, L 1985, *Scanning Electron Microscopy* Springer-Verlag.

Rice, JR 1968, 'A path independent integral and the approximate analysis of strain concentration by notches and cracks', *Journal of Applied Mechanics*, vol. 35, no. 2, pp. 379-386.

Ricks, RA, Howell, PR & Barritte, GS 1982, 'The nature of acicular ferrite in HSLA steel weld metals', *Journal of Materials Science*, vol. 17, no. 3, 1982/03/01, pp. 732-740.

Ritchie, RO 2011, 'The conflicts between strength and toughness', *Nat Mater*, vol. 10, no. 11, 11//print, pp. 817-822.

Ritchie, RO & Thompson, AW 1985, 'On macroscopic and microscopic analyses for crack initiation and crack growth toughness in ductile alloys', *METALLURGICAL TRANSACTIONS A*, vol. 16, no. 2, pp. 233-248.

Robertson, IM 2001, 'The effect of hydrogen on dislocation dynamics', *Engineering Fracture Mechanics*, vol. 68, no. 6, 4//, pp. 671-692.

Robertson, IM, Birnbaum, HK & Sofronis, P 2009, 'Chapter 91 Hydrogen Effects on Plasticity', in JP Hirth & L Kubin (eds), *Dislocations in Solids*, vol. Volume 15, Elsevier, pp. 249-293.

Robertson, IM, Birnbaum, HK & Sofronis, P 2009, 'Hydrogen Effects on Plasticity', in JP Hirth & L Kubin (eds), *Dislocations in Solids*, vol. Volume 15, Elsevier, pp. 249-293.

Rockwell, HM & Rockwell, SP 1919, *Hardness-tester*, USA.

Rossmanith, HP 1997, 'The struggle for recognition of engineering fracture mechanics', *Fracture research in retrospect. Rotterdam: AA Balkema*, pp. 37-93.

Rotfe, ST & Barsom, JM 1977, 'Fracture and Fatigue Control in Structures', Prentice-Hall, London.

Rowland, HA 1882, 'Preliminary notice of the results accomplished in the manufacture and theory of gratings for optical purposes', *Philosophical Magazine Series 5*, vol. 13, no. 84, pp. 469-474.

Schwartz, AJ, Kumar, M, Adams, BL & Field, DP 2009, *Electron Backscatter Diffraction in Material Science*, 2 edn, Springer Science+Business Media, New York.

Shi, L, Yan, Z, Liu, Y, Zhang, C, Qiao, Z, Ning, B & Li, H 2014, 'Improved toughness and ductility in ferrite/acicular ferrite dual-phase steel through intercritical heat treatment', *Materials Science and Engineering: A*, vol. 590, 1/10/, pp. 7-15.

Sigmund, P 1969, 'Theory of sputtering. I. Sputtering yield of amorphous and polycrystalline targets', *Physical review*, vol. 184, no. 2, p. 383.

Sigmund, P 1981, *Sputtering by ion bombardment theoretical concepts*, Springer.

Smith, RL & Sandly, GE 1922, 'An Accurate Method of Determining the Hardness of Metals, with Particular Reference to Those of a High Degree of Hardness*', *Proceedings of the Institution of Mechanical Engineers*, vol. 102, no. 1, pp. 623-641.

Song, J & Curtin, WA 2013, 'Atomic mechanism and prediction of hydrogen embrittlement in iron', *Nat Mater*, vol. 12, no. 2, 02//print, pp. 145-151.

Sorby, HC 1886, 'On the microscopic structures of iron and study of microscopic structures of steel', *J. Iron and Steel Inst*, vol. 1, p. 140.

Speich, GR & Leslie, WC 1972, 'Tempering of steel', *Metallurgical Transactions*, vol. 3, no. 5, 1972/05/01, pp. 1043-1054.

Tabor, D 1956, 'The physical meaning of indentation and scratch hardness', *British Journal of Applied Physics*, vol. 7, no. 5, p. 159.

Takasawa, K, Wada, Y, Ishigaki, R & Kayano, R 2010, 'Effects of grain size on hydrogen environment embrittlement of high strength low alloy steel in 45 MPa gaseous hydrogen', *Materials transactions*, vol. 51, no. 2, p. 347.

Taylor, GI 1934, 'The mechanism of plastic deformation of crystals. Part I. Theoretical', *Proceedings of the Royal Society of London. Series A, Containing Papers of a Mathematical and Physical Character*, pp. 362-387.

Ternovskii, AP, Alekhin, VP, Shorshorov, MK, Khrushchov, MM & Skvortsov, VN 1974, 'Micromechanical testing of materials by depression', *Zavodskaya Laboratoriya*, vol. 39, no. 10, pp. 1242–1247.

Thewlis, G 2003, 'The Nature of Acicular Ferrite in Ferrous Weld Metals and the Challenges for Microstructure Modelling', *Materials Science Forum,* Trans Tech Publ, vol. 426, pp. 4019-4026.

Thewlis, G 2004, 'Classifcation and quantification of microstructures in steels', *Materials Science and Technology*, vol. 20, pp. 143-160.

Thewlis, G, Whiteman, JA & Senogles, DJ 1997, 'Dynamics of austenite to ferrite phase transformation in ferrous weld metals', *Materials Science and Technology*, vol. 13, no. 3, pp. 257-274.

Troiano, AR 1960, 'The role of hydrogen and other interstitials in the mechanical behaviour of metals', *Trans. ASM.*, vol. 52, pp. 54-80.

Uchic, MD, Dimiduk, DM, Florando, JN & Nix, WD 2004, 'Sample Dimensions Influence Strength and Crystal Plasticity', *Science*, vol. 305, no. 5686, August 13, 2004, pp. 986-989.

Vander Voort, GF 1984, *Metallography, principles and practice*, ASM International.

Vehoff, H 1997, 'Hydrogen Related Material Problems', *Topics in Applied Physics*, vol. 76.

Vehoff, H & Neumann, P 1980, 'Crack propagation and cleavage initiation in Fe-2.6%-Si single crystals under controlled plastic crack tip opening rate in various gaseous environments', *Acta Metallurgica*, vol. 28, no. 3, pp. 265-272.

Vehoff, H & Rothe, W 1983, 'Gaseous hydrogen embrittlement in FeSi- and Ni-single crystals', *Acta Metallurgica*, vol. 31, no. 11, pp. 1781-1793.

Volkert, C & Minor, A 2007, 'Focused ion beam microscopy and micromachining', *MRS bulletin*, vol. 32, no. 05, pp. 389-399.

Wang, W, Shan, Y & Yang, K 2009, 'Study of high strength pipeline steels with different microstructures', *Materials Science and Engineering: A*, vol. 502, no. 1–2, 2/25/, pp. 38-44.

Wang, W, Yan, W, Zhu, L, Hu, P, Shan, Y & Yang, K 2009, 'Relation among rolling parameters, microstructures and mechanical properties in an acicular ferrite pipeline steel', *Materials & Design*, vol. 30, no. 9, 10//, pp. 3436-3443.

Wassermann, G 1935, 'Über den Mechanismus der α-γ Umwandlung des Eisens', *Mitteilungen aus dem Kaiser-Wilhelm-Institut für Eisenforschung*, no. 17, pp. 149-155.

Watanabe, T 1994, 'The impact of grain boundary character distribution on fracture in polycrystals', *Materials Science and Engineering: A*, vol. 176, no. 1, pp. 39-49.

Weaver, RJ & Ogborn, JS 2005, 'Cellulosic-covered electrode storage conditions – influence on weld properties', paper presented at Rio Pipeline 2005, Rio de Janeiro, 2005.

Wells, AA 1961, 'Unstable crack propagation in metals: cleavage and fast fracture', *Proceedings of the crack propagation symposium,* vol. 1.

Whan, RE 1986, *Materials characterization*, eds RE Whan & ASMIH Committee vol. 10, ASM International, Materials Park, OH.

Widgery, DJ 1976, 'Deoxidation practice for mild steel weld metal', *Welding Journal*, vol. 55, no. 3, pp. 57-68.

Wildash, C 1999, 'Microstructure factors affecting hydrogen induced cold cracking in high strength steel weld metal', Ph.D. thesis, University of Leeds.

Wongpanya, P, Boellinghaus, T, Lothongkum, G & Hoffmeister, H 2009, 'Numerical modelling of cold cracking initiation and propagation in S 1100 QL steel root welds', *Welding in the World*, vol. 53, no. 3.

Wright, SI 2000, 'Fundamentals of Automated EBSD', in A Schwartz, M Kumar & B Adams (eds), *Electron Backscatter Diffraction in Materials Science*, Springer US, pp. 51-64.

Wright, SI & Nowell, MM 2006, 'EBSD image quality mapping', *Microscopy and Microanalysis*, vol. 12, no. 01, pp. 72-84.

Wurster, S, Motz, C & Pippan, R 2012, 'Characterization of the fracture toughness of micro-sized tungsten single crystal notched specimens', *Philosophical Magazine*, vol. 92, no. 14, 2012/05/11, pp. 1803-1825.

Yan, M & Weng, Y 2006, 'Study on hydrogen absorption of pipeline steel under cathodic charging', *Corrosion Science*, vol. 48, no. 2, 2//, pp. 432-444.

Yang, JR & Bhadeshia, HKDH 1990, 'The dislocation density of acicular ferrite in steel welds', *Weld. J.(Lond.)*, vol. 8.

Yang, JR, Huang, CY, Huang, CF & Aoh, JN 1993, 'Influence of acicular ferrite and bainite microstructures on toughness for an ultra-low-carbon alloy steel weld metal', *Journal of Materials Science Letters*, vol. 12, no. 16, pp. 1290-1293.

Young, RJ & Moore, MV 2005, 'Dual-Beam (FIB-SEM) Systems', in L Giannuzzi & F Stevie (eds), *Introduction to Focused Ion Beams*, Springer US, pp. 247-268.

Yu, GH, Cheng, YH, Chen, L, Qiao, LJ, Wang, YB & Chu, WY 1997, 'Hydrogen accumulation and hydrogen-induced cracking of API C90 tubular steel', *Corrosion*, vol. 53, no. 10, pp. 762-769.

Yurioka, N & Suzuki, H 1990, 'Hydrogen assisted cracking in C-Mn and low alloy steel weldments', *International Materials Reviews*, vol. 35, no. 1, pp. 217-249.

Zaafarani, N, Raabe, D, Roters, F & Zaefferer, S 2008, 'On the origin of deformation-induced rotation patterns below nanoindents', *Acta Materialia*, vol. 56, no. 1, 1//, pp. 31-42.

Zhang, P, Li, SX & Zhang, ZF 2011, 'General relationship between strength and hardness', *Materials Science and Engineering: A*, vol. 529, 11/25/, pp. 62-73.

Zhao, MC, Yang, K & Shan, YY 2003, 'Comparison on strength and toughness behaviors of microalloyed pipeline steels with acicular ferrite and ultrafine ferrite', *Materials Letters*, vol. 57, no. 9–10, 2//, pp. 1496-1500.

Zhong, Y, Xiao, F, Zhang, J, Shan, Y, Wang, W & Yang, K 2006, 'In situ TEM study of the effect of M/A films at grain boundaries on crack propagation in an ultra-fine acicular ferrite pipeline steel', *Acta Materialia*, vol. 54, no. 2, 1//, pp. 435-443.

Zhou, W, Apkarian, R, Wang, Z & Joy, D 2007, 'Fundamentals of Scanning Electron Microscopy (SEM)', in W Zhou & Z Wang (eds), *Scanning Microscopy for Nanotechnology*, Springer New York, pp. 1-40.

Zhu, XK & Joyce, JA 2012, 'Review of fracture toughness (G, K, J, CTOD, CTOA) testing and standardization', *Engineering Fracture Mechanics*, vol. 85, pp. 1-46.

Ziegler, JF & Biersack, JP 2008, 'SRIM-2008, Stopping Power and Range of Ions in Matter'.

Ziegler, JF, Biersack, JP & Littmark, U 1985, 'The stopping power and range of ions in solids', *Pergamon Press, New York*, vol. 4, pp. 40-47.

APPENDIX

Selected Journal Papers

Materials Science & Engineering A 663 (2016) 193–203

Contents lists available at ScienceDirect

Materials Science & Engineering A

journal homepage: www.elsevier.com/locate/msea

A study on the relationship between microstructure and mechanical properties of acicular ferrite and upper bainite

Walter L. Costin, Olivier Lavigne*, Andrei Kotousov

School of Mechanical Engineering, The University of Adelaide, SA 5005, Australia

ARTICLE INFO

Article history:
Received 19 December 2015
Received in revised form
22 February 2016
Accepted 21 March 2016
Available online 24 March 2016

Keywords:
EBSD
Mechanical characterisation
Nano-indentation
Bainite
Acicular ferrite
Fracture

ABSTRACT

Acicular ferrite and bainite are microstructural constituents commonly found in ferritic weld metal and many other ferrous alloys. These often highly localised microstructural volumes are known to have a significant impact on the mechanical properties of the bulk material they constitute. It is well established that acicular ferrite and bainite have substantially different morphologies and features that can be directly linked to their intrinsic mechanical properties. However, in the bulk material they usually co-exist and interact with other microstructural constituents and features. Therefore, the individual contributions of acicular ferrite and bainite still remain unclear. This work utilises micro-testing techniques to evaluate and compare the mechanical properties of these two micro-constituents with an ultimate objective to understand their impact on bulk properties of ferrous alloys. Microscopic regions consisting of either acicular ferrite or upper bainite were first selected and then characterised using a high resolution Scanning Electron Microscope (SEM) and Electron Backscattered Diffraction (EBSD). Conventional nano-indentation and an advanced characterisation procedure were implemented to evaluate elastic modulus, yield strength, hardness and strain hardening exponent of both micro-constituents. The fracture resistance was estimated from micro-fracture tests that were conducted within the selected regions. The experimental studies have indicated that, at the micro-scale, despite their different microstructures, acicular ferrite and upper bainite have very similar mechanical properties. Nevertheless, the fracture resistance of upper bainite was more dominated by the contribution of plastic deformations.

1. Introduction

The microstructure of many multiphase alloys, in particular of ferritic weld metal, consists of diverse constituents which often only occur in very small material volumes, within the micrometer regime and are characterised by distinctive morphologies and specific features such as the grain size [1,2], the grain boundaries characteristics [3], as well as the presence of second phase particles [4] that govern their intrinsic mechanical properties [5]. Acicular ferrite and upper bainite are common microstructural constituents of many ferrous alloys, including weld metal. Both microstructural constituents are formed within a similar temperature range [4,6] and by the same type of transformation mechanisms [4,7]. However, they are known to have substantially different morphologies and features with specific implications on mechanical properties, such as strength and fracture toughness.

Acicular ferrite is characterised by a chaotic arrangement of fine-grained ferrite plates with different orientations that are separated by high angle grain boundaries, while upper bainite consists of sheaves of parallel ferrite laths (or sub-units) with largely mutual orientations separated by low angle boundaries, where cementite precipitates may decorate the lath boundaries [4,8]. Numerous studies on the integrity of weld metal have demonstrated that both strength [9] and fracture resistance [9,10] could be significantly improved by increasing the volume fraction of acicular ferrite. The increases in strength and toughness were largely associated with the small grain size and the high density of high angle grain boundaries, respectively [4,8,9,11]. Medium and low carbon steels with high contents of acicular ferrite have been developed for automotive, pressure vessel and the pipeline industry [11–13]. These steels have a better strength, fracture toughness, H_2S and fatigue resistance [11,12,14,15] in comparison with steels having a primary ferrite-pearlite microstructure. The yield strength and absorbed impact energy (which can be related to fracture toughness) of ferrous alloys with high contents of acicular ferrite have been reported to be respectively in the range of 480–750 MPa and 140–190 J [8,10–13,16].

There is a general agreement [6] that high strength and good fracture toughness can also be achieved in bainitic steels with

* Corresponding author.
E-mail addresses: Olivier.lavigne@adelaide.edu.au, lavigneolivier@hotmail.com (O. Lavigne).

http://dx.doi.org/10.1016/j.msea.2016.03.103
0921-5093/

extremely low carbon contents. These small concentrations allow to eliminate the inter-lath cementite and thereby enhance the fracture toughness of bainitic steels [10]. For bainitic steels the yield strength and absorbed impact energy has been reported to be respectively in the range 500–1000 MPa and 20–70 J at ambient temperature [10,17]. Therefore, it can be concluded that bainitic steels normally have a higher strength in comparison with steels which consist predominantly of acicular ferrite. However, the fracture resistance of steels with high acicular ferrite contents seems to be superior to the one of bainitic steels.

The considerations above are largely based on the outcomes of testing bulk properties of materials where microscopic regions of acicular ferrite and bainite co-existed and physically interacted with other microstructural constituents. However, not much is currently known regarding the intrinsic mechanical properties of acicular ferrite and bainite at such small scales. This paper aims to fill this gap by conducting a series of micro-mechanical tests. Further, we attempt to establish for both constituents a link between their characteristic microstructural features and mechanical properties.

In a weld metal specimen, microscopic regions consisting of acicular ferrite and upper bainite were firstly selected and then characterised using a high resolution Scanning Electron Microscope (SEM) and Electron Backscattered Diffraction (EBSD). The elasto-plastic properties of the individual microstructural constituents were evaluated with a standard nano-indentation technique utilising an advanced characterisation procedure [18]. This procedure allowed for the evaluation of plastic properties in addition to the traditional characteristics, such as hardness and modulus of elasticity.

With nano-indentation testing, it is also possible to evaluate the fracture toughness if the material is sufficiently brittle [19]. However, this is not the case for acicular ferrite and bainite, which both possess large ductility. The only option left to evaluate the fracture resistance at such small scales is to test miniaturised fracture specimens. For this purpose, a Focused Ion Beam (FIB) was employed to fabricate micro-fracture samples (sharply notched cantilevers) within the selected and previously characterised regions of acicular ferrite and upper bainite. This type of micro-mechanical testing was developed in the past decade to examine the fracture toughness of brittle or semi-brittle materials [20–23] at the micro-scale. In this study, a nano-indenter was used to load the micro-fabricated acicular ferrite and upper bainite specimens. The resulting load displacement curves were recorded and analysed with linear and nonlinear approaches of fracture mechanics.

2. Experimental methods

2.1. Overview of experimental tests

The flow chart in Fig. 1 gives a summary of the experimental approach and the different methods and techniques employed in the current work. These methods and techniques are detailed in the following sections.

2.2. Fabrication and extraction of weld specimen

A weld was deposited with 4 mm diameter E6010 cellulosic electrodes between two bevelled, restraint API 5L grade X70 plates. The welding procedure as well as the specifications are given in detail elsewhere [24]. Abrasive wet cutting was then used to cut the weld into four transverse sections with equal thicknesses. All of the experiments were carried out on the third section in the welding direction. This section was mounted, grinded, polished and etched with 2% Nital to reveal the microstructural details for the following investigations.

2.3. Selection of microstructural constituents

Representative regions consisting of either acicular ferrite or upper bainite were identified with an Optical Microscope (OM) and a high resolution Scanning Electron Microscope (SEM). As shown in (Fig. 2a and b), acicular ferrite region was identified by a random arrangement of fine-grained ferrite plates, which formed

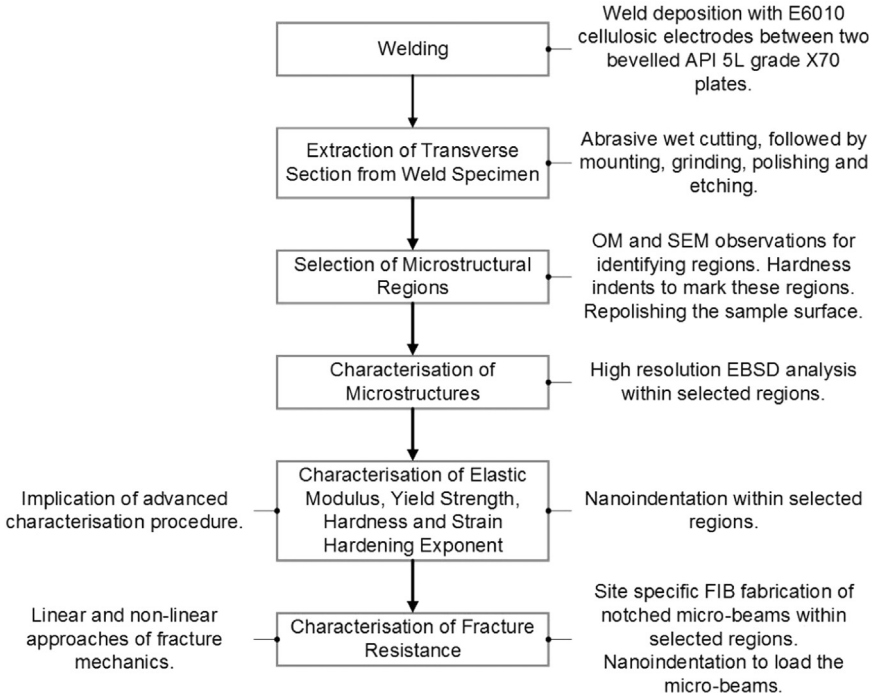

Fig. 1. Summary of the experimental approach.

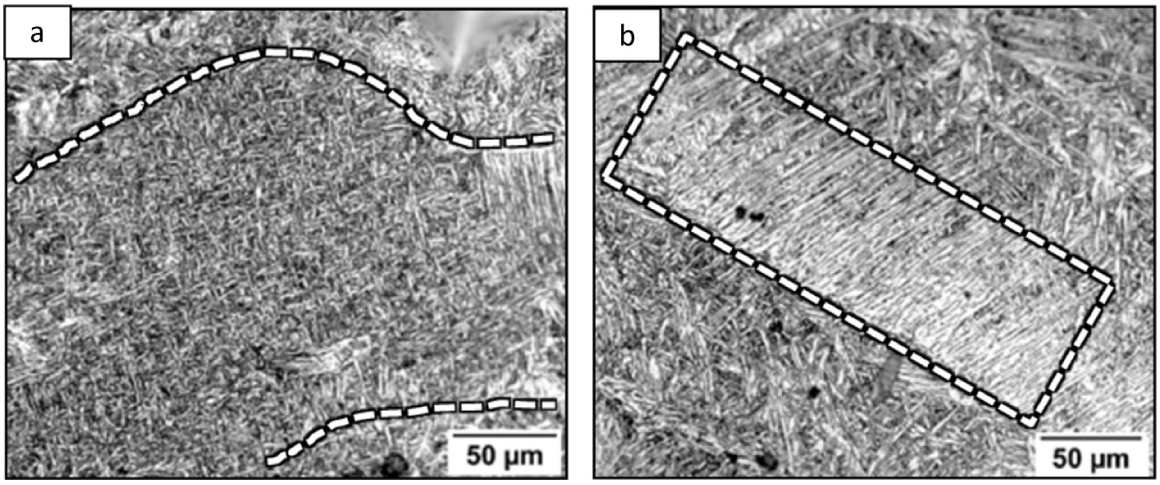

Fig. 2. Optical micrographs of 2% Nital etched weld metal showing: a) acicular ferrite, b) upper bainite.

an interlocking morphology, while the upper bainite region was characterised by parallel aligned ferrite laths. The samples were re-polished for the subsequent EBSD analysis using a semi-automatic polishing machine (Stuers). Final polishing was achieved using a porous neoprene disc with a colloidal silica suspension (0.04 μm).

2.4. EBSD data collection and processing

A FEI Helios Nanolab 600-SEM equipped with an EBSD detector (EDAX Hikari™) was utilised to collect the EBSD scans from the identified microstructural regions. The acceleration voltage of electron beam for the EBSD measurements was 20 kV and the ion beam current was 2.1 nA. The step size was 20 nm with a hexagonal scan grid. A commercial software (EDAX OIM™ Data Analysis 5.2) was used to process the EBSD data.

2.5. Nano-indentation testing

A commercial nano-indentation system (IBIS, Fischer-Cripps Laboratories) with a closed loop motorized sample stage (accuracy 0.25 μm), equipped with a Berkovich diamond tip was used to evaluate the mechanical properties of the selected microstructural constituents in the identified regions. Three indentation tests at a maximum load of 50 mN were conducted. The Young's modulus, the yield strength and the strain hardening exponent where extracted from the load-displacement diagrams following the advanced characterisation procedure developed in [18]. This procedure is presented in the Appendix for the sake of completeness of this paper. Traditional hardness values [19] were also evaluated from the recorded diagrams.

2.6. Site-specific fabrication of notched micro-beams

The micro-beams were fabricated within the selected regions of acicular ferrite and upper bainite. A detailed description of the fabrication procedure of the micro-beams is provided in [25]. The specimen and notch dimensions are shown in Fig. 3(a–c). The lattice damage caused by FIB milling and imaging was found to be negligible with respect to the dimensions of the micro-beams and was, therefore, expected to have no significant effect on the evaluation of mechanical properties of the fabricated specimens [25].

The same nano-indentation system as described in Section 2.5 was implemented to apply a bending force near to the free end of the notched micro-beams, while recording the load-deflection curves. The loading type was displacement-controlled with a load displacement rate of 0.02 μm s^{-1} and a maximum displacement (beam deflection) of 18.5 μm because of the limitations of the instrument. The selected indenter tip was spherical with a relatively large diameter of 40 μm to avoid penetration and to minimise the local deformation in the contact area. The measured displacements, therefore, were dominated by the beam deflection rather than the deformation in the area of contact.

3. Results and discussion

3.1. Characterisation of microstructures

The EBSD data was collected from the planes on the top of the micro-beams. The exposed surfaces in the ion-induced secondary electron (ISE) images in Fig. 4 indicate that the microstructures in the analysed planes were representative for the entire volume of

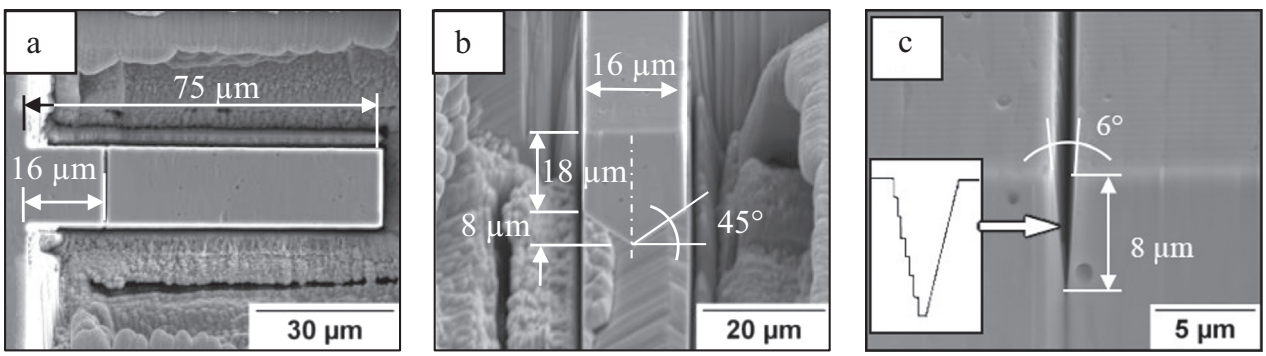

Fig. 3. SEM images showing overall specimen dimensions: a) top view, b) front view and c) close view of the notch. The depth of the notch is 8 μm.

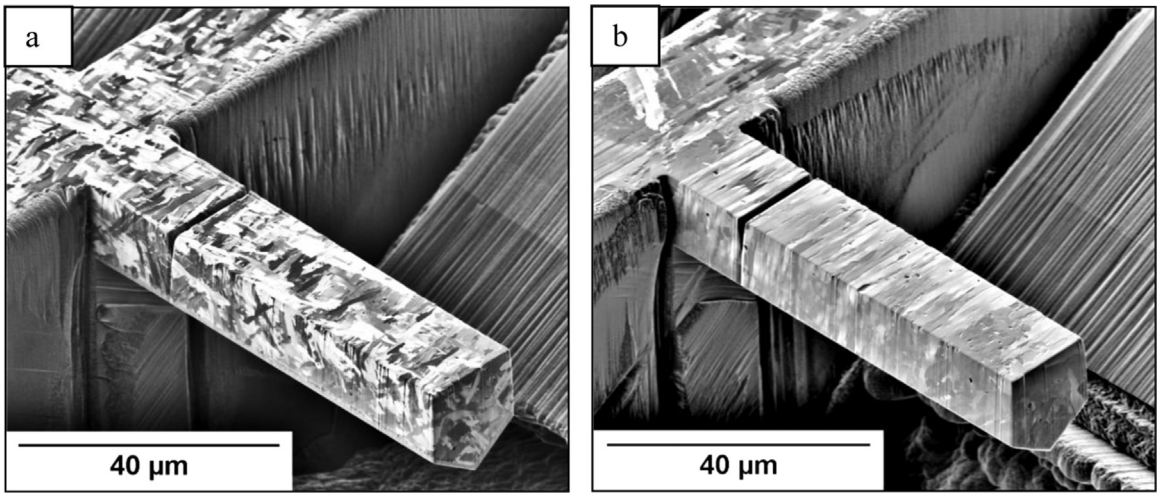

Fig. 4. Ion-induced Secondary Electron (ISE) images revealing that the entire volume of the micro-beams consists of: a) acicular ferrite, b) upper bainite.

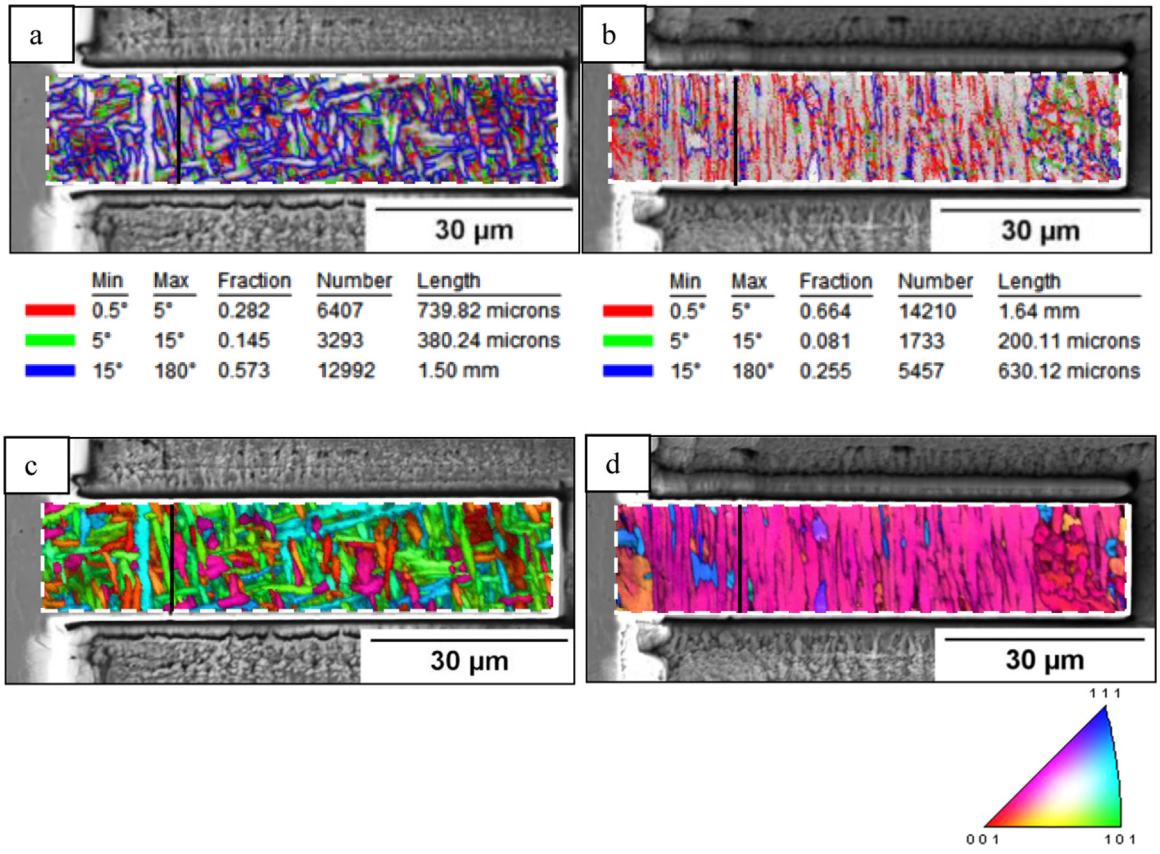

Fig. 5. Superimposed grain boundary and IQ maps for: a) acicular ferrite, b) upper bainite. Superimposed [001] IPF and IQ map for c) acicular ferrite, d) upper bainite.

the individual micro-beams. The superimposed grain boundary and Image Quality (IQ) maps presented in Fig. 5a) and b) show that the acicular ferrite consists of multiple fine interlocking ferrite plates with a large proportion of boundaries with misorientations $> 15°$ while upper bainite consists of a colony of parallel ferrite laths with a large proportion of boundaries with misorientations $< 15°$. It is thereby apparent that the ferrite morphologies have vastly different characteristics although, as mentioned in the introduction, despite both microstructural constituents are normally formed within the same temperature range and by the same type of transformation mechanisms [4,7]. This is mainly because acicular ferrite nucleates intragranulary from inclusions inside the prior austenite grains which prevents the formation of parallel ferrite plates and simultaneously restricts their growth due to multiple impingements [4]. All these factors produce an interlocking microstructure that consists of fine plates with divergent crystallographic orientations, as illustrated in the inverse pole figure (IPF) map in Fig. 5c). Contrary to acicular ferrite, upper bainite nucleates at the prior austenite grain boundaries and forms crystallographic packets which consist of parallel ferrite laths with almost similar orientations (Fig. 5d). These laths are in the presented case almost aligned perpendicularly along the micro-beam as shown in Fig. 5d. The upper bainite is thus expected to exhibit a more anisotropic behaviour than acicular ferrite where the orientations vary between the individual grains.

It is difficult to achieve a consistent microstructure within a

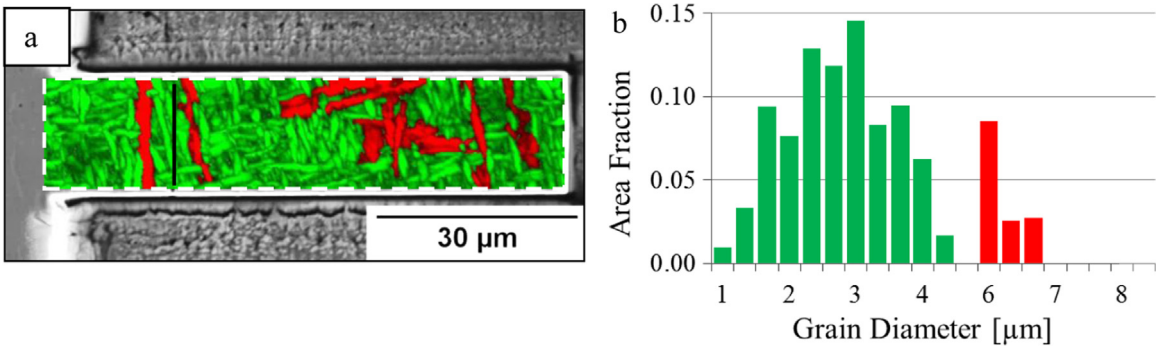

Fig. 6. a) Superimposed Grain Diameter and IQ maps highlighting the distribution of AF (green) and PF(I)+WF(I)+B(I) (red), b) chart illustrating the grain diameter distribution (adjacent data points with misorientations $< 5°$ were considered to be a part of the same grain).

Table 1
Ratio between the phase transformation products and average grain diameter for the micro-beam (cantilever) manufactured within the acicular ferrite region.

	AF /%	PF(I)+WF (I)+B(I) / %	Average grain diameter /μm
Specimen fabricated in acicular ferrite region	86	14	3.25 ± 1.17

finite volume. In weld metal, for example, microstructural constituents usually form aggregates with multiple components which all contribute to the mechanical properties. Acicular ferrite (AF) is often interspersed with different intragranular transformation products of primary ferrite, PF(I), Widmanstätten ferrite, WF(I) and bainite, B(I) [26,27]. However, since the plate or "grain" diameter of acicular ferrite is typically finer (< 5 μm) than most of the other intragranular transformation products (≥ 5 μm) [7], it is possible to distinguish between AF and PF(I)+WF(I)+B(I) by evaluating the grain diameter distribution. It is worth mentioning that the grain diameter here refers to the diameter of a circle having the same area as the ferrite grain or lath being measured, i.e. the equivalent circular area diameter (ECAD). The Grain Diameter map in Fig. 6a highlights individual grains according to their diameter as either green (< 5 μm) or red (≥ 5 μm). Fig. 6b) illustrates the distribution of the different grain diameters within the AF+PF(I)+WF(I)+B(I) aggregate. This data was used to determine the ratio between AF and PF(I)+WF(I)+B(I) as well as the average grain diameter of the aggregate (see Table 1).

The size of the bainite packet was measured as 34 μm (Fig. 7a) and b)). The ferrite lath length is usually considered as the diameter of the bainite packet [28], which is also in a good agreement with the length of the laths measured in Fig. 2b). The lath width was obtained with a SEM from the etched microstructure, prior to

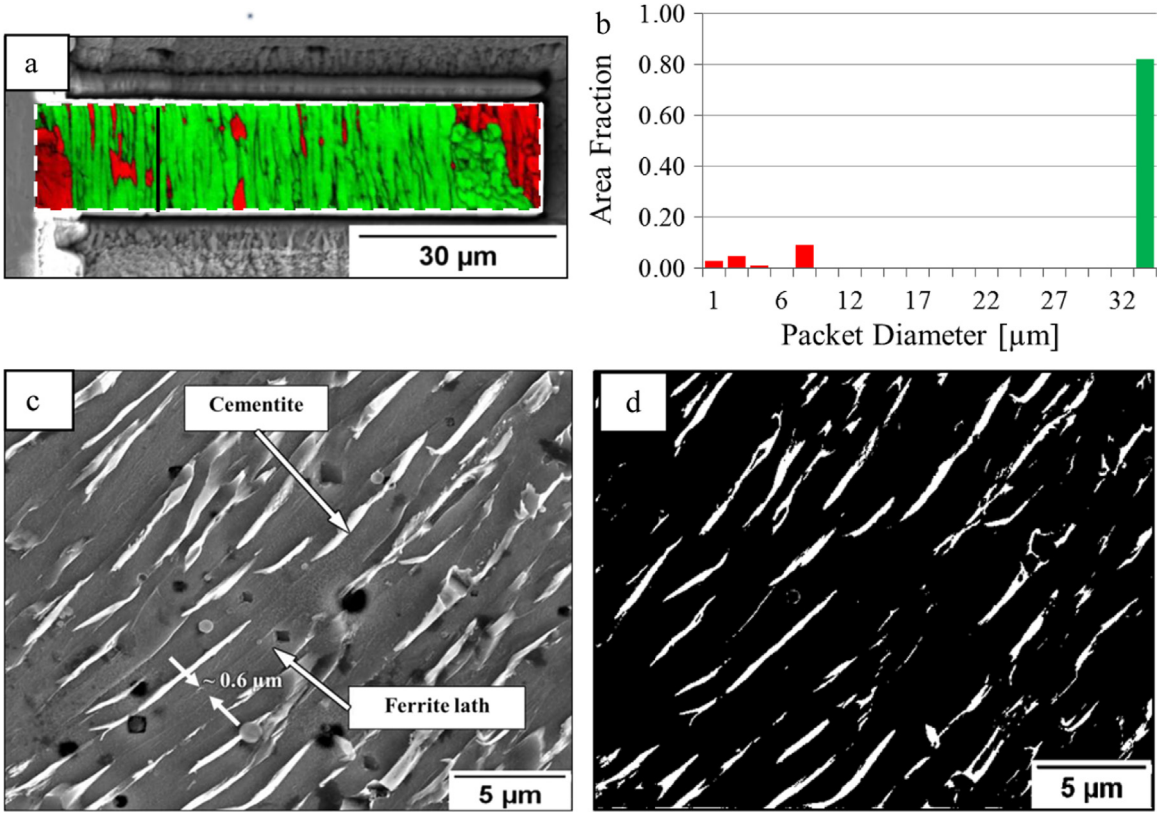

Fig. 7. Upper bainite: a) Superimposed Grain Diameter and IQ map (adjacent data points with misorientations $< 5°$ were considered to be part of the same packet or "grain"), b) chart illustrating the crystallographic packet diameter distribution, c) SE image of the 2% Nital etched microstructure, d) binary representation of the SE image highlighting ferrite (black pixels) and cementite (white pixels) phases.

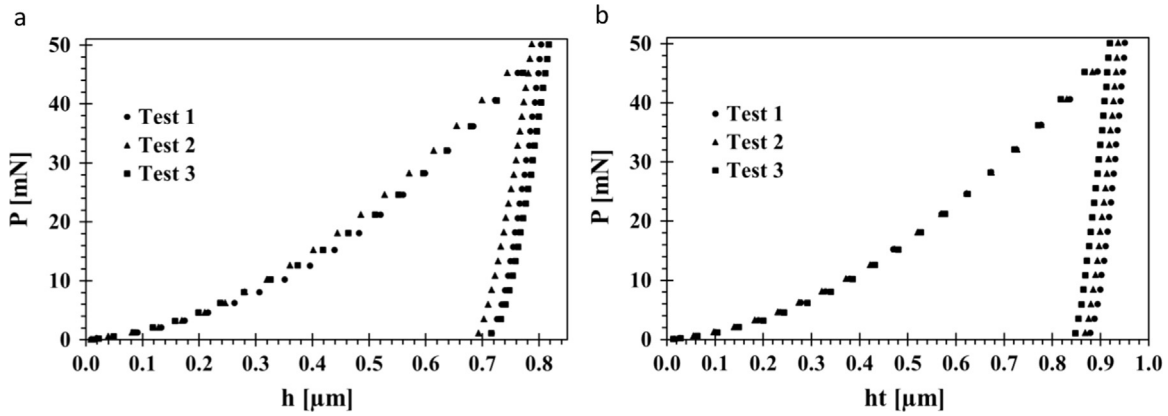

Fig. 8. Load – displacement (depth of indentation) diagrams: a) acicular ferrite and b) upper bainite.

the fabrication of the micro-beam but within the same region (Fig. 7c)). The lath width was averaged over 20 different measurements as 0.6 ± 0.09 μm.

As shown in Fig. 7c), the ferrite laths of upper bainite are often separated by cementite precipitates. Fig. 7d) is a binary representation of Fig. 7c) which was created with an image analysis software (Image J v1.48) in order to differentiate between the proportion of ferrite and cementite. The ratio between the two phases was thereby measured as approximately 90% ferrite and 10% cementite.

3.2. Strength characterisation

The elastic modulus, yield strength and strain hardening exponent were extracted from the load-displacement diagrams (Fig. 8) using the advanced characterisation procedure developed in [18] for ductile materials subjected to instrumented sharp indentation. The outcomes of the calculations are presented in Table 2 together with the measured Vickers hardness. The detail of the extraction of the parameters from the load-displacement diagrams is presented in the Appendix.

The average value of the yield strength for acicular ferrite in the selected region was estimated as 621 MPa. From a theoretical point of view the yield strength can be factorised into a number of intrinsic components with specific contributions [28]:

$$\sigma_{Y=}\sigma_{Fe} + \sum_i x_i\sigma_{SS_i} + \sigma_D + \sigma_{GS}, \quad (1)$$

where σ_{Fe} is the strength of pure, annealed iron, which is about 219 MPa at 300 K [28]. σ_{SS_i} is the substitutional solute strengthening and x_i is the concentration of a substitutional solute which is represented here by a subscript i [28]. σ_D and σ_{GS} are the strengthening contributions related to the dislocation density and the grain size, respectively.

Table 2
Vickers hardness, Young's modulus, yield strength and strain hardening exponent for the acicular ferrite (AF) and upper bainite (UB) regions.

		HV	E / GPa	σ_y/ MPa	n
AF	Test 1	314	204	631	0.193
	Test 2	330	193	814	0.157
	Test 3	308	215	418	0.314
	Mean	**317**	**204**	**621**	**0.221**
	Stdev	**11**	**11**	**198**	**0.082**
UB	Test 1	220	208	560	0.083
	Test 2	228	214	522	0.113
	Test 3	237	196	534	0.25
	Mean	**228**	**206**	**539**	**0.149**
	Stdev	**8**	**9**	**19**	**0.089**

Table 3
Concentration of the substitutional solutes x_i in the weld metal sample determined by GD-EOS.

i	Si	Mn	Ni	Mo	Cr	V	Co
x_i[wt. %]	0.20	1.03	0.13	0.08	0.02	0.02	0

Table 4
Solid solution strengthening terms (in MPa) for ferrite, for 1 wt% of solute (the data was determined for a strain rate of 0.0025 s^{-1} at 23 °C [28]) and for the weld metal sample.

	Si	Mn	Ni	Mo	Cr	V	Co	$\sum_i x_i\sigma_{SS_i}$
$for x_i$=1wt. % [28]	105	45	37	18	5.8	4.5	4.9	220.2
$for x_i$=see Tab. 3	21	46.4	4.8	1.4	0.1	0.1	0	73.8

To estimate σ_{SS_i}, the chemical composition of the weld metal sample was determined by glow discharge optical emission spectrometry (GD-OES), using a HORIBA GD-Profiler 2™ instrument (Table 3).

Table 4 shows the strengthening contribution for each solute as a function of their concentration, using a proportional ratio from the data reported in the first line of the table (from [28]). The total strengthening contribution due to solid solution was thus determined as approximately 74 MPa. The effect of carbon was not considered since its solubility in ferrite is negligible [28].

For acicular ferrite in weld metal, the strengthening contribution due to dislocations, σ_D, has been estimated in literature previously [29] to be approximately 145 MPa, (for a dislocation density of 10^{14} m^{-2} determined by transmission electron microscopy). Based on the Hall-Petch relation [1,2,29], the grain size strengthening σ_{GS} can be expressed as [30]:

$$\sigma_{GS}=210d^{-1/2}, \quad (2)$$

where d (≈1.51 μm) is the average spacing of boundaries above 2° determined by the linear intercept method with random test lines in the EBSD analysis. Consequently, the value of σ_{GS} is estimated to be around 171 MPa.

Adding up all the intrinsic contributions results in an overall strength of approximately 609 MPa, which correlates well with the experimental value from the nano-indentation tests (621 MPa) for acicular ferrite.

For bainite, the strength can also be factorised into individual

components [4]:

$$\sigma_{Y} = \sigma_{Fe} + \sum_{i} x_i \sigma_{SS_i} + \sigma_D + \sigma_{LS} + \sigma_P, \quad (3)$$

where σ_{Fe}, σ_{SS_i} and σ_D have the same meaning as for acicular ferrite. σ_{LS} and σ_P are the strengthening contributions of the lath size and the cementite precipitates, respectively.

Similar to acicular ferrite, the strengthening contributions of pure annealed iron σ_{Fe} and solid solution σ_{SS_i} are about 219 and 74 MPa respectively. The dislocation strengthening contribution σ_D is given by [28]:

$$\sigma_D = k_D \rho_D^{1/2}, \quad (4)$$

where $k_D = 7.34\ 10^{-6}$ (MPa m) [28], and the dislocation density, ρ_D, is reported to be in the range between 10^{14} m^{-2} and 10^{15} m^{-2} for bainite [4]. Taking a mid-range value of ρ_D of 5 10^{14} m^{-2}, this results into $\sigma_D \approx$ 164 MPa.

In the case of bainite, the evaluation of σ_{LS} needs a special consideration since the classical grain size effect theories cannot be directly applied to its microstructural parameters [4]. For very fine lath widths, as encountered in bainite, the dimensions of the slip planes are too small to allow the formation of dislocation pile-ups as required for the classic Hall-Petch formulation [4]. Yielding is then determined by the stress, which is necessary to expand a dislocation loop across the slip plane according to the Langford-Cohen relationship [31]. In such cases the strength is related to the reciprocal of the average lath diameter as follows

$$\sigma_{LS} = k_\epsilon (d)^{-1}, \quad (5)$$

where, k_ϵ is approximately 115 MPa m and d ($\approx$ 1.62 μm) is the mean linear intercept measured on random sections in the EBSD analysis. Consequently, σ_{LS} can be estimated to be around 71 MPa.

The contribution of cementite precipitates σ_P to the overall strength of bainite can be expressed as followed [4]

$$\sigma_P = k_p \Delta^{-1}, \quad (6)$$

where, k_p is given by approximately $0.52 V_\theta$ MPa m, V_θ is the volume fraction of cementite and Δ the average distance between a cementite particle and its two or three nearest neighbors. For V_θ 10% and $\Delta = 1.4$ μm, σ_P can be estimated as 37 MPa.

Adding up the contributions of all the intrinsic components considered for upper bainite leads to an overall strength of approximately 565 MPa which is again in a good agreement with the obtained experimental value of 539 MPa.

Table 2 also shows that the Vickers hardness value for acicular ferrite is estimated to be higher than for upper bainite. The hardness can be directly related to the yield strength using empirically developed relationships [32]. The relative hardness of the tested constituents is consistent with their yield strength values. The values of the Young's modulus for both microstructures are almost similar and correlate well with typical values measured for low carbon steels [33]. The values of the strain-hardening exponent, n, for both microstructures are also within the typical range reported for low carbon steels [34]. Nevertheless, upper bainite displays a lower value of n which could be attributed to the presence of the second phase particles (cementite) in its microstructure [34].

3.3. Micro-fracture testing and characterisation

The fracture properties of ductile materials cannot be characterised with conventional nano-indentation techniques. Indeed, these rely on the measurement of the crack length formed at the indentation corners [35] and can thus only be applied to relatively brittle materials. Therefore, it seems that for relatively ductile materials the only viable option to directly evaluate the fracture resistance at micro- and nano-scales is to test miniaturised fracture specimens. The miniaturisation of such test specimens can be achieved with FIB micro-fabrication techniques as highlighted earlier in the manuscript.

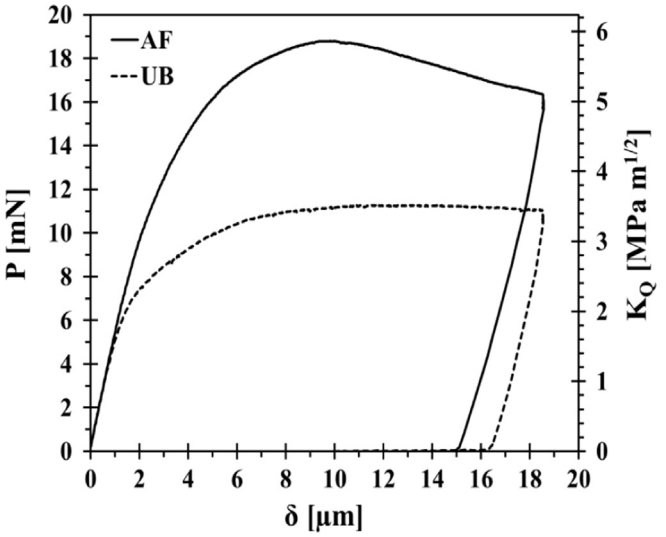

Fig. 9. Load-deflection curve for the micro-beams constituted of acicular ferrite and upper bainite.

The fabricated micro-beams were loaded with the IBIS nano-indentation system as described in Section 2.6. The load-deflection curves obtained for the acicular ferrite and the upper bainite are shown in Fig. 9. The linearity of the load-deflection curves at low loads confirms that the measured displacements were dominated by the beam deflection rather than by the contact deformation or penetration of the indenter. A qualitative analysis of the load-deflection diagrams indicates that the yield strength of acicular ferrite is higher than the yield strength of upper bainite since deviation from the linear behaviour occurred much earlier for the micro-cantilever made of upper bainite. Fig. 9 also indicates that the value of the Young's modulus of the two microstructures seemed to be quite close as the slopes of the linear parts of the load-deflection diagrams are notably similar for both specimens. These observations are in agreement with the results obtained with nano-indentation testing. The closeness of the values of Young's modulus for the two substantially different microstructures is nevertheless quite surprising. Indeed, the modulus of elasticity is expected to be affected by the anisotropy [36], which may be more significant for upper bainite due to the unidirectional orientation of the laths.

After testing, the area at the vicinity of the notch tip was inspected with the high resolution SEM. A relatively small crack growth was observed in both specimens and measured for acicular ferrite and upper bainite to be approximately 1.3 and 0.6 μm, respectively. Fig. 10a) and b) show that the fracture propagation in acicular ferrite is characterised by the formation and coalescence of micro-voids contrary to the upper bainite, where fracture was accompanied by homogeneous deformations. As mentioned previously, the width of the ferrite laths in upper bainite is too small to allow the formation of dislocation pile ups that are able to give rise to localised slip. It is therefore expected that the deformation behaviour of the individual laths is relatively homogeneous [30]. The contribution of the cementite precipitates to the toughness seems to be minimal since there is no evidence for the formation of micro-voids.

For the evaluation of fracture resistance various approaches can

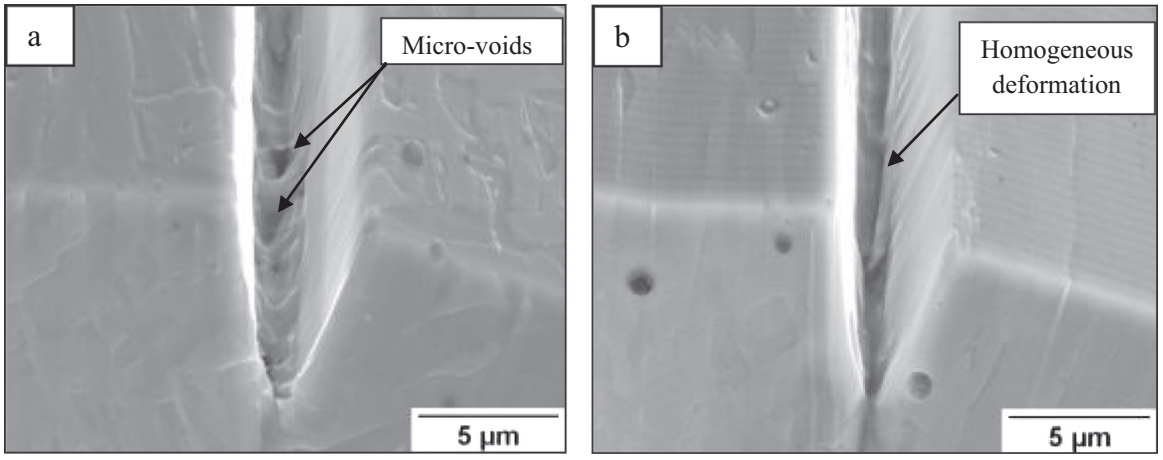

Fig. 10. High resolution SEM images of the notch tip area after loading: a) acicular ferrite specimen, b) upper bainite specimen.

be selected. From the load-deflection diagram (Fig. 9), it can be stated that a linear elastic fracture mechanics (LEFM) approach cannot provide correct values for fracture toughness due to relatively large plastic deformations taking place in both specimens upon loading. This is attributed to the small sample sizes, which fail to fulfil the conditions given in the testing standards by about three orders of magnitude [23]. However, this approach can deliver a lower bound for fracture toughness.

The conditional fracture toughness, K_Q, for the present fracture samples can be found as [22]:

$$K_Q = \frac{P_Q L y}{I}\sqrt{\pi a}\,F\left(\frac{a}{b}\right), \tag{7}$$

where a is the notch depth (8 μm) (Fig. 3c) and F(a/b) is a dimensionless shape factor, which is related to the specimen geometry, P_Q is the applied load determined according to ASTM E-399, L is the distance between the notch and the point of loading on the cantilever, I is the moment of inertia of the beam cross section, and y is the vertical distance between the upper surface and the neutral plane. I and y were calculated using the following equations:

$$I=\frac{wb^3}{12}+\left(y-\frac{b}{2}\right)^2 bw+\frac{w^4}{288}+\left[\frac{b}{6}+(b-y)\right]^2\frac{w^2}{4}, \tag{8}$$

$$y=\frac{\frac{b^2 w}{2}+\frac{w^2}{4}\left(b+\frac{w}{6}\right)}{bw+\frac{w^2}{4}}, \tag{9}$$

where b is the height of the parallel vertical face (18 μm) and w is the width of the micro-beam (16 μm), (see Fig. 3).

The equation for the dimensionless shape factor, F, was provided by Di Maio and Roberts [22] who conducted extensive finite element simulations for a wide range of specimen geometries. For $0.3 \le (a/b) \le 0.5$, Di Maio and Roberts provide the following equation:

$$F\left(\frac{a}{b}\right)=1.85-3.38\left(\frac{a}{b}\right)+13.24\left(\frac{a}{b}\right)^2-23.26\left(\frac{a}{b}\right)^3+16.8\left(\frac{a}{b}\right)^4, \tag{10}$$

For the fabricated specimens (Fig. 3), we have: $I = 1.5545 \times 10^{-8}$ mm^4, y = 0.01112 mm, and F(a/b) = 1.58 at a/b = 0.44.

Fig. 9 shows the variation of K as a function of the applied loading. This plot does not take into account any crack growth nor any large plastic deformations. It just demonstrates the reaction of the specimens to the applied load, which allows the evaluation of the lower limits of fracture toughness, which is 5.9 and 3.5 MPa m$^{1/2}$ for acicular ferrite and upper bainite, accordingly.

The presence of the large yielding region ahead of the crack tip requires non-linear approaches to evaluate the fracture resistance. The most popular non-linear criteria, which are widely used for this purpose at macro-scales, are based on either J-integral, crack tip opening displacement (CTOD) or crack opening angle (COA). The actual ASTM standards rely on the very detailed knowledge of

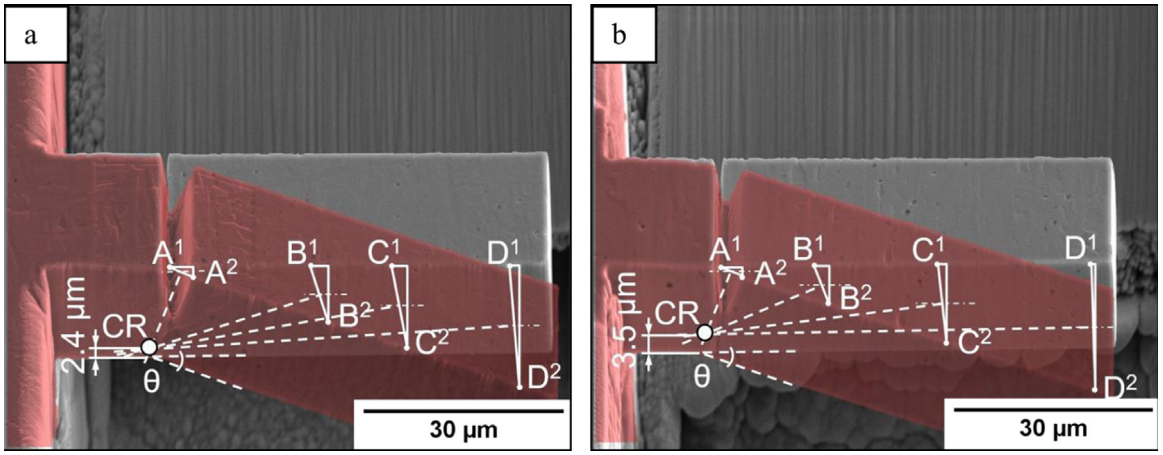

Fig. 11. Superimposed micro-beams tilt corrected SE images, before and after testing, to evaluate the centre of rotation for: a) acicular ferrite, b) upper bainite.

the crack extension. However, in the present tests only a very limited crack growth was observed in the both samples. Moreover, fracture standards for the evaluation of critical J-values (J_C) such as E813 restrict the initial ligament size and thickness, which have to be larger than 25 J_C/σ_y. From the forthcoming analysis it will be demonstrated that this condition is not satisfied by three orders of magnitude as for LEFM but by a factor three. This standard also specifies an offset value for crack extension (typically 0.2 mm), which is not possible to achieve for experiments at this length scale.

Beside the opportunity to measure critical J-values, it is also possible to use the CTOD as a parameter describing the fracture toughness of the microstructural constituents. Methods based on the measurement of CTOD are particularly appealing because of their readily-grasped physical significance and the possibility of direct measurements. In this work we adopted the plastic hinge model, originally proposed by British Standards Institution in 1972 [37]. In this model the centre of rotation was assumed at a depth of $r_e(d - a)$, from the tip of the notch, where r_e the rotation factor and d is the total height of the cantilever (=26 μm). r_e is different for different material properties, loading conditions and the shape of the cross sectional area of the beam. It was reported within the range of 0.3 – 0.5 [38]. From the direct experimental measurements (Fig. 11), the centre of rotation (CR) was located at 10.4 μm from the bottom of the specimens (vertex point) for acicular ferrite specimen and 11.5 μm for upper bainite. This corresponds to r_e =0.42 and 0.36, respectively. Both values are inside the range of the values reported for various fracture specimens and materials.

At a high level of loading the deformations and displacements in beams are largely associated with the rotation of the unsupported part of the cantilever (right to the notch, see Fig. 11a) and b)) about the CR. However, it is thereby apparent that the centre of rotation has a slight shift from the notch tip towards the beam support. This can be explained by the approximate nature of the plastic hinge concept as well as the fact that the beam is quite short and the notch is quite shallow, so a high level of shear stresses was generated as a result of the applied bending load. These factors influence the deformation mechanisms and affect the position of the plastic hinge.

The evaluation of CTOD can be represented as a sum of two components, elastic, δ_e, and plastic, δ_p:

$$\mathrm{CTOD}=\frac{J}{\sigma_Y}=\delta_e+\delta_p=\frac{K^2\left(1-\nu^2\right)}{2\sigma_Y E}+\frac{r_e(d-a)V_p}{r_e(d-a)+a} \tag{11}$$

where K is defined in Eq. (7), ν is the Poisson's ratio (=0.3) and V_p is the plastic component of crack opening displacement at the lateral surface of the specimen, measured as approximately 1.43 μm and 2.14 μm for the acicular ferrite and upper bainite specimens respectively.

The observed crack growth in both samples was assumed to be associated with decrease in the applied load. The CTOD corresponding to the maximum load was 0.82 μm and 1 μm for acicular ferrite and upper bainite, respectively. In accordance with ASTM E813-89 the maximum allowed value of CTOD is (d – a)/20 or (0.8 μm) and the maximum value for crack extension is (d – a)/4 or (4 μm). The first requirement is not met as both $\mathrm{CTOD_Q}$ values are slightly higher than the maximum allowable value, and the second requirement is satisfied as the crack increments have not exceed the value of 5 μm. According to ASTM E1820, the initial ligament length must be 35 times larger in order that $\mathrm{CTOD_Q}$ is a size-independent value, which is also not the case here. Therefore, strictly speaking, the obtained values of the $\mathrm{CTOD_Q}$ have to be treated with caution but can be utilised for comparative purposes.

The conditional fracture toughness $K_{Q,CTOD}$ was evaluated by measuring the crack tip opening displacement $\mathrm{CTOD_Q}$ of the fractured micro-beams and by using the equation [23]:

$$K_{Q,CTOD}=\sqrt{\frac{\bar{E}}{d_n}\sigma_y \mathrm{CTOD_Q}}, \tag{12}$$

where $\bar{E}$ is the reduced modulus defined as $\bar{E}=E/(1-\nu^2)$ and d_n is the Shih factor which is 0.78 for plane strain conditions [22]. These resulted into 12.1 and 12.5 MPa $m^{1/2}$ fracture toughness for acicular ferrite and upper bainite, respectively.

These values are at least by an order of magnitude lower than the typical fracture toughness values for steels reported from conventional fracture tests. This can be explained by the small dimensions of the specimens, which could cause a confinement of plastic deformations that may contribute significantly to the fracture resistance. Another important explanation for the low values of the obtained conditional values of fracture toughness from micro-fracture specimens is that at the micro-scale not all fracture toughening mechanisms may be activated. These mechanisms may include crack bridging and deflection as well as further toughening associated with the subcritical crack growth. The obtained values correspond rather to the toughness at crack initiation, which can significantly increase with the crack extension as observed in conventional fracture tests [39]. Nevertheless, it is worth noting that the K_Q values determined in this work for a relatively ductile material are higher than those reported for brittle and semi-brittle materials (between 0.63 and 8.5 MPa $m^{1/2}$) tested with similar methods at the micro-scale [20–23]. There is currently no data in the literature on the fracture toughness of individual microstructures at such small scales. Therefore, it was not possible to compare the obtained results with the typical fracture toughness values of individual ductile microstructural constituents of steel.

4. Conclusion

In the current paper we attempted to characterise the microstructure and to probe the mechanical properties of microscopic regions of acicular ferrite and upper bainite. These microstructural constituents were reported to have a large influence on the properties of the bulk material they constitute. The yield strength of acicular ferrite and upper bainite was estimated experimentally, with nano-indentation tests, and theoretically, based on physical principles and empirical relationships between microstructure and mechanical properties. This evaluation indicated that the highly localised, intrinsic mechanical properties of acicular ferrite and upper bainite can be directly linked to specific aspects of the individual microstructures such as grain/lath size, grain boundary characteristics and second phase particles. However, despite substantial microstructural differences between acicular ferrite and upper bainite the difference of their yield strength seems to be quite marginal. The values obtained from the nano-indentation experiments were within the range of the yield strength of many ferrous alloys tested with conventional macroscopic methods of mechanical testing.

The values for the Young's modulus from the conducted nano-indentation tests were estimated to be also very similar. The difference was negligible and within the measurement error. These values correlate very well with bulk elastic modulus of other ferrous alloys. The fracture tests also confirmed the similarity of the elastic behaviour of these two microstructural constituents.

For the fracture tests, site specific FIB micro-machining was employed to manufacture sharply notched micro-beams within selected regions consisting of predominantly either acicular ferrite

or upper bainite. The small scale of the specimens restricted the application of both linear and non-linear fracture mechanics approaches to identify fracture controlling parameters. The conditional values of the critical stress intensity factors, K_Q, were obtained based on LEFM, which can be considered as a lower bound of the actual fracture toughness.

The application of the plastic hinge model for the evaluation of CTOD provided very similar fracture toughness values for acicular ferrite and upper bainite. These values were well below the reported values for the fracture toughness of ferritic steels and alloys at the corresponding room temperatures. These low measured values were nevertheless not surprising as there could be many reasons behind the large differences between fracture toughness value reported in the literature and the current measurements. These reasons could include the confinement of plastic deformations in small-scale specimens and the deactivation of significant toughening mechanisms as highlighted earlier. In addition, the calculated values of fracture toughness correspond to the crack initiation stage. It is well known that these values can increase dramatically with the crack advance. However, in the present tests it was impossible to observe the stable propagation and transition to cleavage failure.

The main outcome of this work is that despite the substantial microstructural differences, the mechanical properties of acicular ferrite and upper bainite were found to be quite similar. The main difference in fracture behaviour is that the contribution of the elastic component to the fracture toughness of acicular ferrite is relatively higher than for upper bainite. On the other hand, upper bainite possesses higher ductility leading to very similar values for the conditional fracture toughness.

Acknowledgments

This work was funded by the Energy Pipelines CRC, supported through the Australian Government's Cooperative Research Centres Program. The cash and in-kind support from APGA through its Research and Standards Committee is also gratefully acknowledged. The authors acknowledge the facilities and the scientific and technical assistance, in particular Dr. Angus Netting and Dr. Animesh Basak, of the Australian Microscopy & Microanalysis Research Facility at the University of Adelaide. The authors would like to thank Rahim Kurji (PhD Candidate) for the fabrication of the weld samples as well as Dr Celia Olivero and Dr Patrick Chapon (Horiba Company) for the GD-OES measurements. The authors extend their acknowledgment to Dr Reza Ghomashchi for his help with microstructure characterisation as well as to Prof Valerie Linton for her continuing support.

Appendix

Estimation of Young's modulus, yield strength, strain hardening exponent [18] and hardness values [19] from load-unload nano-indentation curves.

The nominal stress σ is defined by:

$$\sigma=\sigma_y\left(1+\frac{E}{\sigma_y}\varepsilon_p\right)^n \tag{A1}$$

The stress $\sigma_{0.033}$ at a deformation ε_p, of 0.033 is given by:

Table A1

Values of $C, \sigma_{0.033}$, E^*, A, $\left.\frac{dP_u}{dh}\right|_{h_m}$ obtained from the 3 different nano-indentation tests.

		C / N/m^2	$\sigma_{0.033}$ / MPa	E^* / GPa	A / m^2	$\left.\frac{dP_u}{dh}\right\|_{h_m}$ / N/m
AF	Test 1	78.3 10^9	986	174.8	1.59 10^{-11}	837 10^3
	Test 2	85.2 10^9	1123	167.2	1.44 10^{-11}	785 10^3
	Test 3	79.0 10^9	985	181.8	1.40 10^{-11}	841 10^3
UB	Test 1	59.1 10^9	685	177.5	2.54 10^{-11}	1107 10^3
	Test 2	60.0 10^9	694	181.4	2.38 10^{-11}	1096 10^3
	Test 3	61.2 10^9	724	169.3	2.22 10^{-11}	986 10^3

$$\frac{C}{\sigma_{0.033}}=-1.131\left[\ln\left(\frac{E^*}{\sigma_{0.033}}\right)\right]^3+13.635\left[\ln\left(\frac{E^*}{\sigma_{0.033}}\right)\right]^2 -30.594\left[\ln\left(\frac{E^*}{\sigma_{0.033}}\right)\right]+29.267 \tag{A2}$$

Where C is the curvature of the loading curve and is given by:

$$P = Ch^2 \tag{A3}$$

And E^* is the reduced Young's modulus and is given by:

$$E^* = \frac{1}{2.12}\frac{\sqrt{\pi}}{\sqrt{A}}\left.\frac{dP_u}{dh}\right|_{h_m} \tag{A4}$$

With A is the projected area of contact and is given, for a Berkovich indenter, by:

$$A=24.56h_m^2 \tag{A5}$$

By determining the slope of the unloading curve at the maximum load depth, $\left.\frac{dP_u}{dh}\right|_{h_m}$, the strain hardening exponent can be obtained by solving the Eq. (A6):

$$\begin{aligned}\frac{1}{E^*h_m}\left.\frac{dP_u}{dh}\right|_{h_m} &= \left(-1.40557n^3+0.77526n^2+0.1583n-0.06831\right)\left[\ln\left(\frac{E^*}{\sigma_{0.033}}\right)\right]^3+17.93006n^3-9.22091n^2-2.37733n \\ &+0.86295\left[\ln\left(\frac{E^*}{\sigma_{0.033}}\right)\right]^2+\left(-79.99715n^3+40.5562n^2\right. \\ &\left.+9.00157n-2.54543\right)\left[\ln\left(\frac{E^*}{\sigma_{0.033}}\right)\right]+\left(122.65069n^3-63.\right. \\ &\left.88418n^2-9.58936n+6.20045\right)\end{aligned} \tag{A6}$$

The yield strength is obtained solving Eq. (A1) as:

$$\sigma_{0.033} = \sigma_y\left(1+\frac{E}{\sigma_y}0.003\right)^n \tag{A7}$$

Where E is the Young's modulus and is given by:

$$\frac{1}{E^*} = \frac{(1-\nu^2)}{E} + \frac{(1-\nu_i^2)}{E_i} \tag{A8}$$

In Eq. (A8) the quantity $\frac{(1-\nu_i^2)}{E_i}$ is equal to 0.001264.

The universal hardness H, is given by [19]:

$$H = \frac{P_m}{A}$$

And the Vickers hardness, HV is given by [19]:

$HV = 0.094495H$

The values of C, $\sigma_{0.033}$, E^*, A, $\left.\frac{dP_u}{dh}\right|_{h_m}$ obtained from the 3 tests are gathered in Table A1.

References

[1] E.O. Hall, The Deformation and Ageing of Mild Steel: III Discussion of Results, Proc. Phys. Soc. Sect. B 64 (1951) 747–753.
[2] N.J.J. Petch, P. Stables, Delayed Fracture of Metals under Static Load, Nature 169 (1952) 842–843.
[3] T. Watanabe, The impact of grain boundary character distribution on fracture in polycrystals, Mater. Sci. Eng.: A 176 (1994) 39–49.
[4] H.K.D.H. Bhadeshia, Bainite in Steels: transformations, microstructure and properties, IOM Communications, London, 2001.
[5] J.R. Greer, J.T.M. De Hosson, Plasticity in small-sized metallic systems: Intrinsic versus extrinsic size effect, Prog. Mater. Sci. 56 (2011) 654–724.
[6] D.V. Edmonds, R.C. Cochrane, Structure-property relationship in bainitic steels, Metall. Trans. 21A (1990) 1527–1540.
[7] G. Thewlis, Classification and quantification of microstructures in steels, Mater. Sci. Technol. 20 (2004) 143–160.
[8] M. Diaz-Fuentes, A. Iza-Mendia, I. Guttierez, Analysis of Different Acicular Ferrite Microstructures in Low-Carbon Steels by Electron Backscattered Diffraction. Study of Their Toughness Behavior, Metall. Mater. Trans. A 34A (2003) 2505–2516.
[9] R.A. Farrar, P.L. Harrison, Review: acicular ferrite in carbon-manganese weld metals: an overview, J. Mater. Sci. 22 (1987) 3812–3820.
[10] J.R. Yang, C.Y. Huang, C.F. Huang, J.N. Aoh, Influence of acicular ferrite and bainite microstructures on toughness for an ultra-low-carbon alloy steel weld metal, J. Mater. Sci. Lett. 12 (1993) 1290–1293.
[11] W. Wang, W. Yan, L. Zhu, P. Hu, Y. Shan, K. Yang, Relation among rolling parameters, microstructures and mechanical properties in an acicular ferrite pipeline steel, Mater. Des. 30 (2009) 3436–3443.
[12] W. Wang, Y. Shan, K. Yang, Study of high strength pipeline steels with different microstructures, Mater. Sci. Eng. A 502 (2009) 38–44.
[13] L. Shi, Z. Yan, Y. Liu, C. Zhang, Z. Qiao, B. Ning, H. Li, Improved toughness and ductility in ferrite/acicular ferrite dual-phase steel through intercritical heat treatment, Mater. Sci. Eng.: A 590 (2014) 7–15.
[14] M.C. Zhao, B. Tang, Y.Y. Shan, K. Yang, Role of microstructure on sulfide stress cracking of oil and gas pipeline steels, Metall. Mater. Trans. 34A (2003) 1089–1096.
[15] Y. Zhong, F.R. Xiao, J.W. Zhang, Y.Y. Shan, W. Wang, K. Yang, In situ TEM study of the effect of M/A films at grain boundaries on crack propagation in an ultrafine acicular ferrite pipeline steel, Acta Mater. 54 (2006) 435–443.
[16] M.-C. Zhao, K. Yang, Y.-Y. Shan, Comparison on strength and toughness behaviors of microalloyed pipeline steels with acicular ferrite and ultrafine ferrite, Mater. Lett. 57 (2003) 1496–1500.
[17] K. Grassl, S.W. Thompson, G. Krauss, New option for steel selection for automotive applications, SAE Technical paper series no 890508, Society of Automotive Engineers, Warrendale, Pa, 1989.
[18] M. Dao, N. Chollacoop, K.J. Van Vliet, T.A. Venkatesh, S. Suresh, Computational modeling of the forward and reverse problems in instrumented sharp indentation, Acta Mater. 49 (2001) 3899–3918.
[19] A.C. Fischer-Cripps, Nanoindentation, Springer, New York Dordrecht Heidelberg London, 2011.
[20] B.N. Jaya, C. Kirchlechner, G. Dehm, Can microscale fracture tests provide reliable fracture toughness values? A case study in silicon, J. Mater. Res. 30 (2015) 686–698.
[21] J. Ast, T. Przybilla, V. Maier, K. Durst, M. Göken, Microcantilever bending experiments in NiAl – Evaluation, size effects, and crack tip plasticity, J. Mater. Res. 29 (2014) 2129–2140.
[22] D. Di Maio, S.G. Roberts, Measuring fracture toughness of coatings using focused-ion-beam-machined microbeams, J. Mater. Res. 20 (2005) 299–302.
[23] S. Wurster, C. Motz, R. Pippan, Characterization of the fracture toughness of micro-sized tungsten single crystal notched specimens, Philos. Mag. 92 (2012) 1803–1825.
[24] R. Ghomashchi, W. Costin, R. Kurji, Evolution of weld metal microstructure in shielded metal arc welding of X70 HSLA steel with cellulosic electrodes: a case study, Mater. Charact. 107 (2015) 317–326.
[25] W.L. Costin, O. Lavigne, A. Kotousov, R. Ghomashchi, V. Linton, Investigation of Hydrogen Assisted Cracking in Acicular Ferrite using Site-Specific Micro-Fracture Tests, Mater. Sci. Engineering: A 651C (2016) 859–868.
[26] G. Thewlis, The Nature of Acicular Ferrite in Ferrous Weld Metals and the Challenges for Microstructure Modelling, Mater. Sci. Forum 426 (2003) 4019–4026.
[27] G. Thewlis, J.A. Whiteman, D.J. Senogles, Dynamics of austenite to ferrite phase transformation in ferrous weld metals, Mater. Sci. Technol. 13 (1997) 257–274.
[28] H.K.D.H. Bhadeshia, Models for the elementary mechanical properties of steel welds, Institute of Materials, London, 1997, 229-284.
[29] J.R. Yang, H.K.D.H. Bhadeshia, The dislocation density of acicular ferrite in steel welds, Weld. J. Res. Suppl. 69 (1990) 305s–307s.
[30] N. Kamikawa, K. Sato, G. Miyamoto, M. Murayama, N. Sekido, K. Tsuzaki, T. Furuhara, Stress–strain behavior of ferrite and bainite with nano-precipitation in low carbon steels, Acta Mater. 83 (2015) 383–396.
[31] J.P. Naylor, The influence of the lath morphology on the yield stress and transition temperature of martensitic-bainitic steels, Metall. Trans. A 10 (1979) 861–873.
[32] P. Zhang, S.X. Li, Z.F. Zhang, General relationship between strength and hardness, Mater. Sci. Eng.: A 529 (2011) 62–73.
[33] Smithells Metals Reference Book, 7th Ed., E.A. Brandes, G.B. Brook (Eds), Butterworth-Heinemann, Oxford, 1992.
[34] Z. Fan, H. Mingzhi, S. Deke, The relationship between the strain-hardening exponent n and the microstructure of metals, Mater. Sci. Eng.: A 122 (1989) 211–213.
[35] A.G. Evans, E.A. Charles, Fracture Toughness Determinations by Indentation, J. Am. Ceram. Soc. 59 (1976) 371–372.
[36] D.E.J. Armstrong, A.J. Wilkinson, S.G. Roberts, Measuring anisotropy in Young's modulus of copper using microcantilever testing, J. Mater. Res. 24 (2009) 3268–3276.
[37] Methods for Crack Opening Displacements (COD) Testing, DD 19:1972, British Standards Institution, London, 1972.
[38] S.G. Druce, B.L. Eyre, A critical assessment of elasto-plastic fracture mechanics, J. Nucl. Mater. 80 (1979) 1–12.
[39] X.-K. Zhu, J.A. Joyce, Review of fracture toughness (G, K, J, CTOD, CTOA) testing and standardization, Eng. Fract. Mech. 85 (2012) 1–46.

Materials Science & Engineering A 651 (2016) 859–868

Contents lists available at ScienceDirect

Materials Science & Engineering A

journal homepage: www.elsevier.com/locate/msea

Investigation of hydrogen assisted cracking in acicular ferrite using site-specific micro-fracture tests

Walter L. Costin [a], Olivier Lavigne [a,*], Andrei Kotousov [a], Reza Ghomashchi [a], Valerie Linton [b]

[a] School of Mechanical Engineering, The University of Adelaide, SA 5005, Australia
[b] Energy Pipelines Cooperative Research Centre, Faculty of Engineering, University of Wollongong, NSW 2522, Australia

ARTICLE INFO

Article history:
Received 21 September 2015
Received in revised form
13 November 2015
Accepted 14 November 2015

Keywords:
EBSD
Micromechanics
Steel
Welding
Hydrogen embrittlement
Stress intensity factor threshold

ABSTRACT

Hydrogen assisted cracking (HAC) is a common type of failure mechanism that can affect a wide range of metals and alloys. Experimental studies of HAC are cumbersome due to various intrinsic and extrinsic parameters and factors (associated with stress, hydrogen and the materials microstructure) contributing to the hydrogen crack kinetics. The microstructure of many materials consists of diverse constituents with characteristic features and mechanical properties which only occur in very small material volumes. The only way to differentiate the effect of these individual constituents on the hydrogen crack kinetics is to miniaturise the testing procedures. In this paper we present a new experimental approach to investigate hydrogen assisted crack growth in a microstructural constituent, i.e. acicular ferrite. For this purpose, sharply notched micro-cantilevers were fabricated with a Focus Ion Beam within this selected microscopic region. Acicular ferrite can be found in many ferrous alloys including ferritic weld metal and has specific features that control its intrinsic susceptibility to HAC. These features were characterised via Electron Backscatter Diffraction and the specimens were subsequently loaded under uncharged and hydrogen charged conditions with a nano-indenter. The outcomes of the testing, demonstrated that the threshold stress intensity factor, K_{th}, to initiate crack propagation in acicular ferrite ranges between 1.56 MPa $m^{1/2}$ and 4.36 MPa $m^{1/2}$. This range is significantly below the values of K_{th} reported for various ferrous alloys in standard macro-tests. This finding indicates that the mechanisms and resistance to HAC at micro-scale could be very different than at the macro-scale as not all fracture toughening mechanisms may be activated at this scale level.

1. Introduction

Hydrogen assisted cracking (HAC) is a prevalent failure mechanism that affects most metals and alloys. Johnson in 1875 was the first to report about the deleterious effects of hydrogen on the mechanical properties of iron and steels [1]. This phenomenon is historically referred to as Hydrogen Embrittlement (HE) because macroscopically the presence of hydrogen in metals generally leads to reduction in fracture energy and ductility promoting brittle failure. The term HAC was later suggested by Beachem who argued that hydrogen assisted crack propagation may imply microscopic deformation processes that are not necessarily the result of the cessation, restriction, or exhaustion of ductility [2], however, from a mechanistic point of view both designations refer to the same phenomenon.

HAC can be classified as either Internal Hydrogen Assisted Cracking (IHAC), which is the main focus of the current paper, or Hydrogen Environment Assisted Cracking (HEAC). In IHAC, atomic hydrogen can be introduced throughout the microstructure by manufacturing operations (casting, welding, surface-chemical cleaning, electrochemical machining, electroplating, and heat treatment) as well as due to environmental exposure (cathodic electrochemical reactions or gaseous hydrogen exposure). Subcritical crack growth can occur if a hydrogen charged material with a susceptible microstructure is subjected to a sufficient stress level. Meanwhile, HEAC involves the conjoint action of mechanical loading and chemical reaction, i.e. the stress is necessary during the hydrogen uptake to facilitate cracking. Therefore, IHAC and HEAC are distinguished by the source of the supplied hydrogen but share common aspects, i.e. cracking occur in both cases when the three causal conditions are simultaneously present: (1) susceptible microstructure, (2) sufficiently high levels of hydrogen and (3) stress [3].

Hydrogen is widely considered as one of the future sources of

* Corresponding author.
E-mail addresses: Olivier.lavigne@adelaide.edu.au, lavigneolivier@hotmail.com (O. Lavigne).

http://dx.doi.org/10.1016/j.msea.2015.11.044
0921-5093/

clean energy [4]. A large scale of production, storage and transportation of hydrogen is likely to be escaladed in the next few decades. Because of the technological importance of HAC for the past, present and future applications, greater amount of efforts have been directed to the development of experimental and theoretical approaches to predict and evaluate the effect of hydrogen on the life expectancy and integrity of structural components [2,3,5–9]. However, HAC continues to plague applications of, specifically, high strength metals and alloys [3]. Various, often controversial views [7,10–14] have been proposed to describe the physical mechanisms by which hydrogen actually affects plasticity and fracture resistance in metals. Detailed reviews of these approaches can be found in [3,15]. However, it is the Linear Elastic Fracture Mechanics that provides a basis allowing the incorporation of hydrogen cracking failure mechanism into structural integrity management [16]. In accordance with this fracture theory pioneered by Naval Research Laboratory in 1965 [17] a single stress related parameter, the stress intensity factor, K, governs the crack initiation and crack growth rates. This concept was confirmed by many other studies over the past 60 years [3,18–22]. From the structural integrity point of view three characteristics of the fracture behaviour have to be identified experimentally: (a) a threshold stress intensity factor, K_{th} (or other terminology), below which crack does not propagate, (b) crack growth rates (da/dt) at $K > K_{th}$ and (c) fracture toughness K_C. Effective laboratory methods have been developed and standardised [23] to determine the threshold and kinetics for hydrogen assisted cracking, which are necessary for the safe design of structures subjected to the risk of HAC. IHAC testing procedures may involve several stages: a fracture mechanics specimen, typically fatigue pre-cracked, which can be stressed under either constant or rising load, crack mouth opening displacement or constant K. These procedures are substantially more complex and time consuming in comparison with the standard fracture testing. For example, the identification of the threshold stress intensity factor, K_{th}, requires several thousand hours of testing time [23].

Due to a wide range of parameters affecting the HAC phenomenon (such as the rate and mode of loading, constraint conditions, hydrogen charging method, temperature, specimen size, diverse microstructural factors, etc.) the outcomes of conventional HAC tests demonstrate a large scatter [5]. In the development of experimental methods to characterise HAC over the past 50 years, a great effort has been directed to eliminate these diverse parameters influencing the reproducibility of the test results. In addition, the utilisation of the stress intensity factor and plane strain conditions as well as controlled hydrogen charging allowed an accurate measure of the mechanical stress and environmental conditions, two main factors affecting HAC. However, the microstructure of metal and alloys (which is the third main factor affecting HAC) typically consists of diverse constituents with specific features and mechanical properties that only occur in microscopic volumes. To investigate the HAC susceptibility of such small volumes it is therefore necessary to significantly reduce the size of the specimens down to the characteristic size of the individual microstructural constituent.

Katz et al. [24] were the first who proposed the application of nano-indentation to examine the micro-mechanisms of hydrogen related failures. This idea was extended by Barnoush and Vehoff [5] who presented a method for determining the onset of plasticity in very small volumes (perfect crystals) subjected to hydrogen charging. Several different materials were tested with this method. For example, it was found that hydrogen reduces the critical stress required for the onset of plasticity. However, this method is not capable of providing a quantitative evaluation of fracture properties similar to conventional fracture tests, such as stress intensity factor threshold or crack growth rates. It seems that the only viable approach for a direct quantitative evaluation of the fracture properties of very small material volumes is the miniaturisation of fracture specimens and testing down to micro-scale [25].

The miniaturisation of fracture tests became possible over the past decade with an increasing efficiency and accuracy of Focused Ion Beam (FIB) workstations, which has resulted in a reproducible fabrication of micro-scaled specimens. Several researchers have already employed FIB micromachining to fabricate micro-pillars for performing compression tests on uncharged and hydrogen charged specimens [26,27]. These experiments demonstrated the hydrogen-deformation interrelationships at microscopic scales. However, FIB micro-machining also allows fabricating standard fracture specimens with microscopic dimensions [28,29]. This idea has been realised in the current work to investigate the effects of hydrogen on the crack kinetics in a selected microstructural constituent with particular features. Sharply notched micro-cantilevers were fabricated with a FIB into a localised region fully consisting of acicular ferrite which is a common microstructural constituent of ferritic weld metal and alloys. This microstructural region has characteristic features that largely determine its mechanical properties as well as its susceptibility to HAC. The micro-cantilevers were characterised via Electron Backscatter Diffraction (EBSD) and subsequently tested under uncharged and hydrogen charged conditions with a nano-indenter. However, HAC fracture testing standards, developed for macro-examinations, could not be followed precisely in our experimental campaign, specifically in terms of the test duration to identify the onset of hydrogen cracking or K_{th}, fatigue pre-cracking and realisation of plane strain conditions. Constant loading was applied for twelve hours to simulate the time delayed nature of the IHAC in a micro-scale specimen. Unexpectedly, the fracture mechanics characteristics derived from the present tests were found to be very different to the corresponding values reported for conventional sized fracture specimens.

2. Material and methods

Weld metal is an example of a material that typically consists of diverse microstructural constituents with distinctive features and mechanical properties. The properties of individual constituents can only be revealed when testing small material volumes, and are therefore not directly assessable with conventional methods of mechanical testing [5,30]. It is well-known that the presence of hydrogen can significantly compromise the structural integrity of the weld metal (as well as of the heat affected zone). Hydrogen Assisted Cold Cracking (HACC), which is a particular manifestation of IHAC, is a well-known weld failure mechanism that may occur after the deposited weld has cooled down to temperatures below 200 °C. A critical structural defect can be developed within minutes to even days after welding [31]. Due to its time delayed nature the onset of Weld Metal Hydrogen Assisted Cold Cracking (WM HACC) may be undetected and, eventually, result in catastrophic failure.

2.1. Material-microstructural constituent

A weld metal specimen was sourced from API 5 L grade X70 samples welded with 4 mm diameter E6010 cellulosic electrodes. The welding procedure is presented in details in [32]. Under these welding conditions, the yield strength of the weld metal is expected to range between the yield strengths of the E6010 electrode (420 MPa) and the X70 parent metal (480 MPa).

A localised region of the weld metal specimen consisting of acicular ferrite was identified for further micro-fracture tests (Fig. 1a and b). This microstructural constituent represents a

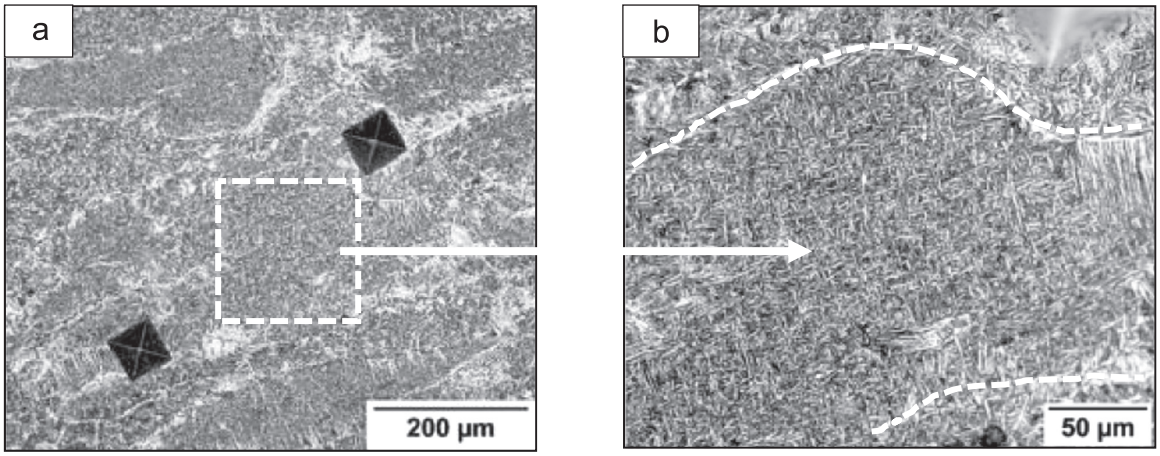

Fig. 1. (a) and (b) Optical micrograph of 2% Nital etched section shows acicular ferrite defined by the random arrangement of fine-grained ferrite plates and the distinct interlocking morphology.

particular interest for the weld metal integrity. Previous investigations reported that of all typical ferritic weld metal microstructures, acicular ferrite seems to have the most beneficial impact on the strength, toughness as well as the HACC resistance of welded joints [33,34]. This was mainly related to a small grain size and high density of high angle grain boundaries, which apparently increase the resistance to cleavage like fracture and simultaneously acts as a hydrogen trap, thereby preventing the hydrogen to diffuse to more HACC susceptible regions [34].

2.2. FIB fabrication of the micro-cantilevers

The fabrication of the micro-cantilevers within the selected region was accomplished with a FEI Helios Nanolab 600 Dual Beam™ FIB. The first step of the process was to mill three trenches with a stair step pattern mode for each micro-cantilever using an intense ion beam current density (21 nA/30 kV). The sample was tilted 90° with respect to the incident ion beam. The ratio between the final specimen length and trench depth had to be selected appropriately to ensure that the deflected cantilever do not touch the bottom of the trench during loading. In this case the trench depth was 50 μm and the final cantilever length was 75 μm. For the second step of the fabrication process an ion beam with a less intense current density (2.8 nA/30 kV) was used to mill (polish) the sidewalls. The sample was then tilted 45° to the incident ion beam to cut the bottom of the micro-beam. The operation was then repeated on the other side to create a symmetric pentagonal profile. Finally, a stair step pattern and an ion beam with a very low intensity (0.46 nA/30 kV) were utilised to mill a sharp notch of 8 μm depth, 16 μm away from the beam support. Fig. 2 shows the final geometry of a typical notched micro-cantilever fabricated out of the selected microstructure. The ion-induced secondary electron image reveals that the entire volume of the fabricated micro-cantilever consists predominantly of acicular ferrite (Fig. 2a). Fig. 2b shows the detailed dimensions of the sample. Preliminary micro-fracture tests of three cantilevers with slightly different dimensions fabricated within acicular ferrite [35] had demonstrated a reproducible behaviour. On this basis, two cantilevers were manufactured for the purpose of the current study. One cantilever was charged with hydrogen and then mechanically loaded; the other specimen was tested under as-fabricated (uncharged) conditions and was utilised as a reference. The deviations of the dimensions between the individual micro-cantilevers were within $\pm$ 100 nm range.

The lattice damage caused by FIB milling and imaging was evaluated using the program TRIM 2013 [36]. Simulations were generated for 30 kV Ga^+ ions impinging at an incidence angle of 0° (imaging) and at a glancing angle of 89° (milling of the sidewalls) onto the surface of an iron target. The distributions were calculated for 1000 ions for each of the incidence angles. The

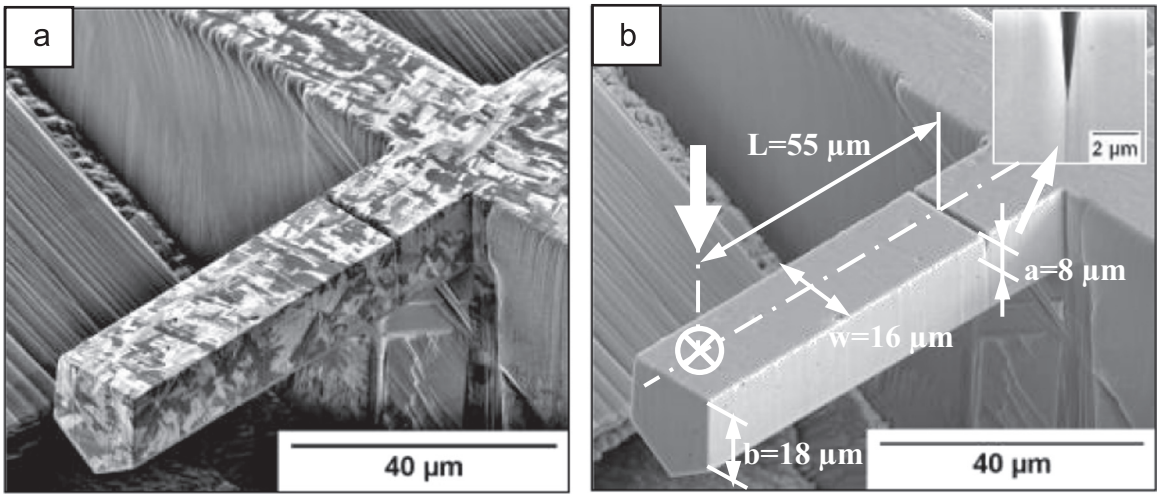

Fig. 2. (a) ion-induced secondary electron image reveals that the entire volume of a fabricated micro-cantilever consists of acicular ferrite, (b) dimensions of the micro-cantilever.

lattice damage caused by FIB milling and imaging was respectively evaluated to approximately 20 nm and 30 nm in material's depth. These simulations were consistent with the maximum damaged layer measured by TEM and Auger electron spectroscopy on copper under perpendicular ion impact at 30 kV (approximately 50 nm) [37]. The size of the damaged layer was negligible with respect to the dimensions of the micro-cantilevers and was, therefore, expected have no significant effect on the mechanical properties of the fabricated specimens [37,38].

2.3. EBSD data collection and processing

EBSD was applied to obtain a detailed quantitative characterisation of grain size, grain boundary misorientation, texture, and phase identity within the selected region. EBSD data was directly collected from the plane on top of the micro-cantilevers using the FEI Helios Nanolab 600 equipped with an EBSD detector (EDAX Hikari™) and the EDAX OIM™ Data Collection and Analysis 5.2 software (TSL Co., Ltd.). Acceleration voltage of SEM beam for the EBSD measurement was 20 kV and the beam current was 2.1 nA. The step size was 20 nm with a hexagonal scan grid. The sample surfaces were polished using a semi-automatic LaboForce polishing machine (Struers). The final polishing was achieved using a porous neoprene disc with a colloidal silica suspension (0.04 μm) prior to the micro-beam fabrication step.

2.4. Hydrogen charging

For the pre-charged sample, the as-fabricated micro-cantilever was electrochemically charged with hydrogen for 90 min by applying a cathodic current density of $-20\ \mathrm{mA\,cm^{-2}}$ in a 0.05 M H_2SO_4 solution. By using these parameters it was possible to maintain the surface integrity of the specimen (Fig. 3).

The hydrogen electrochemical oxidation method was applied to estimate the total amount of hydrogen absorbed during the charging procedure [39–41]. The oxidation currents were obtained by keeping the specimens at a potential of $+168\ \mathrm{mV_{Ag/AgCl}}$ in a deaerated 0.2 M NaOH solution for 2 h. This potential, which is higher than the hydrogen equilibrium potentials and lower than the passive film breakdown potential of the metal, allowed the oxidation reaction of the metal to be limited in this solution (see the uncharged reference curve, Fig. 4), and the oxidation reaction of hydrogen to be induced simultaneously. The total quantity of the hydrogen absorbed (Q_H^{abs}) by the weld metal can be thus expressed as:

$$Q_H^{abs} = \int_0^t \left[I_H(t) - I_{ref}(t) \right] dt, \quad \text{at } E_{anodic} = \text{const.} \tag{1}$$

where I_H (t) is the oxidation current for the hydrogen charged specimen and I_{ref} (t) is the oxidation current for the specimen without hydrogen (Fig. 4). According to Faraday's law, hydrogen concentration, C_H, is related to Q_H^{abs} by the relation:

$$C_H = \frac{Q_H^{abs}}{zFv} \tag{2}$$

where F is the Faraday constant (96487 C $\mathrm{mol^{-1}}$), v is the effective volume of the specimen (in this case 0.5754 $\mathrm{cm^3}$) and z is the number of electrons ($z=1$). With the selected charging parameters, the hydrogen concentration in the specimen was thus measured as $1.038\times10^{-6}\ \mathrm{mol\,cm^{-3}}$, which corresponds to 0.132 ppm.

All electrochemical tests were conducted with a Gamry interface 1000™, using the specimens as the working electrode, a platinum mesh as the counter electrode and a silver/silver chloride electrode as the reference. All electrolytes used were prepared with analytical grade reagents and distilled water. The experiments were all performed at room temperature.

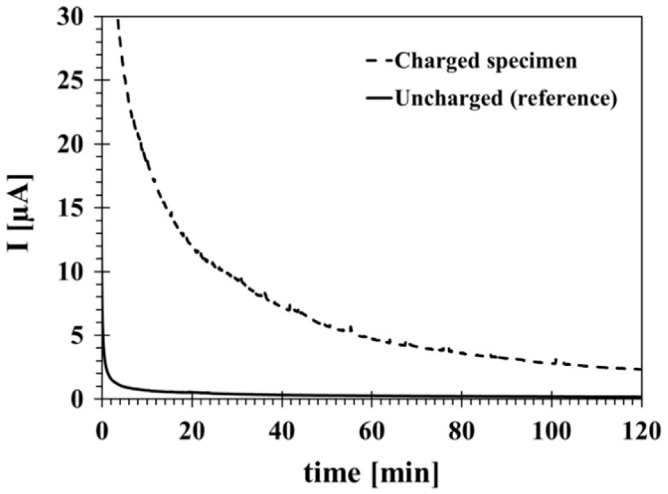

Fig. 4. Hydrogen discharging process under anodic polarisation ($+168\ \mathrm{mV_{Ag/AgCl}}$) in 0.2 M NaOH for the electrochemically charged specimen (at $20\ \mathrm{mA\,cm^{-2}}$ for 90 min in 0.05 M H_2SO_4 solution) and the reference specimen (uncharged).

2.5. Stress intensity factor evaluation

An IBIS software controlled nanoindentation system (Fischer-Cripps Laboratories Pty Ltd.) was used as a load cell to apply a bending force near the free end of the notched micro-cantilevers, while recording the load-deflection curves. The loading type was displacement-controlled with a loading displacement rate of $0.02\ \mu\mathrm{m\,s^{-1}}$ and a maximum displacement (beam deflection) for uncharged specimen of 18.5 μm because of the limitations of the instrument (nano-indenter). The selected indenter tip was spherical with a relatively large diameter of 40 μm to avoid penetration

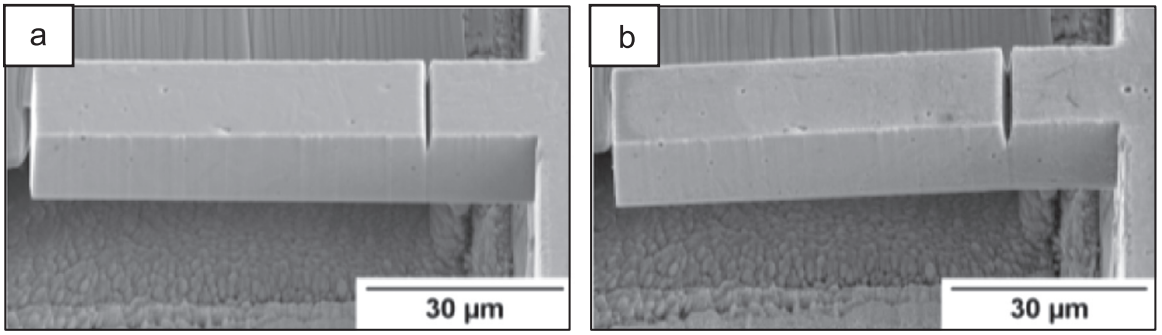

Fig. 3. SEM images showing the as-fabricated and tested micro-cantilever beam: (a) prior to the hydrogen charging procedure and testing, (b) after hydrogen charging procedure and testing (at the constant load of 14 mN) showing the conservation of the surface integrity despite the hydrogen charging procedure.

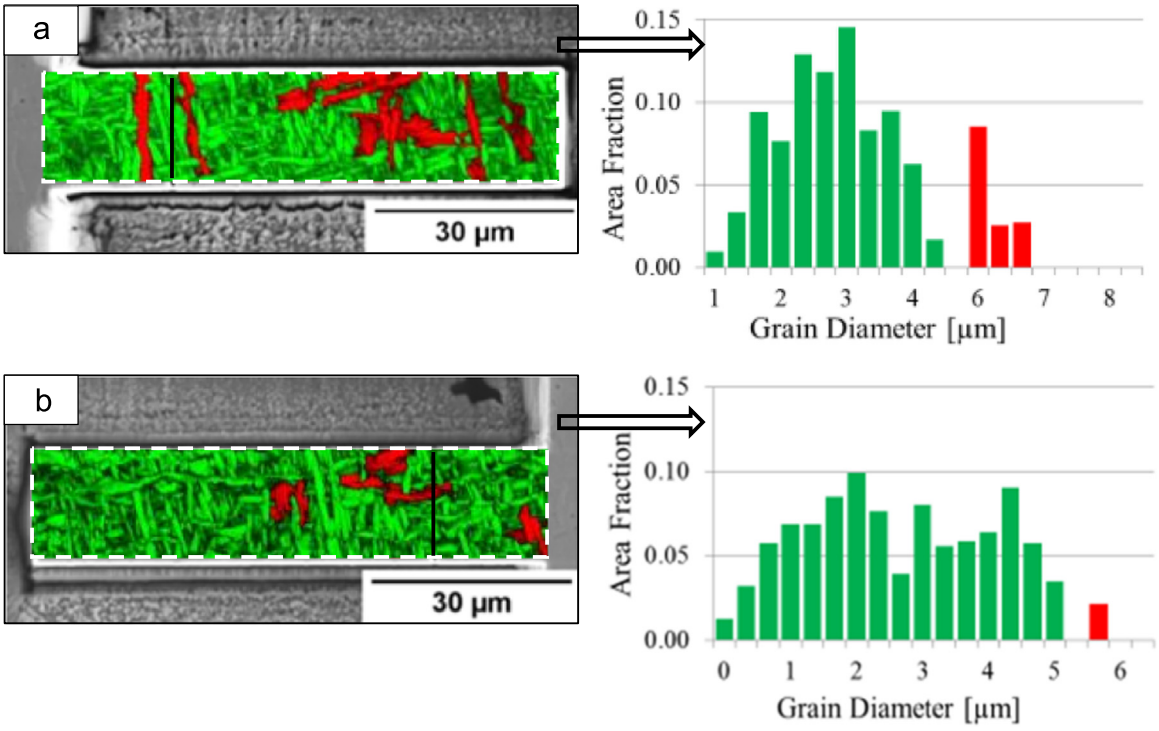

Fig. 5. Superimposed Grain Diameter and Image Quality (IQ) map highlighting the distribution of acicular ferrite (green) and PF(I)+WF(I)+B(I) (red) for: (a) the uncharged micro-cantilever, (b) the pre-charged micro-cantilever. The histogram charts illustrates the associated grain diameter distribution. Adjacent data points with misorientations $< 5°$ were considered to be part of the same grain. (For interpretation of the references to colour in this figure legend, the reader is referred to the web version of this article.)

and to minimise the local deformation in the contact area. The measured displacements, therefore, were dominated by the beam deflection rather than the deformation in the area of contact.

In order to simulate the time delayed nature of HACC, constant loads (5 mN and 14 mN) were applied for 12 h to the hydrogen pre-charged micro-cantilever.

The stress intensity factors K_I corresponding to the pentagonal cross-section of the micro-cantilevers were calculated from the following equation [25]:

$$K_I = \sigma\sqrt{\pi a}\, F\left(\frac{a}{b}\right) \tag{3}$$

where σ is the nominal stress, a is the notch depth (8 μm) and $F(a/b)$ is a dimensionless shape factor, which is related to the specimen geometry. For a cantilever subjected to a bending force, P, σ can be calculated as:

$$\sigma = \frac{PLy}{I}, \tag{4}$$

where P is the applied load, L is the distance between the notch and the point of loading on the cantilever (Fig. 2b), I is the moment of inertia of the beam cross section, and y is the vertical distance between the upper surface and the neutral plane. I and y were calculated using the following equations [25]:

$$I = \frac{wb^3}{12} + \left(y - \frac{b}{2}\right)^2 bw + \frac{w^4}{288} + \left[\frac{b}{6} + (b - y)\right]^2 \frac{w^2}{4}, \tag{5}$$

$$y = \frac{\frac{b^2 w}{2} + \frac{w^2}{4}\left(b + \frac{w}{6}\right)}{bw + \frac{w^2}{4}}, \tag{6}$$

where b is the height of the parallel vertical face (18 μm) and w is the width of the micro-beam (16 μm), (see Fig. 2b). The equation for the dimensionless shape factor, F, was provided by Di Maio and Roberts [25] who conducted extensive finite element simulations for a wide range of specimen geometries and provided the following equation for $0.3 \le (\frac{a}{b}) \le 0.5$:

$$F\left(\frac{a}{b}\right) = 1.85 - 3.38\left(\frac{a}{b}\right) + 13.24\left(\frac{a}{b}\right)^2 - 23.26\left(\frac{a}{b}\right)^3 + 16.8\left(\frac{a}{b}\right)^4, \tag{7}$$

For the fabricated specimens (Fig. 2b), we have: $I = 1.5545 \times 10^{-8}\ \text{mm}^4$, $y = 0.01112$ mm, and $F(a/b) = 1.58$ at $a/b = 0.44$.

The applicability of Eqs. (3)–(7) to the current specimen geometry was also verified with 3D linear-elastic finite element calculations. These calculations demonstrated that the difference between the numerical results and the analytical predictions is less than 20%. For simplicity reasons the analytical approach was selected for the quantitative analysis of the micro-scale testing results. These results are presented in Section 4.

3. Results

3.1. EBSD characterisations

The microstructural features for the fabricated micro-cantilevers were characterised via EBSD before hydrogen charging and mechanical loading as presented below.

3.1.1. Comparison of the microstructural architecture

The Grain Diameter map in Fig. 5a and b highlights the morphology and size distribution of individual grains according to their Equivalent Circular Area Diameter (green < 5 μm or red ≥ 5 μm) for the uncharged and pre-charged micro-cantilevers respectively. The histogram charts illustrate the distribution of the

Table 1
Ratio between the phase transformation products and average grain diameter for both uncharged and pre-charged micro-cantilevers.

	AF (%)	PF(I)+WF(I)+B (I) (%)	Average grain diameter (μm)
Uncharged specimen	86	14	3.25 ± 1.17
Pre-charged specimen	94	6	2.97 ± 1.05

different grain diameters within the aggregate. The data was used to determine the ratio between the percentage of acicular ferrite (AF) and other ferritic phases of primary ferrite PF(I), Widmanstätten ferrite WF(I) and bainite B(I) as well as the average grain diameter of the micro-cantilevers, i.e. AF+PF(I)+WF(I)+B (I) aggregate, (Table 1). The identification of the different phases was based on the size and shape of the individual grains according to the classification scheme for microstructures in steel welds proposed by Thewlis [42]. The results show that for the pre-charged micro-cantilever the proportion of acicular ferrite was slightly higher and the average grain diameter consequently lower than that for the uncharged micro-cantilever.

3.1.2. Comparison of grain boundary characteristics

The map in Fig. 6a and b highlights the grain boundary distribution of acicular ferrite in the uncharged and pre-charged micro-cantilevers respectively. The main proportion of boundaries were high angle boundaries (misorientation > 15°). The complete absence of grains with misorientation differences in the approximate range of 20–47° indicates that all the ferrite plates were formed within the same prior austenite grain [43,44]. The comparison of the grain boundary misorientation distributions between the uncharged and the pre-charged micro-cantilever shows no significant variations (Table 2).

The EBSD characterisations confirmed that the microstructure

Table 2
Grain boundary length distribution (in μm).

	0.5–15°	Coincident site lattice Σ3	15–180°
Uncharged specimen	1120	216	1284
Pre-charged specimen	1191	331	1378

was largely uniform across the specimens and the variations of the microstructural features between the fabricated micro-cantilevers were almost negligible.

3.2. Estimation of the acicular ferrite yield strength

The nano-indenter equipped with a Berkovich diamond tip was used to measure the hardness and Young's modulus of the considered acicular ferrite region. Three indentation tests at a maximum load of 50 mN were conducted and the results were averaged as follows. The Young's modulus, universal hardness and Vickers hardness were measured as respectively: 195 ± 13 GPa, 3.36 ± 0.12 GPa and 317 ± 11 HV. An estimation of the yield strength of the acicular ferrite can be made using the empirical relationship between strength and hardness for X65 as derived in [45]:

$$\sigma_Y = 2\,\mathrm{HV} + 105, \tag{8}$$

which results in a yield strength of 740 MPa. The yield strength of the acicular ferrite has been reported to be in the range of 480–750 MPa [46–49]. The differences can be attributed to the steel composition as well as the testing procedures.

3.3. Mechanical loading

Fig. 7 shows the load-deflection curves for the uncharged and

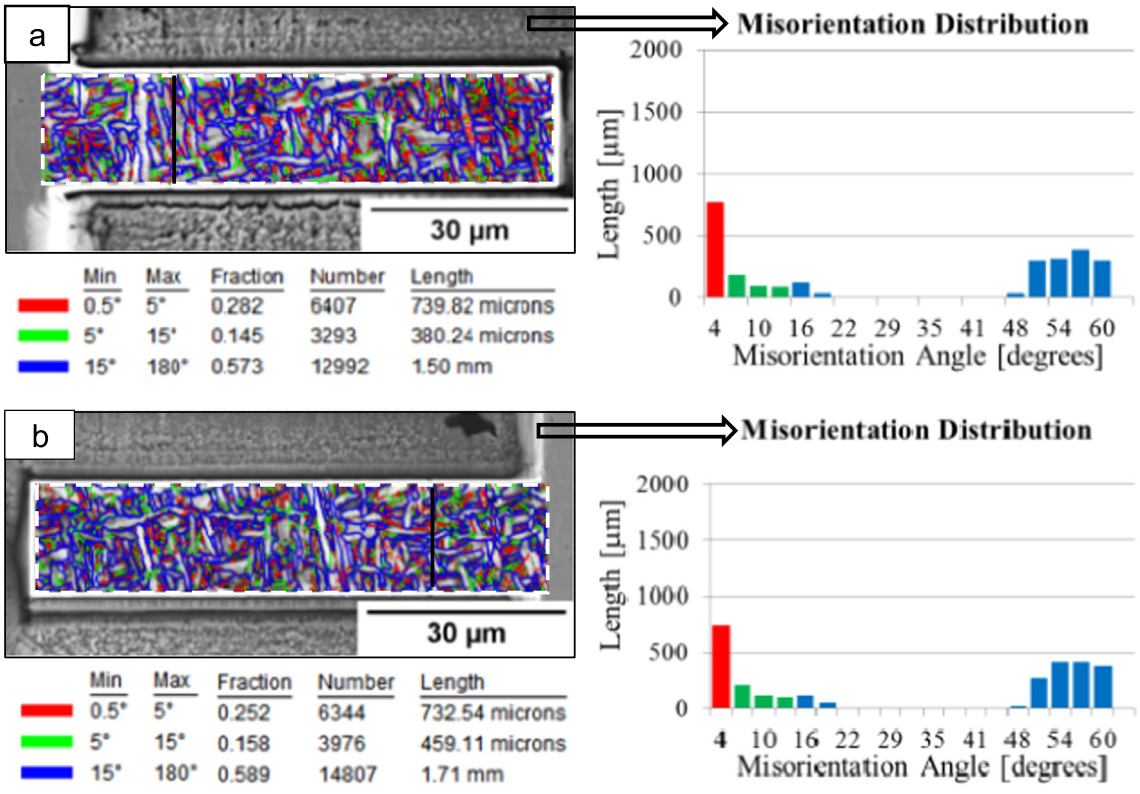

Fig. 6. Superimposed Grain Boundary and IQ map for (a) the uncharged micro-cantilever, (b) the pre-charged micro-cantilever, revealing a large proportion of boundaries with misorientation > 15°.

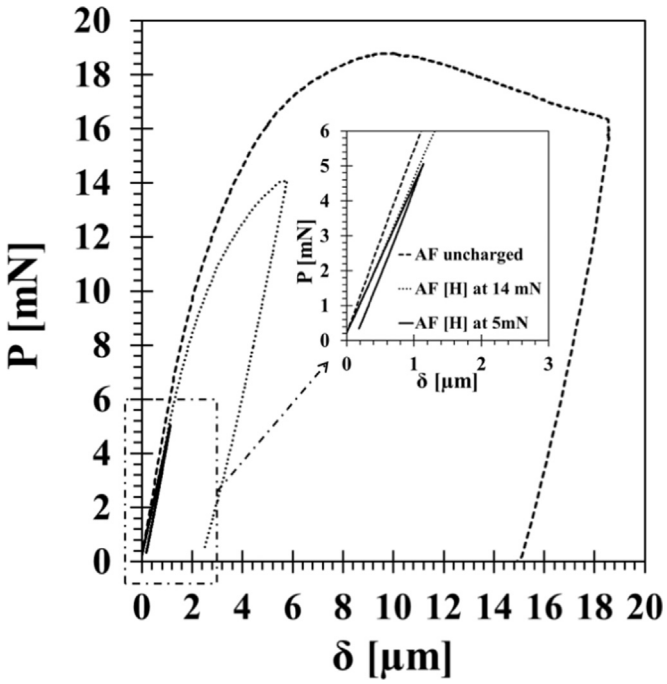

Fig. 7. Load-deflection curves for un-charged and pre-charged [H] acicular ferrite (AF) micro-cantilevers.

pre-charged sharply notched specimens. The uncharged specimen was loaded until failure. It was used to identify the critical failure load and identify the range of loading conditions for the hydrogen charged specimen. The hydrogen charged specimen was tested at constant loads of 5 mN and 14 mN, which correspond to approximately 25% and 75% of the critical failure load for the uncharged specimen, respectively. These loads, in accordance with Eqs. (3)–(7), generated stress intensity factors values of respectively 1.56 and 4.36 MPa $m^{1/2}$. Each of these loads was applied approximately within five minutes after completion of the hydrogen charging procedure and held constant for 12 h.

The traditional crack growth monitoring method based on the measurement of specimen compliance [50] was not possible as Young's modulus changed during the prolonged tests. In the charged specimens Young's modulus was notably lower as indicated by lower values of the slope of the linear part of the load-deflection diagram (Fig. 7). During unloading after 12 h of holding time, Young's modulus of pre-charged specimen has fully recovered to the corresponding value of the uncharged specimen. This indicates that hydrogen largely diffused out of the sample during the 12-h tests. Therefore, the crack growth (or absence of the crack propagation) was carefully evaluated from fractographic observations after the testing as presented below.

3.4. Fractographic observations

The fracture mode of the uncharged micro-cantilever was ductile and resulted in severe blunting of the notch tip (Fig. 8a), while an apparently brittle crack initiated from the notch tip of the hydrogen pre-charged micro-cantilever tested at the constant load of 14 mN (Fig. 8b and c). The crack length of 1.55 μm seemed thereby to be insufficient to cause cross-sectional failure. The fracture morphology of the crack was defined by tear ridges that followed the direction of the crack propagation (Fig. 8d–f). The opposing fracture surfaces matched thereby ridge to ridge. In addition, the high resolution secondary electron images in Fig. 8d–f also reveal that the hydrogen charging introduced some minor surface damage as evident in the regions adjacent to the crack path. No cracks, plastic deformations, deflection or changes to the original shape (Fig. 2) were observed for the pre-charged cantilever loaded at the constant load of 5 mN.

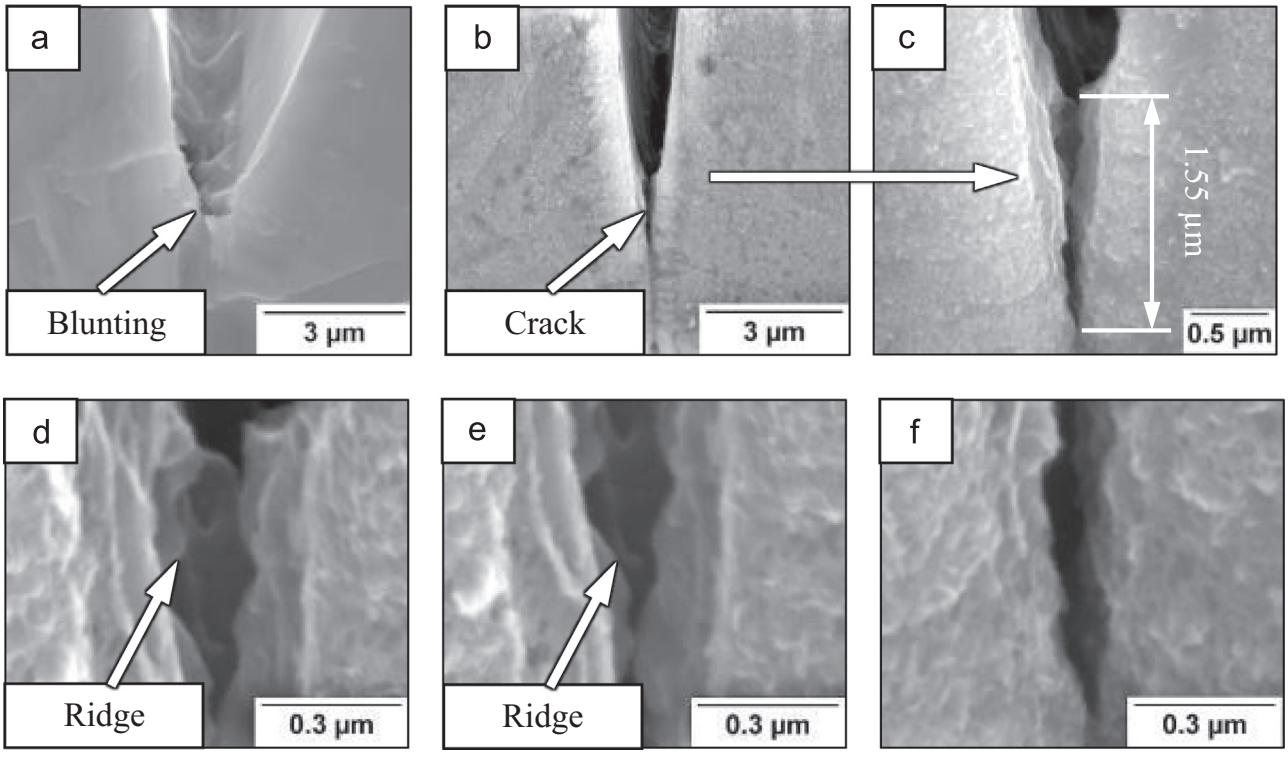

Fig. 8. Secondary electron images showing notch tip after testing for: (a) uncharged micro-cantilever, (b) pre-charged micro-cantilever, (c) pre-charged micro-cantilever at higher magnification. Secondary electron images showing the fracture surface morphologies at: (d) crack initiation, (e) crack propagation, (f) crack arrest.

4. Discussion

The outcomes of testing the HACC susceptibility of the acicular ferrite are summarised in Table 3. This table also provides the corresponding values of stress intensity factors as calculated using the analytical approach presenter earlier (Section 2.5), as well as the averaged crack growth rate as evaluated from fractographic examinations.

From the conducted experiments it was not possible to identify precisely the value of $K_{th.}$ However, it can be stated that the threshold value ranges between 1.56 and 4.36 MPa $m^{1/2}$. This identified range is significantly below the typical values of K_{th} for low and medium carbon steels. Indeed, the threshold below which crack does not grow in X70 weld metal charged with a similar concentration of hydrogen has been reported to be around 147 MPa $m^{1/2}$ [22]. In medium carbon steels having the values of yield strength close to those of the weld metal and acicular ferrite (i.e. between 580 and 830 MPa) the K_{th} was measured under various testing conditions between 42 and 88 MPa $m^{1/2}$ [18,19]. Similarly, for low carbon steels with yield strength values between 310 and 760 MPa the K_{th} laid typically between 37 and 78 MPa $m^{1/2}$ [20,21]. Appears a K_{th} nevertheless exists at the microstructural level, as no cracking was observed at the constant applied load of 5 mN and the hydrogen was largely diffused out of the sample at the end of the test restricting further crack growth assisted by hydrogen.

At applied loading above 10 mN the load deflection curves, for both charged and uncharged specimens, demonstrate a non-linear behaviour, which indicates that the near notch (crack) tip plastic zone becomes significant with respect to the sizes of the micro-cantilever. In this case non-linear fracture mechanics parameters, such as J-integral or crack opening displacement could be more appropriate for the characterisation of stress state near the crack tip. Based on the ASTM E1820 standard [51] a procedure for the evaluation of J-integral in micro-tests was provided in [50]. However, the stress intensity factor was used in our study as a measure of the intensity of strain-stress field at the notch tip to allow comparison with the corresponding values obtained from standard (macroscopic) tests.

Since dissolved monoatomic hydrogen occupies a specific volume within interstitial lattice sites, it tends to migrate from compressed to expanded regions within the crystal lattice until an equilibrium concentration profile is established [52]. Hydrostatic tensile stresses are hence a driving force for interstitial lattice diffusion of hydrogen towards the dilatation zone, which is located at the notch (crack) tip, where hydrogen may accumulate and thereby incrementally degrade the localised fracture resistance of the microstructure with time [53]. A sufficient level of hydrogen concentration necessary for failure formation may thus only occur periodically, in highly localised regions, explaining the slow crack growth rate. In these microscopic regions, failure may then occur either due to the formation of microvoids [2,14,54], or due to the formation of miniscule cracks [11,12]. In both cases the crack would propagate gradually due to ductile tearing (formation of tear ridges, as observed in Fig. 8d–f) if the remaining ligaments are too weak to accommodate the stresses. The crack growth rate was measured to be several orders of magnitudes lower than it is typically reported at the macroscopic level. Indeed, the lower bound values of subcritical crack growth near the threshold level were reported at around 10^{-9} m s^{-1} [18,21], and in our tests the crack growth rate averaged over 12 h was as low as 3.59×10^{-11} m s^{-1}.

A qualitative analysis of the load-deflection curves (Fig. 7) indicates that the yield strength and Young's modulus of hydrogen pre-charged specimen are lower. This implicates that hydrogen had caused a notable decrease of the both properties of the acicular ferrite microstructure since for charged specimens the slope of the linear part of load deflection diagrams is notably smaller and deviation from linear behaviour occurs much earlier. This behaviour can be explained within the microscopic theories developed in the past. The HELP (Hydrogen Enhanced Localized Plasticity) model (theory) [2,14] provides a rational explanation for a decrease of the yield strength. This model postulates a hydrogen enhanced dislocation mobility which in turn may promote microscopic plastic deformation at lower stress levels. Also, the AIDE (Adsorption Induced Dislocation Emission) model [54] suggests that the weakening of the inter-atomic bonds at the crack tip facilitates the injection of dislocations which results in an extensive dislocation activity at the vicinity of the crack tip and may therefore also lead to a reduction of the localised yield strength. The observed decrease of the Young's modulus is also consistent with most of the previous results reported in the literature [21,55,56], and it was attributed to the reduction of the cohesive energy of the iron lattice [55].

Table 3
Summary of the micromechanical test parameters and results for acicular ferrite charged with 0.132 ppm of hydrogen.

Load (mN)	σ (MPa)	K_I (MPa $m^{1/2}$)	Crack growth	Averaged crack growth rate (m s^{-1})
5	198.1	1.56	no	–
14	550.8	4.36	yes	3.59×10^{-11}

5. Conclusion

This work for the first time has demonstrated that micro-fracture tests can be successfully accomplished for an individual microstructural constituent within a very small material volume, pre-charged with hydrogen and under controlled loading conditions. For acicular ferrite, the selected constituent in this study, under pre-charged conditions with 0.132 ppm of hydrogen, it was found that:

- The threshold stress intensity factor, K_{th}, of acicular ferrite sourced from weld metal is well below the corresponding threshold for weld metal, low and medium carbon steels having similar yield strength levels. The K_{th} values to initiate fracture propagation in acicular ferrite is measured between 1.56 MPa $m^{1/2}$ and 4.36 MPa $m^{1/2}$, which is almost one and two order of magnitude lower than for carbon steels and weld metal, respectively. This finding is very intriguing as acicular ferrite is normally considered to be particularly beneficial for the strength and fracture toughness as well as for the WMHACC resistance of welded joints. However, the latter consideration was based on outcomes of testing macro-samples incorporating acicular ferrite together with other constituents rather than on a micro-samples fully consisting of this microstructural constituent [34].
- The crack growth rates in the vicinity of the threshold, appear to be significantly lower than those reported from the previous macroscopic tests.
- The yield strength and the elastic modulus decreased with the presence of hydrogen, which is consistent with the most of previous macro- and micro-results reported in the literature.

In summary, the main outcome of the conducted tests is the demonstration that subcritical hydrogen cracks can grow at the micro-scale at stress intensity factors well below the stress intensity factor threshold measured with conventional tests at the macro-scale. It seems that all fracture toughening mechanisms may not be fully activated at the micro-scale. These mechanisms

may include roughness or plasticity induced closure, which cannot be developed in micro-samples due to the limited crack growth increments [57].

This study was only limited to acicular ferrite as the main purpose was to demonstrate the possible miniaturisation of IHAC fracture testing at the scale of individual microstructural constituents. The comparison of HACC resistance of diverse microstructural constituents was beyond the scope of the current paper. However, the presented method can be applied to different types of materials and microstructures to study the susceptibility of individual constituents to hydrogen cracking as well as to probe the change of their intrinsic mechanical properties. These studies will contribute to the understanding of the fundamental microstructural factors that control the IHAC susceptibility of many metals and alloys and thus enable the design of more IHAC resistant materials through microstructural engineering by avoiding IHAC susceptible microstructural constituents and promoting IHAC resistant ones.

Acknowledgements

This work was funded by the Energy Pipelines CRC, supported through the Australian Government Cooperative Research Centres Program (RP1-02B). The funding and in-kind support from the APGA-RSC (81107701) is gratefully acknowledged. The authors would like to thank Rahim Kurji (Ph.D. Candidate) for the fabrication of the weld samples. The authors acknowledge the facilities, and the scientific and technical assistance of the Australian Microscopy & Microanalysis Research Facility at the University of Adelaide, in particular its former director Mr. John Terlet, its current director Dr. Angus Netting, Mr. Leonard Green and Dr. Animesh Basak. Without their dedication and wealth of knowledge this work would not have been possible.

References

[1] W.H. Johnson, On some remarkable changes produced in iron and steel by the action of hydrogen and acids, Nature 11 (1875) 393.
[2] C.D. Beachem, A new model for hydrogen-assisted cracking (hydrogen “embrittlement”), Metall. Trans. 3 (1972) 441–455.
[3] R.P. Gangloff, Hydrogen assisted cracking of high strenght alloys, in: I. Milne, R. O. Richie, B. Karihaloo (Eds.), Comprehensive Structural Integrity, Elsevier Science, New York, 2003, pp. 31–101.
[4] S. Chu, A. Majumdar, Opportunities and challenges for a sustainable energy future, Nature 488 (2012) 294–303.
[5] A. Barnoush, H. Vehoff, Recent developments in the study of hydrogen embrittlement: Hydrogen effect on dislocation nucleation, Acta Mater. 58 (2010) 5274–5285.
[6] P.J. Ferreira, I.M. Robertson, H.K. Birnbaum, Hydrogen effects on the interaction between dislocations, Acta Mater. 46 (1998) 1749–1757.
[7] S.P. Lynch, Metallographic contributions to understanding mechanisms of environmentally assisted cracking, Metallography 23 (1989) 147–171.
[8] H. Vehoff, W. Rothe, Gaseous hydrogen embrittlement in FeSi- and Ni-single crystals, Acta Metall. 31 (1983) 1781–1793.
[9] M.L. Martin, I.M. Robertson, P. Sofronis, Interpreting hydrogen-induced fracture surfaces in terms of deformation processes: a new approach, Acta Mater. 59 (2011) 3680–3687.
[10] H.H. Johnson, A.R. Troiano, Crack initiation in hydrogenated steel, Nature 179 (1957) 777.
[11] A.R. Troiano, The role of hydrogen and other interstitials in the mechanical behaviour of metals, Trans. ASM 52 (1960) 54–80.
[12] R.A. Oriani, Testing of the decohesion theory of hydrogen induced crack propagation, Scr. Metall. 6 (1972) 681–688.
[13] R.A. Oriani, J.P. Hirth, M. Smialowski, Hydrogen Degradation of Ferrous Alloys, Noyes, Park Ridge, NJ, USA, 1985.
[14] H.K. Birnbaum, P. Sofronis, Hydrogen-enhanced localized plasticity—a mechanism for hydrogen-related fracture, Mat. Sci. Eng. A 176 (1994) 191–202.
[15] S.P. Lynch, Hydrogen embrittlement (HE) phenomena and mechanisms, in: V. S. Raja, T. Shoji (Eds.), Stress Corrosion Cracking: Theory and Practice, Woodhead Publishing Ltd., Cambridge, 2011, pp. 90–126.
[16] J.M. Barsom, S.T. Rolfe, Fracture and Fatigue Control in Structures, 2nd Ed., Prentice-Hall, Englewood Cliffs, NJ, 1987.
[17] B.F. Brown, C.D. Beachem, A study of the stress factor in corrosion cracking by use of the precracked cantilever-beam specimen, Corros. Sci. 5 (1965) 745–750.
[18] A.W. Loginow, E.H. Phelps, Steels for seamless hydrogen pressure vessels, Corrosion 31 (1975) 404–412.
[19] W.W. Gerberich, Y.T. Chen, A threshold stress intensity concept for environmental cracking, Int. J. Fract. 9 (1973) 369–371.
[20] G.-H. Yu, B.-L. Jiang, L.-J. Qiao, Y.-B. Wang, W.-Y. Chu, Threshold stress intensity for hydrogen—induced cracking of tubular steel, Scr. Mater. 12 (1997) 1467–1470.
[21] S. Homrossukon, S. Mostovoy, J.A. Todd, Investigation of hydrogen assisted cracking in high and low strength steels, J. Press. Vessel Technol.: Trans. ASME 131 (2009) 1–11.
[22] V. Olden, A. Alvaro, O.M. Akselsen, Hydrogen diffusion and hydrogen influenced critical stress intensity in an API X70 pipeline steel welded joint – experiments and FE simulations, Int. J. Hydrog. Energy 37 (2012) 11474–11486.
[23] ASTM, Standard Test Method for Determining a Threshold Stress Intensity Factor for Environment-Assisted Cracking of Metallic Materials, Designation E1681-99, vol. 03.01, ASTM International, West Conshohocken, PA, 2000.
[24] Y. Katz, N. Tymiak, W.W. Gerberich, Nanomechanical probes as new approaches to hydrogen/deformation interaction studies, Eng. Fract. Mech. 68 (2001) 619–646.
[25] D. Di Maio, S.G. Roberts, Measuring fracture toughness of coatings using focused-ion-beam-machined microbeams, J. Mater. Res. 20 (2005) 299–302.
[26] M. Deutges, I. Knorr, C. Borchers, C.A. Volkert, R. Kirchheim, Influence of hydrogen on the deformation morphology of vanadium (100) micropillars in the α-phase of the vanadium–hydrogen system, Scr. Mater. 68 (2013) 71–74.
[27] N. Kheradmand, J. Dake, A. Barnoush, H. Vehoff, Novel methods for micromechanical examination of hydrogen and grain boundary effects on dislocations, Philos. Mag. 92 (2012) 3216–3230.
[28] S. Wurster, C. Motz, M. Jenko, R. Pippan, Micrometer-sized specimen preparation based on ion slicing technique, Adv. Eng. Mater. 12 (2010) 61–64.
[29] B.N. Jaya, V. Jayaram, Fracture testing at small-length scales: from plasticity in Si to brittleness in Pt, JOM: J. Miner. Met. Mater. Soc. (2015), http://dx.doi.org/10.1007/s11837-015-1489-2.
[30] J.L. Davidson, S.P. Lynch, A. Majumdar, in: J.L. Davidson, D.L. Olson (Eds.), Hydrogen Managament in Steel Weldments, The Organising Committee of the Joint Seminar on behalf of Defence Science and Technology Association and Welding Technology Institute of Australia Melbourne, Australia, 1997.
[31] N. Yurioka, H. Suzuki, Hydrogen assisted cracking in C–Mn and low alloy steel weldments, Int. Mater. Rev. 35 (1990) 217–249.
[32] R. Ghomashchi, W. Costin, R. Kurji, Evolution of weld metal microstructure in shielded metal arc welding of X70 HSLA steel with cellulosic electrodes: a case study, Mater. Charact. 107 (2015) 317–326.
[33] N. Alam, H. Li, L. Chen, D. Dunne, B. Feng, I. Squires, F.J. Barbaro, Fracture-microstructure relationships of hydrogen assisted cracking in steel weldments, Mater. Res. 3 (1996) 74–78.
[34] E. Mazancová, Z. Rucká, K. Mazanec, Comparison of microfractographic behaviour of acicular ferrite and bainite and hydrogen cracking resistance, Arch. Mater. Sci. 28 (2007) 95–99.
[35] W.L. Costin, O. Lavigne, V. Linton, I.H. Brown, A.G. Kotousov, F.J. Barbaro, R. Ghomashchi, Micromechanical examination of the relationship between weld metal microstructure and hydrogen assisted cold cracking (Paper no.: S10-02), in: Proceedings of the 6th International Pipeline Technology Conference, Ostend, Belgium, October 2013.
[36] J.F. Ziegler, J.P. Biersack, U. Littmark, The Stopping Power and Range of Ions in Solids, Pergamon Press, New York, 1985.
[37] D. Kiener, C. Motz, M. Rester, M. Jenko, G. Dehm, FIB damage of Cu and possible consequences for miniaturized mechanical tests, Mater. Sci. Eng. 459 (2007) 262–272.
[38] J. Ast, T. Przybilla, V. Maier, K. Durst, M. Göken, Microcantilever bending experiments in NiAl – evaluation, size effects, and crack tip plasticity, J. Mater. Res. 29 (2014) 2129–2140.
[39] M. Yan, Y. Weng, Study on hydrogen absorption of pipeline steel under cathodic charging, Corros. Sci. 48 (2006) 432–444.
[40] J. Capelle, I. Dmytrakh, Z. Azari, G. Pluvinage, Evaluation of electrochemical hydrogen absorption in welded pipe with steel API X52, Int. J. Hydrog. Energy 38 (2013) 14356–14363.
[41] T.H. Nam, J.G. Kim, Y.S. Choi, Electrochemical hydrogen discharge of high-strength low alloy steel for high-pressure gaseous hydrogen storage tank: effect of discharging temperature, Int. J. Hydrog. Energy 38 (2013) 999–1003.
[42] G. Thewlis, Classification and quantification of microstructures in steels, Mater. Sci. Technol. 20 (2004) 143–160.
[43] Z. Nishiyama, X-ray Investigation on the Mechanism of the Transformation From Face-centered Cubic Lattice to Body-centered Cubic Lattice, Science Report of the Tohoku Imperial University, no. 23, 1934, pp. 637–664.
[44] G. Wassermann, Über den Mechanismus der α-γ Umwandlung des Eisens', Mitteilungen aus dem Kaiser-Wilhelm-Institut für Eisenforschung, no. 17, 1935, pp. 149–155.
[45] S.H. Hashemi, Strength–hardness statistical correlation in API X65 steel, Mater. Sci. Eng. A 528 (2011) 1648–1655.
[46] M.-C. Zhao, K. Yang, Y.-Y. Shan, Comparison on strength and toughness behaviors of microalloyed pipeline steels with acicular ferrite and ultrafine ferrite, Mater. Lett. 57 (2003) 1496–1500.
[47] Y. Weng, Ultra-Fine Grained Steels, Co-published by Mettalurgical Industry Press, Beijing and Springer-Verlag GmbH Berlin Heidelberg, Beijing, New York,

2009, p. 26.
[48] M. Diaz-Fuentes, A. Iza-Mendia, I. Guttierez, Analysis of different acicular ferrite microstructures in low-carbon steels by electron backscattered diffraction. Study of their toughness behavior, Metall. Mater. Trans. A 34A (2003) 2505–2516.
[49] L. Shi, Z. Yan, Y. Liu, C. Zhang, Z. Qiao, B. Ning, H. Li, Improved toughness and ductility in ferrite/acicular ferrite dual-phase steel through intercritical heat treatment, Mater. Sci. Eng. A 590 (2014) 7–15.
[50] S. Wurster, C. Motz, R. Pippan, Characterization of the fracture toughness of micro-sized tungsten single crystal notched specimens, Philos. Mag. 92 (2012) 1803–1825.
[51] ASTM, Standard Test Method for Measurement of Fracture Toughness, Designation E1820-13E01, ASTM International, West Conshohocken, PA, 2013.
[52] R. Kirchheim, Solid State Physics, Academic Press, Cambridge, MA, USA, 2004.
[53] I.M. Bernstein, The role of hydrogen in the embrittlement of iron and steel, Mater. Sci. Eng. 6 (1970) 1–19.
[54] S.P. Lynch, Environmentally assisted cracking: overview of evidence for an adsorption-induced localised-slip process, Acta Met. 36 (1988) 2639–2661.
[55] M. Ortiz, J. Ovejero-Garcia, Effect of hydrogen on Young's modulus of AISI 1005 and 1070 steels, J. Mater. Sci. 27 (1992) 6777–6781.
[56] D. Psiachos, T. Hammerschmidt, R. Drautz, Ab initio study of the modification of elastic properties of α-iron by hydrostatic strain and by hydrogen interstitials, Acta Mater. 59 (2011) 4255–4263.
[57] J. Codrington, A. Kotousov, A crack closure model of fatigue crack growth in plates of finite thickness under small-scale yielding conditions, Mech. Mater. 41 (2) (2009) 165–173.